The Dissertation Committee for Keaton John Bell
certifies that this is the approved version of the following dissertation:

Pulsational Oddities at the Extremes of the DA White Dwarf Instability Strip

Committee:

D. E. Winget, Supervisor

M. H. Montgomery, Co-supervisor

Charles F. Claver

S. O. Kepler

E. L. Robinson

J. Craig Wheeler

Pulsational Oddities at the Extremes of the DA White Dwarf Instability Strip

by

Keaton John Bell

DISSERTATION

Presented to the Faculty of the Graduate School of

The University of Texas at Austin

in Partial Fulfillment

of the Requirements

for the Degree of

DOCTOR OF PHILOSOPHY

THE UNIVERSITY OF TEXAS AT AUSTIN

August 2017

Dedicated to my grandparents.

Acknowledgments

As much as I love the study and practice of observational astronomy, one of the things that attracted me most to this field was my perception of astronomers as supportive, thoughtful, and encouraging. I have found this to be very true of my colleagues in the Department of Astronomy at the University of Texas at Austin. I could not have successfully completed this PhD thesis without the help and support of many important people. I would be remiss to not acknowledge their contributions here.

It was the infectious enthusiasm that Don expressed to me at an evening party during my recruitment visit to the department that influenced my decision to pursue my PhD at Texas. By selecting a research group in advance, I was able to hit the ground running with excitement for white dwarf stars. While the specific focus of my work has shifted slightly over the years (as Don said it would), Don's encouragement never faltered. I have benefited greatly from Don's deep intuition as both a theorist and observer of white dwarf stars. I owe my care in observing to the drills that we ran in a closed dome as it poured rain through our entire first run at McDonald Observatory together.

Mike's supervision has been very complementary to Don's. For me, whose talents are mostly observational, Mike is never hesitant to point out when something I want to observe is theoretically unfeasible. He is able to

explain technical concepts to me in a way that I can easily understand and he is my go-to colleague when I have trouble working though a complex line of reasoning. Besides our cooperative research ventures, our work training undergraduates in astronomical research skills though the Freshman Research Initiative White Dwarf Stream has been a highlight of my time at UT.

My other committee members have been great allies as well. Discussions with Rob have really stirred my interest in data analysis and statistical methods, and he has provided some key insights that have made me a better scientist. Craig has been extremely supportive from the day we met at an American Astronomical Society meeting and he informed me that I would be admitted to UT-Austin. Kepler has been a close scientific collaborator, and he regularly shares valuable insights on survey data and recent papers via email or Skype. Chuck brought the Large Synoptic Survey Telescope into focus as an important facility for future stellar variability studies, and I have internalized as a career goal to be heavily involved in the analysis of these data.

The other members of the UT white dwarf group have helped me along my path. J.J. was both the senior graduate student and my roommate for my first two years in the department, and his prolific graduate work was a model for my own efforts. He has remained my closest collaborator and most constructive critic. Barbara and I have contributed observations to each other's projects, and I always appreciate the observational ideas, scientific context, and career advice that she shares in our group discussions. Zach has impressed me with his recent work to improve our instrumentation at McDonald, and

I am glad to be turning over the role of primary group observer to someone so enthusiastic and capable. While our scientific projects haven't overlapped tremendously, I am always interested to hear more about the work Fabi is doing with clusters, as I am with the experimental work Ross and Thomas are doing creating white dwarf photospheres at Sandia National Labs. It seems fitting that Thomas and I should defend our dissertation the same week since we joined the white dwarf group together from the same undergraduate institution. Karen is like an honorary member of the group and I really appreciate her support in life and in observing at McDonald.

My 225 nights of observing on the McDonald Observatory 2.1-meter Otto Struve telescope is a recent record. I owe a lot to the support staff out there, especially Dave, John, and Coyne. Thank you for keeping everything running smoothly, for making constant improvements, and just for stopping by to say hello. The Astronomers Lodge was like a second home to me, but with better food thanks to Emma, Anneke, and the rest of the staff. I can't wait for my next opportunity to observe at McDonald again.

I cannot exhaustively thank everyone with whom I have had the pleasure to collaborate on and communicate white dwarf science, but I want to highlight a few: the ELM Survey group (Mukremin, Warren, and Alex); Boris, Pier-Emmanuel, and others at Warwick; Chris's group at UNC; my Brazilian colleagues, including Ingrid and Alejandra; and individually Agnes, Alejandro, and Anjum.

The folks at the Central Texas Astronomical Society—Dean Chandler

in particular—have been very generous in making their 0.6-meter telescope at Meyer Observatory available to me and my students.

Though it predates the work described here, I must also thank my undergraduate research advisor, Suzanne Hawley from the University of Washington, as well as her graduate students Eric Hilton and Jim Davenport, for originally getting me interested and engaged in stellar variability research.

Most of my friends in Austin have been astronomy graduate students, and I have enjoyed celebrating and commiserating over the years with the likes of John, Chalence, Chris, Jacob, Kevin, J.J., Gully, Manos, Brian, Kyle, Marshall, Emma, Matt, and everyone else who has joined me for an after-work beer at Friday happy hour at Crown and Anchor through the years. Playing intramural softball with my teammates on the Ultra Deep-Fielders has also been good for my mental and physical health. I must also specifically thank Tom for organizing so many great social events over the years including volleyball, dinners, and holiday and boat parties.

Grace has been my greatest supporter and closest friend for over four years. When I have faced particularly stressful deadlines or problems, she has put in extra effort to take care of more than her share of the housework. But mostly we've just had a whole lot of fun together. I love you Grace! Kitty too.

Finally, my parents taught me the importance of education and have supported me my entire life. I set high standards for myself thanks to my upbringing and so far it's mostly working out. Thanks Mom and Dad!

Pulsational Oddities at the Extremes of the DA White Dwarf Instability Strip

Publication No. _____

Keaton John Bell, Ph.D.
The University of Texas at Austin, 2017

Supervisor: D. E. Winget
Co-supervisor: M. H. Montgomery

White dwarf stars are the remnant products of the vast majority of Galactic stellar evolution. They are compact objects that serve as remote laboratories for studying high energy/density physics. The outer regions of hydrogen-atmosphere (DA) white dwarfs become convective and able to drive global, nonradial, gravity-mode pulsations below roughly 12,500 K. The pulsations propagate through and are affected by the interior structures of these stars. The oscillations cause a pulsating star to exhibit brightness variations at its characteristic frequencies as a physical system. These frequencies can be measured through Fourier analysis of time series photometric observations.

I have focused my studies on new pulsational phenomena near the cool and low-mass edges of the DA white dwarf instability strip, using extensive space-based data from the *Kepler* spacecraft and the *K2* mission, as well as high-speed ground-based photometry from the 2.1-meter Otto Struve Telescope at McDonald Observatory (where I have personally observed 225 nights).

The extensive short-cadence (1-min exposures) light curve of the first DAV (DA variable) identified within the original *Kepler* field of view provided one of the most complete and sensitive records of white dwarf pulsations ever. The light curve also revealed a new, completely unexpected outburst-like phenomenon. I detected 178 instances of significant brightness enhancement in 20 months of observations of the cool DAV KIC 4552982. Recurring with a quasi-period of 2.7 days, the outbursts last 4–25 hours and increase the stellar flux by up to 17%. I estimate the energy of each outburst to be of-order 10^{33} ergs.

After the *Kepler* spacecraft suffered the loss of a second reaction wheel in May 2013, it began the *K2* mission, visiting new fields along the ecliptic roughly every 80 days. This allowed us to increase the number of DAVs with extensive space-based photometry, and we quickly discovered a second, more dramatic example of this new outburst behavior in PG 1149+057 (Hermes et al. 2015b). I have led the efforts to characterize the outbursts in DAVs ever since and have detected these events in eight DAVs through *K2* Campaign 10. Notably, spectroscopic effective temperature constraints place all known members of this new outbursting class of DAV near the cool (red) edge of the instability strip. With a growing outbursting class of DAV, we begin to study their ensemble outburst properties to inform a theory of their physical mechanism.

Much of my work from McDonald Observatory has continued in the recent tradition of discovering and characterizing new pulsating extremely low-mass (ELM) white dwarfs. After identifying candidate ELM variables

(ELMVs) from the ELM Survey catalog and parameters from model fits to the Sloan Digital Sky Survey spectroscopic data, I obtained time series photometric observations on the 2.1-meter Otto Struve telescope. I published SDSS J1618+3854 as the sixth member of this new class of variable star. However, most of the variability that I measured for this project was inconsistent with expectations for cooling track ELM white dwarfs. This includes long pulsation periods, high pulsation amplitudes, long eclipse timescales, and an overabundance of photometric variables that are not in confirmed short-period binaries from time series radial velocity measurements. Either the surface gravities of another class of star are being systematically overestimated from model fits to hydrogen line profiles in stellar spectra, or these observations are revealing an unexpectedly large population of recently formed pre-ELM white dwarfs. In total, I have discovered and characterized the variability of nine new pulsating stars in the spectroscopic parameter space of ELM white dwarfs, and I also developed an improved framework for interpreting measurements of tidally induced ellipsoidal variations in photometric binaries.

Beyond these main results of my thesis on extreme pulsating white dwarfs, I have also explored the limits of the detectability of stellar pulsations in extreme photometric data sets. I analyze long-cadence (30-minute) *K2* observations of two fairly typical DAVs in one such study, where the pulsations are severely undersampled. While accurate frequency determinations are nontrivial in such cases, I am able to recover the super-Nyquist frequencies of some pulsation modes with full *K2* precision with the help of a few hours

of ground-based observations. The space-based data, in turn, enables me to select the intrinsic frequency from the complex alias structure of multi-night ground-based data, providing a practical demonstration of the importance of carefully considering the spectral window. I apply what I have learned about undersampled data to anticipate upcoming pulsating star science in the next generation of synoptic time domain photometric surveys such as the Zwicky Transient Facility and the Large Synoptic Survey Telescope.

Table of Contents

Acknowledgments **v**

Abstract **ix**

List of Tables **xviii**

List of Figures **xx**

Chapter 1. Overview **1**

1.1 White Dwarfs 2

1.2 DA White Dwarfs 4

1.3 The DA White Dwarf Instability Strip 6

1.4 The Extremes of the DA White Dwarf Instability Strip 9

1.4.1 Dependence of DAV Pulsations on $T_{\rm eff}$ 9

1.4.2 Dependence of DAV Pulsations on $\log g$ 11

1.5 Pulsational Oddities at the Extremes of the DA White Dwarf Instability Strip 13

1.5.1 A New Outburst Phenomenon Near the Red Edge of the ZZ Ceti Instability Strip 14

1.5.2 Asteroseismic Evidence of Spectroscopic Misclassification at the Extremely Low-mass End of the ZZ Ceti Instability Strip 17

1.5.3 Tangential Explorations of Photometrically Variable White Dwarfs 19

Chapter 2. Pulsations and a New Outburst Phenomenon in the Longest Light Curve of a ZZ Ceti: KIC 4552982 **22**

2.1 Introduction 24

2.2 *Kepler* Photometry and Data Reduction 27

2.3 Outbursts in the *Kepler* Light Curve 28

2.3.1 Outburst Characteristics 29
2.3.2 Discussion of Outbursts 34
2.4 White Dwarf Pulsation Analysis 42
2.4.1 Mode Stability and Frequency Determination 43
2.4.2 Period Spacing 51
2.4.3 Comparison with Asteroseismic Models 53
2.4.4 Rotational Splitting 56
2.5 Conclusions and Future Work 58

Chapter 3. Outbursts in Two New Cool Pulsating DA White Dwarfs 61

3.1 Introduction 62
3.2 The Third Outburster: EPIC 211629697 64
3.2.1 Outbursts 66
3.2.2 Pulsations 69
3.3 The Fourth Outburster: EPIC 229227292 71
3.3.1 Outbursts 73
3.3.2 Pulsations 74
3.3.3 Spectroscopy 76
3.4 A Wider Search for Outbursts 78
3.4.1 EPIC 211891315: A Possible Single Outburst 84
3.5 Discussion and Conclusions 88

Chapter 4. New Outbursting ZZ Ceti Variables Through K2 Campaign 10 96

4.1 Time Series Photometry Analysis of Four New Outbursting ZZ Cetis 97
4.1.1 EPIC 229228364 99
4.1.2 EPIC 220453225 100
4.1.3 EPIC 220329764 101
4.1.4 EPIC 228952212 103
4.2 New Spectroscopic Parameters 105
4.3 Observational Summary of the New Outbursting Class of ZZ Ceti 107
4.4 Opportunities for Future Observational and Theoretical Advances 111

Chapter 5. Pruning The ELM Survey: Characterizing Candidate Low-mass White Dwarfs Through Photometric Variability 116
5.1 Introduction . . . 117
5.2 Observations . . . 121
5.3 Analysis . . . 123
5.3.1 Pulsating Stars . . . 124
5.3.1.1 SDSS J1735+2134 . . . 124
5.3.1.2 SDSS J2139+2227 . . . 126
5.3.1.3 SDSS J1355+1956 . . . 128
5.3.2 Photometric Binaries . . . 131
5.3.2.1 WD J0308+5140 . . . 131
5.3.2.2 SDSS J1054−2121 . . . 133
5.3.3 Null Results . . . 136
5.4 Discussion . . . 140
5.5 Summary and Conclusions . . . 145

Chapter 6. Fishing in the sdAs: Pulsating Stars including an Extremely Low-Mass White Dwarf 147
6.1 Time Series Photometric Observations . . . 151
6.2 Pulsating sdA Stars . . . 155
6.2.1 SDSS J1618+3854 . . . 157
6.2.2 SDSS J1131-0742 . . . 163
6.2.3 SDSS J0756+5027 . . . 169
6.2.4 SDSS J1142+3747 . . . 171
6.2.5 SDSS J2238+1253 . . . 172
6.2.6 SDSS J1604+0627 . . . 175
6.3 Null Detections of Note . . . 177
6.3.1 SDSS J1310-0142 . . . 178
6.3.2 SDSS J0908-0002 . . . 179
6.4 Conclusions and Future Work . . . 180

Chapter 7. White Dwarf Radius Constraints from Ellipsoidal Variations in Tight Binaries 182
7.1 Ellipsoidal Variations of SDSS J1054−2121 . . . 183

Chapter 8. Destroying Aliases from the Ground and Space: Super-Nyquist ZZ Cetis in *K2* Long Cadence Data 189

8.1 Introduction . . . 191
8.2 Observations . . . 193
8.2.1 Long-cadence *K2* photometry . . . 193
8.2.2 Time series photometry from the ground . . . 196
8.2.3 Spectroscopy . . . 197
8.3 Comparability of Data Sets . . . 198
8.3.1 Nyquist aliasing . . . 199
8.3.2 Phase smearing . . . 201
8.3.3 Passband differences . . . 202
8.3.4 Spectral window . . . 203
8.3.5 Intrinsic mode variation . . . 204
8.4 Comparing Data Sets . . . 205
8.4.1 EPIC 210377280 . . . 207
8.4.2 EPIC 220274129 . . . 215
8.5 Discussion and Conclusions . . . 224

Chapter 9. Pulsating White Dwarfs in Sparse Time Domain Surveys 228

9.1 Frequency Detection in Sparse Time Domain Survey Photometry 231
9.2 A New Amplitude-Only Signal Processing Technique . . . 234
9.3 Variability Depth and ZZ Cetis in LSST . . . 238

Appendices 246

Appendix A. Contributed Observations 247

A.1 WD 1145+017 – disintegrating planetesimals transiting a white dwarf . . . 248
A.2 SDSS J0651+2844 – eclipsing double white dwarf binary decaying from gravitational radiation . . . 249
A.3 SDSS J1529+2928 – starspot modulation from a massive white dwarf . . . 250

Appendix B. OLD MAID: OnLine Data Management And Interactive Display Software **252**

Bibliography **255**

List of Tables

2.1 Apparent photometric magnitudes of KIC 4552982 36
2.2 Properties of Lorentzian fits to significant frequencies of pulsational variability in the FT. 49

3.1 Properties of Outbursting DAVs 89
3.2 White Dwarfs Not Observed to Outburst with *Kepler* Observations 93

4.1 New Spectroscopic Parameters for Outbursting ZZ Cetis . . . 106
4.2 Newest Outburst Properties of oDAVs 108

5.1 Target Physical Parameters from The ELM Survey 120
5.2 Journal of Observations 122
5.3 Pulsation Properties of SDSS J1735+2134 127
5.4 Pulsation Properties of SDSS J2139+2227 127
5.5 Pulsation Properties of SDSS J1355+1956 130
5.6 Least-squares Amplitudes 135
5.7 Limits on Pulsations in NOVs 138

6.1 sdA Spectroscopic Parameters 154
6.2 Journal of Observations 156
6.3 Pulsation Properties of SDSS J1618+3854 159
6.4 Significant Period Aliases of SDSS J1618+3854 MMT RV Data 161
6.5 Pulsation Properties of SDSS J1131-0742 165

7.1 Revised System Parameters for SDSS J1054−2121 188

8.1 *K2* Target Observing Summary 195
8.2 Journal of McDonald Observations 196
8.3 Spectroscopic Parameters 198

8.4 Significant *K2* Aliases for EPIC 210377280 209
8.5 Frequency Solution for EPIC 210377280 213
8.6 Significant *K2* Aliases for EPIC 220274129 217
8.7 Frequency Solution for EPIC 220274129 222

9.1 Best Fit Amplitudes for Example Simulation 237
9.2 ZZ Ceti Recovery for 1% R.M.S. Variability 244
9.3 ZZ Ceti Recovery for 3% R.M.S. Variability 244

List of Figures

2.1 Representative segments of the *Kepler* light curve of KIC 4552982 as a function of days since the start of Q14 observations. The top panel shows the full Q14 light curve. The one-month shaded region in the top panel is expanded in the middle panel. The one-week shaded region in the middle panel is expanded in the bottom panel. The solid line is the light curve smoothed with a 3-hour-wide Epanechnikov (inverted parabola) kernel. The point-to-point scatter dominates the pulsation amplitudes in the light curve, so pulsations are not apparent to the eye. The white dotted line marks the significance criterion for our outburst detection algorithm, and outbursts determined to be significant are highlighted. We discuss this algorithm and these outburst events in Section 2.3. 27

2.2 Histogram of delay times between successive outbursts that meet our detection criteria. The mean recurrence timescale is 2.7 days and the standard deviation is 1.3 days. 29

2.3 Autocorrelation of the Q11-Q17 *Kepler* light curve of KIC 4552982. The positive autocorrelation coefficients at short (< 8 hour) time lag simply demonstrate that outbursts often persist to this duration. The range of time lags that produce negative autocorrelation coefficients is interesting, as it shows that an outburst is less likely to happen within 2 days of another. Beyond this recharge time, outbursts are consistent with being random (the solid lines are the 95% confidence intervals for random data). 31

2.4 Examples of outburst events. Top: most energetic. Second: median energy. Third: multi-peaked. Bottom: mean profile. The black curves are smoothed with a 3-hour-wide Epanechnikov kernel. The regions determined as belonging to the outburst by our algorithm are indicated with darker gray points. 32

2.5 Histogram of equivalent durations for the 167 outbursts observed in their entirety. 33

2.6 The spectral energy distribution of KIC 4552982 in U, g, r, i from the KIS survey and a J-band magnitude from the UKIRT J-band Public Archive. The synthetic spectrum Koester (2010) near the spectroscopically determined atmospheric parameters is plotted for reference. We see no infrared excess, allowing us to rule out a cool dwarf star companion to the white dwarf as the source of the observed outbursts. 37

2.7 Top: the thermal timescale as a function of depth in our model. The 10-hr average outburst duration timescale and the 2.7-day recurrence timescale are marked with vertical dotted lines. Bottom: the fractional flux carried by convection through the static model atmosphere. The relevant outburst timescales are of order the thermal timescale at the base of the convection zone, which is the timescale suspected to be most relevant to the cessation of pulsations at the cool edge of the instability strip. . . 41

2.8 Fourier transform of the entire Q11-Q17 *Kepler* light curve of KIC 4552982 in the region of significant pulsational variability (amplitude scale in mma = 0.1 %). 43

2.9 Sliding FT of a 5-day window over the entire *Kepler* light curve. The color bar at the top of the figure gives the amplitude scale in mma (= 0.1 %). The modes in the 700–1300 μHz frequency range (left panel) are observed to wander in phase (frequency) and amplitude while the mode at 2757.54 μHz is relatively stable. 44

2.10 Top: Lorentzian fits to 17 bands of pulsational power in the 4-μHz boxcar smoothed FT. The horizontal line at 0.0468 mma is our significance criterion. The Lorentzians are best fits to the power (amplitude squared) above the median noise level in hand-selected (black) regions of the light curve. Bottom: We refine our fit parameters by simultaneously fitting these 17 bands to the original, unsmoothed FT. The final parameters of these Lorentzians are listed in Table 2.2. 46

2.11 The rotational triplet surrounding the 2765.66 μHz mode. The power was fit with the displayed set of Lorentzians. The highest-frequency component consists of a single point above the noise that is fit to its peak power by the Lorentzian. 48

2.12 The period transform of the full *Kepler* light curve in the region of observed pulsational power bands. The locations of the expected $\ell = 1$ modes from the mean period spacing determined in Figure 2.13 are marked as dotted vertical lines. These lines are drawn darker where they fall within 7 seconds of one of our measured mode periods listed in Table 2.2 51

2.13 The period transform of the period transform reveals a significant mean period spacing at 41.9 seconds and its harmonic. This likely corresponds to a mean period spacing of $\ell = 1$ modes. 52

2.14 Histograms of mean period spacings calculated for $\ell = 1$ and $\ell = 2$ sequences throughout our model grid. The measured spacing for KIC 4552982 of 41.9 seconds fits exclusively within the $\ell = 1$ distribution. 54

2.15 The locations of models through M_* – $T_{\rm eff}$ space with mean $\ell = 1$ period spacings equal to the measured spacing of 41.9 seconds. The individual runs of solutions correspond to $\log M_{\rm H}/M_\star$ values from -4.00 (top track) to -6.00 (bottom track) in 0.50 resolution. All models that fit the observations have $M_* > 0.60$ $M_\odot$. The spectroscopically determined parameters are overplotted in white, and are in slightly better agreement with models nearer the high-$M_{\rm H}$ end. 55

3.1 *Left:* The *K2* Campaign 5 light curve of EPIC 211629697. The short-cadence data are displayed in black (during quiescence) and gray (during the 15 detected outbursts). The long-cadence data are shown in red. *Right:* A detailed view of the outburst of median energy (see text). The units on the x-axes are the same in both panels. The scales of the y-axes are identical, with greater apparent scatter in the left panel due only to the overlap of points. 66

3.2 Fourier transform of the entire *K2* light curve of EPIC 211629697, including outbursts. The dashed line gives the 0.1% False Alarm Probability (FAP) significance threshold for a single peak determined from bootstrapping (see text). The peak at 2053.514 μHz (486.97 s) and 3 frequencies in the range 764–913 μHz (1095–1309 s) reach amplitudes that exceed this significance threshold. We discard all low-frequency peaks below 100 μHz (see text). 69

3.3 The *K2* Campaign 6 light curve of EPIC 229227292. The short cadence data are presented in black (in quiescence) and gray (in outburst), with the long cadence data in red. *Left:* The full light curve featuring 33 significant outbursts. *Right:* A detailed view of the outburst of median energy, with the same y-axis scale and x-axis units. 72

3.4 FT of the *K2* light curve of EPIC 229227292. We detect several peaks in the range $800 - 1250$ μHz ($800 - 1250$ s), and two peaks at 1945.048 and 2697.423 μHz (≈ 371 and 514 s) that exceed our 0.1% FAP significance threshold (dashed line). The peak just below the significance threshold at 3456.41 μHz (289 s) is highly suggestive of being astrophysical signal (see text). 74

3.5 Running FT of EPIC 229227292, showing how the amplitude of pulsations changes in relation to outbursts. Vertical dotted lines mark the times of maximum brightness during the detected outbursts in Figure 3.3; we use a 3-day sliding window, which smears the events. We note that the rapid growth/decay of power in individual modes commonly coincides with a detected outburst (e.g., the dropping out of power near 1209 μHz that immediately follows the outburst near Day 24). This strongly suggests that the observed pulsations respond to outbursts in EPIC 229227292, as was observed in PG 1149+057 (Hermes et al. 2015b). 76

3.6 The best-fit atmosphere model (red) plotted over the average of the SOAR spectra (black) of EPIC 229227292 shows the agreement in the Balmer lines. Each spectral line is offset vertically by a factor of 0.3 for clarity. 77

3.7 The location of the four known outbursting DAVs (red squares) in $\log g$–$T_{\rm eff}$ parameter space, as well as the candidate EPIC 211891315 (orange triangle; see Section 3.4.1). The crosses show white dwarfs observed by *K2* which do not show outbursts (Table 3.2), confining this outburst phenomenon to the coolest pulsating white dwarfs, between roughly 10,600 K and 11,200 K. Previously known DAVs are shown in cyan circles (Tremblay et al. 2011a; Gianninas et al. 2011), and non-outbursting pulsating white dwarfs observed with *Kepler* are shown in yellow (with error bars; see Table 3.2). The empirical instability strip is demarcated with blue and red dashed lines (Tremblay et al. 2015). All atmospheric parameters have been corrected for the 3D-dependence of convection (Tremblay et al. 2013). The dash-dotted gray lines mark evolutionary cooling tracks for 0.6 $M_{\odot}$ and 0.8 $M_{\odot}$ white dwarfs (Fontaine et al. 2001). 80

3.8 The long-cadence light curve of EPIC 211891315 (K_p = 19.4 mag) from *K2*. We highlight with solid gray the single feature starting near Day 52.3 that looks compellingly like an astrophysical brightening event. The three yellow hatch regions indicate identified instrumental systematics corresponding to (in chronological order): an argabrightening event, a likely CME, and a local background flux enhancement (see text). 85

3.9 We confirmed pulsations in ground-based observations of the candidate outbursting white dwarf EPIC 211891315. We show the original FT in black, and the prewhitened FT in red, after subtracting the four significant pulsation frequencies that are marked with triangles at 1322.0, 1780, 2057.7, and 1021.7 μHz. The dashed grey line marks the running $4\langle A \rangle$ significance threshold. 87

4.1 Light curve of EPIC 229228364. The left panel shows the full short-cadence *K2* light curve (black) and a 30-minute-smoothed long-cadence light curve (red). The gray segments of the light curve mark detected outbursts. The right panel zooms in on a representative, median-energy outburst. 99

4.2 Fourier transform of EPIC 229228364. The 0.1% significance threshold was calculated from 10,000 bootstrap randomizations. 100

4.3 Light curve of EPIC 220453225. The left panel shows the full short-cadence *K2* light curve (black) and a 30-minute-smoothed long-cadence light curve (red). The gray segments of the light curve mark detected outbursts. The right panel zooms in on a representative, median-energy outburst. 100

4.4 Fourier transform of EPIC 220453225. The 0.1% significance threshold was calculated from 10,000 bootstrap randomizations. 101

4.5 Light curve of EPIC 220329764. The left panel shows the full long-cadence *K2* light curve (black), with the detected outbursts marked with red points and highlighted in yellow. The right panel zooms in on a representative, median-energy outburst. 102

4.6 Fourier transforms of EPIC 220329764 light curves obtained from the McDonald Observatory 2.1-meter Otto Struve Telescope on three different nights in August 2016. While we do not detect variability above the significance threshold on the first night, the do measure stellar pulsations on the next two nights. 104

4.7 Light curve of EPIC 228952212. The left panel shows the full short-cadence *K2* light curve (black) and a 30-minute-smoothed long-cadence light curve (red). The gray segments of the light curve mark detected outbursts. The right panel zooms in on a representative, median-energy outburst. 105

4.8 Fourier transform of EPIC 228952212. The 0.1% significance threshold was calculated from 10,000 bootstrap randomizations. 105

4.9 Location of presently known outbursting DAVs in $\log g$–$T_{\rm eff}$ parameter space. The oDAVs listed in Table 4.1 are marked with squares of different colors. The yellow circles and gray crosses correspond to the DAVs and long-cadence white dwarf targets that do not exhibit outbursts in *K2* data through Campaign 6 (from Bell et al. 2016). The dashed lines are the empirical instability strip boundaries (Tremblay et al. 2015), and the dash-dotted lines are cooling tracks for 0.6 and 0.8 $M_{\odot}$ white dwarfs (Fontaine et al. 2001), for context. The cyan circles are ZZ Cetis known from the ground (Gianninas et al. 2011), with the addition the "odd duck" SDSS J2350−0054 from (Mukadam et al. 2004, with updated spectroscopic parameters from Kepler et al. 2016) to highlight the existence of ZZ Cetis cooler than the empirical strip boundaries. 107

4.10 Peak flux enhancement versus outburst duration for all detected outbursts, color-coded by target to match the squares in Figure 4.9. 109

4.11 Approximate outburst energy versus delay since last outburst for events that are not separated by greater than 3-hour gaps in monitoring, color-coded by target to match the squares in Figure 4.9. 109

4.12 Outburst energy distributions show the rates that stars exhibit outbursts of at least a given energy. Color-coded by target to match the squares in Figure 4.9. The trend of higher outburst energy with lower $\log g$ is likely due to a poor method of approximating the outburst energy. 110

4.13 Comparison of the highest amplitude outburst of EPIC 201806008 observed by *K2* (left; Hermes et al. 2015b) and a compelling outburst detection from ASAS-SN (right). 113

5.1 The light curves of SDSS J1735+2134 from 4 nights are displayed in black dots. The x-axis units are hours since the start of the 30 Apr 2016 run. The y-axis gives the ratio of the measured flux relative to the mean flux. Our 4-period model fit to the data is displayed as a solid line. 125

5.2 Fourier transforms of the original (black) light curves, increasingly prewhitened data (lighter shades of gray; see text), and final residuals (red) for SDSS J1735+2134 in the region of significant pulsational power. The dashed line is the final $4\langle A\rangle$ significance threshold for the data prewhitened by the four sinusoids characterized in Table 5.3. 126

5.3 Fourier transform of the original (black) and fully prewhitened (red) light curves of SDSS J2139+2227 covering the full region of significant pulsational power. The dashed line is the final $4\langle A\rangle$ significance threshold for the data prewhitened by the three sinusoids characterized in Table 5.4 and indicated here with triangles. 128

5.4 The light curves of SDSS J1355+1956 from three consecutive nights in May 2016. The best-fit two-sinusoid model is plotted over the data. 129

5.5 The Fourier transform of the scaled original (black) and fully prewhitened (red) light curves of SDSS J1355+1956 from May 2016. The dashed line shows the final $4\langle A\rangle$ significance threshold for the prewhitened light curve. The frequencies of the two significant modes in Table 5.5 are marked with triangles. . . . 130

5.6 The phase-folded light curve of WD J0308+5140 shows evidence of eclipses that implies a primary star radius $\gtrsim 0.4\ R_{\odot}$. The blue hatched region marks the observed eclipse. 132

5.7 The phase-folded, binned light curve of SDSS J1054−2121 shows evidence of ellipsoidal variations and relativistic Doppler beaming. Our best fit model is plotted over the data in red. . 134

5.8 Each plot in the top panel displays the divided light curve with the largest overall trend for each of the four targets that do not show clear signs of intrinsic stellar variability. The solid red lines show the best-fit differential extinction model for each. Our analysis of the residuals displayed in the bottom panel reveals no significant astrophysical signal. 137

5.9 The locations of known pulsating stars with ELM-like spectra in $\log g$–$T_{\rm eff}$ space. Pulsating ELMVs confirmed with RV variations (Hermes et al. 2012a, 2013a; Kilic et al. 2015a) are indicated with yellow diamond markers. Pulsating ELM WD candidates without measured RV variations are marked with squares, including three objects from this work and the targets published in Hermes et al. (2013c) and Bell et al. (2015b). The filled black square represents SDSS J1355+1956, which cannot be a WD, and the white square is SDSS J1618+3854 (Bell et al. 2015b) that has not yet been observed with time series spectroscopy. Objects with constraints on a lack of pulsations from time series photometry are marked with × symbols (this work; Hermes et al. 2012a, 2013a,c). Pulsating pre-ELM WDs from Maxted et al. (2013, 2014); Corti et al. (2016) and Gianninas et al. (2016) are marked with orange narrow diamonds. Typical $\log g \sim 8$ ZZ Ceti pulsators from Gianninas et al. (2011), corrected for 3D convection effects (Tremblay et al. 2013), are marked with yellow triangles. The empirical DA instability strip published in Gianninas et al. (2015) is marked with dashed lines. The objects presented in this work are outlined with thicker black borders. 143

6.1 Positions of observed candidate pulsating sdAs in spectroscopic $\log g$–$T_{\rm eff}$ space. Black filled circles mark the parameters determined from solar-z models, while white filled circles are from pure-H models. Parameters determined for the same object are connected by lines. Circles outlined in red are new pulsating stars from this work. The diamonds mark ELMVs confirmed from RV variation measurements (Hermes et al. 2012a, 2013a; Kilic et al. 2015a). Gray circles mark previously published pulsating stars either without time series spectroscopic observations (Corti et al. 2016) or with no detected RV variation signals (Hermes et al. 2013c; Bell et al. 2017a). 153

6.2 April 2014 observations of SDSS J1618+3854 with the best fit solution overlaid. 158

6.3 Fourier transform (FT) of the April 2014 light curve of SDSS J1618+3854 displayed in Figure 6.2. The significant peaks are marked with triangles, and the FT of the residuals (red) and final significance threshold (blue) are also displayed. 159

6.4 χ^2 versus orbital period for MMT RV measurements of SDSS J1618+3854. There are four significant period aliases that are described in Table 6.4. The phase folded RV curve of the strongest alias is plotted in Figure 6.5. 160

6.5 MMT RV measurements of SDSS J1618+3854 folded on the strongest period alias. 161
6.6 Best fit model of the pulsational nonlinearities of SDSS J1618+3854 to the 24 April 2014 light curve using the tools of Montgomery (2005). Figure from Bell et al. (2015b). 162
6.7 Light curve of SDSS J1131-0742 from two nights in January 2015. 164
6.8 FT of SDSS J1131-0742 light curves from January 2015. 164
6.9 RV measures of SDSS J1131-0742 from Warren Brown. 167
6.10 Alex Gianninas' best fit model to the FAST spectrum of SDSS J1131-0742. 168
6.11 Light curve of SDSS J0756+5027 from McDonald Observatory on 11 Feb 2015. 169
6.12 Phase folded CSS data on SDSS J0756+5027. 170
6.13 Light curve of SDSS J1142+3747 from two nights in May 2017. 171
6.14 FT from two nights of data on SDSS J1142+3747 in May 2017. 171
6.15 SDSSJ2238+1253 light curve. 173
6.16 SDSSJ2238+1253 FT. 173
6.17 RV measurements of SDSS J2238+1253 from Warren Brown. . 174
6.18 SDSSJ1604+0627 light curve. 175
6.19 SDSSJ1604+0627 FT. 176
6.20 Left: light curve of SDSS J1310-0142 from 14 March 2015, boxcar smoothed over each 5 adjacent points. Right: FT of the raw light curve. The $4\langle A \rangle$ threshold is a rule-of-thumb significance criterion that supports that this star exhibits multi-modal pulsations. 178
6.21 Catalina Sky Survey photometry of SDSS J0908-0002, folded on a period of 9.15 hours. 179
6.22 Short McDonald Observatory light curve of SDSS J0908-0002 from 26 April 2015 confirms the eclipsing system. 179

7.1 The results of Monte Carlo simulations of our constraints on the parameters of the binary system SDSS J1054−2121. The dark gray logarithmic histograms include all models with $M_2 < 3\ M_\odot$. The light gray histograms include only those models that were selected in proportion to the adopted Gaussian likelihood distribution for the system's ellipsoidal variation amplitude (Figure 7.2). Our improved constraints are summarized in Table 7.1. 186

7.2 The distribution of expected EV amplitudes given prior spectroscopic constraints on the binary system SDSS J1054−2121 is displayed in dark gray. The light gray distribution shows the solutions that we accepted from our Monte Carlo simulations in proportion to a Gaussian distribution consistent with the photometric EV amplitude measurement. 187

8.1 Balmer line profiles from the SOAR spectra of EPIC 210377280 (left) and EPIC 220274129 (right). The best fit 1D models are overplotted in red, and their parameters are indicated at the bottom of each panel. 197

8.2 The effect of continuous time series sampling on the measured amplitude and frequency of a signal. Signals with intrinsic frequencies beyond the Nyquist frequency will be aliased into the sub-Nyquist regime (right axis) with significantly decreased amplitudes (left axis). 200

8.3 Top: Fourier transform of the *K2* observations of EPIC 210377280 out to the Nyquist frequency with a 0.1% false alarm probability (FAP) significance threshold (see text). Significant signals are marked with colored triangles. Bottom: The spectral window from four nights of McDonald Observatory observations of EPIC 210377280 over a five night span in Feb 2016. The highest alias is located 11.6 μHz away from the central peak. The x-axes of both panels have the same scale. 208

8.4 Top: Fourier transform of the McDonald observations of EPIC 210377280 with the *K2* sensitivity function overlaid (*K2* observations are not sensitive to the shaded region to a FAP of 0.1%). Vertical lines mark integer multiples of the *K2* Nyquist frequency. The possible intrinsic frequencies and expected amplitudes (corrected for phase smearing and bandpass differences) corresponding to the measured aliases in the *K2* FT are indicated with diamond markers (color coded to match the top panel of Figure 8.3). Bottom: Prewhitening sequence for EPIC 210377280 (progresses left to right, then down). Black arrows indicate alias frequency selections supported by *K2* observations; white arrows point to peaks selected from ground-based data alone. The red dashed line in all panels shows the $4\langle A \rangle$ significance threshold for the ground-based data. The last panel highlights the residual power in our fully prewhitened light curve. 210

8.5 The frequency solution overlaid on the ground-based observations of EPIC 210377280 from McDonald Observatory. 214

8.6 Top: Fourier transform of the *K2* observations of EPIC 220274129 out to the Nyquist frequency with a 0.1% false alarm probability (FAP) significance threshold (see text). We identify rotationally split mode triplets with connected arrows (see text). Bottom: The spectral window from four nights of McDonald Observatory observations of EPIC 220274129 over a five night span in Oct/Nov 2016. The highest alias is located 11.5 μHz away from the central peak. The x-axes of both panels have the same scale. 216

8.7 Same as Figure 8.4, except for EPIC 220274129. Mode-by-mode frequency adoption and prewhitening progresses in the sequence of smaller panels from left to right, then top to bottom. The vertical dashed lines and diamonds indicate candidate frequencies and amplitudes underlying the *K2* signals, color-coded to match the triangles in Figure 8.6. The last panel highlights residual power in the fully prewhitened light curve. 219

8.8 The frequency solution overlaid on the ground-based observations of EPIC 220274129 from McDonald Observatory. 223

9.1 Simulated light curve (left) and Fourier transform (right) of a mono-periodic pulsating star in the LSST wide-fast-deep survey. See text for discussion. 233

9.2 Left: a sinusoid plotted through one period. Right: the probability density function (PDF) of values randomly sampled from a sinusoid. 235

9.3 Left: measured histogram of flux values for randomly sampled 3-sinusoid signal. Right: Fourier transform of histogram and best-fit Bessel function decompositions. 237

9.4 An example calculation of the probability density functions of a photometric variable measured for pure-signal, pure-noise, and signal+noise sources at a generic input test magnitude and signal for a single pointing. The top panel shows histograms, and the bottom shows cumulative distributions, which better indicate the percentage of overlap. See text for discussion. 240

9.5 Example output of the VarDepth MAF metric run on the current baseline cadence, minion_1016, after 10 years of survey operations. Input parameters and SQL queries were set to calculate the magnitude limit for detecting 90% of pulsators with 1% r.m.s. variability from a cut on the measured variance in the r band (allowing contamination from 10% of nonvariable sources). 242

9.6 Simulated distribution of Galactic ZZ Cetis with r-band magnitudes between 16 and 27. 243

A.1 Light curves of WD 1145+017 from four consecutive nights in February 2016 show transits of multiple planetesimals around the white dwarf, the morphologies of which evolve over these few nights. The light curves are folded on an average orbital period of 4.493 days, with each night offset by −0.5 in relative flux. 248

A.2 Folded discovery light curve of spot modulation in the massive DA white dwarf SDSS J1529+2928 from McDonald Observatory on 09 June 2015 (gray) with a smoothed version plotted in black. 250

B.1 Screen shot of the OLD MAID software working on time series photometry of the 12.75-minute eclipsing double-white-dwarf binary SDSS J0651+2844 (Hermes et al. 2012b, 2017 in prep; Section A.2). 253

Chapter 1

Overview

The incremental advance of science is gradual, spanning generations. The work described in this thesis builds upon an existing narrative that was developed largely through the PhD theses of previous students of the white dwarf group of the University of Texas Department of Astronomy. This chapter serves to describe the state of the field of ZZ Ceti asteroseismology as I began my work, particularly in those areas that my work most directly advances. I end this chapter by describing how my major observational projects fit into this larger context and I preview my main results.

The story of white dwarf stars has been reviewed elsewhere and in more detail. Althaus et al. (2010) and Koester (2013) provide excellent general overviews of white dwarfs, while Winget & Kepler (2008) and Fontaine & Brassard (2008) focus mainly on their pulsational properties. My academic grandfather[1], Hugh Van Horn, recently authored a very accessible historical account of the field called "Unlocking the Secrets of White Dwarf Stars" (2015).

[1] `http://academictree.org/astronomy/tree.php?pid=727357&pnodecount=6`

1.1 White Dwarfs

White dwarf stars are important objects to both physics and astronomy. The typical white dwarf has a mass of 0.6 solar masses, but a radius of only ~ 1 Earth radius, corresponding to a surface gravity of $\log g \approx 8$ (in c.g.s. units). This implies that the average white dwarf density is a factor of one million higher than that of the Sun, so white dwarfs serve as remote laboratories for the observational study of extreme physics beyond the domain accessible to terrestrial labs. Their internal temperatures can reach upward of 100 million Kelvin, and the temperatures of their atmospheres can exceed 100 thousand Kelvin.

White dwarfs are supported against gravitational collapse by electron degeneracy pressure. They have reached the limit of how tightly electrons can be packed together, governed by the Pauli exclusion and Heisenberg uncertainty principles. A counterintuitive consequence of their structures being governed by quantum mechanical effects is their mass-radius relationship: more massive white dwarfs occupy a smaller volume than less massive white dwarfs, and accretion of matter onto a white dwarf causes shrinking. There is an extreme limit to this at around $1.4\,M_{\odot}$ (exact value dependent on composition) where the radius of the star approaches zero (Chandrasekhar 1931). This mass is usually referred to as the Chandrasekhar limit, and white dwarfs that accrete matter to this limit are expected to explode as Type Ia supernovae. Since these explosions happen at a uniform mass (neglecting magnetic fields and rotation), Type Ia supernovae are expected to reach fairly uniform

peak luminosities, meaning that we can determine their distances by measuring their apparent peak brightnesses. These "standard candles" become billions of times more luminous than the Sun and are used to measure the farthest extragalactic distance scales in the Universe. It was the comparison of the peak brightnesses of exploding white dwarfs in Type Ia supernovae with the redshifts of their host galaxies that revealed the existence of dark energy (Riess et al. 1998; Perlmutter et al. 1999), the still-mysterious dominant constituent of the Universe in terms of mass-energy (69%; Planck Collaboration 2016) that is accelerating the expansion of the Universe.

Nearly 98% of all stars in the Milky Way (those with initial masses $\lesssim 6$–$9.5\,M_{\odot}$; Williams et al. 2009) will conclude their evolution as white dwarfs. This means that white dwarfs provide important observational boundary conditions for the theory of stellar evolution—we can understand the complicated processes of the later stages of nuclear burning and mass loss by investigating their remnant products. The Sun will become a white dwarf in another 5 billion years, and our studies of white dwarfs help us to understand the ultimate fate of our own Solar System and the planets it contains.

Once they are formed, white dwarf evolution is dominated by cooling. Through our understanding of the timescales of various cooling processes, we can determine the age of a white dwarf from its current temperature or luminosity. Since the Milky Way has a finite age, the oldest white dwarfs still have not cooled completely. Winget et al. (1987) realized that the age of the Galaxy could be constrained independently by measuring the white dwarf lu-

minosity function, publishing a new age for the Galactic disk of 9.3 ± 2.0 Gyr. This method of white dwarf cosmochronology can be used to constrain the age of any coevol stellar population. The shape of the white dwarf luminosity function also reveals important information about the physical processes relevant to white dwarf cooling, including neutrino losses (dominant in the hottest white dwarfs), crystallization (which releases latent heat), and the presence of theoretical particles (such as axions). Lamb & van Horn (1975) explored the physical sources of deviations from the simple, yet incredibly instructive, radiative cooling model of Mestel (1952, well summarized by van Horn 1971). García-Berro & Oswalt (2016) provide a recent review of the white dwarf luminosity function.

1.2 DA White Dwarfs

Roughly 85% of white dwarfs spectroscopically display atmospheres dominated by hydrogen (Kleinman et al. 2013), which are classified as DA white dwarfs. The majority of the other white dwarfs have atmospheres dominated by helium (DB), with a few more rare types dominated by carbon (DQ), metals (DZ), etc. White dwarfs that exhibit spectral features of multiple elements simultaneously are labeled with a combination of letters, the most common being DAZ stars: white dwarfs with weak metal lines in addition to strong Balmer absorption.

The high gravities of white dwarfs causes chemical stratification (Schatzman 1945), with the heaviest elements sinking deeper into the

interior. Even though hydrogen—the dominant chemical constituent of the Universe—makes up only $\lesssim 0.01\%$ of DA white dwarfs by mass, this layer is still optically thick. DB white dwarfs are understood to be devoid of hydrogen, with helium constituting their outermost layers. Since metals should rapidly sink below the photospheres of white dwarf stars (e.g., Koester & Wilken 2006), the metals observed in the spectra of DAZs must be constantly replenished, most likely from the debris of planetary systems that had orbited the white dwarf progenitor (see recent review chapter by Di Stefano 2011).

The physical properties of DA white dwarfs are commonly determined from spectroscopy, where the measured profiles of the Balmer lines (at optical wavelengths) are compared with stellar atmosphere models to yield surface gravity ($\log g$) and effective temperature ($T_{\rm eff}$) values. These are then commonly compared to stellar evolutionary models to yield measurements of the white dwarf mass, radius, bolometric luminosity, age, etc. Balmer lines reach their maximum strength near $T_{\rm eff} = 13{,}500\,{\rm K}$ at $\log g = 8$. The selection between degenerate hot and cool spectroscopic solutions on either side of this boundary is typically guided by broadband photometry (e.g., Bergeron et al. 1995), but this is complicated by interstellar extinction.

As the sample size of spectroscopically observed DA white dwarfs grew, particularly with the Sloan Digital Sky Survey, it became apparent that typical $\log g$ values measured from spectroscopic model fits showed an empirical rise with decreasing $T_{\rm eff}$ below roughly 12,500 K. This was not expected from

theory, nor could it be understood. Independent mass constraints from gravitational redshifts of white dwarf spectral lines did not corroborate this $\log g$ upturn (Falcon et al. 2010). Considering potential resolutions to this unphysical spectroscopic discrepancy, Koester et al. (2009a) identified an insufficient treatment of convection as the most likely culprit. This has largely been supported by the results of 3D hydrodynamic convection simulations (Tremblay et al. 2011b), which infer lower $\log g$ values for convective DA white dwarfs. It has become customary to apply 3D correction factors to the results of 1D spectroscopic model fits (Tremblay et al. 2013; 2015 for extremely low-mass white dwarfs).

1.3 The DA White Dwarf Instability Strip

DA white dwarfs are observed as photometrically variable pulsating stars as they cool through the range $12{,}500 \gtrsim T_{\rm eff} \gtrsim 10{,}800\,{\rm K}$ (near the average surface gravity $\log g \approx 8.0$; this range is dependent on surface gravity, as described in Section 1.4). It is no coincidence that this corresponds to the former $\log g$ upturn problem described above. Below about 13,000 K, electrons begin to recombine with the hydrogen in the outermost atmospheric layer of a DA, establishing a partial ionization zone with increased opacity. Convective energy transport via bulk fluid motions begins as radiation gets dammed up in this region, heating matter and making it buoyant. The depth and total energy content of the convection zone is extremely temperature dependent (e.g., Montgomery 2005). As the convection zone responds to local fluid variations,

it can drive global stellar oscillations (Brickhill 1991; Goldreich & Wu 1999a). The pulsating DA white dwarfs are commonly referred to as both DAVs (DA Variables) and ZZ Ceti stars (after their prototype). I use these terms nearly interchangeably in this manuscript.

DAVs oscillate with nonradial gravity mode pulsations. In contrast to isotropic radial modes, nonradial pulsations have the angular geometries of spherical harmonics, resulting from the spherically symmetric stellar gravitational potential. These can be defined by two quantum numbers: the degree ℓ equals the number of nodal lines at the surface; and the azimuthal order m equals the number of these that pass through the polar axis, with values between $-\ell$ and $+\ell$, depending on the direction that the waves travel. The additional quantum number k (some authors use n) describes the number of nodes in the radial direction, or the radial overtone number.

The restoring force for gravity modes (g modes) is buoyancy, as opposed to acoustic waves that are restored by pressure (p modes). The gas displacement associated with g modes is primarily horizontal, while p modes are mostly vertical. The g modes typically have longer periods than p modes—usually 3–20 minutes in white dwarfs. The comparison of pulsation observations through different filters supports that the flux variations are primarily from temperature changes rather than geometric distortions (Robinson et al. 1982), as is expected for g modes.

A white dwarf only sustains pulsations at frequencies that correspond to possible standing waves given its specific structure. In physics, these standing

waves are called "eigenfunctions," and they oscillate at the observed frequencies of photometric variability. The analysis of normal vibrational modes is a fundamental technique of physics—the same concept underlies the study of atomic and molecular spectral lines. The pulsations are global; they propagate through the star, probing the interior conditions with frequencies that are tuned by the specific stellar structure. By comparing measured pulsation frequencies against theoretical models, we can constrain the interior conditions of white dwarfs that are otherwise obscured below the photospheres of non-pulsating stars. The more pulsation frequencies that we detect, the more observational constraints we have on a system. In analogy to how geologists use waves from earthquakes to sound the interior of the Earth, we refer to the study of pulsating stars as asteroseismology. Aerts et al. (2010) provide a practical recent treatment of the tools and results of asteroseismology, while Unno et al. (1989) is the definitive classic text on pulsation physics.

Although it has not been definitively demonstrated, the near ubiquity of stellar pulsations observed within the DAV instability strip supports that it is "pure" (Castanheira et al. 2007); i.e., all DA white dwarfs are expected to pulsate as they cool through this narrow temperature range. This means that the asteroseismic constraints that we place on the contents of pulsating DAVs can be generalized to the larger population of DA white dwarfs as a whole.

Pulsations cause temperature variations at the photosphere, which modulates the disk-integrated flux. We measure this in pulsating white dwarf stars by obtaining time series photometry. This is essentially the same as

recording time lapse movies of a stars that change in brightness. We measure the flux from the target star in each image relative to other stars in the field of view, allowing us to correct for the effects of transparency variations during the image sequence. The record of stellar brightness variations over time is called a light curve. We typically measure the characteristics of stellar pulsations by computing the Fourier transform of light curves, which mathematically determines the amplitudes and significance of variability over a range of frequencies. I explore the subtleties of how the data acquisition details can complicate these measurements in Section 8.3.

1.4 The Extremes of the DA White Dwarf Instability Strip

The parameter space of the DAV instability strip is typically mapped to the spectroscopically determined $\log g$ and $T_{\rm eff}$ values. Previous observational work, most notably from other University of Texas theses, have uncovered important relationships between the pulsation properties of DAVs and these spectroscopic parameters.

1.4.1 Dependence of DAV Pulsations on $T_{\rm eff}$

Mukadam et al. (2006) measured the pulsation properties of 46 ZZ Cetis and explored their dependence on effective temperature. This is the most comprehensive study of its type to date, but similar trends were explored previously by, e.g., Clemens (1993) and Kanaan et al. (2002). In their work,

Mukadam et al. were careful that their comparisons made use of spectroscopic parameters that were obtained in a uniform way, since differences in instruments and analyses are known to introduce systematic errors to the fits (e.g., Fuchs et al. 2017). As ZZ Cetis cool across the instability strip, their typical pulsation periods are observed to increase (as Mukadam et al. characterized by the amplitude-weighted mean period). This is expected theoretically since the thermal timescale of the convection zone increases as it deepens across the ZZ Ceti instability strip, making it more efficient at driving pulsation modes with longer periods (Winget 1982). The total observed pulsational power of ZZ Cetis is observed to gradually rise below the hot (blue) edge of the instability strip, before sharply decreasing at the cool (red) edge. Mukadam et al. (2006) also found that ZZ Cetis near the red edge tend to be "richer" pulsators, exhibiting more independent pulsation modes (one, on average) compared to red edge pulsators.

There are also striking changes to the stability of pulsation mode properties as ZZ Cetis cool across the strip. Several of the hot ZZ Cetis show exceedingly steady pulsations; in fact, the 215 second mode in G117+B15A is the most stable known optical clock, to the extent that we can even measure the rate of period change due to white dwarf cooling $\dot{P} = (3.57 \pm 0.82) \times 10^{-15}\,\mathrm{s\,s^{-1}}$ (Kepler et al. 2005). Mullally et al. (2008) constrained the possible orbits and masses of exoplanets around hot ZZ Cetis by searching for periodic phase modulations of the pulsation signatures caused by stellar reflex motion. As of the most recent update by Winget et al. (2015), this method has not yet identified

any specific planet candidates.

ZZ Cetis near the cool edge of the instability strip behave very differently. Observations from different seasons on the cool ZZ Cetis GD 154 (Pfeiffer et al. 1996), G29–38 (Kleinman et al. 1998), and HL Tau 76 (Dolez et al. 2006), for example, reveal dramatic changes in pulsation amplitude. From year to year, the dominant pulsation mode can change completely, and the same set of mode frequencies is often not detected. Cool ZZ Ceti pulsations are *not* particularly stable in phase, frequency, or amplitude.

1.4.2 Dependence of DAV Pulsations on $\log g$

The pulsation properties of DAVs also change with the surface gravity, $\log g$. At the temperatures of DAVs, $\log g$ is essentially a proxy for white dwarf mass. The DA mass distribution is sharply peaked around a value of $0.624\,M_{\odot}$ (Kepler et al. 2017), though it is non-Gaussian, with sub-populations clustered at both higher and lower masses (Kleinman et al. 2013). The clumping of these extreme populations suggests that they contain white dwarfs that formed through alternative pathways to single-star evolution, namely white dwarf mergers and binary mass transfer evolution, respectively.

Massive white dwarfs that form in isolation would be composed primarily of heavier ions like oxygen, neon, and magnesium if their progenitors underwent carbon fusion. Those that coalesced from less massive white dwarfs will contain the lighter byproducts of earlier nucleosynthetic stages only. Stellar pulsations are sensitive to white dwarf core composition and can be exploited

to constrain the relative efficiency of these evolutionary pathways. Since the ions of massive white dwarfs are so densely packed, their Coulomb interactions are stronger and they will begin to form a crystalline lattice at higher temperatures than less massive white dwarfs. The average charge per ion affects the temperature of crystallization too. Asteroseismology of massive white dwarfs can constrain their crystallized fraction—an important test of dense matter physics. There have been many observational efforts to detect massive DAVs, with the record for most-massive currently held by the $1.20 \pm 0.03\,M_{\odot}$ GD 518 (Hermes et al. 2013b). My advisor Mike Montgomery's thesis addressed massive white dwarf pulsations and crystallization in great detail (1998).

The lowest mass white dwarfs do not have this same single/double star formation dichotomy; the main sequence lifetimes of single-star progenitors of white dwarfs less massive than $\approx 0.3\,M_{\odot}$ would exceed the age of the Galaxy (Marsh et al. 1995; Kilic et al. 2007), There has only been enough time for the observed population of extremely low-mass (ELM) white dwarfs to have formed through post-main-sequence common envelope mass transfer. In this scenario, the envelope of a star ascending the red giant branch is stripped by a tight binary companion, leaving behind a degenerate helium core (Nelemans et al. 2001). This evolutionary picture is supported by the overwhelming fraction of ELM white dwarfs confirmed as belonging to tight binary systems through radial velocity variation measurements (Brown et al. 2016). Asteroseismology of ELM white dwarfs can illuminate the details of this complicated mass transfer process by probing the chemical content of the remnant products.

The discoveries of the first five pulsating ELM white dwarfs were made on the McDonald Observatory 2.1m telescope near the outset of my PhD work (Hermes et al. 2012a, 2013a,c). Theoretical work on the pulsation properties of ELM white dwarfs has been produced by Córsico & Althaus (2014a, 2016a); Córsico et al. (2016c); Istrate et al. (2016a); Calcaferro et al. (2017).

Finally, there is a $\log g$-dependence on the location of the instability strip boundaries, which moves to lower $T_{\rm eff}$ at lower $\log g$. Empirically determined boundaries that account for the latest 3D treatment of convection are parameterized in Tremblay et al. (2015). The outer layers of more massive DA white dwarfs have higher densities and are therefore more opaque, causing them to become convective and able to drive pulsations at higher temperatures than less massive DA white dwarfs. We also note that since the characteristic dynamical timescale for stars is $\propto 1/\sqrt{\bar{\rho}}$, less massive DAVs generally exhibit longer pulsation periods.

1.5 Pulsational Oddities at the Extremes of the DA White Dwarf Instability Strip

My thesis work has primarily focused on understanding the pulsational properties of DA white dwarfs at the cool edge of the ZZ Ceti instability strip, as well as those in the parameter space of extremely low-mass pulsating white dwarfs. I preview my main results in this section, and I also introduce the complementary side projects that make up part of my thesis work.

1.5.1 A New Outburst Phenomenon Near the Red Edge of the ZZ Ceti Instability Strip

I joined the white dwarf research group at UT-Austin at an opportune time. A month after my arrival, the *Kepler* Spacecraft began acquiring short cadence (1 min) photometric observations of the first ZZ Ceti variable known within its field of view, which the senior graduate student of the group, J. J. Hermes, had recently identified (Hermes et al. 2011). I took on the analysis of this unprecedented data set for my second-year graduate research project. Over 1.5 years of nearly uninterrupted space-based precision photometry on this target, KIC 4552982, promised to reveal the most complete record of pulsations in a ZZ Ceti to date. The most striking feature of the data was, however, unexpected: we detected 178 brightening events in the *Kepler* light curve. These "outbursts" last as long as a day, raise the instantaneous flux of the star by up to 17%, and recur with a quasi-period of 2.7 days. After carefully ruling out instrumental or contaminant sources of the outbursts, I characterized the first observations of this new physical behavior in Bell et al. (2015c). Model fits to spectroscopic observations of KIC 4552982 indicate that it is one of the coolest, canonical-mass ZZ Cetis known at $10{,}860 \pm 120$ K. This extensive data set—still the longest, nearly continuous light curve ever acquired for a ZZ Ceti—revealed a more complete record of mode amplitude and frequency instability than any previous work (see discussion in Section 1.4.1). The low-frequency modes are "resolved," and we can determine the underlying eigenfrequencies to higher precision than is possible from short observing

runs on cool ZZ Cetis. This data set was also the first to suggest a dichotomy between mode coherence at low and high frequency—an observation that has led to a new physical appreciation for the interaction between pulsation modes and convection (Montgomery et al., in prep.). From the Fourier transform of the light curve, I characterized 20 pulsation periods of this star, identifying a clear $\ell = 1$ sequence, as well as rotational splitting that enabled me to constrain the rotation period of this star to 17.47 ± 0.04 hours. This paper is reproduced in its entirety as Chapter 2. A more detailed asteroseismic analysis of the published pulsation periods is underway (Alejandra Romero, private communication).

With the failure of a second reaction wheel in May 2013, *Kepler* lost the ability to maintain its pointing on the original mission field. To salvage the spacecraft, the *K2* mission was devised to use pressure from the solar wind to obtain stable pointing on new fields along the ecliptic for roughly 80 days at a time. While the shorter extent of observations per field limits *K2*'s sensitivity to detecting exoplanets via the transit method, the new observing strategy has greatly increased the number of pulsating white dwarfs that we have uninterrupted multi-day precision photometry on.

The *K2* light curves have overwhelmingly revealed that outbursts are related to pulsations and are common near the empirical cool edge of the ZZ Ceti instability strip. The most dramatic example of an outbursting cool ZZ Ceti was found in *K2* Campaign 1; PG 1149+057 exhibits outbursts with peak flux enhancements of up to 45% and is bright enough that we can track the

evolution of pulsations through the events (Hermes et al. 2015b). The observed increase in pulsation amplitudes and frequencies during outbursts proves that the outbursts originate from the ZZ Ceti and will inform possible models for the underlying physical mechanism.

In Bell et al. (2016)—which makes up Chapter 3—I analyzed the *K2* light curves of 52 white dwarfs observed through Campaign 6 near the ZZ Ceti instability strip, detecting two additional ZZ Cetis that exhibit recurring outbursts. EPIC 211629697 and EPIC 229227292 both have spectroscopic effective temperatures that place them near the empirical red edge. I also find a single candidate outburst event in the long cadence light curve of EPIC 211891315—an interpretation that is slightly supported by the confirmation of stellar pulsation in this star from ground-based follow-up photometry.

K2 continues to observe pulsating and outbursting ZZ Cetis in new fields every $\approx$ 80 days and is expected to continue through Campaign 16 (ending 2018 Feb). By the time *K2* has exhausted its fuel, it will have observed $\sim$ 100 pulsating white dwarfs (J. J. Hermes, private communication). We continue to analyze new data releases, especially looking for additional outbursting ZZ Cetis. So far, through Campaign 10, we have discovered an additional four: EPIC 229228364, EPIC 220453225, EPIC 220329764, and EPIC 228952212. The analysis of the first two was previewed in Bell et al. (2017b). I characterize the spectroscopic, outburst and pulsation properties of all currently known members of this new outbursting subclass of ZZ Ceti variable in Chapter 4.

1.5.2 Asteroseismic Evidence of Spectroscopic Misclassification at the Extremely Low-mass End of the ZZ Ceti Instability Strip

The second major focus of my thesis work has been on pulsating DA white dwarfs near the low-mass extreme of the mass distribution. As I began my observing career, the McDonald Observatory 2.1-meter telescope had just become *the* discovery machine for a new pulsating class of extremely low-mass (ELM; $\lesssim 0.3\,M_{\odot}$) white dwarf (Hermes et al. 2012a, 2013a,c; with one additional pulsating ELM discovered more recently from Gemini by Kilic et al. 2015a). I described the context of this work in Section 1.4.2.

Appreciating this rich research area, I led the continued campaign to detect and characterize new pulsating stars in this parameter space. I derived my target lists through collaboration with the ELM Survey team (Brown et al. 2016, and references therein), which had produced all of the published ELM variables (ELMVs) so far, as well as from new model fits to Sloan Digital Sky Survey (SDSS) spectroscopy led by my thesis committee member S. O. Kepler (2015; 2016). While I did identify several new photometric variables from my ELMV candidate lists, their properties did not generally conform to our expectations of ELM white dwarfs, leading me to challenge some of the basic assumptions of this subfield.

I published the results of my times series photometric survey of nine candidate ELMVs from the ELM Survey papers VI and VII (Gianninas et al. 2015; Brown et al. 2016) as Bell et al. (2017a), which I reproduce here in Chapter 5. Five out the the nine candidates exhibit photometric variability:

three as pulsating stars, and two as photometric binaries. The new pulsating stars are, however, all among the few spectroscopically classified ELMs that were not found to exhibit the radial velocity variability expected given their theoretical formation from common envelope binaries. Furthermore, the 4.31-hour pulsation period of one of these stars exceeds the physical limit for surface reflection in a white dwarf (Hansen et al. 1985). Of the photometric binaries, the ellipsoidal variation and Doppler beaming signals of one system was consistent with its spectroscopic classification as an ELM white dwarf, but the eclipse duration of the other put a lower limit on the primary star's radius of 0.4 $R_{\odot}$—too large for a cooling track white dwarf. Taken together, these observations reveal that another type of star is being systematically mistaken for ELM white dwarfs from spectral line fitting. Considering that two previously published ELMVs also do not show radial velocity variations in time series spectroscopy, I revise the total number of confirmed ELMVs in this work to the four from Hermes et al. (2012a, 2013a) and Kilic et al. (2015a).

White dwarf model fits to SDSS spectroscopy from Data Releases 10 and 12 (Kepler et al. 2015, 2016) revealed thousands of stars with best fit parameters in the ELM regime, which were labeled "sdA" stars. I sought to understand this unexpectedly large number of objects with ELM-like spectra through time series photometry. I describe my observations of a handful of sdAs in Chapter 6. I detect clear pulsation signatures in six out of 24 sdA stars that my collaborators and I observed. While the observed properties support that most of these new variables are not cooling track white dwarfs, at least

one appears to be an ELMV.

1.5.3 Tangential Explorations of Photometrically Variable White Dwarfs

With over 225 nights of observing on the McDonald 2.1-meter Otto Struve Telescope, as well as my involvement in the quarterly outpouring of variable white dwarf data from *K2*, I have had the opportunity to work on a number of side projects that are only tangentially related to the two main foci of my thesis described above. Depending on the size of each undertaking, I have included these in my thesis either as additional chapters or appendices. For completeness, here is an overview of those components in order of their appearance.

In Chapter 7, I develop an improved framework for obtaining radius constraints on ELM white dwarfs from measurements of photometric ellipsoidal variations. I apply this technique to better constrain the properties of the new photometric variable SDSS J1054-2121. This chapter was originally included in an early draft of Bell et al. (2017a), but it distracted from the main narrative of that paper. This work is a refinement of the general approach developed in Hermes et al. (2014b). The tools I describe in this chapter are also useful for predicting ellipsoidal variation amplitudes of photometric binary candidates in different filters.

Chapter 8 describes a novel combination of data on two ZZ Ceti pulsators: long-cadence *K2* observations and single-site ground based light curves.

Significant aliasing renders each of these data sets non-ideal for precision asteroseismology. Signals in the *K2* observations, while of extremely high precision, suffer Nyquist aliasing since the white dwarf pulsation periods are shorter than the 30-minute exposure time. Gaps in the ground based observations introduce aliases to the spectral window from cycle-count ambiguities. Together, these data sets complement each other, enabling us to recover a subset of accurate pulsation periods at full *K2* precision. Along the way, I discuss the observational effects that act to confuse frequency solutions and use these data to demonstrate common analytical pitfalls.

During this work, I have becoming increasingly interested in the prospect of studying stellar pulsations with data from future large synoptic photometric surveys, yet I have been so inundated with existing data that I have made only limited explorations in this area. I have focused on generated synthetic data to demonstrate which survey design considerations are most important for capturing the signatures of stellar pulsations. I describe a few simulations of pulsating white dwarf photometry sparsely sampled in the time domain in Chapter 9. These are most relevant to the upcoming Large Synoptic Survey Telescope and the Zwicky Transient Facility projects that will begin data acquisition in the coming years.

As McDonald Observatory's most frequent observer of time series photometry over the past four years, I have been able to contribute important observations to many interesting side projects. I highlight a few of these data sets in a gallery of contributed observation in Appendix A, with the permission

of the primary investigators. These include observations of disintegrating planetesimals around a white dwarf, a double white dwarf binary decaying from gravitational radiation, and a massive white dwarf with a strong rotational signature from starspot modulation.

To enable on-the-fly decision making and optimal use of telescope time, I developed an interactive online data reduction and analysis pipeline for the ProEM high speed photometry CCD that is in use at McDonald Observatory. I describe this software in the final Appendix B.

Chapter 2

Pulsations and a New Outburst Phenomenon in the Longest Light Curve of a ZZ Ceti: KIC 4552982 *

The *Kepler* mission (Borucki et al. 2010) was designed to detect the transit signatures of Earth-like planets around Sun-like stars. It recorded data for over 150,000 pre-selected targets within a 115 $\deg^2$ field near the constellation Cygnus with 30-minute exposures. It could also obtain light curves at a short 1-minute cadence for 512 targets, sufficiently frequent to measure white dwarf pulsations with typical periods of 3–20 minutes. *Kepler* mission observed for four years until the second of four reaction wheels failed, rendering the spacecraft unable to maintain pointing on its original field.

No ZZ Ceti variables were known within the original *Kepler* field,

*This work was previously published as Bell, K. J., Hermes, J. J., Bischoff-Kim, A., Moorhead, S., Montgomery, M. H., Østensen, R., Castanheira, B. G. and Winget, D. E., 2015, *KIC 4552982: Outbursts and Asteroseismology from the Longest Pseudo-continuous Light Curve of a ZZ Ceti*, ApJ, 809, 14. I led this work with the help of many collaborators: J. J. Hermes proposed the observations and contributed important ideas and analytical tests; A. Bischoff-Kim calculated a grid of asteroseismic models that we compared the observations to; S. Moorhead computed the mean outburst profile; M. H. Montgomery advised my work and computed relevant timescales in white dwarf models; R. Østensen gave valuable feedback on the first draft and produced the "sliding FT" figure; B. G. Castanheira helped me to interpret the asteroseimic results; and D. E. Winget advised the project, suggesting important tests to do and contributing ideas about the physical nature of outbursts.

mainly due to the lack of multi-color survey photometry in this part of the sky to *Kepler*'s limiting magnitude. Hermes et al. (2011) discovered the first ZZ Ceti observable by the *Kepler* mission, and we obtained over 1.5 years of short-cadence data on KIC 4552982 before the mission abruptly ended. These observations provide the most complete record of ZZ Ceti pulsations to-date. The unprecedented extent of the light curve provides precise, high signal-to-noise detections of pulsation signatures with hardly any gaps. I led the analysis of these data for my second-year project as a graduate student at UT-Austin. These data made it possible for me to precisely measure the pulsation properties of this star for asteroseimic analysis and to resolve their relative incoherence that has not been done from the ground. I asteroseismically measured the rotation period of KIC 4552982 to be 17.47 ± 0.04 hr.

Beside this pulsational and asteroseismic analysis that motivated these observations, these data revealed an unexpected new outburst-like phenomenon in this star. This new physical behavior became a centerpiece of my thesis work that I focus on in the next three chapters. KIC 4552982 exhibited 178 quasi-periodic brightening events that increased the stellar flux by up to 17%, lasted between 4–25 hours, and recur every 2.7 days on average. The content of this chapter was published as (Bell et al. 2015c). Through the continued discovery of this behavior in other ZZ Cetis from the second mission of the *Kepler* spacecraft, *K2*, we would come to learn that this behavior is common near the empirical cool edge of the instability strip.

2.1 Introduction

As they cool, white dwarfs — the endpoints of more than 97% of stars in our Galaxy — evolve through instability strips on the H-R Diagram where they pulsate due to convective driving (Brickhill 1991; Goldreich & Wu 1999a). ZZ Ceti variables have partially ionized hydrogen atmospheres and pulsate in the surface temperature range 12,600 K $> T_{\rm eff} >$ 10,800 K near the mean hydrogen-atmosphere (DA) white dwarf mass of 0.6 $M_{\odot}$ (Tremblay et al. 2013). The characteristics of the pulsation modes that are excited in stars are determined by the specifics of their internal structures. The tools of asteroseismology enable us to interpret measurements of white dwarf brightness variations to potentially constrain their masses, radii, compositions, chemical stratification, equations of state, rotation, crystallized fractions, etc. (see reviews by Winget & Kepler 2008; Fontaine & Brassard 2008; Althaus et al. 2010). This method allows us to conduct important investigations into the behavior of matter under the extreme physical conditions of white dwarf interiors that are beyond what is accessible for study in terrestrial laboratories.

Asteroseismology of white dwarf stars is conducted primarily through Fourier analysis of photometric light curves. While ground-based observations of pulsating white dwarfs have been collected since 1964 (Landolt 1968), the terrestrial vantage point comes with its disadvantages. Aliasing caused by daily gaps in the data and breaks due to inclement weather can introduce artifacts to Fourier transforms (FTs). Since spectral resolution and signal-to-noise improve with a longer observational baseline and more complete coverage, ob-

servations spanning multiple nights are often required to resolve the individual frequencies of a rich pulsation spectrum. Efforts to surpass these limitations include extended, global observations with networks of telescopes distributed in longitude, with the greatest contributions to white dwarf science coming from the Whole Earth Telescope collaboration (Nather et al. 1990).

More recently, the *Kepler* space mission has enabled asteroseismic research of unprecedented quality by obtaining extended time series photometry of a consistent field with a high duty cycle (see, e.g., Gilliland et al. 2010a; Christensen-Dalsgaard & Thompson 2011). Besides the presently described work, detailed asteroseismic studies of pulsating white dwarfs enabled by the original *Kepler* mission include analysis of a V777 Her star (helium-atmosphere variable white dwarf; KIC 8626021; Østensen et al. 2011; Bischoff-Kim & Østensen 2011; Córsico et al. 2012; Bischoff-Kim et al. 2014) and another ZZ Ceti (KIC 11911480; Greiss et al. 2014). In its present two-wheel configuration, *Kepler* has also provided asteroseismic data on the ZZ Ceti variable GD 1212 (Hermes et al. 2014b) and a ZZ Ceti with an M dwarf binary companion (Hermes et al. 2015a). *Kepler* will observe additional white dwarf pulsators in upcoming K2 mission fields (Howell et al. 2014).

Hermes et al. (2011) sought and discovered the first ZZ Ceti in the original *Kepler* field of view: WD J191643.83+393849.7. They gathered ∼21 hr of time-series photometry on the 2.1-meter Otto Struve telescope at McDonald Observatory and identified seven frequencies of brightness variability, though with admittedly large uncertainties. They also obtained four low- to medium-

resolution spectra for the white dwarf and fit the Balmer line profiles to models to determine its values of $T_{\rm eff}$ = 11,129 ± 115 K, $\log g$ = 8.34 ± 0.06, and $M_\star$ = 0.82 ± 0.04 $M_\odot$. Now equipped with corrective terms that take into account the effects of 3-dimensional convection (Tremblay et al. 2013), we revise the spectroscopically derived values to $T_{\rm eff}$ = 10,860 ± 120 K, $\log g$ = 8.16 ± 0.06 in this work, and interpolate the model cooling sequences of Renedo et al. (2010) to get $M_\star = 0.69 \pm 0.04\ M_\odot$. These properties place the white dwarf at the empirical red (cool) edge of the ZZ Ceti instability strip (Tremblay et al. 2013).

This target at $19^{\rm h}16^{\rm m}43^{\rm s}.83$, $39°38'49.7''$ was assigned *Kepler* ID KIC 4552982 and was observed by the *Kepler* spacecraft at short cadence from Q11 until the second reaction wheel failure during Q17. The resulting data provide the longest (∼20-month) pseudo-continuous light curve of a ZZ Ceti ever obtained. Besides resolving a rich pulsation spectrum, the *Kepler* light curve revealed a surprising outburst phenomenon unlike any previously studied white dwarf behavior.

In Section 2.2 we describe the methods used to optimally reduce the *Kepler* light curves. In Section 2.3 we characterize and discuss the nature of the energetic outbursts recorded for the first time in the *Kepler* photometry. Our asteroseismic analysis makes up Section 2.4, where we measure the pulsational properties of the star to constrain the stellar mass, hydrogen layer mass and stellar rotation rate. We summarize our findings and conclude in Section 2.5.

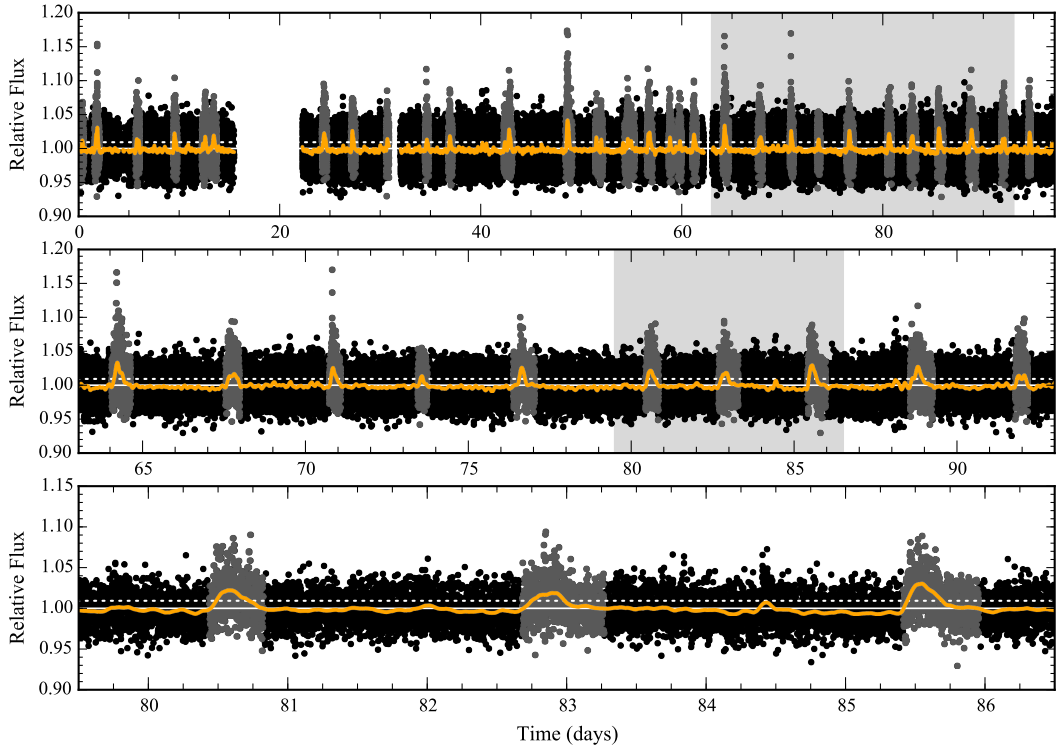

Figure 2.1: Representative segments of the *Kepler* light curve of KIC 4552982 as a function of days since the start of Q14 observations. The top panel shows the full Q14 light curve. The one-month shaded region in the top panel is expanded in the middle panel. The one-week shaded region in the middle panel is expanded in the bottom panel. The solid line is the light curve smoothed with a 3-hour-wide Epanechnikov (inverted parabola) kernel. The point-to-point scatter dominates the pulsation amplitudes in the light curve, so pulsations are not apparent to the eye. The white dotted line marks the significance criterion for our outburst detection algorithm, and outbursts determined to be significant are highlighted. We discuss this algorithm and these outburst events in Section 2.3.

2.2 *Kepler* Photometry and Data Reduction

Following the discovery by Hermes et al. (2011) that WD J191643.83 +393849.7 (KIC 4552982) pulsates, this target was prioritized by the *Ke-*

pler Asteroseismic Science Consortium (KASC) for short-cadence monitoring by the *Kepler* spacecraft (58.85 s image^{-1}; Gilliland et al. 2010b). It has a recorded *Kepler* magnitude of $K_P = 17.9$. The object was observed from Quarter 11 (Q11) through Q17 (2011 September 29 to 2013 May 11).

The *Kepler* data were reduced with the PyKE software package (Still & Barclay 2012) following the method described by Kinemuchi et al. (2012). We defined custom apertures for light-curve extraction from the Target Pixel Files to maximize target signal-to-noise. We then masked out the outburst events (described in Section 3) from the raw light curves and found that linear least-squares fits of the top six Cotrending Basis Vectors from each quarter characterized and allowed us to correct for the systematic instrumental trends in the light curve. Finally, we excluded points that were flagged for questionable data quality by the *Kepler* pipeline, and we manually removed statistical outliers falling $> 5\sigma$ from the local, 10-d median, ensuring that no clipped points were related to astrophysical photometric variations. Our final light curve contains 746,916 data points and has a 86% duty cycle. The representative Q14 light curve that we acquired after normalizing and combining each month of data is provided in Figure 2.1.

2.3 Outbursts in the *Kepler* Light Curve

With a mean standard deviation from measurement noise of 1.8% dominating the pulsation amplitudes in the *Kepler* light curve, its visually striking features are the occasional large brightness enhancements that occur through-

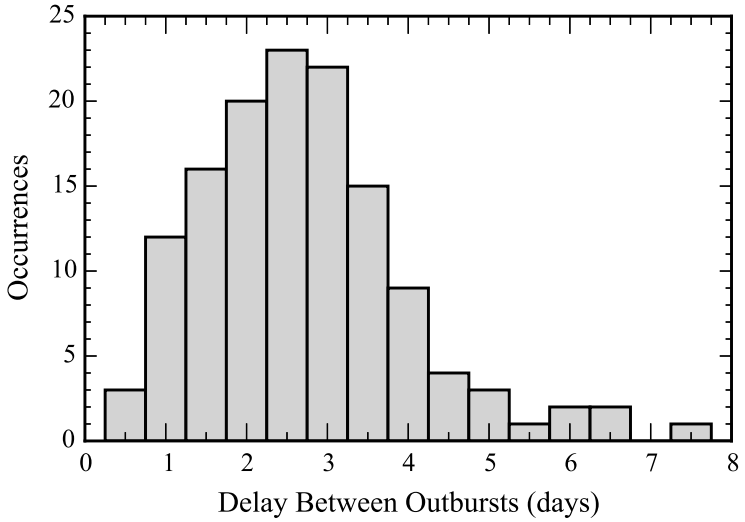

Figure 2.2: Histogram of delay times between successive outbursts that meet our detection criteria. The mean recurrence timescale is 2.7 days and the standard deviation is 1.3 days.

out the 20 months of observations (visible in Figure 2.1). We see no evidence of a faint, red companion, and argue these observations likely mark the first detection of a new white dwarf outburst phenomenon.

2.3.1 Outburst Characteristics

We define an automatic detection algorithm to locate significant outbursts in the light curve. Each month of data is smoothed with a 3-hour-wide Epanechnikov (inverted parabola; Epanechnikov 1969) kernel to reduce scatter while retaining the outburst signatures. Outbursts are identified where the light curve exceeds a significance threshold of 4× the standard deviation of the smoothed flux for 30 consecutive minutes. We interpret the target to

be in outburst until the smoothed flux returns to the median value of 1.0. We iteratively search for outbursts by recalculating the significance threshold from "quiescent" (outside known outbursts) portions of the light curve until no additional outbursts are identified. The values that we adopt for this detection scheme are tuned such that the algorithm identifies all outbursts that are obvious to the eye without selecting regions that do not stand up to human scrutiny. Our search yields 178 events of significant (peak $2-17\%$) brightness increases that typically last $\approx 4-25$ hours. We display the histogram of delay times between detected outbursts in Figure 2.2. These outbursts appear to occur stochastically in time with an average delay of 2.7 days and a standard deviation of 1.3 days.

These timescale properties are reflected in the autocorrelation of the light curve, shown in Figure 2.3. The autocorrelation function depicts how likely it is to measure excesses in flux separated by different lags of time. The light curve was smoothed in 30-minute bins to average over any correlation from pulsations. The solid horizontal lines mark the 95% confidence thresholds of $\pm 2/\sqrt{N_e}$, where N_e is the effective sample size (Chatfield 2004). We approximate the effective sample size from the number of light curve bins compared at each time lag, multiplied by $(1-\mathrm{ACF}_1)/(1+\mathrm{ACF}_1)$, where ACF_1 is the autocorrelation coefficient at the smallest time lag. For a random time series, 95% of autocorrelation coefficients would be expected to fall within these bounds. We see positive autocorrelation at $<$ 8-hour time lag as this is the characteristic duration of an outburst. Beyond an apparent recharge time

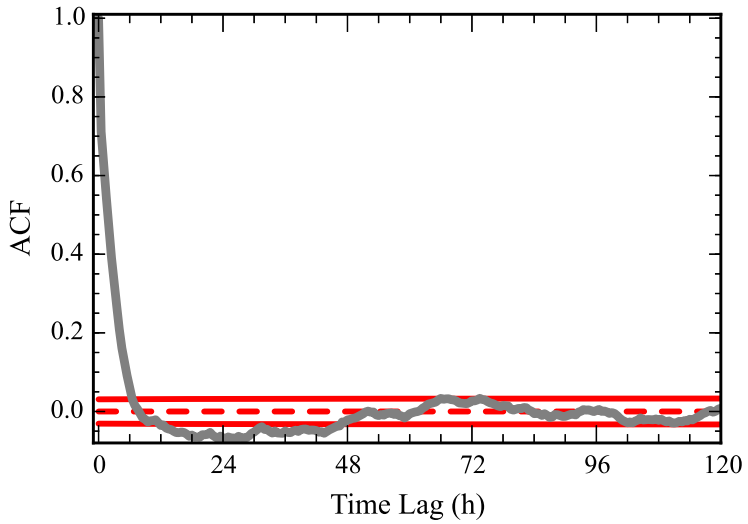

Figure 2.3: Autocorrelation of the Q11-Q17 *Kepler* light curve of KIC 4552982. The positive autocorrelation coefficients at short ($<$ 8 hour) time lag simply demonstrate that outbursts often persist to this duration. The range of time lags that produce negative autocorrelation coefficients is interesting, as it shows that an outburst is less likely to happen within 2 days of another. Beyond this recharge time, outbursts are consistent with being random (the solid lines are the 95% confidence intervals for random data).

of roughly 2 days, outbursts are consistent with occurring at random. The outbursts appear to be aperiodic, so we cannot formulate an event ephemeris to predict the timing of future outburst events.

Figure 2.4 displays regions of the light curve surrounding a few representative events in more detail. The top panel shows the most energetic event found in the light curve, the second panel shows a median-energy event, the third panel shows a multi-peaked event, and the bottom panel displays the mean event profile that is representative of these events as a whole. We

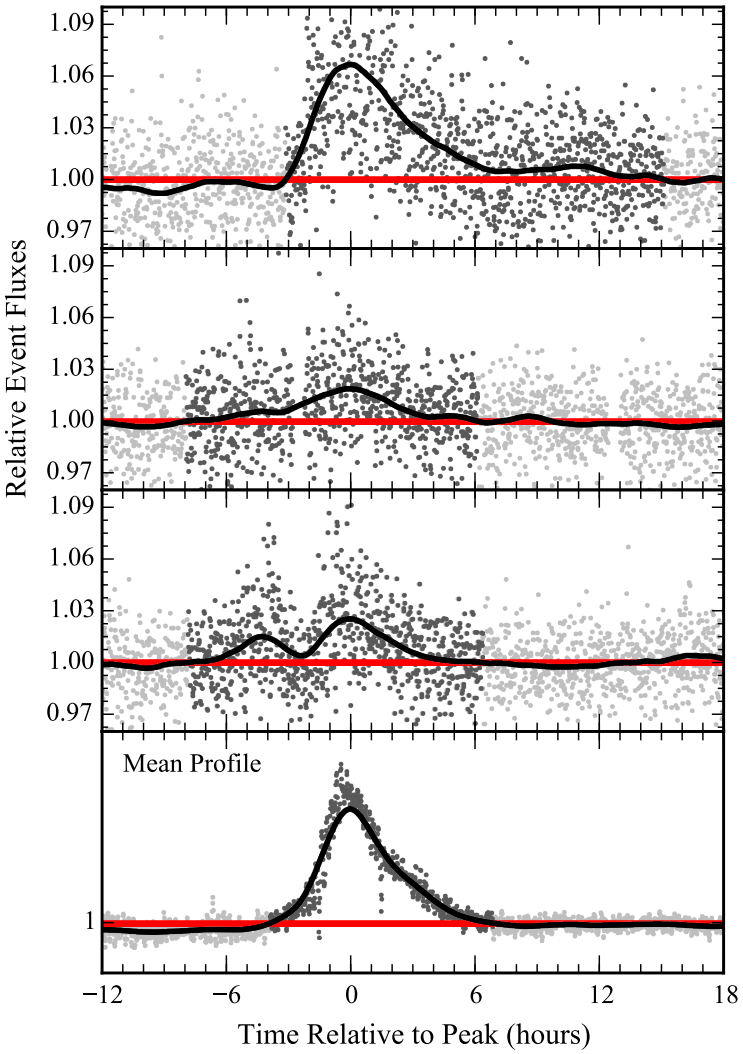

Figure 2.4: Examples of outburst events. Top: most energetic. Second: median energy. Third: multi-peaked. Bottom: mean profile. The black curves are smoothed with a 3-hour-wide Epanechnikov kernel. The regions determined as belonging to the outburst by our algorithm are indicated with darker gray points.

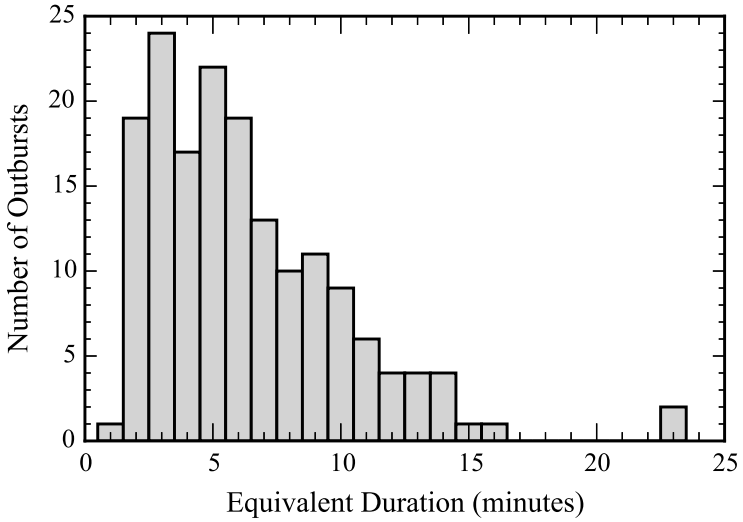

Figure 2.5: Histogram of equivalent durations for the 167 outbursts observed in their entirety.

calculated this mean profile by aligning the moments of peak brightness of all the detected events and averaging points into 58.85-s time bins.

To quantify the energies of these outbursts in the *Kepler* bandpass, we measure their equivalent durations (Gershberg 1972). These are measured in the same way as spectral line equivalent widths: we integrate the flux above the local mean for the duration of the event, normalized to the mean flux level. Assuming that the outbursts originate from the target star, this results in a value with units of time equaling the duration that the star would shine in quiescence to output the same amount of energy in the observed bandpass as the measured excess from the brightening event. A histogram of the measured equivalent durations of the 167 outbursts that were recorded without inter-

ruption from gaps in the data is displayed in Figure 2.5 and the continua used for the example outbursts are included in Figure 2.4. The median equivalent duration of detected outbursts is 5.5 minutes (the corresponding outburst is displayed in the second panel of Figure 2.4). Our detection algorithm is tuned to detect large outbursts and is likely incomplete in identifying the lowest-energy events.

2.3.2 Discussion of Outbursts

The outburst characteristics that we measure are unlike any previously studied white dwarf behavior. We argue here that these events originate from the white dwarf target KIC 4552982 and mark the first detection of a new astrophysical phenomenon. The data in hand are insufficient for us to identify the physical mechanism that drives these events. While we suggest possible connections to the evolutionary state of KIC 4552982, more intensive observational and theoretical explorations into their nature are left for future work.

Each quarter of *Kepler* data was separated by rolls of the spacecraft that positioned the KIC 4552982 stellar image on a repeating sequence of four different CCD detectors. Since the outbursts are prevalent in all quarters of *Kepler* data, they cannot be instrumental artifacts of any one of the detectors. Furthermore, these are not widespread systematic artifacts since they do not correlate with any of the *Kepler*-provided Cotrending Basis Vectors that catalog trends common amongst light curves for many objects. No other short-cadence targets show this phenomenon. We also find no correlation between

the outbursts and the short-cadence light curve that we extracted for KIC 4552992 – a star with $K_p = 18.934$ mag that is separated from KIC 4552982 by 12.5" and fell mostly within the same CCD subregions read out for the target. We note that this other source is well separated from our target and did not contribute flux to our custom photometric apertures.

From the discovery paper (Hermes et al. 2011), we have five low- to medium-resolution spectra of KIC 4552982 that cover a combined wavelength range from 4500 to 7200 Å. None show evidence of a companion from either radial velocity variations or spectral features that are not common of a DA (hydrogen atmosphere) white dwarf in this wavelength regime. Since the discovery paper on KIC 4552982, new 3-dimensional convection simulations have mapped the parameters determined from 1-dimensional spectroscopic model fits to values that largely resolve a mass discrepancy in the 1-dimensional approach (Tremblay et al. 2013). We apply these corrective terms and revise the spectroscopically derived values from Hermes et al. (2011) to $T_{\rm eff}$ = 10,860 ± 120 K, $\log g = 8.16 \pm 0.06$. The white dwarf radius, as interpolated from the model cooling sequences of Renedo et al. (2010), enables the conversion to $M_\star = 0.69 \pm 0.04\ M_\odot$. These parameters maintain that KIC 4552982 is one of the coolest known ZZ Ceti pulsators with a mass near or slightly above the peak of the DA white dwarf mass distribution (e.g., Falcon et al. 2010 find $\langle M_{\rm DA} \rangle = 0.647^{+0.013}_{-0.014}\ M_\odot$ from gravitational redshift measurements).

Apparent photometric magnitudes for KIC 4552928 are available from the *Kepler*-INT Survey (KIS; Greiss et al. 2014) in U, g, r, and i filters. We

Table 2.1. Apparent photometric magnitudes of KIC 4552982

Filter	Vega magnitude	AB magnitude
U	17.362 ± 0.007	18.15 ± 0.01
g	17.755 ± 0.005	17.68 ± 0.01
r	17.677 ± 0.007	17.84 ± 0.01
i	17.565 ± 0.009	17.94 ± 0.01
J	17.76 ± 0.03	18.70 ± 0.03

include these magnitudes in Table 2.1 along with the J-band magnitude acquired from the UKIRT public archive[1]. All of these are reported in the Vega photometric system. To compare these magnitudes in a spectral energy distribution (SED), we convert from the Vega system to physical AB magnitudes using the conversion factors calculated by Blanton & Roweis (2007) for the U, g, r, i filters, and the conversion of Hewett et al. (2006) for the J filter. We plot the SED of KIC 4552982 against a synthetic spectrum of a $T_{\rm eff} = 11{,}000$ K, $\log g = 8.25$ white dwarf (Koester 2010) for reference in Figure 2.6. We note that the photometry appears consistent with the model out to the infrared, demonstrating the absence of any cool main sequence companion that we might entertain as the possible source of the brightening events in the *Kepler* data. We did not deredden the magnitudes, which might account for the slight discrepancy in the U-band.

It is not likely that the outbursts are transient events from some line-

[1] `http://keplerscience.arc.nasa.gov/ToolsUKIRT.shtml`

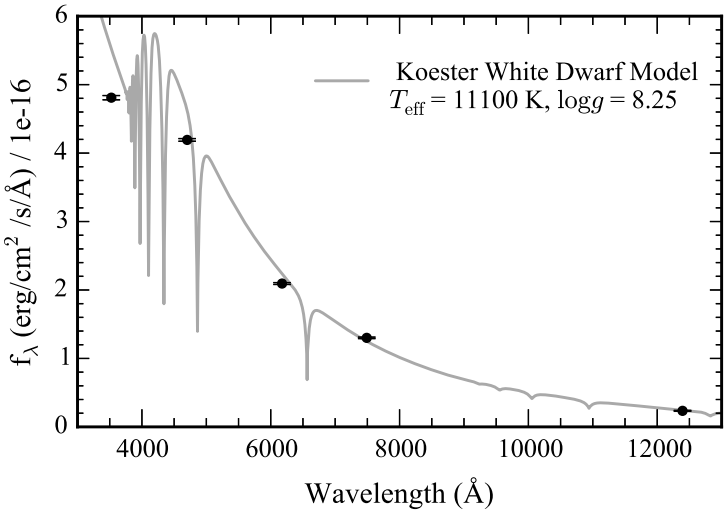

Figure 2.6: The spectral energy distribution of KIC 4552982 in U, g, r, i from the KIS survey and a J-band magnitude from the UKIRT J-band Public Archive. The synthetic spectrum Koester (2010) near the spectroscopically determined atmospheric parameters is plotted for reference. We see no infrared excess, allowing us to rule out a cool dwarf star companion to the white dwarf as the source of the observed outbursts.

of-sight flare star, rather than intrinsic to the pulsating white dwarf. While the slightly shorter rise time than decay time of the mean outburst profile in the bottom panel of Figure 2.4 is qualitatively reminiscent of flares observed from low-mass main sequence stars, the observed flux increases are not nearly as rapid as the impulsive phases of classical stellar flares (Moffett 1974; Benz & Güdel 2010). Extensive studies of flares from early-type M dwarfs (M4 and earlier; Hawley et al. 2014; Davenport et al. 2014) in the short cadence *Kepler* data and from later-type M dwarfs from ground-based photometry (Hilton 2011) do not find such frequent, energetic flares as we detect in our data. The

durations and pulse shapes of flares from K dwarfs in the *Kepler* long-cadence data also do not match our observations (Walkowicz et al. 2011). That the quiescent flux of a line-of-sight flare star in the *Kepler* bandpass must be orders of magnitude less than the white dwarf target to not be detected in the observed spectra or SED means that the already improbable energies/peaks/durations of the outbursts are only extreme lower-limits if they do not originate from the white dwarf.

To constrain whether the outbursts could be coming from any spatially offset faint transient source — flare star or otherwise — we searched for correlations between the photometric centroids within the *Kepler* images (plate scale $\approx 4''$ pixel^{-1}) and the occurrences of outbursts using the approach of Bryson et al. (2013). Our analysis was inconclusive. Although the photometry shows significant centroid offsets when comparing the light curve during outbursts to quiescent moments, the shifts are in inconsistent directions on the sky in different quarters. When comparing just the higher-flux to lower-flux frames from quiescent segments of the light curve, an identical centroid analysis again shows significant shifts of comparable magnitude in identical directions. The measured centroid shifts of as much as $0.04''$ are likely dominated by variations in pixel sensitivity rather than the presence of any transient offset by more than of order $0.1''$.

Some white dwarfs host surface magnetic fields locally as strong as $\sim$ 1000 MG (e.g., PG 1031+234; Latter et al. 1987). We do not undertake any attempt to physically model the output of magnetic reconnection flares in

white dwarfs for this analysis; however, the available spectra of KIC 4552982 do not show line splitting that would evidence that it is highly magnetic (resolved Zeeman splitting is expected for $B \geq 10^6$ Gauss; Wickramasinghe & Ferrario 2000). Since this first object to exhibit this behavior is not nearly one of the more strongly magnetic white dwarfs studied, it is difficult to ascribe the outbursts to magnetic processes. Since the timescales of dynamic events like flares should scale roughly with the dynamical timescale (free-fall time), we do not expect to see flares of multi-hour duration on a white dwarf with a ~ 1 s dynamical timescale.

We collected 42 hours of follow-up, higher signal-to-noise photometry with the Argos photometer (Mukadam & Nather 2005) on the McDonald Observatory 2.1-meter Otto Struve telescope over eight nights through a $BG40$ filter in 2013 August with hopes of catching the system in outburst. Unfortunately we made no such detection. Given the distribution of observing windows when we were able to get useful data, there was a 47% chance that we would have caught the peak of an outburst. We also do not detect this phenomenon when reanalyzing the original discovery data of Hermes et al. (2011).

De Marco et al. (2015) analyze the *Kepler* light curve of the central star of planetary nebula Kn 61, which exhibits brightening events every 2–12 days, each lasting 1–2 days with amplitudes of 8–14%. These events are similar to the outbursts on KIC 4552982, at least in that they are also unlike previously studied behavior. While the authors are unable to conclusively demonstrate

a mechanism for observed outbursts in Kn 61, they explore accretion as a possible energy source. Extending this analysis, they equate the energy of a median outburst on KIC 4552982 to 5×10^{-15} $M_{\odot}$ of accreted material. We note with some interest that this is within the range of measured asteroid masses (Hilton 2002), but there is currently no known dynamical mechanism to drop circumstellar debris onto a white dwarf with this fairly regular and relatively rapid recurrence timescale (Jura 2008). Assuming a total asteroid population mass of order the Solar System asteroid belt mass (1.8×10^{24} g; Binzel et al. 2000), this rapid accretion would deplete the mass reservoir in a mere $\sim$1000 yr. With an outburst frequency far shorter than the calcium diffusion timescale of $\sim$40 yr for a $T_{\rm eff}$ = 10,860 K, $\log g = 8.16$ white dwarf (Koester & Wilken 2006), we would expect such rapid accretion to cause strong absorption at the calcium H & K doublet. We do not detect this signature in the available spectra (Hermes et al. 2011).

With $T_{\rm eff} = 10{,}860 \pm 120$ K, KIC 4552982 is one of the coolest ZZ Cetis known (Tremblay et al. 2013). The mechanism that shuts down pulsations at the empirical cool edge of the ZZ Ceti instability strip is not fully understood, but may be related to the thermal timescale at the base of the convection zone exceeding some critical value (e.g., Van Grootel et al. 2013). To explore this timescale in KIC 4552982, we use the Warsaw-New Jersey stellar envelope code (Pamyatnykh 1999) to calculate a static pure-hydrogen atmosphere model that matches the measured spectroscopic parameters with the ML2/$\alpha = 1.0$ mixing-length prescription for convection. We display the run of

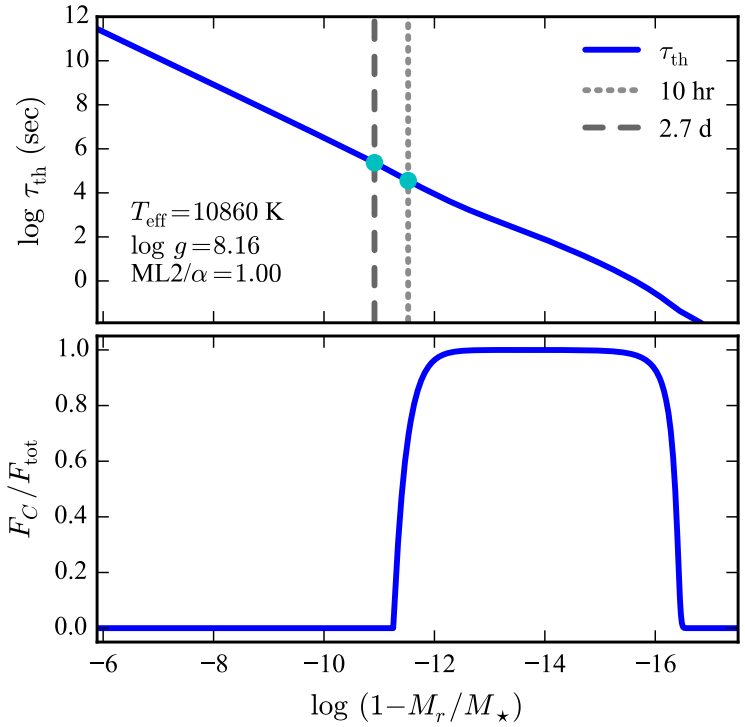

Figure 2.7: Top: the thermal timescale as a function of depth in our model. The 10-hr average outburst duration timescale and the 2.7-day recurrence timescale are marked with vertical dotted lines. Bottom: the fractional flux carried by convection through the static model atmosphere. The relevant outburst timescales are of order the thermal timescale at the base of the convection zone, which is the timescale suspected to be most relevant to the cessation of pulsations at the cool edge of the instability strip.

the thermal timescale and the convection profile in the outer 10^{-6} of the star by mass in Figure 2.7. We note that the thermal timescale at the base of the convection zone is of the same order as the outburst duration and recurrence timescales (and much longer than the $\sim$1 second dynamical timescale). If this is more than just a numerical coincidence, then it is possible that this outburst

behavior is a more general property of ZZ Ceti variables as they evolve out of the instability strip.

While more than 180 ZZ Cetis have been previously discovered and studied, there has been a slight bias towards the detection of pulsators near the hot edge of the instability strip. This is because their pulsations are exceptionally stable, enabling studies of white dwarf evolutionary cooling (e.g., Kepler et al. 2005) and possible planetary companionship (Mullally et al. 2008). By virtue of falling within the *Kepler* field, KIC 4552982 has become the most extensively observed cool-edge ZZ Ceti. That this outburst behavior has not been previously detected in other cool-edge pulsators may be due partially to this selection bias. The routine practice of dividing low-order polynomials from ground-based light curves to correct for changes in atmospheric extinction may also have obscured this behavior in previous observations.

2.4 White Dwarf Pulsation Analysis

The 20-month light curve yields one of the richest pulsation spectra ever resolved for a ZZ Ceti variable. If the energetic outbursts do, in fact, originate from the white dwarf, they likely affect the stellar pulsations in a measurable way. We explore the observed variations in pulsation mode properties that may be related to these outbursts, but unfortunately the signal-to-noise of the *Kepler* light curve is insufficient to study these variations on timescales less than the mean outburst timescale in much detail. We proceed with an asteroseismic analysis that assumes that the outbursts do not significantly

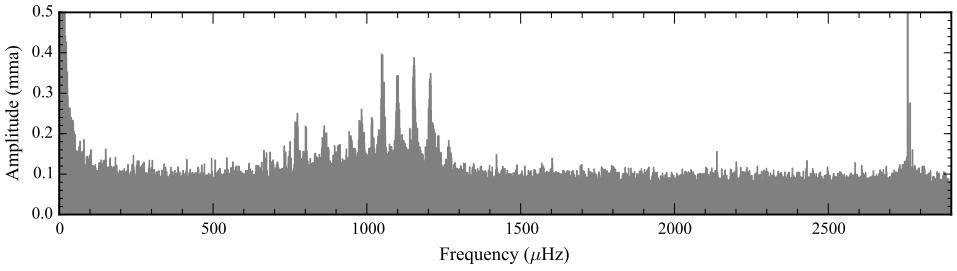

Figure 2.8: Fourier transform of the entire Q11-Q17 *Kepler* light curve of KIC 4552982 in the region of significant pulsational variability (amplitude scale in mma = 0.1 %).

alter the locations of the peaks in the power spectrum of KIC 4552982 and reserve comments on the possible interplay between these dynamic processes for our concluding remarks.

2.4.1 Mode Stability and Frequency Determination

Figure 2.8 shows the Fourier transform (FT) of the entire Q11-Q17 light curve through the full region of significant pulsational variability. This FT was computed with the Period04 software (Lenz & Breger 2004). We exclude all known instrumental artifacts that are harmonics of the long-cadence sampling rate of 566.41 μHz (Gilliland et al. 2010b) from this analysis. The power at the low-frequency limit of the FT is introduced primarily by the aperiodic outbursts and mostly goes away if we remove the outburst events from the light curve before computing the FT. Since this $1/f$ noise decays sufficiently before the low end of the frequency range of pulsations and the FT of the full light curve (including outbursts) yields an overall lower noise level in the

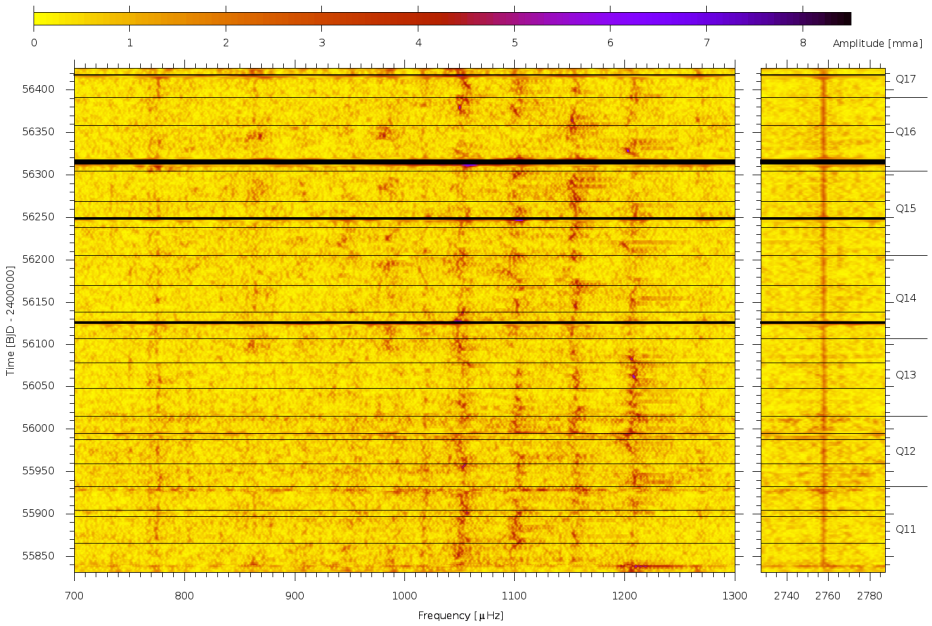

Figure 2.9: Sliding FT of a 5-day window over the entire *Kepler* light curve. The color bar at the top of the figure gives the amplitude scale in mma (= 0.1 %). The modes in the 700–1300 μHz frequency range (left panel) are observed to wander in phase (frequency) and amplitude while the mode at 2757.54 μHz is relatively stable.

spectrum, we do not exclude the outbursts from the light curve for our Fourier analysis.

The features of the FT of particular asteroseismic significance are the 17 bands of power in the 600–1450 μHz frequency range and the sharp rotational triplet feature surrounding 2765.66 μHz. The broad power bands clearly do not reflect the sharp, 0.020-μHz-wide spectral window (the signature of a perfect sine wave sampled identically to the data). This is the result of modulation of the pulsation properties of the observed modes. This modulation in

amplitude and frequency is clearly seen in the sliding FT of Figure 2.9. The sliding FT is computed by sliding a 5-day window over the entire light curve and computing the FT at 1-day steps. This time-resolved 2-dimensional FT is shown in color contour, where darker areas indicate greater power in the FT. We observe that all the pulsations in the 700–1300 μHz range (left panel) show rapid changes in frequency and amplitude on a timescale of a few days. The frequency shifts of the main peaks appear to be correlated, demonstrating that these drifts cannot be ascribed purely to stochastic behavior of the individual modes. The higher amplitudes in the sliding FT compared to the full FT in Figure 2.8 demonstrates that the instantaneous mode amplitudes are larger than the peaks of the widened power bands. These data offer the most extensive coverage of mode variations that are typical of cool ZZ Cetis (see, e.g., Pfeiffer et al. 1996; Kleinman et al. 1998; Hermes et al. 2014b). The variations in mode properties may be related to the outbursts observed in the light curve (Section 2.3), but we were unable to demonstrate this connection from the data. Meanwhile, the mode at 2757.54 μHz (right panel) is relatively stable.

We interpret each band of power to be linked to a single significant pulsation mode in the star. Since the wide nature of these bands prevents us from simply selecting and prewhitening the highest peaks in the FT, we instead adopt a method of fitting each band in the power spectrum (the squared FT) with a Lorentzian function:

$$L(\nu) = \frac{P\gamma^2}{(\nu - \nu_0)^2 + \gamma^2} + \langle FT(\nu)^2 \rangle. \tag{2.1}$$

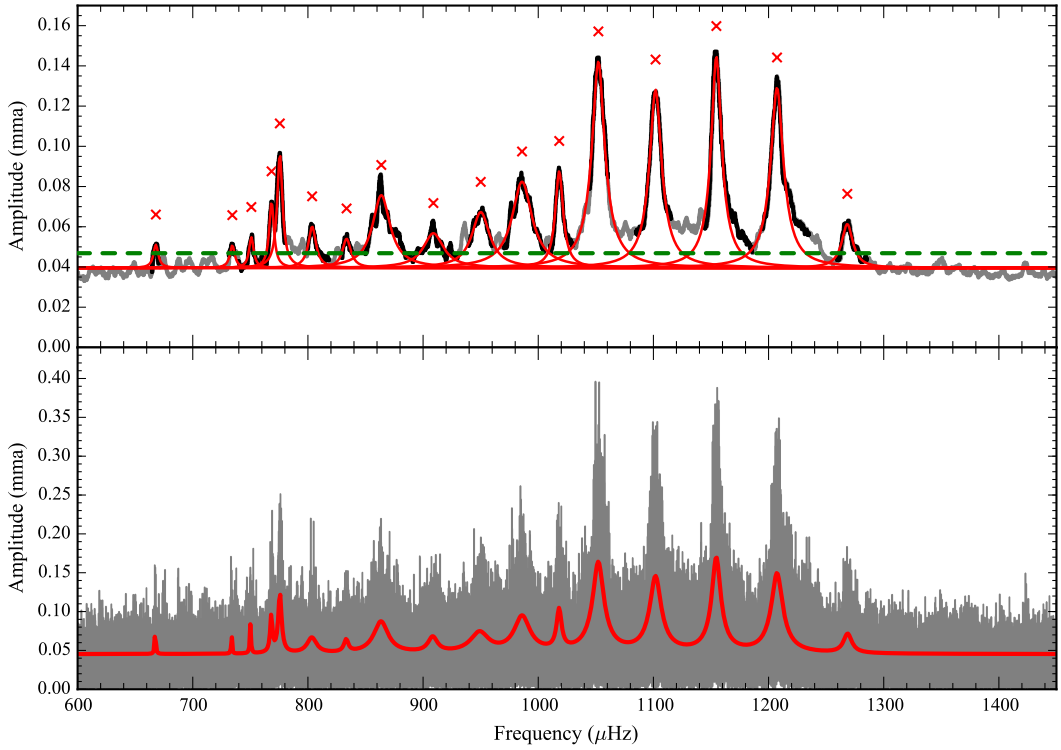

Figure 2.10: Top: Lorentzian fits to 17 bands of pulsational power in the 4-μHz boxcar smoothed FT. The horizontal line at 0.0468 mma is our significance criterion. The Lorentzians are best fits to the power (amplitude squared) above the median noise level in hand-selected (black) regions of the light curve. Bottom: We refine our fit parameters by simultaneously fitting these 17 bands to the original, unsmoothed FT. The final parameters of these Lorentzians are listed in Table 2.2.

While Lorentzians are used to fit signatures of the stochastically driven pulsations in Sun-like stars and red giants, we emphasize that stochastic driving is unlikely to be efficient in pulsating white dwarfs since the stochastic driving timescale ($\sim$ 1 second) is much shorter than the observed pulsation periods ($\sim$ 10 minutes; Saio 2013). We choose to fit Lorentzians as a convenience.

We use slightly different methods for identifying and fitting Lorentzians to the significant frequencies in each region of the FT that are adapted to suit the different feature widths.

For the dense bands of pulsational power in the 600–1450 μHz range, we first identify which bands are significant from the 4-μHz boxcar-smoothed FT displayed in the top panel of Figure 2.10. We use a bootstrap method to calculate a very conservative significance threshold. We randomly rearrange the light curve points 10,000 times, keeping the same time sampling. We then calculate the FT in the 600–1450 μHz range, apply the 4 μHz smoothing, and record the highest value in the smoothed FT for each shuffled light curve. We set our significance threshold equal to the 99.7 percentile in the distribution of maximum values in each shuffled, smoothed FT. We find this value at 0.0468 mma (1 mma = 0.1%) in the smoothed FTs. This means there is only a $\sim 0.3\%$ chance that we would find *any* peak in the smoothed FT above 0.0468 mma due to noise alone. However, in regions near a pulsational power band, the wide feature can raise actual noise peaks above this threshold, so we conservatively fit only unambiguously significant features near larger power bands. The peaks of the features we select are each marked with a $\times$ in the top panel of Figure 2.10. Our least squares Lorentzian fits use 5 μHz initial guesses for the HWHM at these locations (selected so that the resulting fits match the intended features by eye). We fit Lorentzians only to the regions immediately surrounding the selected features (the black portions of the smoothed FT in the top panel of Figure 2.10). The resulting Lorentzian fits to these features

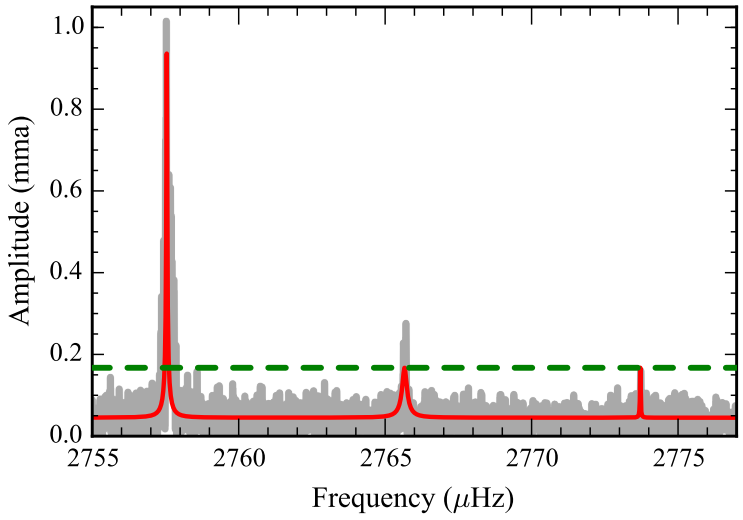

Figure 2.11: The rotational triplet surrounding the 2765.66 μHz mode. The power was fit with the displayed set of Lorentzians. The highest-frequency component consists of a single point above the noise that is fit to its peak power by the Lorentzian.

are displayed in the figure.

While the smoothed FT is useful for selecting significant peaks in frequency space, the smoothing can affect the HWHMs of the Lorentzian fits. Since these HWHMs may have an astrophysical significance, we refine our fit parameters by fitting to the unsmoothed FT. We refit all of the Lorentzians concurrently with a common bias-level parameter to fit the average noise level. The result of this fit is plotted over the unsmoothed FT in the bottom panel of Figure 2.10. Because these power bands encompass a forest of high- and low- amplitude peaks, the final Lorentzians fit through the average amplitudes and do not reach the maximum peaks of the features. The central frequencies,

Table 2.2. Properties of Lorentzian fits to significant frequencies of pulsational variability in the FT.

Mode	Period (s)	Frequency (ν_0; μHz)	HWHM (γ; μHz)	Lorentzian height (P; mma^2)
f_1[a]	1498.32	667.42	0.34	0.0062
f_2	1362.95	733.70	0.26	0.0056
f_3[a]	1333.18	750.09	0.46	0.0050
f_4[ab]	1301.73	768.21	0.97	0.0070
f_5[ab]	1289.21	775.67	1.38	0.0132
f_6[a]	1244.73	803.38	4.50	0.0023
f_7[a]	1200.18	833.21	2.15	0.0018
f_8[a]	1158.20	863.41	6.59	0.0055
f_9	1100.87	908.38	4.51	0.0023
f_{10}	1053.68	949.06	8.61	0.0032
f_{11}	1014.24	985.96	7.13	0.0066
f_{12}	982.23	1018.09	2.21	0.0081
f_{13}[a]	950.45	1052.13	4.58	0.0246
f_{14}[a]	907.59	1101.82	4.75	0.0189
f_{15}[a]	866.11	1154.59	3.68	0.0266
f_{16}[a]	828.29	1207.31	4.67	0.0202
f_{17}[a]	788.24	1268.65	3.93	0.0029
f_{18}[ab]	362.64	2757.54	0.013	0.8743
f_{19}[ab]	361.58	2765.66	0.007	0.0260
f_{20}[ab]	360.53	2773.71	0.009	0.0260[c]

[a]Likely part of the $\ell = 1$ sequence based on alignment with the mean $\ell = 1$ period spacing or observed rotational splitting.

[b]Likely rotationally split components of an $\ell = 1$ mode.

[c]This fit matches the single peak for this component in the power spectrum with a height corresponding to peak power.

HWHMs, and heights of the Lorentzian fits are listed with the central mode periods in Table 2.2. Their relation to Equation 2.1 is also indicated.

Figure 2.11 shows a higher-frequency region of the original, unsmoothed FT. Here we observe a triplet of significant variability with near-even frequency spacing. We calculate a significance threshold of 99.7% confidence at 0.167 mma by a bootstrap approach similar to our calculation for the lower-frequency power bands. The difference between the 0.167 mma significance threshold here and the 0.0468 mma threshold for the smoothed FT at lower frequency results purely from the boxcar smoothing of the latter. While only the two lowest-frequency components rise above this significance threshold, we relax our criterion for the third peak because it falls in step with the others as is expected for rotational splitting (see Section 2.4.4) and is only barely below our very conservative signifiance threshold. We simultaneously fit the three features with Lorentzians as we did for the wider power bands using 1 μHz for the initial guesses for the HWHM and adopting the bias level fit in the previous region. The third component consists of a single peak above the noise, and the height of the Lorentzian fits the peak power of that mode. These best-fit parameters are included in Table 2.2.

We adopt these 20 frequencies as the mean pulsation mode frequencies of KIC 4552982. Since we used an unconventional method for determining these mode parameters for pulsating white dwarfs, it is difficult to assign absolute uncertainties. We advise that researchers wishing to fit their own asteroseismic models to these frequencies weight their fits by $1/\mathrm{HWHM}^2$ for each mode. Since we resolve the frequency variations over our extended light curve, our frequency determinations should be far more accurate than the

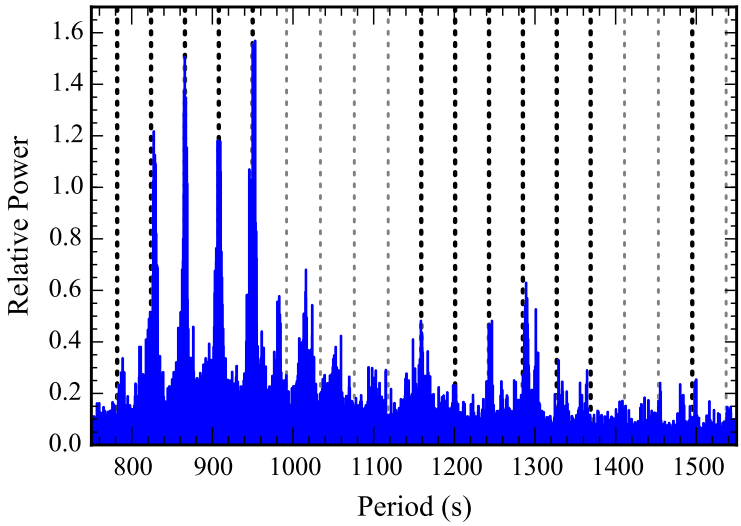

Figure 2.12: The period transform of the full *Kepler* light curve in the region of observed pulsational power bands. The locations of the expected $\ell = 1$ modes from the mean period spacing determined in Figure 2.13 are marked as dotted vertical lines. These lines are drawn darker where they fall within 7 seconds of one of our measured mode periods listed in Table 2.2

HWHM.

2.4.2 Period Spacing

The periods of the nonradial g-mode pulsations characteristic of white dwarfs of a given degree (ℓ) and sequential radial order (k) reach an even spacing at the asymptotic limit of high k. Because of geometric cancellation, we expect the pulsations we detect to be of degree $\ell = 1$ or $\ell = 2$ (Dziembowski 1977). With such a rich pulsation spectrum, we can hope to sample these sequences sufficiently well to determine the mean period spacing with radial order of one or both of these sequences.

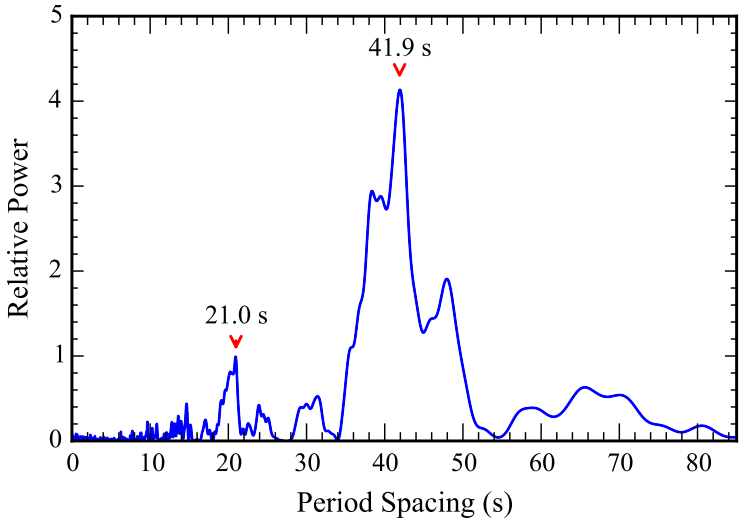

Figure 2.13: The period transform of the period transform reveals a significant mean period spacing at 41.9 seconds and its harmonic. This likely corresponds to a mean period spacing of $\ell = 1$ modes.

We approach this measurement by taking the period transform of the period transform of the entire light curve as is described in its application to the DOV (pulsating hot pre-white dwarf) star PG 1159-035 in Winget et al. (1991, Section 5.2.1). We emphasize that this approach is independent of the period determination in Section 2.4.1. We arrive at the period transform by simply inverting the x-axis of the FT in the region of dense pulsational power bands (between 500 and 1500 μHz, corresponding to a period range 667–2000 s). This intermediate result is shown in Figure 2.12. If the signals from pulsations correspond to one or more sequences with evenly spaced periods, the period transform of this period transform should reveal the spacings. We show the resulting power spectrum in Figure 2.13 and mark two peaks of

interest: a significant spacing at 41.9 ± 0.2 s and its overtone at 20.97 ± 0.02 s (uncertainties determined from 100 Monte Carlo simulations with PERIOD04). This overtone arises from the decidedly non-sinusoidal nature of the periodic signal in the period transform. Using the phase information we get from least-squares sinusoidal fits, we mark the locations of expected modes in the even period-spacing sequence as vertical dotted lines in Figure 2.12 and indicate those modes that fall within 7 seconds of the measured spacing with darker dotted lines and with footnotes in Table 2.2.

2.4.3 Comparison with Asteroseismic Models

We consider a grid of more than 14,000 DA white dwarf cooling models that we calculated from the White Dwarf Evolution Code (WDEC; Lamb & van Horn 1975; Wood 1990) following the treatment described in Bischoff-Kim et al. (2008). We vary the following three parameters that most influence the mean period spacing, with noted resolution: 10,000 K $\leq T_{\rm eff} \leq$ 12,000 K (200 K resolution), 0.500 $M_{\odot} \leq M_{*} \leq$ 0.800 $M_{\odot}$ (0.005 $M_{\odot}$ resolution), and $-6.00 \leq \log M_{\rm H}/M_{\star} \leq -4.00$ (in steps of 0.10). This set of models widely encompasses the spectroscopic M_{*}, $T_{\rm eff}$ values of KIC 4552982. Each of these models has a helium layer mass of $\log M_{\rm He}/M_{\star} = -2.00$ (close to the value calculated for 0.7 $M_{\odot}$ white dwarfs by Lawlor & MacDonald 2006). The core profiles have central abundances of 30% carbon and 70% oxygen and are homogeneous out to 0.5 M_{r}/M_{*} (chosen to be in good agreement with Salaris et al. 1997).

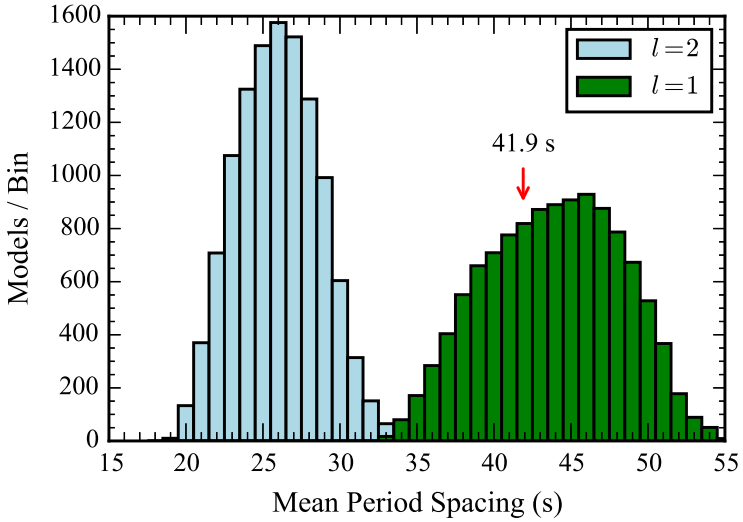

Figure 2.14: Histograms of mean period spacings calculated for $\ell = 1$ and $\ell = 2$ sequences throughout our model grid. The measured spacing for KIC 4552982 of 41.9 seconds fits exclusively within the $\ell = 1$ distribution.

The measured mean period spacing of 41.9 ± 0.2 s fits well within the distribution of calculated mean spacings in our models for $\ell = 1$ modes. For $\ell = 2$ modes, the models predict mean spacings nearer to 26 s. These distributions are compared in Figure 2.14 .

We suggest that the modes that fall in step with the measured mean period spacing are likely part of the $\ell = 1$ sequence with footnotes in Table 2.2. Undoubtedly, some $\ell = 2$ modes may by chance fall in line with this sequence and be misidentified. Mode trapping and the dominance of different rotationally split components of the modes (see Section 2.4.4) can shift individual frequencies significantly from an equal period spacing, so some of the modes that we do not observe to closely match the mean spacing may also

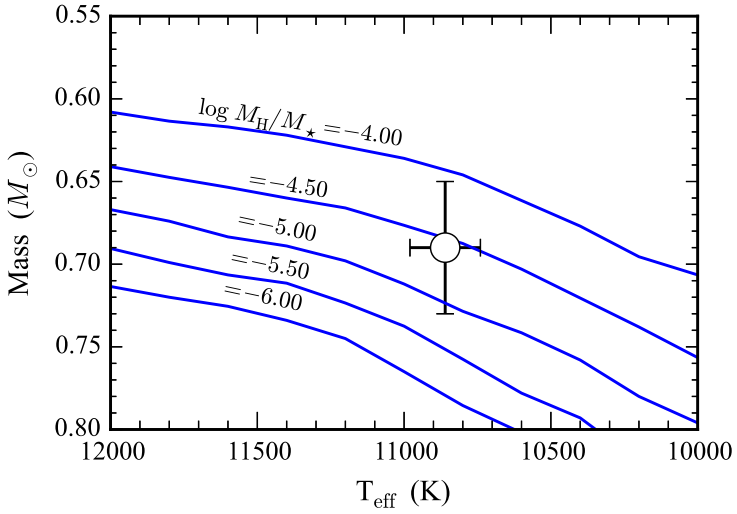

Figure 2.15: The locations of models through M_* – $T_{\rm eff}$ space with mean $\ell = 1$ period spacings equal to the measured spacing of 41.9 seconds. The individual runs of solutions correspond to $\log M_{\rm H}/M_\star$ values from -4.00 (top track) to -6.00 (bottom track) in 0.50 resolution. All models that fit the observations have $M_* > 0.60\ M_\odot$. The spectroscopically determined parameters are overplotted in white, and are in slightly better agreement with models nearer the high-$M_{\rm H}$ end.

have $\ell = 1$. The dominance of different rotationally split components should not greatly affect our asteroseismic inferences (Metcalfe 2003).

We display the run of models with mean $\ell = 1$ spacings of 41.9 s through M_*, $T_{\rm eff}$ space for selected hydrogen layer masses in our model grid in Figure 2.15. The mean period spacing of g-modes is most sensitive to the overall mass, and our model comparison demonstrates asteroseimically that KIC 4552982 is likely more massive than 0.6 $M_\odot$— in good agreement with the spectroscopic mass determination.

The spectroscopic point is plotted with error bars over the $\log M_{\rm H}/M_\star$ tracks for reference. We observe that while the uncertainty in the spectroscopically determined M_* spans multiple tracks at the resolution of our model grid, the spectroscopic point agrees best with a $\log M_{\rm H}/M_\star$ value of -4.70 and generally falls nearer to the maximal $\log M_{\rm H}/M_\star$ extent of our model grid at -4.00.

2.4.4 Rotational Splitting

At higher frequency than the region of dense pulsational power bands, we noted three modes split evenly in frequency (Figure 2.11). Even frequency spacing can result from rotational splitting of a mode into $2\ell + 1$ components (Unno et al. 1989). While we emphasize that our absolute uncertainties in the individual frequencies determined in Section 2.4.1 are smaller than the HWHM of our Lorentzian fits, we will treat the HWHM here as proxies for uncertainty. From these values, we calculate a mean frequency splitting of 8.09 ± 0.02 μHz.

With only three components in the rotational multiplet, we are unable to definitively assign a spherical degree, ℓ, to this mode, so we consider the three most likely possibilities: these are either all $m = -1, 0, 1$ components of a $\ell = 1$ triplet, three consecutive components of a $\ell = 2$ quintuplet, or the $m = -2, 0, 2$ components of a $\ell = 2$ quintuplet.

We derive first-order analytical rotation rates under the assumption that the rotation period is much longer than the period of the split mode and that the white dwarf rotates as a solid body. We use the relation that

$\Delta\nu_{k\ell m} = (m/P_{rot}) \times (1 - C_{k\ell})$ (Brickhill 1975) for solid body rotation. At the limit of high k ($k \gtrsim 10$), $C_{k\ell}$ approaches $1/\ell(\ell+1)$. If we assume that this is an $\ell = 2$ mode, we are safely in the asymptotic limit ($k \sim$ 11 or 12 according to our models). If these are adjacent splittings of a $\ell = 2$ mode (i.e., $m = -2, -1, 0$, $m = -1, 0, 1$ or $m = 0, 1, 2$), we derive a rotation period of 28.63 ± 0.07 hours. If these are $\ell = 2$, $m = -2, 0, 2$ modes, we get twice that rotation period at $P_{rot} = 57.26 \pm 0.13$ hours. If this is the rotationally split triplet of a $\ell = 1$ mode, we cannot safely assume that these modes are in the asymptotic limit. We guide our interpretation for this case by comparing the mode periods to our asteroseismic model with parameters $T_{\rm eff}$ = 10,800 K and $M_* = 0.700\ M_\odot$ and $\log M_{\rm H}/M_\star = -4.70$. This model most closely matches our measured mean $\ell = 1$ period spacing and our spectroscopically determined atmospheric parameters. The measured 361.58-s period measured for the central component of the triplet falls between the following two $\ell = 1$ modes in the model: $k = 5$ at 311.6 s with $C_{k\ell} = 0.491$, and $k = 6$ at 379.0 s with $C_{k\ell} = 0.492$. These $C_{k\ell}$ values essentially match the asymptotic result, and we adopt the mean of these values to calculate a rotational period of 17.47 ± 0.04 hours. These periods are all plausible considering the range of asteroseismically determined rotation periods of other white dwarfs (Kawaler 2004), and they support our assumption that the rotation period is much longer than the pulsation periods.

Revisiting the region of wide pulsational power bands between 600–1450 μHz (Figure 2.10), we see suggestions of structure at a similar ≈ 8 μHz

spacing. This includes a pair of frequencies that passed our significance criteria and are indicated with a footnote in Table 2.2: f_4, f_5. Since these bands fall in line with the $\ell = 1$ mean period spacing pattern from our analysis in Section 2.4.2, we prefer the $\ell = 1$ rotation period of 17.47 ± 0.04 hours for this star.

2.5 Conclusions and Future Work

The *Kepler* light curve for KIC 4552982 exhibits two features of great interest: clear outburst phenomena and a rich spectrum of pulsations with frequency and amplitude modulations. We argue that these outbursts likely originate from the pulsating white dwarf and are the first observations of a new astrophysical phenomenon. Such energetic events likely affect the pulsations in a measurable way. Owing to the low signal-to-noise of the *Kepler* photometry of this faint target, we are unable to study changes in the pulsation spectrum strictly before and after the observed outburst events.

The most compelling evidence for the outbursts affecting the pulsations is the relative sharpness of the triplet of high-frequency modes surrounding 2765.66 μHz compared to the wide bands of power at lower frequency. If these modes are all of the same degree, ℓ, the lower-frequency, higher-k modes are more sensitive to regions nearer the surface of the star. We demonstrate that most of the modes we observe are likely part of a $\ell = 1$ sequence. The detected relative unsteadiness of the lower-frequency modes may then be an indication that the outbursts are a surface phenomenon (a similar argument is made for solar-type pulsators by Karoff 2014). However, variations in the pulsation

frequencies and amplitudes are commonly observed in cool ZZ Cetis, so this is not the only viable interpretation. If outbursts of the type we see in KIC 4552982 turn out to be common of cool ZZ Cetis, they may be related to the frequency modulations observed in these other stars.

We updated the spectroscopic parameters of Hermes et al. (2011) with corrections from 3D convective simulations to get $T_{\rm eff} = 10{,}860 \pm 120$ K, $\log g = 8.16 \pm 0.06$, and $M_\star = 0.69 \pm 0.04\ M_\odot$. These parameters place KIC 4552982 at the extreme cool edge of the ZZ Ceti instability strip where pulsations are just shutting down. We demonstrate that the average duration (≈ 10 hours) and recurrence (≈ 2.7 days) timescales observed for the outbursts are of order the thermal timescale at the base of the convection zone and suggest that these outbursts could be a feature common to all white dwarfs with this convection zone depth, and therefore temperature.

We identify 20 independent pulsation frequencies including rotationally split components as characterized in Table 2.2. Comparing the measured mean period spacing of the nearly sequential k-overtones of likely $l = 1$ modes to our models, the asteroseismology supports the spectroscopic finding for the white dwarf mass: $M_* > 0.6\ M_\odot$. These spectroscopic parameters match our asteroseismic models with 41.9 ± 0.2 s mean period spacings slightly better closer to the thick outer hydrogen layer end of our grid ($\log M_{\rm H}/M_\star = -4.00$) rather than the thin limit of our models ($\log M_{\rm H}/M_\star = -6.00$). We also derive a likely rotation period of 17.47 ± 0.04 hours if the observed modes surrounding 2765.66 μHz are a rotationally split $\ell = 1$ triplet.

The sheer extent of this nearly continuous 20-month light curve has provided an unparalleled look at dynamic white dwarf processes. Continued asteroseismic interpretation of the identified pulsation frequencies and outburst characteristics will hopefully lead to additional constraints on the internal structure of KIC 4552982.

Chapter 3

Outbursts in Two New Cool Pulsating DA White Dwarfs *

Following the failure of a second reaction wheel aboard the *Kepler* spacecraft, it was no long able to maintain pointing on the original mission field. In order to salvage the spacecraft, a clever scheme was devised that utilizes solar wind pressure for stability, enabling observations of new fields roughly every 80 days along the ecliptic (Howell et al. 2014). While the shorter baseline of observations of each field is not ideal for exoplanet studies, white dwarf asteroseismology has benefited greatly from the increase in the number of pulsators in the larger survey footprint of this *K2* mission.

Following the discovery of a new outburst phenomenon in the *Kepler* observations of the cool ZZ Ceti star KIC 4552982 (Bell et al. 2015c, and Chapter 2), *K2* quickly revealed another example of this behavior in the brighter ZZ Ceti PG 1149+057 (Hermes et al. 2015b). These data clearly showed that

*This work was previously published as Bell, K. J., Hermes, J. J., Montgomery, M. H., Gentile Fusillo, N. P., Raddi, R., Gänsicke, B. T., Winget, D. E., Dennihy, E., Gianninas, A., Tremblay, P.-E., Chote, P. and Winget, K. I., 2016, *Outbursts in Two New Cool Pulsating DA White Dwarfs*, ApJ, 829, 82. I led the photometric analysis in this work. The co-authors helped to identify the discussed stars as white dwarfs for *K2* observations, to extract the *K2* light curves, to obtain and interpret spectroscopy, and to collect follow-up observations from McDonald Observatory.

pulsation frequencies and amplitudes both increase during outbursts, proving that this effect is in the white dwarf. The flux enhancement from the combined outburst and increased pulsation amplitudes reached as high as 45% in the most energetic outburst.

As *K2* continued to observe new fields, we kept finding new examples of outbursting ZZ Cetis. The content of this chapter has been published as Bell et al. (2016). We present two new outbursting ZZ Cetis through Campaign 6, and constrain the absence of outbursts from other white dwarfs that had been observed by *Kepler* and *K2* at that time. We demonstrate that this behavior is common near the cool edge of the ZZ Ceti instability strip and that only pulsating white dwarfs exhibit outbursts. Chapter 4 brings this observational effort up to date through the most recently released Campaign 10 data.

3.1 Introduction

White dwarf stars are the remnant products of 97% of Galactic stellar evolution. About 80% of white dwarfs spectroscopically display atmospheres dominated by hydrogen (DA; Tremblay & Bergeron 2008). Convective driving (Brickhill 1991; Goldreich & Wu 1999a) of nonradial gravity-mode pulsations (Robinson et al. 1982) in DA white dwarfs between 12,500 K $> T_{\rm eff} >$ 10,600 K (for typical $\log g \approx 8.0$; Tremblay et al. 2015) causes these objects to appear photometrically variable. The frequencies of photometric variability are eigenfrequencies of these stars as physical systems, providing a powerful tool for studying their interior structures (see reviews by Winget & Kepler

2008; Fontaine & Brassard 2008; Althaus et al. 2010).

The *Kepler* spacecraft has provided unrivaled monitoring of pulsating white dwarfs, both in its original mission and during the two-reaction-wheel mission, *K2* (Howell et al. 2014). The first and longest-observed pulsating DA white dwarf (DAV) known to lie within the original mission field is KIC 4552982 (WD J191643.83+393849.7; Hermes et al. 2011). This target was observed nearly continuously every minute for more than 1.5 yr. Unexpectedly, these data revealed at least 178 brightness increases that recurred stochastically on an average timescale of 2.7 d. The events increased the total flux output of the star by $2 - 17\%$ and lasted $4 - 25$ hr (Bell et al. 2015c).

Hermes et al. (2015b) described a second DAV to display similar outburst behavior: PG 1149+057, observed in *K2* Campaign 1. These outbursts caused the mean flux level to increase by up to 14%, which would correspond to a nearly 750 K global increase in the stellar effective temperature, with a recurrence timescale of roughly 8 d and a median duration of 15 hr. Mean pulsation frequencies and amplitudes were both observed to increase in this star during outbursts, and the combined flux enhancement from outbursts and high amplitude pulsations reached as high as 45%. The outbursts affect the pulsation properties of PG 1149+057, and Hermes et al. (2015b) unambiguously ruled out a close companion or a line-of-sight contaminant as the source of this phenomenon.

Spectroscopic effective temperatures place both of these white dwarfs very near to the empirical cool edge of the DAV instability strip—the boundary

below which pulsations have not been detected in white dwarfs. While nonadiabatic pulsation codes successfully reproduce the observed hot edge of the DAV instability strip, they typically predict a cool edge thousands of Kelvin below what is observed (e.g., Van Grootel et al. 2012). The discovery of a new astrophysical phenomenon that operates precisely where our models are discrepant with observations suggests that the continued discovery and study of cool outbursting DAVs may inform fundamental improvements to the theory of stellar pulsations.

In this paper we present the identification of two new outbursting DAVs that were observed by *K2* along with one candidate outburster. EPIC 211629697 was observed at short cadence in *K2* Campaign 5 and EPIC 229227292 in Campaign 6. Both stars are qualitatively similar in outburst and pulsational properties to the two previously published objects. We characterize these stars in Sections 3.2 and 3.3, respectively. Additionally, we inspect the light curves of the hundreds of other white dwarfs already observed by *K2* in Section 3.4, and describe a candidate single outburst in the long-cadence data of EPIC 211891315. We summarize the current members of the outbursting class of DAV and discuss possible physical mechanisms and outburst selection effects in Section 3.5.

3.2 The Third Outburster: EPIC 211629697

We targeted the DA white dwarf EPIC 211629697 (K_p = 18.4 mag, SDSSJ 084054.14+145709.0) for short-cadence (58.8 s) monitoring as part

of our *K2* Guest Observer program searching for candidate pulsating white dwarfs (GO5043). The effective temperature from an automated fit to a spectrum from the Sloan Digital Sky Survey (SDSS; Kleinman et al. 2013) put this white dwarf within the empirical DAV instability strip, although it was not previously known to pulsate. We have updated the one-dimensional atmospheric parameters from the SDSS spectrum by refitting these data with the latest atmosphere models described in Tremblay & Bergeron (2009), which use the ML2/α = 0.8 prescription of the mixing-length theory, and corrected the values to compensate for the three-dimensional dependence of convection (Tremblay et al. 2013). We find this white dwarf has $T_{\rm eff}$ = 10,780 $\pm$ 140 K and $\log g = 7.94 \pm 0.08$, corresponding to a mass of 0.57 ± 0.04 $M_{\odot}$.

The light curve was obtained at short cadence in *K2* Campaign 5, spanning 2015 April 27 02:25:19 UT to 2015 July 10 22:36:12 UT. The raw pixel-level data were extracted and detrended using the pipeline described in Armstrong et al. (2015), which corrects for attitude readjustments of the spacecraft on multiples of every 5.9 hr. Our extraction uses a fixed pattern of 4 pixels centered on the target. Despite the large *Kepler* pixels, there is no contamination from nearby stars in our extraction.

Subsequently, we clip the light curve of 77 outliers that lie $>4\sigma$ below or $>6\sigma$ above the local median flux (calculated for 30 m bins along the light curve, where σ is the standard deviation of flux measurements), leaving 107,682 observations over 74.84 d. We then subtract out a 6th-order polynomial fit to

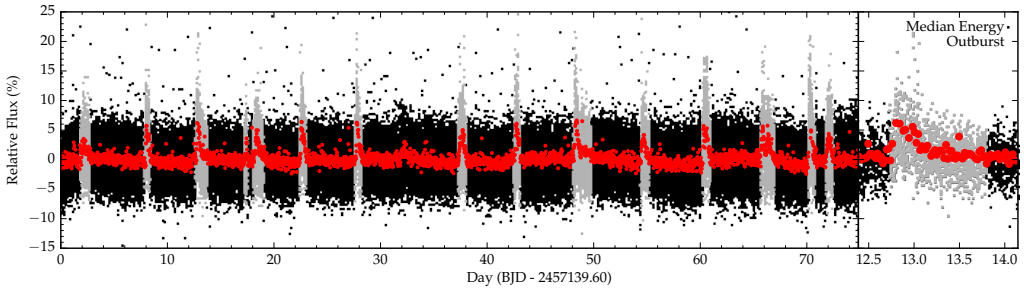

Figure 3.1: *Left:* The *K2* Campaign 5 light curve of EPIC 211629697. The short-cadence data are displayed in black (during quiescence) and gray (during the 15 detected outbursts). The long-cadence data are shown in red. *Right:* A detailed view of the outburst of median energy (see text). The units on the x-axes are the same in both panels. The scales of the y-axes are identical, with greater apparent scatter in the left panel due only to the overlap of points.

the full light curve to mitigate some of the long-term instrumental systematics.

In addition to this short-cadence light curve, we also analyze the pre-search data conditioned long-cadence light curve produced by the *Kepler* Guest Observer office (Twicken et al. 2010).

The reduced short- and long-cadence *K2* light curves of EPIC 211629697 are presented in Figure 3.1. We display the Fourier transform (FT) of the entire short-cadence light curve (including outbursts) in Figure 3.2.

3.2.1 Outbursts

We detect a total of 15 outbursts that cause significant brightness enhancements in the *K2* observations of EPIC 211629697. These outbursts are identified by an automatic algorithm wherever two consecutive points in the long-cadence light curve exceed 3 times the overall standard deviation mea-

sured in the light curve. We define the start and end times of each outburst as where the long-cadence light curve first crosses the median measured flux level immediately before and after these significantly high flux excursions. We mask out these regions of the light curve and recompute the overall standard deviation, repeating the candidate outburst search until no new features are flagged. For EPIC 211629697, this process yields 16 candidate outburst detections. We scrutinize these candidate events in both the long- and short-cadence light curves, determining one candidate to be a spurious detection that is not present in the short-cadence data. The remaining 15 outbursts are highlighted in the left panel of Figure 3.1.

The outbursts increase the mean stellar brightness by between $6-15\%$ (defined as the greatest median value of any 6 consecutive points in the short-cadence light curve during each outburst), and the mean time between consecutive outbursts is roughly 5.0 d. The median measured outburst duration is 16.3 hr.

We characterize the excess energy of the outbursts in the *Kepler* bandpass by calculating their equivalent durations (integrated excess flux in the short-cadence light curve, similar to a spectroscopic equivalent width), as described in Bell et al. (2015c). Equivalent durations equal the amount of time that the white dwarf would have to shine in quiescence to output as much flux in the *Kepler* bandpass as the flux excess measured during these outbursts. The median equivalent duration that we measure for an outburst in EPIC 211629697 is 21 min (this outburst, the third, is displayed in better detail

in the right panel of Figure 3.1). The maximum measured equivalent duration is 35 min.

These equivalent durations can be converted to approximate outburst energies by making a few simplifying assumptions: that the flux enhancement from an outburst is the same at all wavelengths, and that outbursts are isotropic. We calculate the bolometric luminosity of EPIC 211629697 using the StefanBoltzmann law and the parameters of the model that yielded the best fit to the SDSS spectrum (Tremblay & Bergeron 2009; Fontaine et al. 2001). This value of $L_{\rm bol} = 8.36 \times 10^{30}\,{\rm erg\,s^{-1}}$ is the scaling factor between equivalent duration and outburst energy, yielding a median outburst energy of $1.1 \times 10^{34}\,{\rm erg}$, and a maximum energy of $1.8 \times 10^{34}\,{\rm erg}$.

We note that our ability to detect outbursts is limited by the signal-to-noise of the light curve. EPIC 211629697 is relatively faint, at $K_p = 18.4\,{\rm mag}$, and the final threshold for two consecutive points in the long cadence light curve to flag an outburst in our detection scheme is set to 2.39%. It is possible that this star undergoes smaller-amplitude outbursts that we are unable to detect in this data set. The summary characterization of outbursts given above represents the detected outbursts and may not be directly comparable to outbursts from other DAVs that were observed with different photometric precision.

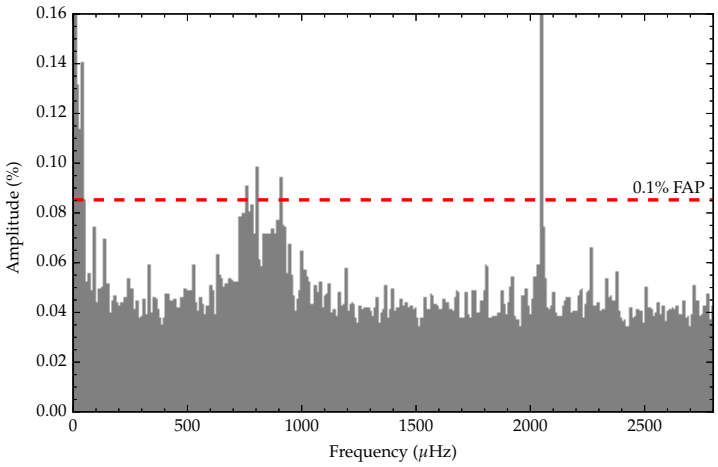

Figure 3.2: Fourier transform of the entire *K2* light curve of EPIC 211629697, including outbursts. The dashed line gives the 0.1% False Alarm Probability (FAP) significance threshold for a single peak determined from bootstrapping (see text). The peak at 2053.514 μHz (486.97 s) and 3 frequencies in the range 764–913 μHz (1095–1309 s) reach amplitudes that exceed this significance threshold. We discard all low-frequency peaks below 100 μHz (see text).

3.2.2 Pulsations

We detect significant but low-amplitude pulsations in EPIC 211629697, and show the FT in Figure 3.2. Asteroseismic analysis is beyond the scope of this paper and will be addressed in future publications, but we do characterize the pulsation frequencies generally in this observationally-focused work. All FTs in this paper are oversampled by a factor of 20.

We use a bootstrap method to identify statistically significant signals in the FT. After prewhitening the light curve of known instrumental artifacts that are harmonics of the long-cadence sampling rate (Gilliland et al. 2010b), we

shuffle the points in the light curve and recalculate the FT 10,000 times (Bell et al. 2015c). This shuffling preserves the exact time sampling of the original light curve, but destroys the coherence of any underlying signals. We treat the FTs of the shuffled light curves as proxies for the underlying noise spectrum, though this yields a conservative estimate for the typical noise level because the photometric scatter is inflated by the mixed-in signal. For this reason, we understate our true confidence in signal that exceeds our significance criterion.

When we consider the full set of 10,000 noise simulations, we find that the peak value anywhere in the FT—out to the Nyquist frequency—exceeds a value of 0.0853% in fewer than 1/1000 runs. We indicate this value with a dashed line in Figure 3.2 as the 0.1% false alarm probability (FAP) threshold for any individual peak in the FT.

Besides the noise at low-frequency (below $100\,\mu$Hz) that results from both the presence of outbursts in the light curve and residual systematics of the *K2* photometry, including the ~ 5.9 hr thruster firing timescale, there are numerous signals resulting from stellar pulsations that exceed this significance threshold in the FT. The highest peak is the sharp signal at $2053.514 \pm 0.007\,\mu$Hz that reaches an amplitude of $0.161 \pm 0.014\%$ (formal analytical uncertainties calculated following Montgomery & Odonoghue 1999 with the Period04 software; Lenz & Breger 2004). The FT also reveals 3 significant resolved frequencies in the range 764–913 μHz. This cluster of significant frequencies likely corresponds to a sequence of pulsational power bands—modes that are not strictly coherent over the course of observations—as were observed

in the previous two cases of outbursting cool DAVs. The signal-to-noise of this data set is not sufficient for easily identifying an exhaustive list of individual frequencies associated with pulsational eigenmodes of this star, so we characterize generally the pulsational properties of this star as consisting of bands of power in the range 764–913 μHz with a more stable mode at the higher frequency, 2053.514 μHz. The actual frequency range of excited pulsational modes in the power band region is likely broader than the formally significant range reported, which is limited by the photometric signal-to-noise and baseline of observations.

3.3 The Fourth Outburster: EPIC 229227292

We targeted EPIC 229227292[1] (K_p = 16.7 mag, ATLASJ 134211.62 −073540.1) for short-cadence *K2* monitoring using an early data release of the VST/ATLAS survey, which is a deep *ugriz* photometric survey of the southern hemisphere (Shanks et al. 2015). Based on its high reduced proper motion and *ugr* colors, we considered the object a high-probability white dwarf near the DAV instability strip and proposed observation in *K2* Campaign 6 (proposal GO6083).

As with EPIC 211629697, we extracted and detrended the short-cadence light curve using the pipeline described in Armstrong et al. (2015) and use the long-cadence light curve from the *Kepler* Guest Observer office.

[1]This target received a duplicate EPIC identifier, and is also cataloged as EPIC 229228124.

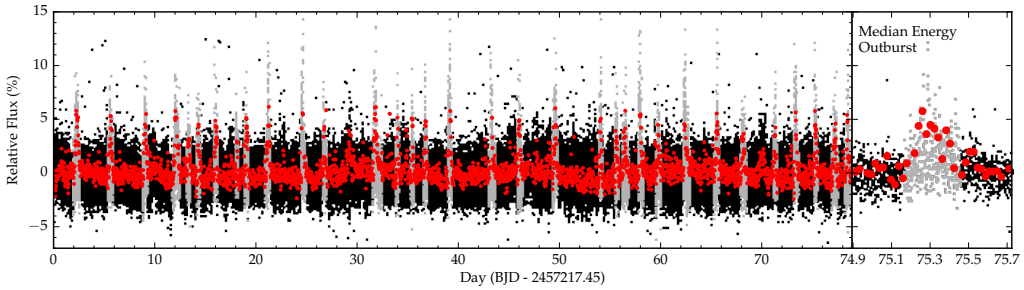

Figure 3.3: The *K2* Campaign 6 light curve of EPIC 229227292. The short cadence data are presented in black (in quiescence) and gray (in outburst), with the long cadence data in red. *Left:* The full light curve featuring 33 significant outbursts. *Right:* A detailed view of the outburst of median energy, with the same y-axis scale and x-axis units.

We clipped the short-cadence data of outliers $>4\sigma$ below or $>8\sigma$ above the local median (32 total, with the higher threshold above the median value to preserve astrophysical signal), leaving 113,635 individual observations over 78.93 d. Our final light curves, spanning 2015 July 13 22:54:00 UT to 2015 September 30 21:08:31, are displayed in Figure 3.3. The FT of the entire short-cadence light curve, including the data in outburst, is shown in Figure 3.4.

One complication in our extraction came from the presence of charge bleed in the *K2* target pixels caused by the saturation of naked-eye M dwarf, 82 Virginis (a.k.a. the known variable m Vir, J134136.78−084210.7), which falls roughly 1 deg south of EPIC 229227292. Our 3×3 pixel extraction aperture centered on the white dwarf excludes this hot column. We have also ensured that this object does not contaminate our photometry by inspecting

the light curve extracted from only the top and bottom two pixels of this charge bleed column, where we do not see evidence of brightening events from m Vir on the same timescale as the outbursts. As we discuss in Section 3.3.2, the outbursts affect the pulsations, confirming that these brightening events are occurring on the white dwarf.

3.3.1 Outbursts

We identify 33 significant outbursts in the long-cadence light curve of EPIC 229227292 with the same automated method as used for EPIC 211629697 (after discarding four spurious detections that are not corroborated by the short-cadence data). These outbursts are highlighted in the left panel of Figure 3.3. The outbursts reach amplitudes of 4–9% (the peak local median of 6 consecutive points in the short cadence light curve), with a median duration of 10.2 hr before returning to quiescence. The mean time between outbursts is 2.4 d.

The detected outbursts have equivalent durations (proportional to outburst energy in the *Kepler* bandpass) between $2.6 - 12$ min, with a median of 5.8 min. Following the same approach as for EPIC 211629697 and using the spectroscopic and model parameters determined in Section 3.3.3, we convert these to total outburst energies in the range $1.4 - 6.3 \times 10^{33}$ erg, with a median energy of 3.1×10^{33} erg. The outburst of median equivalent duration is displayed in the right panel of Figure 3.3.

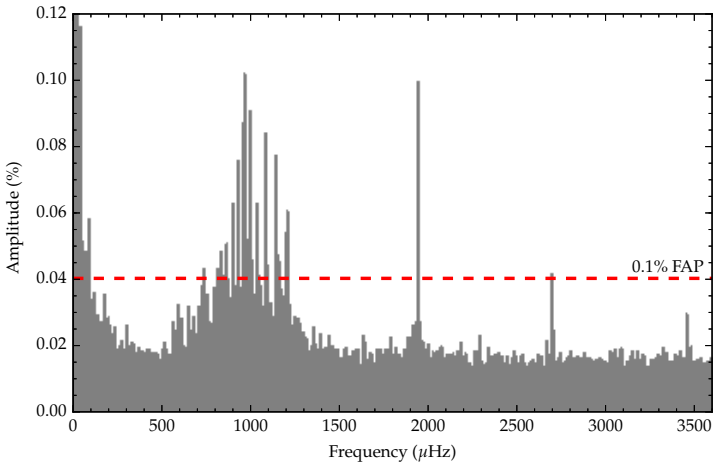

Figure 3.4: FT of the *K2* light curve of EPIC 229227292. We detect several peaks in the range $800 - 1250\,\mu$Hz ($800 - 1250$ s), and two peaks at 1945.048 and 2697.423 μHz (≈ 371 and 514 s) that exceed our 0.1% FAP significance threshold (dashed line). The peak just below the significance threshold at 3456.41 μHz (289 s) is highly suggestive of being astrophysical signal (see text).

3.3.2 Pulsations

The FT of the full EPIC 229227292 light curve (including outbursts) in the region of astrophysical power is presented in Figure 3.4. We use the same bootstrap approach as before to calculate a 0.1% FAP significance threshold of 0.0403% for single peaks in the FT. Again, we do not believe any power $< 100\,\mu$Hz arises directly from stellar pulsations.

Owing to higher photometric signal-to-noise for this brighter object, our significance criterion is much lower and we can discern more details of the pulsational signatures in the FT. We detect at least 11 wide bands of pulsational power clustered in the range $800 - 1250\,\mu$Hz, with two relatively

stable pulsation modes at higher frequencies: 1945.048 ± 0.005 and $2697.423 \pm 0.013\,\mu$Hz (analytical uncertainties; Montgomery & Odonoghue 1999). The peak at $3456.41 \pm 0.02\,\mu$Hz is also highly suggestive, rising to a signal-to-noise of 4.95 (defined as the ratio of the peak amplitude to the local mean amplitude in the FT, $\langle \mathrm{A} \rangle$), but does not meet our adopted significance criterion. With our significance threshold being a conservative estimate, it is difficult to assess the precise likelihood of this frequency belonging to a pulsation mode in the star, but we mention it as a tentative astrophysical signal. The approach to determining detection thresholds in the FTs of *K2* short-cadence observations of Baran et al. (2015) assigns a confidence of $\approx 90\%$ to peaks with this signal-to-noise ratio, so this is likely the highest frequency pulsation mode observed in an outbursting DAV so far.

The high signal-to-noise of the EPIC 229227292 data also enables us to explore changes in the pulsations on shorter timescales through the running FT, displayed for the 20th to 55th day of observations in Figure 3.5. This shows the evolution of the FT as calculated for a three-day sliding window on the light curve in the region of pulsational power bands. Individual mode amplitudes are observed to grow and decay dramatically on the timescale of days. The times of detected outburst peaks are indicated with vertical dotted lines. We note that the outbursts coincide in many cases with the sudden growth or decay of mode amplitudes, suggesting that the outbursts play a role in redirecting pulsational energy, and that they at least have some effect on the pulsations.

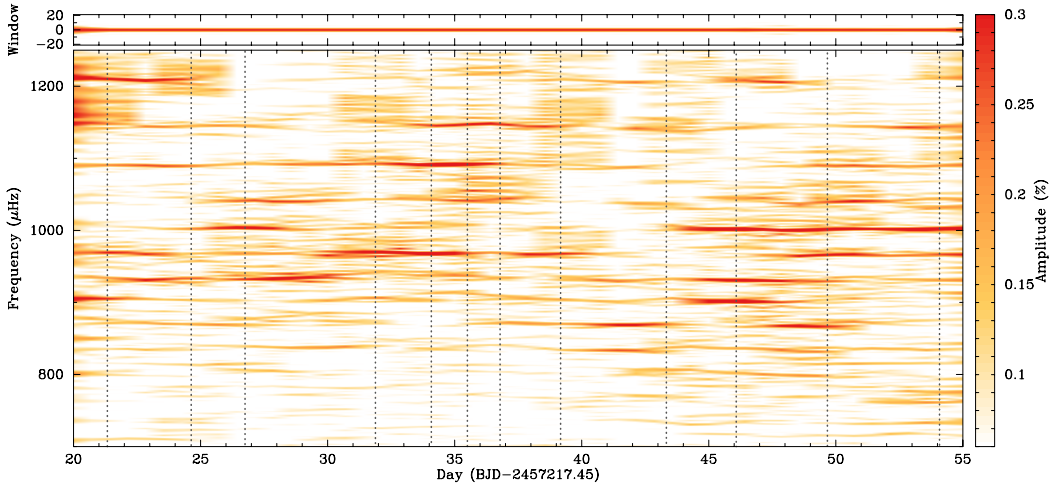

Figure 3.5: Running FT of EPIC 229227292, showing how the amplitude of pulsations changes in relation to outbursts. Vertical dotted lines mark the times of maximum brightness during the detected outbursts in Figure 3.3; we use a 3-day sliding window, which smears the events. We note that the rapid growth/decay of power in individual modes commonly coincides with a detected outburst (e.g., the dropping out of power near 1209 μHz that immediately follows the outburst near Day 24). This strongly suggests that the observed pulsations respond to outbursts in EPIC 229227292, as was observed in PG 1149+057 (Hermes et al. 2015b).

3.3.3 Spectroscopy

No spectroscopy of EPIC 229227292 existed previous to this work. After discovering pulsations, we followed up this white dwarf using the Goodman spectrograph on the 4.1 m SOAR telescope (Clemens et al. 2004). We obtained 6×180 s exposures taken consecutively on 2016 February 15, covering roughly $3700 - 5200$ Å with a dispersion of 0.84 Å pixel^{-1}. Using a 3″ slit, our resolution was seeing limited; seeing was steady around 1.1″ during our observations, yielding a roughly 3.2 Å resolution. Each exposure had a signal-to-noise (S/N)

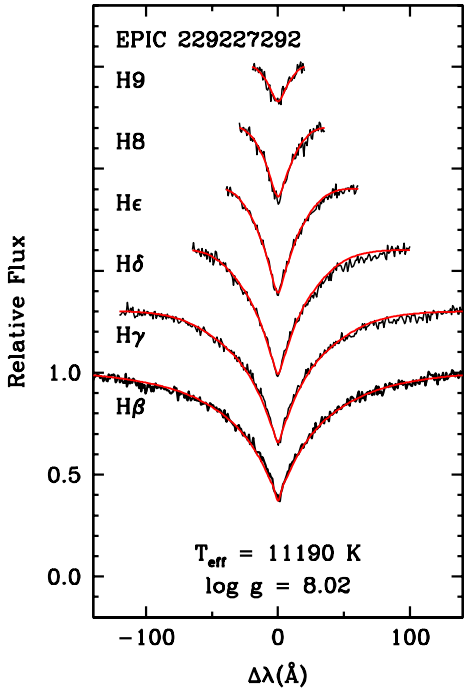

Figure 3.6: The best-fit atmosphere model (red) plotted over the average of the SOAR spectra (black) of EPIC 229227292 shows the agreement in the Balmer lines. Each spectral line is offset vertically by a factor of 0.3 for clarity.

of roughly 17 per resolution element in the continuum at 4600 Å, for an overall S/N $\simeq$ 41. Including overheads, our observations span roughly 18.5 min, covering at least one pulsation cycle for most oscillations.

We processed the images using the STARLINK packages FIGARO and KAPPA, and optimally extracted the spectra (Horne 1986) using the PAMELA package (Marsh 1989). Wavelength and flux calibration were performed with an FeAr lamp and the spectrophotometric standard GD 71, using the MOLLY

package[2].

We fit each individual spectrum with a set of one-dimensional pure-hydrogen-atmosphere models and fitting procedure described in Gianninas et al. (2011) and references therein, which use ML2/α = 0.8. We found the weighted mean of these individual exposures, and used the 3D convective corrections of Tremblay et al. (2013) to determine the atmospheric parameters of EPIC 229227292 to be $T_{\rm eff} = 11{,}190 \pm 170$ K and $\log g = 8.02 \pm 0.05$, corresponding to a mass of $0.62 \pm 0.03\ M_{\odot}$ (Fontaine et al. 2001). The best-fit atmosphere model is plotted over the spectroscopic data in Figure 3.6 to demonstrate the quality of the fit.

These atmospheric parameters indicate that EPIC 229227292 is consistent with being the hottest outbursting DAV discovered so far, but this white dwarf is still located close to the cool edge of the DAV instability strip. We estimate that this white dwarf was in outburst for 19% of the 78.93 d that it was monitored by *K2*. There is thus a roughly one-in-five chance that some of our spectroscopy was taken in outburst, which may contribute to the relatively high $T_{\rm eff}$ measured.

3.4 A Wider Search for Outbursts

As part of a search for transits and rotational variability of stellar remnants, *K2* has already observed several hundred white dwarfs in the first

[2]http://www.warwick.ac.uk/go/trmarsh

six campaigns, mostly at long cadence with exposures taken every 29.4 min. These targets have been proposed by a number of different teams[3], leading to the discovery of the first transits of a white dwarf: the object WD 1145+017[4], observed in *K2* Campaign 1, is transited every ∼4.5 hr by a disintegrating minor planet (Vanderburg et al. 2015).

In all, more than 300 spectroscopically confirmed DA white dwarfs have been observed by *K2* through Campaign 6, spanning temperatures from 4800 K up to 100,000 K. These light curves provide a unique opportunity to immediately constrain the temperature distribution of outbursting white dwarfs. Our automatic detection algorithm considers only the long-cadence light curves, demonstrating that these observations are sufficient to detect outbursts since the events typically have durations of many hours (see Figures 3.1, 3.3).

We put these outbursting and non-outbursting white dwarfs into context in Figure 3.7. We focus in detail on a subset of 52 white dwarfs that have effective temperatures within 2000 K of 10,900 K, roughly the mean effective temperature of the first four outbursting DAVs. In all cases, the atmospheric parameters have been obtained from the SDSS spectra using the models described in Tremblay et al. (2011a) and ML2/α = 0.8, with the exception of EPIC 203705962 (Kawka & Vennes 2006) and EPIC 212564858 (Koester et al.

[3]The white dwarfs described in this section were proposed for *K2* observations by teams led by M. Kilic, M. R. Burleigh, Seth Redfield, Avi Shporer, Steven D. Kawaler, and our team.

[4]WD 1145+017 was proposed jointly by teams led by M. Burleigh, M. Kilic, and Seth Redfield, searching for transits.

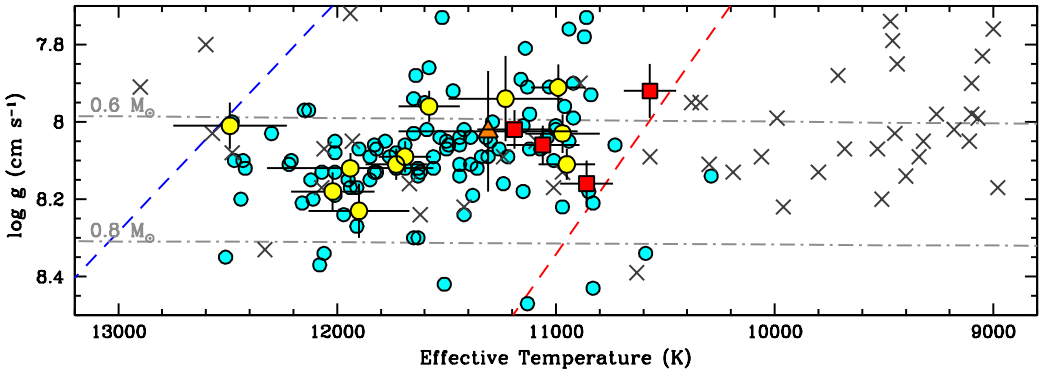

Figure 3.7: The location of the four known outbursting DAVs (red squares) in $\log g$–$T_{\rm eff}$ parameter space, as well as the candidate EPIC 211891315 (orange triangle; see Section 3.4.1). The crosses show white dwarfs observed by *K2* which do not show outbursts (Table 3.2), confining this outburst phenomenon to the coolest pulsating white dwarfs, between roughly 10,600 K and 11,200 K. Previously known DAVs are shown in cyan circles (Tremblay et al. 2011a; Gianninas et al. 2011), and non-outbursting pulsating white dwarfs observed with *Kepler* are shown in yellow (with error bars; see Table 3.2). The empirical instability strip is demarcated with blue and red dashed lines (Tremblay et al. 2015). All atmospheric parameters have been corrected for the 3D-dependence of convection (Tremblay et al. 2013). The dash-dotted gray lines mark evolutionary cooling tracks for 0.6 $M_{\odot}$ and 0.8 $M_{\odot}$ white dwarfs (Fontaine et al. 2001).

2009b). All parameters have been corrected for the 3D-dependence of convection (Tremblay et al. 2013) and are listed in Table 3.2.

The long-cadence light curves for this subsample were obtained from the Mikulski Archive for Space Telescopes (MAST). In each case, we have either used extracted and de-trended light curves from the pipeline described in Vanderburg & Johnson (2014) (VJ) or, from Campaign 3 and onward, the pre-search data conditioned light curves produced by the *Kepler* Guest Observer office (GO). Both pipelines mitigate for attitude corrections from

K2 thruster firings, but in slightly different ways, and we include in Table 3.2 which pipeline we use for our outburst analysis. We have ensured that the apertures used enclose only the white dwarf target.

Many of these targets are very faint, with $K_p > 19.0$ mag, which is why we did not propose short-cadence observations of those with temperatures inside the empirical instability strip. However, *K2* has proven itself stable enough to deliver useful long-cadence photometry on these faint targets; a $K_p = 19.2$ mag target typically has roughly 1.2% r.m.s. scatter, which increases to roughly 3% for a $K_p = 19.5$ mag target. We assign limits on a non-detection of outbursts in these targets in Table 3.2. These limits were calculated by comparing the highest three consecutive points in the long-cadence light curves with the overall standard deviation of flux measurements (σ). The long-cadence light curves of the known outbursting DAVs all show multiple occurrences of at least three consecutive points exceeding 3σ that correspond with identified outbursts. The data for the objects listed in Table 3.2 do not have three points exceeding 3σ anywhere in the light curve, with three exceptions: EPIC 211891315 shows evidence of a single possible outburst, which we describe in more detail in Section 3.4.1; EPIC 228682333 shows significant flux deviations in the first few points of the light curve which is likely the result of a poor reduction; EPIC 212100803—the faintest star in our sample—registers a brief sequence of three anomalously high points 39.11 days into observations immediately preceding a *Kepler* GO quality flag for simultaneous thruster firing, coarse point mode of the spacecraft, and a reaction wheel desaturation

event. For these reasons, we do not accept the flagged points in the latter two objects as outbursts to the limits given in Table 3.2.

In addition to these targets observed at long cadence, we have also inspected the *Kepler* light curves of 11 pulsating white dwarfs that had previously published spectroscopic parameters and were proposed for short-cadence observations by our team to study their oscillations. We will present asteroseismology on these targets in forthcoming work, but we can rule out outbursts to various limits in each of these DAVs by considering their long-cadence observations in a manner identical to the other objects. Their atmospheric parameters were determined in the same way as our other targets, and constraints on the presence of outbursts in these light curves are included at the bottom of Table 3.2.

Figure 3.7 shows that outbursts are narrowly confined to the lowest-temperature region of the empirical DAV instability strip between roughly 11,300 K and 10,600 K, below which pulsations are no longer observed. None of the other spectroscopically confirmed DAs observed by *K2* with temperatures outside this plot range show obvious outbursts, either.

Notably, there are two pulsating white dwarfs that have effective temperatures inside the region where we have detected the four other outbursting DAVs.

KIC 4357037, with $10{,}950 \pm 130$ K and $\log g = 8.11 \pm 0.04$ determined from WHT spectroscopy (Greiss et al. 2016), was observed continuously for

36.3 d in the original *Kepler* mission, but did not show outbursts to a limit of at least 0.8%. However, the pulsation spectrum of this white dwarf does not resemble a cool white dwarf, let alone the outbursting DAVs, with weighted mean pulsation period (WMP $= \sum A_i P_i / \sum A_i$, where A_i are the measured amplitudes corresponding to P_i, the measured periods) of roughly 342.4 s. WMPs systematically increase as white dwarfs cool and develop deeper convection zones, with values near 342.4 s typically observed in white dwarfs with $T_{\rm eff}$ $> 11,650$ K (see, e.g., Mukadam et al. 2006, where the "BG04" sample from Bergeron et al. 2004 and Gianninas et al. 2005 is most comparable with the parameters derived in this work). The interloper KIC 4357037 may thus be hotter in actuality than its spectroscopic temperature suggests.

EPIC 60017836 (also known as GD 1212; $T_{\rm eff} = 10{,}970 \pm 170$ K; $\log g$ = 8.03±0.05; Hermes et al. 2014b), was observed for 9.0 continuous days during engineering time in preparation for *K2* operations. With a *Kepler* magnitude of 13.3, we can rule out outbursts to an amplitude limit of 0.2% that recur on timescales $\lesssim$ 9.0 d. The pulsation spectrum of this star is qualitatively similar to those of the outbursting DAVs, with a cluster of modes between $800 - 1270\,\mu$Hz, and additional significant peaks at higher frequency. EPIC 60017836 is scheduled to be re-observed by *K2* in Campaign 12, which will allow us to explore the possibility of outbursts from this target with recurrence timescales $\gtrsim$ 9 d.

3.4.1 EPIC 211891315: A Possible Single Outburst

The *K2* photometry for many of these faint objects is affected by long-term systematics, which are often aperiodic variations with timescales of several days. These trends very often also show up in the background flux, which is the median value of the background pixels that lie outside of the aperture used to extract the target photometry. These long-term trends often arise from solar coronal mass ejections (CMEs), small spacecraft thermal variations, so-called argabrightenings (see *Kepler* data release notes[5]), and electronic artifacts, such as rolling bands caused by time-varying crosstalk (e.g., Clarke et al. 2014).

In our inspection of the 52 DA white dwarfs within 2000 K of 10,900 K, we found one object with a light curve that shows a significant brightening event that does not correlate with changes in other light curves on the same CCD module. The long-cadence *K2* Campaign 5 light curve of that white dwarf, EPIC 211891315 (K_p = 19.4 mag, SDSSJ 090231.76+183554.9), is shown in Figure 3.8.

There are two noted data anomalies with *K2* data taken in Campaign 5, neither of which correlate with our observed brightness increase. The first, an unexplained argabrightening event, occurred roughly 38 d into the campaign. The second, an increase in the median dark current likely caused by a CME, lasted for roughly one day starting 55.5 d into the campaign.

[5] `http://keplerscience.arc.nasa.gov/k2-data-release-notes.html`

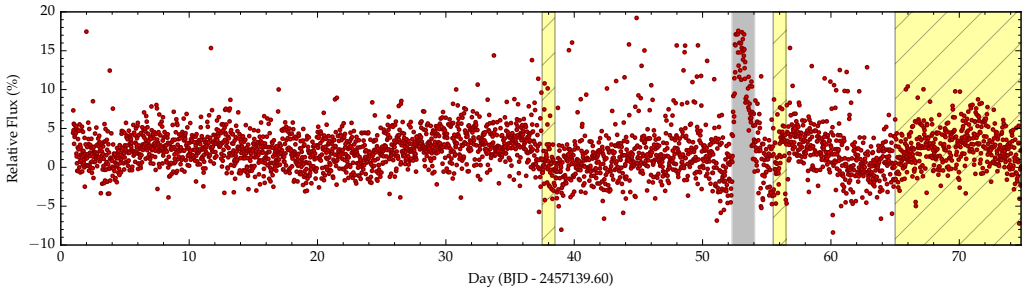

Figure 3.8: The long-cadence light curve of EPIC 211891315 ($K_p = 19.4$ mag) from *K2*. We highlight with solid gray the single feature starting near Day 52.3 that looks compellingly like an astrophysical brightening event. The three yellow hatch regions indicate identified instrumental systematics corresponding to (in chronological order): an argabrightening event, a likely CME, and a local background flux enhancement (see text).

We note that the brightening event we tentatively categorize as an outburst between Days $52.3 - 54.1$ does not correlate with any trends in the background flux, whereas the brightening at the end of the light curve between Days $65 - 75$ is correlated with an increase in background flux, strongly suggesting it is instrumental. We also rule out an asteroid or other contaminant moving through the photometric aperture during Days $52.3 - 54.1$ by inspecting the raw pixel data with the K2FLIX visualization tool (Barentsen 2015). We tentatively identify EPIC 211891315 as a candidate outbursting DAV. Our fit to the SDSS spectrum indicates this is a $11{,}310 \pm 410$ K and $\log g = 8.03 \pm 0.16$ white dwarf, included as an orange triangle in Figure 3.7.

If this is an outburst of the same nature as in other DAVs observed by *Kepler*, it is by far the most energetic ever observed with an equivalent duration of 4.58 hr, corresponding to an approximate total energy output of

1.5×10^{35} erg.

Because the exposure time of long-cadence *K2* light curves is much longer than typical DAV pulsation periods, we followed this target up with high-speed photometry using the ProEM Camera on the 2.1m Otto Struve Telescope at McDonald Observatory. We observed EPIC 211891315 for 4 hr on the night of 2015 December 17 with 14 s exposures through a broadband *BG*40 filter, which cuts off light redward of 6000 Å to reduce sky noise. We obtained another 5 hr of 10 s exposures on 2015 December 18 through the *BG*40 filter.

The frames were dark subtracted and flat-fielded with standard IRAF tasks. Aperture photometry was measured with the CCD_HSP package that utilizes IRAF tasks from the PHOT package (Kanaan et al. 2002). We used the WQED software tools (Thompson & Mullally 2013) to divide the flux measured for the target by the normalized flux from comparison stars in the field to correct for transparency variations, then divided each night's light curve by a second-order polynomial to account for differential airmass effects on stars with different colors. We repeated this process using a range of circular aperture sizes and adopt the apertures that yield the highest signal-to-noise. The FT of these two nights of data is displayed in Figure 3.9.

With a total of 9 hr of ground-based, time-series photometry over two nights, we were able to cleanly prewhiten (fit and subtract) significant sinusoidal signals from these data. For this reason, we adopt a different significance criterion for this data set. We measure the mean local amplitude along

the FT, $\langle A \rangle$, and use the standard $4\langle A \rangle$ significance threshold for single-site ground-based photometry (Breger et al. 1993).

We identify significant signals through an iterative process of calculating the FT and significance threshold, prewhitening all significant peaks, then recalculating the FT and threshold for the prewhitened light curve. We repeat this until no additional significant peaks are identified. Figure 3.9 displays the FTs of the original (black) and prewhitened (red) data with the final significance threshold and four significant frequencies marked. We establish EPIC 211891315 as a new DAV. The four significant pulsation modes that we detect have frequencies 1322.0 ± 0.4 (2.22% amplitude), 1779.0 ± 0.4 (1.99%),

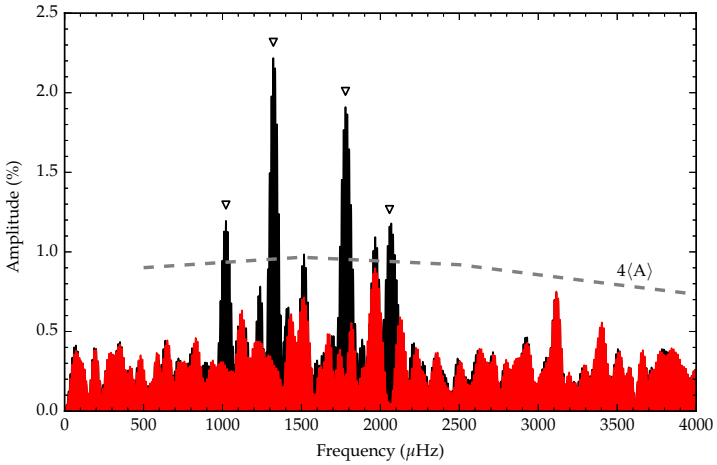

Figure 3.9: We confirmed pulsations in ground-based observations of the candidate outbursting white dwarf EPIC 211891315. We show the original FT in black, and the prewhitened FT in red, after subtracting the four significant pulsation frequencies that are marked with triangles at 1322.0, 1780, 2057.7, and 1021.7 μHz. The dashed grey line marks the running $4\langle A \rangle$ significance threshold.

2057.7 ± 0.7 (1.19%), and 1021.7 ± 0.7 μHz (1.12%).

The confirmation of pulsations in this white dwarf provides marginal supporting evidence that the single brightening event during *K2* observations was a bona fide outburst. However, given the prevalence of systematic artifacts in the *K2* light curves of such faint targets, we are not comfortable confirming that EPIC 211891315 is a new outbursting white dwarf, especially with only one event detected. Additionally, the observed pulsations have overall much higher frequencies than what we have measured in the four confirmed outbursting DAVs, with a weighted mean period of 685.9 s. For now, we classify EPIC 211891315 as only a candidate outbursting white dwarf.

3.5 Discussion and Conclusions

The four confirmed members of the outbursting class of DAV have three distinct commonalities: (1) repeated outbursts, recurring on irregular intervals of order days and lasting for several hours; (2) effective temperatures that put them near the cool, red edge of the DAV instability strip; and (3) rich pulsation spectra dominated by low-frequency ($800 - 1400$ s period) pulsations that are unstable in amplitude/frequency with at least one stable mode at significantly higher frequency ($350 - 515$ s, and maybe as short as 290 s), which in the first two cases appeared to be an $\ell = 1$ from rotational splittings (Bell et al. 2015c; Hermes et al. 2015b). We summarize their main characteristics in Table 3.1.

Table 3.1. Properties of Outbursting DAVs

Name	K_p (mag)	$T_{\rm eff}$ (K)	$\log g$ (cgs)	τ_{recur} (d)	Med. Duration (hr)	Max. Flux (%)	Max. Energy (erg)	Reference
KIC 4552982	17.9	10,860(120)	8.16(0.06)	2.7	9.6	17	2.1×10^{33}	Bell et al. (2015c)
PG 1149+057	15.0	11,060(170)	8.06(0.05)	8.0	15	45	1.2×10^{34}	Hermes et al. (2015b)
EPIC 211629697	18.4	10,570(120)	7.92(0.07)	5.0	16.3	15	1.8×10^{34}	This work
EPIC 229227292	16.7	11,190(170)	8.02(0.05)	2.4	10.2	9	3.1×10^{33}	This work

The discovery of repeated outbursts in four of the first 16 DAVs observed by the *Kepler* spacecraft indicates that this is not an incredibly rare phenomenon. However, it does beg the question of how outbursts have been missed during the first 45 years of studies of pulsating white dwarfs.

In this context, the minimum outburst duration observed offers a clue: So far, every outburst lasts for more than several hours. Nearly all previous ground-based, time-series photometry of pulsating white dwarfs involves differential photometry: dividing the target by a (usually redder) comparison star to compensate for changing atmospheric conditions. Due to color-dependent extinction effects, nearly all groups have adopted a methodology of dividing out at least a second-order polynomial to normalize the light curves (e.g. Nather et al. 1990). It is possible that outbursts were observed during previous ground-based studies of pulsating white dwarfs but were unintentionally de-trended from the data. Notably, the DBV (pulsating helium-atmosphere white dwarf) GD 358 underwent a large-scale brightening event in 1996, which may have been the first documented case of an outburst in a pulsating white dwarf (Nitta et al. 1999; Montgomery et al. 2010).

The physical mechanism that causes outbursts remains an exciting open question. Hermes et al. (2015b) suggested that, following the theoretical framework laid out by Wu & Goldreich (2001), the outbursts could be the result of nonlinear three-mode resonant coupling. In this model, energy is transferred from an observed, overstable parent mode to daughter modes via parametric resonance, one or both of which may be damped by turbulence in the convec-

tion zone and deposit their newfound energy there.

All four of the outbursting white dwarfs have some of the longest pulsation periods observed in DAVs, excluding the extremely low-mass white dwarfs (Hermes et al. 2013b). Wu & Goldreich (2001) predicted that mode coupling would be most prevalent in the coolest white dwarfs with the longest-period pulsations, simply because there are more possible modes with which to couple.

By inspecting the light curves of the more than 300 spectroscopically confirmed DA white dwarfs observed already by *K2*, we have shown that outbursts only occur in a narrow temperature range, between roughly 11,300 K and 10,600 K. This temperature range falls just hot of the empirical red edge of the DAV instability strip, below which pulsations are no longer observed.

The red edge of the DAV instability strip has been notoriously difficult to predict from nonadiabatic pulsation codes, which suggest that white dwarfs should have observable pulsations down to at least 6000 K (e.g. Van Grootel et al. 2012). There have been two proposed mechanisms to bring the theoretical red edge in line with observations.

Hansen et al. (1985) suggested that there is a critically maximal mode period, beyond which g-modes are no longer reflected off the outer mode cavity and thus evanesce. Van Grootel et al. (2013) showed that applying this critical mode period for $\ell = 1$ modes to the thermal timescale at the base of the convection zone can successfully reproduce the empirical red edge of the DAV instability strip across a wide range of white dwarf masses.

Additionally, a series of papers by Wu & Goldreich proposed amplitude saturation mechanisms in the coolest DAVs from turbulent viscosity of the convection zone as well as resonant three-mode interactions as ways to cause a hotter red edge than nonadiabatic predictions (Goldreich & Wu 1999b; Wu & Goldreich 2001). If outbursts are indeed caused by nonlinear mode coupling, this suggests amplitude saturation as an important contributor to the cessation of observability of pulsations in the coolest DAVs.

The measured properties of outbursts provide observational leverage for efforts to understand pulsational mode selection and driving, especially in the context of the few short-period modes that are selected in all four of the outbursting DAVs. Fortunately, DAV pulsations are extremely sensitive to structural changes in white dwarfs, and our understanding of outbursts will benefit from further asteroseismic analysis of these objects that will be the subject of future work.

K2 continues to obtain extensive space-based photometry on new fields roughly every three months, and we look forward to inspecting future data releases for additional instances of this exciting physical phenomenon.

Table 3.2: White Dwarfs Not Observed to Outburst with *Kepler* Observations

EPIC ID	K_p	$T_{\rm eff}$ (K)	$\log g$ (cgs)	Pipe.[a]	Field	Dur. (d)	Lim(%)	Ref.[b]
212154350	19.8	12900(790)	7.91(0.21)	VJ	5	73.9	8.1	1
212100803	20.0	12600(650)	7.80(0.21)	GO	5	74.8	16.7	1
206284230	19.0	12570(430)	8.03(0.11)	GO	3	69.1	2.5	1
210484300[c]	19.0	12490(450)	8.52(0.09)	VJ	4	68.6	2.9	1
211975984	19.3	12480(440)	8.08(0.11)	VJ	5	73.9	5.6	1
211888384	18.3	12330(210)	8.33(0.05)	GO	5	74.8	1.3	1
228682421	19.7	12070(450)	8.17(0.13)	VJ	5	73.9	6.1	1
211564222	19.8	12060(510)	8.07(0.16)	VJ	5	73.9	11.6	1
211934410	19.0	11940(280)	7.72(0.11)	VJ	5	73.9	3.4	1
201754145	19.4	11930(460)	8.05(0.15)	VJ	1	80.1	3.4	1
201331010	19.3	11670(290)	8.16(0.09)	VJ	1	80.1	2.8	1
228682407	19.9	11620(680)	8.24(0.21)	VJ	5	73.9	13.6	1
228682371	19.9	11420(480)	8.22(0.17)	VJ	5	73.9	8.2	1
228682428	19.8	11380(610)	8.52(0.22)	GO	5	74.8	11.1	1
211891315	19.4	11310(410)	8.03(0.16)	VJ	5	73.9	n/a[d]	1
228682357	19.9	11240(390)	8.09(0.15)	VJ	5	73.9	6.4	1
211330756	19.9	11090(600)	8.05(0.27)	GO	5	74.8	14.3	1
201259883	19.7	11010(450)	8.17(0.21)	VJ	1	80.1	8.0	1
228682400	19.9	10970(410)	8.13(0.20)	VJ	5	73.9	22.7	1
212169533	19.9	10890(460)	7.90(0.23)	GO	5	74.8	15.6	1
212091315	19.4	10630(210)	8.39(0.14)	VJ	5	73.8	3.7	1
211886776	19.0	10570(150)	8.09(0.09)	VJ	5	73.9	2.1	1
203705962	15.1	10380(120)	7.95(0.09)	VJ	2	77.5	0.2	2
228682361	19.8	10340(220)	7.95(0.17)	VJ	5	73.9	4.2	1

Table 3.2 (cont'd): White Dwarfs Not Observed to Outburst with *Kepler* Observations

EPIC ID	K_p	$T_{\rm eff}$ (K)	$\log g$ (cgs)	Pipe.[a]	Field	Dur. (d)	Lim(%)	Ref.[b]
212071753	18.9	10300(150)	8.11(0.12)	VJ	5	73.9	3.8	1
206302487	18.7	10190(110)	8.13(0.10)	VJ	3	66.8	1.3	1
211932844	17.9	10060(80)	8.09(0.07)	VJ	5	73.9	1.4	1
211519519	18.9	9990(130)	7.99(0.13)	VJ	5	73.9	2.1	1
228682409	20.0	9960(160)	8.22(0.15)	GO	5	74.8	13.5	1
201513373	18.2	9800(80)	8.13(0.08)	VJ	1	80.0	0.9	1
201789520	18.4	9710(80)	7.88(0.09)	VJ	1	80.0	1.2	1
201498548	18.3	9680(60)	8.07(0.07)	VJ	1	80.0	1.5	1
201663682	19.0	9530(110)	8.07(0.12)	VJ	1	80.1	4.5	1
201810512	18.4	9510(90)	8.20(0.09)	VJ	1	80.0	1.7	1
228682315	19.5	9470(150)	7.74(0.19)	GO	5	74.8	11.0	1
201838978	18.7	9460(80)	7.79(0.10)	VJ	1	80.1	2.5	1
211932489	19.8	9450(180)	8.03(0.20)	VJ	5	73.9	5.6	1
201834393	18.7	9440(90)	7.85(0.11)	VJ	1	80.1	2.7	1
201887383	18.8	9400(100)	8.14(0.11)	VJ	1	80.0	6.5	1
201521421	19.2	9340(160)	8.09(0.17)	VJ	1	80.1	2.0	1
201879492	18.1	9320(70)	8.05(0.08)	VJ	1	80.0	1.8	1
201816218	18.4	9260(80)	7.98(0.09)	VJ	1	80.0	1.1	1
211768391	18.5	9250(80)	7.60(0.12)	VJ	5	73.9	2.1	1
211692110	18.8	9180(90)	7.59(0.13)	VJ	5	73.9	2.2	1
201224667	18.6	9180(110)	8.02(0.13)	VJ	1	80.0	3.2	1
201723220	17.7	9110(50)	8.05(0.05)	VJ	1	80.0	0.8	1
211788137	18.6	9100(100)	7.98(0.12)	VJ	5	73.9	3.0	1
228682387	18.8	9100(90)	7.90(0.11)	VJ	5	72.0	1.6	1

Table 3.2 (cont'd): White Dwarfs Not Observed to Outburst with *Kepler* Observations

EPIC ID	K_p	$T_{\rm eff}$ (K)	$\log g$ (cgs)	Pipe.[a]	Field	Dur. (d)	Lim(%)	Ref.[b]
201700041	19.2	9070(160)	7.99(0.19)	VJ	1	80.1	3.3	1
212564858	15.7	9050(110)	7.83(0.03)	GO	6	78.9	0.3	3
228682333	17.8	9000(60)	7.76(0.09)	VJ	5	73.9	2.6	1
228682427	18.6	8980(90)	8.17(0.10)	VJ	5	73.9	4.9	1
Pulsating White Dwarfs Not Observed to Outburst with SC *Kepler* Observations								
201730811	15.7	12490(260)	8.01(0.06)	VJ	1	80.1	1.8	4
212395381	15.7	12020(190)	8.18(0.05)	GO	6	73.9	2.5	5
10132702	19.1	11940(380)	8.12(0.04)	GO	K1	30.8	2.5	6
211916160	19.0	11900(230)	8.23(0.07)	VJ	5	73.9	2.1	1
7594781	18.2	11730(140)	8.11(0.04)	GO	K1	31.8	0.6	6
211926430	17.7	11690(120)	8.09(0.04)	VJ	5	73.9	3.1	1
11911480	18.1	11580(140)	7.96(0.04)	GO	K1	82.6	1.9	6
201719578	18.1	10990(125)	7.91(0.06)	VJ	1	80.1	2.1	1
211596649	19.0	11230(260)	7.94(0.11)	VJ	5	73.8	2.4	1
60017836	13.3	10970(170)	8.03(0.05)	GO	Eng	9.0	0.2	5
4357037	18.3	10950(130)	8.11(0.04)	GO	K1	36.3	0.8	4

[a] *K2* reduction pipeline, where GO is the *Kepler* Guest Observer light curve, and VJ is the Vanderburg & Johnson (2014) optimally extracted light curve.

[b] Spectroscopic sources: (1) Tremblay et al. (2011a); (2) Kawka & Vennes (2006); (3) Koester et al. (2009b); (4) Hermes et al. (2015a); (5) Gianninas et al. (2011); (6) Greiss et al. (2016)

[c] The atmosphere model that best fits the Balmer line profiles of the spectrum of EPIC 210484300 disagrees with its photometric colors from SDSS.

[d] EPIC 211891315 shows evidence of a single outburst and was observed to pulsate in follow-up, ground-based observations as discussed in Section 3.4.1.

Chapter 4

New Outbursting ZZ Ceti Variables Through K2 Campaign 10 *

Chapter 3 reproduced the most recent refereed publication about the discovery of outbursting cool ZZ Ceti pulsators (oDAVs) from extended *Kepler* and *K2* observations through *K2* Campaign 6. That paper brought the total number of oDAVs up to four, with one additional candidate that may have exhibited a single, particularly energetic outburst: EPIC 211891315. The *K2* mission has now publicly released data through Campaign 10, and we have continued to find new cool ZZ Ceti variables that exhibit this behavior. In this chapter I describe these most recent discoveries and summarize the current class of eight (or nine) ZZ Cetis with observed outbursts. I also provide new spectroscopic parameters from a uniform set of spectra obtained and fit by collaborators J. J. Hermes and P.-E. Tremblay. The light curves and Fourier transforms of the first two new objects were published in conference proceed-

*This work was previously published as Bell, K. J., Hermes, J. J., Montgomery, M. H., Winget, D. E., Gentile Fusillo, N. P., Raddi, R., and Gänsicke, B. T., 2017, *The First Six Outbursting Cool DA White Dwarf Pulsators*, 20th European White Dwarf Workshop, 509, 303. I led the photometric analysis in this work. J. J. Hermes identified the outbursting objects from his *K2* light curve extractions. M. H. Montgomery and D. E. Winget advised me in this work. N. P. Gentile Fusillo, R. Raddi, and B. T. Gänsicke helped to identify these objects as candidate pulsating white dwarfs for *K2* observation.

ings of the 20th European White Dwarf Workshop (Bell et al. 2017b).

The results in this chapter are preliminary. I will prepare a more complete manuscript for refereed publication following the submission of this thesis.

4.1 Time Series Photometry Analysis of Four New Outbursting ZZ Cetis

Due to their infrequency, irregularity, and durations of tens of hours, all known outbursting ZZ Cetis have been identified from extensive *Kepler*/*K2* data. The streak continues with four additional oDAVs since the work published in Bell et al. (2016, Chapter 3). In the following subsections, I detect and characterize the outbursts (quantitatively) and pulsations (qualitatively) in the *K2* light curves of these newest oDAVs. Descriptions of the pipelines and processing of each light curve—as well as follow-up photometry in the case of EPIC 220329764—will be described separately for each object.

My algorithm for detecting and characterizing outbursts in the *K2* data was described in Section 3.2.1. To summarize, I calculate the standard deviation (σ) of the long cadence light curve and flag any occurrence of three consecutive points above 3σ as a candidate outburst (so all outbursts are necessarily longer than 1.5 hr). I mask these candidate events from the light curve and search again, iterating until no new candidates are found. I then carefully vet every candidate event, comparing the long- and short-cadence light curves (when available) to ensure that instrumental anomalies are identified

and rejected.

I interpolate to find the previous and next times that the long-cadence light curve crossed its median to calculate the outburst duration. Because of the smoothing of the underlying signal by the 30-minute long-cadence exposures, I use the short-cadence data, when available, to measure the peak flux enhancement of an outburst. I record the highest median of seven adjacent relative flux measurements as the outburst peak to avoid individual noisy measurements from dominating this value. I measure the equivalent duration of an outburst (the duration that the star would have to shine in quiescence to output the same amount of energy in the observational bandpass as the total excess energy from the outburst, similar to a spectroscopic equivalent width) by numerically integrating the light curve above its median from the detected start to end of the event. Finally, I estimate the physical energy output of an outburst (assuming that the fractional brightness enhancement is the same at all wavelengths and that the outbursts are isotropic) by multiplying its equivalent duration by the white dwarf's expected luminosity from the Stefan-Boltzmann law and its spectroscopic and model parameters. We use values from new spectra that are presented in Section 4.2.

All plotted Fourier transforms (FTs) have been calculated with the Period04 software (Lenz & Breger 2004). The 0.1% False Alarm Probabilities (FAP) for signals in the FTs were calculated with the same bootstrapping approach described in the previous two chapters (using a fast implementation of the FFT for unevenly sampled data; Press & Rybicki 1989).

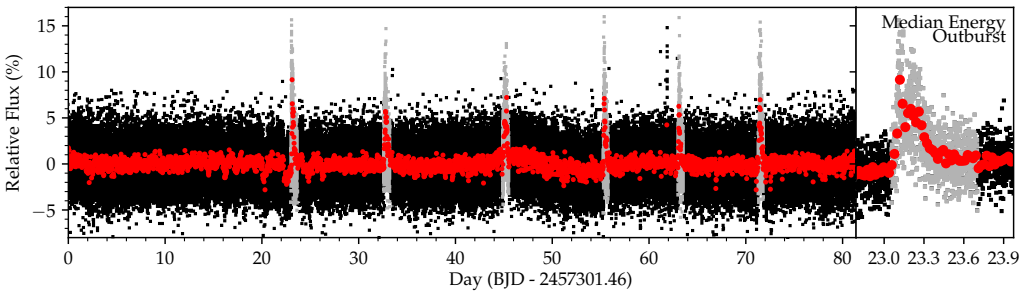

Figure 4.1: Light curve of EPIC 229228364. The left panel shows the full short-cadence *K2* light curve (black) and a 30-minute-smoothed long-cadence light curve (red). The gray segments of the light curve mark detected outbursts. The right panel zooms in on a representative, median-energy outburst.

4.1.1 EPIC 229228364

EPIC 229228364 was observed by *K2* at short cadence for 81.4 days in Campaign 7. We detect six outburst in the light curve displayed in Figure 4.1, with a median-energy outburst features in the right panel. These last between 11.4 and 15.5 hours, the brightest causing the overall flux to increase by 15%. The average time between detected outbursts is 11.6 days. Equivalent durations are in the range 11.4–15.5 min, with a median of 13.7 min. From the new spectroscopic parameters to be introduced in Section 4.2, the maximum observed outburst energy is roughly 6.3×10^{33} erg.

The FT of the short-cadence *K2* light curve of EPIC 229228364 is displayed in Figure 4.2. Two peaks in the typical range of ZZ Ceti pulsation frequencies exceed the 0.1% FAP significance threshold at 894.48 and 927.47 μHz. These are likely part of broadened features corresponding to pulsation modes that vary in phase/frequency/amplitude as are observed in other oDAVs, but

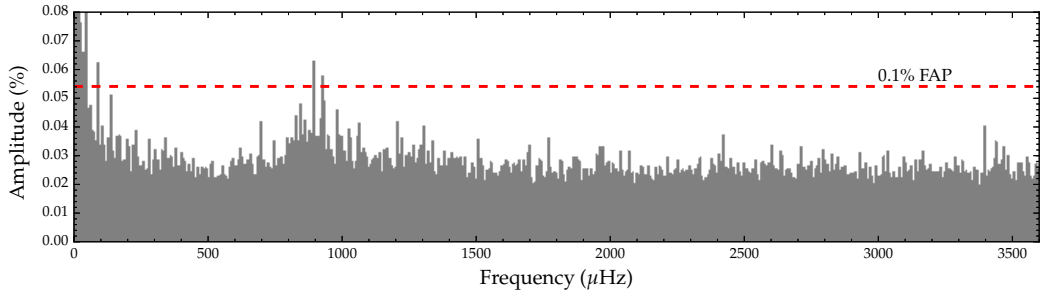

Figure 4.2: Fourier transform of EPIC 229228364. The 0.1% significance threshold was calculated from 10,000 bootstrap randomizations.

the signal-to-noise is not sufficient in this light curve to fit these features.

4.1.2 EPIC 220453225

The short-cadence light curve of EPIC 220453225 from *K2* Campaign 8 is displayed in Figure 4.3. The 15 outbursts that we detect in this light curve are highlighted in the left panel, with the median-energy outburst featured in

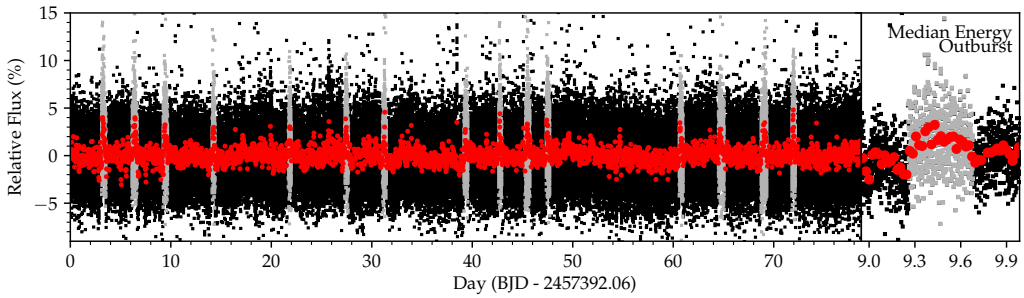

Figure 4.3: Light curve of EPIC 220453225. The left panel shows the full short-cadence *K2* light curve (black) and a 30-minute-smoothed long-cadence light curve (red). The gray segments of the light curve mark detected outbursts. The right panel zooms in on a representative, median-energy outburst.

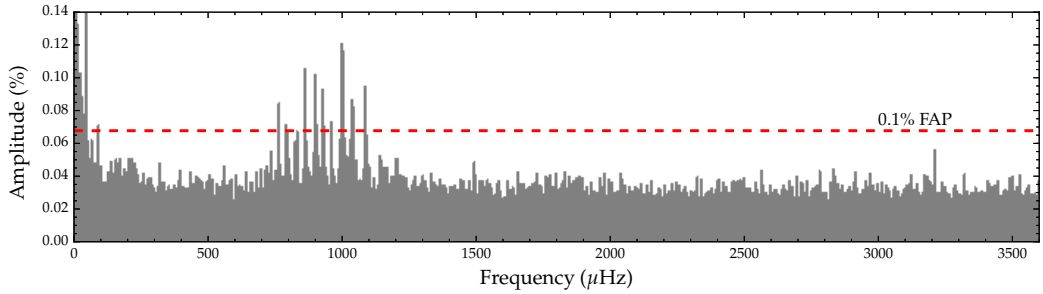

Figure 4.4: Fourier transform of EPIC 220453225. The 0.1% significance threshold was calculated from 10,000 bootstrap randomizations.

more detail in the right panel. The outbursts have durations of 5.9–13.3 hr (median 8.6 hr), peak flux enhancements of 5.7–9.4% (median 7.7%), equivalent durations of 5.0–12.4 min (median 9.3 min), and estimated energies of 2.6–6.4 $\times 10^{33}$ erg (median 4.8 $\times 10^{33}$ erg). The detected outbursts recur every 4.9 days on average.

The FT of the *K2* data on EPIC 220453225 is displayed in Figure 4.4. There are at least 10 significant bands of pulsational power present in the range 760–1100 μHz that exceed the 0.1% FAP significance threshold of 0.0677%. Characterization of 16 independent pulsation frequencies in the range 718–3211 μHz will be included in a forthcoming paper from Hermes et al. (2017d, in prep.).

4.1.3 EPIC 220329764

EPIC 220329764 was only observed in long cadence (30 min) during the 78.7-day *K2* Campaign 8. The light curve is displayed in Figure 4.5. Since

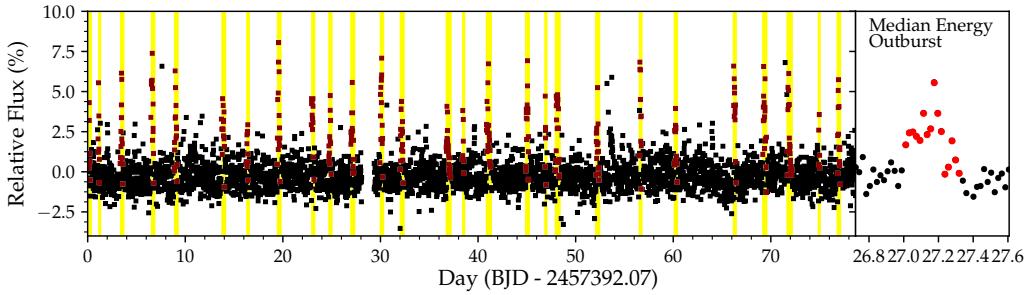

Figure 4.5: Light curve of EPIC 220329764. The left panel shows the full long-cadence *K2* light curve (black), with the detected outbursts marked with red points and highlighted in yellow. The right panel zooms in on a representative, median-energy outburst.

my outburst detection algorithm operates on the long-cadence data, we identify 27 brightening events recurring on an average timescale of 2.9 days. The outbursts last 2.9–11.3 hr (6.8 hr median), with equivalent durations of 3.5–16.8 min (10.8 min median). Because we do not have concurrent short-cadence data from *K2*, we measure the peak flux enhancement from the highest measurement during each outburst in the long-cadence light curve, which yields a lower limit because the long exposures smooth the underlying signal. The outbursts reach at least 3–8% (5.5% median). Using the spectroscopic parameters presented in Section 4.2, we convert the measured equivalent durations to approximate energies $1.8–8.7 \times 10^{33}$ erg (5.6×10^{33} erg median).

So far, every white dwarf observed to exhibit this outburst phenomenon has been a ZZ Ceti pulsator. The long cadence data are not sensitive to these pulsations (at least in this star; see Chapter 8 for exceptions). We decided to follow-up this object with high-speed photometry with the ProEM Camera

on the McDonald Observatory 2.1-meter Otto Struve Telescope. Don and Karen Winget were at the telescope in early August 2016 and observed this target for > 3 hours on each of three consecutive nights. The first night of data disappointingly showed no evidence of significant photometric variability to an approximate limit of 0.5% semi-amplitude. The next two nights did, however, reveal significant pulsational power. The FTs for each of the three nights are displayed in Figure 4.6. While the simplest explanation of this change in measured behavior is beating between closely spaced modes masking the signal from the first night, the measured average outburst timescale of 2.9 days suggests that an outburst event is likely to have occurred close in time to one of these measurements. Observations of high signal-to-noise short-cadence *K2* light curves have demonstrated that outbursts can dramatically affect pulsation amplitudes (most dramatically demonstrated for PG 1149+057 in Hermes et al. 2015b). We cannot definitively demonstrate whether this is the case with the data in hand, yet my difficulty in fitting and phasing the individual pulsation modes across these three nights of data is consistent with this explanation.

4.1.4 EPIC 228952212

The *K2* Campaign 10 data is the most recently released, and we have found yet another outbursting ZZ Ceti in this field, EPIC 228952212. J. J. Hermes extracted the short-cadence light curve from the pixel level data, and I also consider the *Kepler* Guest Observer long cadence extraction in my analy-

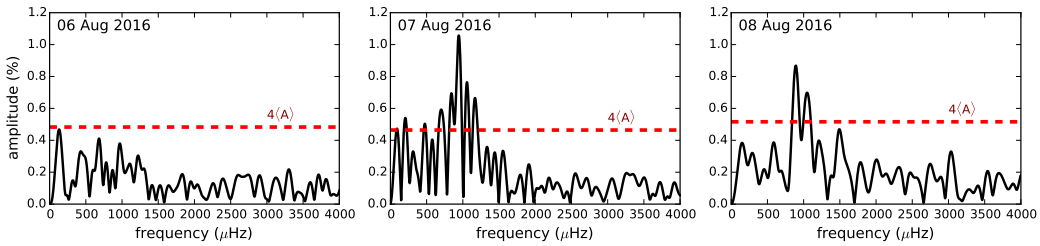

Figure 4.6: Fourier transforms of EPIC 220329764 light curves obtained from the McDonald Observatory 2.1-meter Otto Struve Telescope on three different nights in August 2016. While we do not detect variability above the significance threshold on the first night, the do measure stellar pulsations on the next two nights.

sis. Both light curves are displayed in Figure 4.7. The 14-day gap in coverage was caused by the failure of a CCD module[1]. In the 48-day span following the gap, we detected four outbursts with durations 14.1, 12.3, 9.0, and 6.3 hr, peak flux enhancements of 14, 9, 9, and 8%, and equivalent durations of 14.5, 10.9, 3.6, and 3.9 min, in chronological order. The average time between detected outbursts is 10.2 days. Using the spectroscopic values presented in Section 4.2, the approximate outburst energies are 8.1, 6.1, 2.0, and 2.2×10^{33} erg.

The FT of the 48 days of short-cadence data following the gap is displayed in Figure 4.8. Multiple bands of power exceed the 0.1% FAP significance criterion between 1175–1350 μHz, with other suggestive peaks falling just short of this conservative threshold.

[1] `https://keplerscience.arc.nasa.gov/k2-data-release-notes.html`

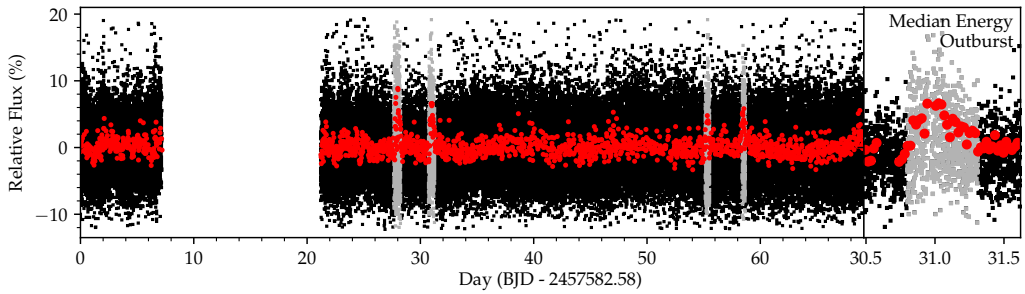

Figure 4.7: Light curve of EPIC 228952212. The left panel shows the full short-cadence *K2* light curve (black) and a 30-minute-smoothed long-cadence light curve (red). The gray segments of the light curve mark detected outbursts. The right panel zooms in on a representative, median-energy outburst.

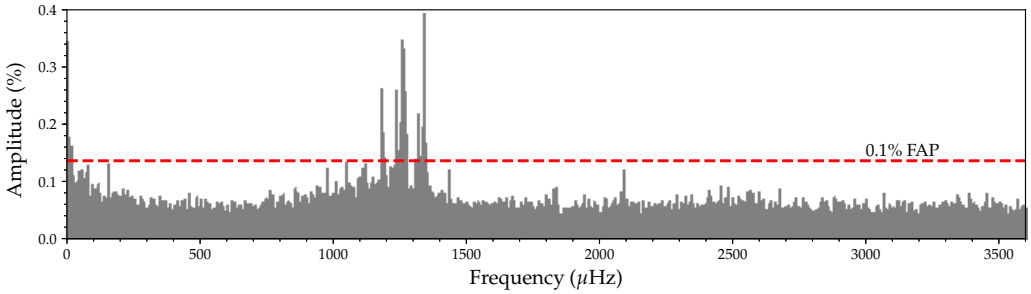

Figure 4.8: Fourier transform of EPIC 228952212. The 0.1% significance threshold was calculated from 10,000 bootstrap randomizations.

4.2 New Spectroscopic Parameters

J. J. Hermes has acquired spectra of the first seven oDAVs observed in *K2* with the Goodman spectrograph on the 4.1-meter SOAR telescope (Clemens et al. 2004). P.-E. Tremblay fit the Balmer line profiles with one-dimensional pure-hydrogen-atmosphere models with ML2/α = 0.8 following the methodology described in Tremblay et al. (2011a, with uncertainties deter-

Table 4.1. New Spectroscopic Parameters for Outbursting ZZ Cetis

Name	$T_{\rm eff}$ (1D) (K)	$\log g$ (1D) (cgs)	$T_{\rm eff}$ (3D) (K)	$\log g$ (3D) (cgs)	Mass (3D) ($M_{\odot}$)
KIC 4552982[1]	11130(120)	8.34(0.06)	10860	8.16	0.69(0.04)
EPIC 201806008	11200(130)	8.182(0.038)	10910	8.019	0.61(0.02)
EPIC 211629697	10890(130)	7.950(0.046)	10600	7.772	0.48(0.02)
EPIC 229227292	11530(140)	8.146(0.038)	11210	8.028	0.62(0.02)
EPIC 229228364	11330(140)	8.172(0.038)	11030	8.026	0.62(0.02)
EPIC 220453225	11540(140)	8.153(0.038)	11220	8.035	0.62(0.02)
EPIC 220329764	11500(140)	8.148(0.038)	11180	8.026	0.62(0.02)
EPIC 228952212	11400(160)	8.076(0.050)	11080	7.949	0.58(0.02)

[1]From previous work (Hermes et al. 2011; Bell et al. 2015c)

mined following Gianninas et al. 2011). Table 4.1 lists the best-fit parameters of $T_{\rm eff}$ and $\log g$, along with those values corrected for the effects of three-dimensional convection (Tremblay et al. 2013), and masses inferred from the white dwarf evolutionary sequences updated from Fontaine et al. (2001)[2]. The details of these observations, reductions, and analysis will be published in a forthcoming paper (Hermes et al. 2017, in prep.). The locations of all known oDAVs in spectroscopic $\log g$–$T_{\rm eff}$ parameter space (3D corrected) are plotted in Figure 4.9. With the four additional discoveries detailed in this chapter, it remains true that all of the DAVs that exhibit outbursts are located near the cool edge of the instability strip, and that only pulsating DAVs outburst.

[2]Available online at `http://www.astro.umontreal.ca/~bergeron/CoolingModels/`

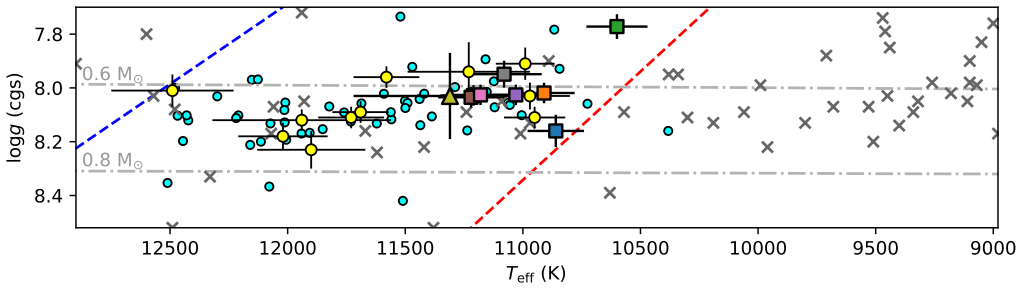

Figure 4.9: Location of presently known outbursting DAVs in $\log g$–$T_{\rm eff}$ parameter space. The oDAVs listed in Table 4.1 are marked with squares of different colors. The yellow circles and gray crosses correspond to the DAVs and long-cadence white dwarf targets that do not exhibit outbursts in *K2* data through Campaign 6 (from Bell et al. 2016). The dashed lines are the empirical instability strip boundaries (Tremblay et al. 2015), and the dash-dotted lines are cooling tracks for 0.6 and 0.8 $M_\odot$ white dwarfs (Fontaine et al. 2001), for context. The cyan circles are ZZ Cetis known from the ground (Giannini et al. 2011), with the addition the "odd duck" SDSS J2350−0054 from (Mukadam et al. 2004, with updated spectroscopic parameters from Kepler et al. 2016) to highlight the existence of ZZ Cetis cooler than the empirical strip boundaries.

4.3 Observational Summary of the New Outbursting Class of ZZ Ceti

I have collected summary statistics characterizing the typical outburst properties of all presently known oDAVs in Table 4.2. I have updated these values for the first two discovered oDAVs, KIC 4552982 (Bell et al. 2015c) and EPIC 201806008 (Hermes et al. 2015b), after redoing these measurements with the same methodology of the newer objects for uniformity.

Beyond the established pattern that only ZZ Cetis near the cool edge of the instability strip exhibit outbursts, I am interested in further exploring

Table 4.2. Newest Outburst Properties of oDAVs

Name	K_p (mag)	τ_{recur} (d)	Med. Duration (hr)	Max. Flux (%)	Max. Energy (erg)
KIC 4552982[1]	17.9	2.7	9.6	15	2.1×10^{33}
EPIC 201806008[2]	15.0	8.0	15	29	1.2×10^{34}
EPIC 211629697[3]	18.4	5.0	16.3	15	2.0×10^{34}
EPIC 229227292[3]	16.7	2.4	10.2	9	6.3×10^{33}
EPIC 229228364[4,5]	17.9	9.7	13.7	15	7.6×10^{33}
EPIC 220453225[4,5]	18.0	4.9	8.6	9	6.4×10^{33}
EPIC 220329764[5]	18.6	2.9	6.8	8[a]	8.7×10^{33}
EPIC 228952212[5]	18.5	10.2	10.6	14	8.1×10^{33}

[1]Bell et al. (2015c)

[2]Hermes et al. (2015b)

[3]Bell et al. (2016)

[4]Some values presented in Bell et al. (2017b)

[5]This work

[a]Flux enhancements may be underestimated from long-cadence data.

relationships between the outburst properties that may help us to develop a theory for their physical mechanism. Figures 4.10 and 4.11 explore two such trends amongst individual events: peak flux enhancement vs. outburst durations, and outburst energy vs. delay between events, respectively. There is a positive correlation between both pairs of measurements. The plotted points are color-coded to match the squares in Figure 4.9. Figure 4.11 particularly suggests that the relationship between outburst energy and delay time for different oDAVs are characterized by different slopes. The overall increased delay time before more energetic outbursts suggests a "charging" effect, where

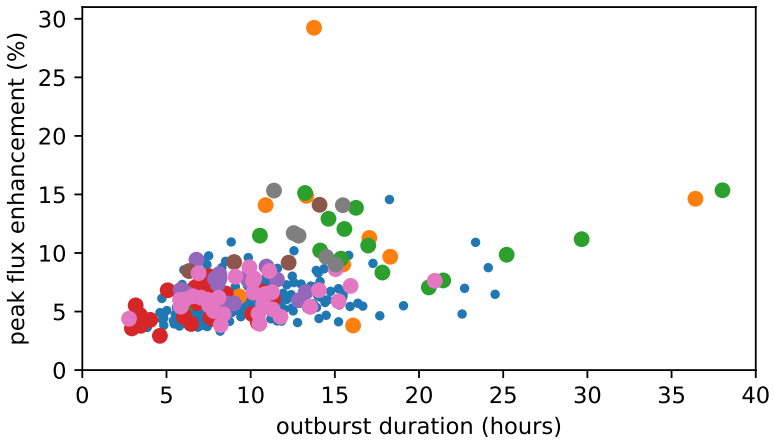

Figure 4.10: Peak flux enhancement versus outburst duration for all detected outbursts, color-coded by target to match the squares in Figure 4.9.

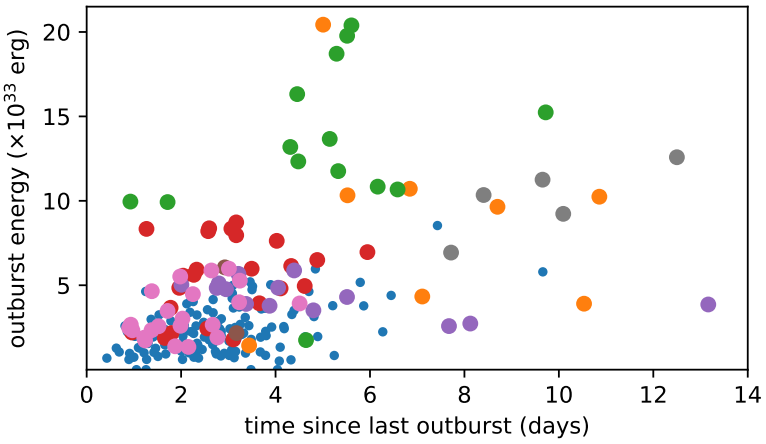

Figure 4.11: Approximate outburst energy versus delay since last outburst for events that are not separated by greater than 3-hour gaps in monitoring, color-coded by target to match the squares in Figure 4.9.

energy must build up to power more extreme outbursts.

Finally, Figure 4.12 displays outburst frequency distributions for every

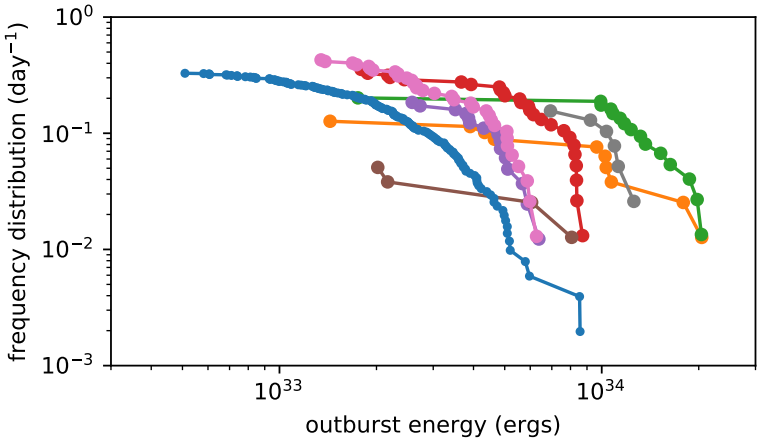

Figure 4.12: Outburst energy distributions show the rates that stars exhibit outbursts of at least a given energy. Color-coded by target to match the squares in Figure 4.9. The trend of higher outburst energy with lower $\log g$ is likely due to a poor method of approximating the outburst energy.

outbursting ZZ Ceti (calculated like the flare frequency distributions of Gershberg 1972). The turnover at low energy is likely due to incompleteness of our detections at the lowest energies, which the turnover at high energy suggests a physical limitation on outbursts. For comparison, the ZZ Ceti outbursts appear to saturate at $\sim 10^{34}$ erg, while solar flares max out at around 10^{32} erg (e.g., Wang & Dai 2013). The suggestive trend between higher energy distributions and spectroscopic $\log g$ is likely due to an overly simplistic method of converting equivalent durations to outburst energies. This will be replaced with a more sophisticated calculation prior to the submission of this work for refereed publication.

4.4 Opportunities for Future Observational and Theoretical Advances

My thesis research has spanned the discovery of this new outburst behavior in the *Kepler* light curve of the first ZZ Ceti identified in the original field of view, through the growth of the class of oDAVs to the point that we can begin studying their ensemble properties. There is still much work to be done in this area, both observational and theoretical. I close this section by outlining and speculating what I consider to be some of the promising areas of development for oDAVs in the immediate future.

Kepler is expected to have enough fuel to last, hopefully, through *K2* Campaign 17, and J. J. Hermes has been the Principle Investigator submitting *K2* Guest Observer proposals to continue monitoring likely and known ZZ Cetis in upcoming fields at short cadence. We expect to roughly double the number of ZZ Cetis with extensive space-based photometry in this time, and the number of oDAVs should double, too.

The fact that we have only detected this behavior in space-based observations is partially due to the infrequency of outbursts, but also because of their long timescales. Since airmass and transparency variations can imprint low-frequency variations onto our data, we routinely fit and remove low-order polynomials from ground-based light curves prior to Fourier analysis (Nather et al. 1990). This could also remove the signature of outbursts. The large amount of archival data at UT-Austin should be carefully revisited with an eye for missed events. One student of the UT College of Natural Sciences'

Freshman Research Initiative, Luke Stevens, attempted this for quite a few objects, but he found no clear evidence of outbursts. Cool ZZ Cetis have been empirically well-known to change their pulsation characteristics dramatically from night to night, so pulsational hints of outbursts may have also been ignored historically for this reason. If the unknown outburst mechanism also operates in helium-atmosphere pulsating white dwarfs, it may have been first observed as the "whoopsie" or "sforzando" during August 1996 Whole Earth Telescope observations of GD 358 (Kepler et al. 2003).

It would be worthwhile to do targeted ground-based observations in the future to hunt for outbursts. *Kepler* and *K2* only observed in a single passband and we could not be alerted of ongoing outbursts in real time. With small telescopes or planned transient surveys, we could monitor the outburst state of a large number of candidate oDAVs, quickly moving to obtain multi-color photometry and spectroscopy when an outburst is detected. These data could constrain whether the outbursts are local or global phenomena, assisting us greatly in developing a physical model of the process.

The data from transient surveys will be useful in their own right. While *Kepler* and *K2* only saved data for pre-identified objects of interest in limited areas on the sky, existing and upcoming synoptic surveys will observe ZZ Cetis in a much larger volume. While observations of each target will be more sparse, projects like the Palomar Transient Factory (data became public in December 2016, though I was unable to find signs of outbursts in known oDAVs), Zwicky Transient Facility, and Large Synoptic Survey Telescope have

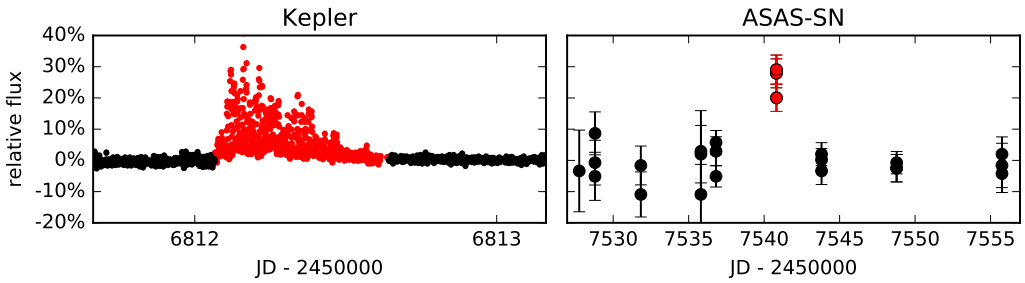

Figure 4.13: Comparison of the highest amplitude outburst of EPIC 201806008 observed by *K2* (left; Hermes et al. 2015b) and a compelling outburst detection from ASAS-SN (right).

the sensitivity to detect the significant excess flux from an outburst, some in multiple filters. The All-Sky Automated Survey for Supernovae (ASAS-SN; Shappee et al. 2014) made a compelling detection of flux enhancement[3] in the highest amplitude outbursting ZZ Ceti known, EPIC 201806008, as shown in Figure 4.13. This type of data will improve our statistics on outburst rates as a function of global stellar properties, and may reveal something about outburst temperatures.

We certainly also need to make advances in the theory of cool ZZ Ceti outbursts. The suggestion (originally brought up to me by J. J. Hermes) that gets kicked around the most invokes a mechanism from Wu & Goldreich (2001) whereby a pulsation mode can reach an amplitude saturation threshold where it dumps its energy into two daughter modes. The sum of these daughter mode frequencies must be close to the parent frequency. If these modes are

[3]Data publicly available from the ASAS-SN light curve server at `asas-sn.osu.edu` (Kochanek et al. 2017)

globally damped, this energy may go into heating the convection zone. This temperature change would make the star brighter overall. It would also cause the convection zone to become shallower, partially explaining the higher observed pulsation amplitudes during outbursts (especially in EPIC 201806008; Hermes et al. 2015b). The change in the stellar structure in the outer parts of the star would shift the frequencies of pulsation modes that are most sensitive to that region, and we do observe that low-radial-order modes are more stable in frequency during outbursts. Power at lower frequencies shifts to slightly higher frequencies during outbursts, perhaps because the thermal timescale at the base of the convection zone decreases.

I was recently invited to present this work at UC-Berkeley and I discussed this idea with a theorist there, Jing Luan. She is also a proponent of this idea, but suggested that this parametric instability should happen in all ZZ Cetis, it may just be that the inertia of hotter ZZ Ceti pulsation modes is so high that they cannot dump their energy quickly enough to cause an outburst. I added that this could happen more frequently in cooler ZZ Cetis because we empirically observe that their pulsation modes are less coherent in frequency, so they may sweep through resonances with daughter modes, lowering the amplitude threshold for energy transfer. Jing has been exploring this mechanism in some detail and I hope to see a publication on this topic from her soon.

Further development of an outburst theory should explain the differences observed in outburst energies and timescales between different stars, and

how this might relate to global or structural parameters revealed through spectroscopy and precision asteroseismology—work that is largely still pending.

Finally, we have noted all along that the cool edge of the instability strip has been empirically determined and is not theoretically well understood. The recent thorough attempt to computationally model the red edge by Van Grootel et al. (2012) reached the same conclusion as many efforts that proceeded it: pulsations are theoretically expected to continue many thousands of Kelvin below the observed $T_{\rm eff}$ cutoff. While highly speculative, it is possible that this newly discovered physical process could be the missing ingredient necessary to finally explain the red edge of the ZZ Ceti instability strip.

Chapter 5

Pruning The ELM Survey: Characterizing Candidate Low-mass White Dwarfs Through Photometric Variability*

My primary research goal from McDonald Observatory has been to discover and characterize pulsating DA white dwarfs at the low end of the white dwarf mass distribution. Extremely low-mass (ELM; $\lesssim 0.3\,M_{\odot}$) white dwarfs must have formed through mass transfer in tight binaries, since the Galaxy is not old enough for them to be produced from single stars. This has been widely supported by measurements of short-period radial velocity variations in time series spectroscopy by the ELM Survey (Hermes et al. 2012a, 2013a,c; Bell et al. 2015b; Kilic et al. 2015a). A pulsating variable class of these objects (ELMVs) was just being discovered at McDonald Observatory as I began my research there. All of these targets were identified by the ongoing ELM Survey,

* This work was previously published as Bell, K. J., Gianninas, A., Hermes, J. J., Winget, D. E., Kilic, M., Montgomery, M. H., Castanheira, B. G., Vanderbosch, Z., Winget, K. I. and Brown, W. R., 2017, *Pruning The ELM Survey: Characterizing Candidate Low-mass White Dwarfs through Photometric Variability*, ApJ, 835, 180. I led the photometric observations and analysis in this work. A. Gianninas, M. Kilic, and W. R. Brown spectroscopically characterized the studied objects and assisted in their interpretation. B. G. Castanheira, Z. Vanderbosch, K. I. Winget, and D. E. Winget all contributed photometric observations from McDonald Observatory. J. J. Hermes, D. E. Winget, and M. H. Montgomery helped me to develop the context for discussing these results.

and I decided to follow up candidate ELMVs from their most recent two publications. I discovered three new pulsating variables, but none were among the ELM Survey targets confirmed in binaries. The dominant 4.31-hr pulsation in one exceeds the physical limit for a cooling-track white dwarf. Two other targets turned out to be photometric binaries, and while the ellipsoidal variations measured in one support its classification as an ELM white dwarf (see Chapter 7), the long eclipses in the other implied a primary star radius that exceeds $0.4\,R_{\odot}$—again inconsistent with a cooling-track white dwarf. I published the following work as Bell et al. (2017a), in which I argue that the ELM Survey suffers systematic misclassification for objects with spectroscopically inferred $T_{\rm eff} \lesssim 9{,}000$ K.

5.1 Introduction

The Galaxy is not old enough for $\lesssim 0.3\,M_{\odot}$ white dwarfs (WDs) to have formed in isolation, even from high-metallicity systems (Kilic et al. 2007). These objects are instead formed as the remnants of mass transfer in post-main-sequence common-envelope binaries. A close companion can strip away material if a star overflows its Roche lobe while ascending the red giant branch, leaving behind an extremely low-mass (ELM) WD with a degenerate helium core and hydrogen-dominated atmosphere (e.g., Nelemans et al. 2001). Althaus et al. (2013) and Istrate et al. (2016a) have calculated the most recent evolutionary ELM WD models, and Heber (2016, Section 8) provides a nice overview of these objects.

The ELM Survey (Brown et al. 2010, 2012, 2013, 2016; Kilic et al. 2011a, 2012; Gianninas et al. 2015) is a spectroscopic effort to discover and characterize ELM WDs. So far, this survey has measured spectra of 88 objects with parameters from line profiles consistent with He-core WDs ($5.0 \lesssim \log g \lesssim 7.0$ and 8000 K $\lesssim T_{\rm eff} \lesssim$ 22,000 K). Membership to close ($P_{\rm orb} < 25\,{\rm hr}$) binary systems through measured radial velocity (RV) variations supports the mass-transfer formation scenario for 76 targets.

The reliability of spectral line profiles as an ELM diagnostic is challenged by the discovery of thousands of objects that exhibit spectra consistent with low-$\log g$ WD models with $T_{\rm eff} \lesssim$ 9,000 K in recent Sloan Digital Sky Survey (SDSS) data releases (Kepler et al. 2016). The nature of this large population is under debate, as different observational aspects weigh for-or-against different physical interpretations, including ELM WDs, main sequence A stars in the Galactic halo, or binaries comprised of a subdwarf and a main sequence F, G, or K dwarf (Pelisoli et al. 2017). These objects are labeled as "sdA" stars, with the ELM classification reserved only for those with supporting orbital parameters from RV variations. Only ≈15% of ELM Survey objects are found to have $T_{\rm eff} <$ 9,000 K.

Six pulsating stars have been published as ELM WDs in a low-mass extension of the hydrogen-atmosphere (DA) WD instability strip from time series photometry obtained at McDonald Observatory (Hermes et al. 2012a, 2013a,c; Bell et al. 2015b). However, only the first three discovered show RV variations in available time series spectroscopy. Another pulsating ELM vari-

able (ELMV) in a binary system with a millisecond pulsar was reported by Kilic et al. (2015a). Stellar pulsations in these objects provide the potential to constrain the details of their interior structures and to better understand their formation histories through asteroseismology. The pulsational properties of ELM WDs have been explored theoretically by Van Grootel et al. (2013) and Córsico & Althaus (2014a, 2016a). The DA WD instability strip is both empirically and theoretically found to shift to lower $T_{\rm eff}$ with lower $\log g$, intersecting the population of sdAs in the ELM regime.

ELM WDs can also exhibit photometric variability that results from their binary nature, including signatures of eclipses, ellipsoidal variations (tidal distortions), and relativistic Doppler beaming (also called Doppler boosting; Shporer et al. 2010; Kilic et al. 2011b; Hermes et al. 2014a). In the case of the 12.75-minute binary SDSS J0651+2844, these have enabled the measurement of orbital decay from gravitational radiation (Hermes et al. 2012b).

In addition to these variables, numerous stars have been published as pulsating precursors to ELM WDs (pre-ELMs). Maxted et al. (2013, 2014) discovered two recently stripped cores of red giants that pulsate in binary systems with main sequence A stars. Corti et al. (2016) reported on two variable stars that occupy a region of parameter space where they could plausibly be either pre-ELM WD or SX Phoenicis pulsators. Finally, Gianninas et al. (2016) discovered three pre-ELMs with mixed H/He atmospheres that pulsate at higher temperatures than an extrapolation of the empirical DA WD instability strip due to the presence of He in their atmospheres. Córsico et al. (2016c) have

Table 5.1. Target Physical Parameters from The ELM Survey

SDSS	R.A. (h:m:s)	Dec. (d:m:s)	$T_{\rm eff}$ (K)	$\log g$ (cm s^{-1})	M_1 ($M_\odot$)	g_0 (mag)	$P_{\rm orb}$ (days)	K_1 (km s^{-1})	Ref. (ELM)
J0308+5140	03:08:18.19	+51:40:11.5	8380(140)	5.51(0.10)	0.151(0.024)	13.05(0.01)	0.8059(0.0004)	78.9(2.7)	6
J1054−2121	10:54:35.78	−21:21:55.9	9210(140)	6.14(0.13)	0.168(0.011)	18.49(0.01)	0.104(0.007)	261.1(7.1)	6
J1108+1512	11:08:15.51	+15:12:46.7	8700(130)	6.23(0.06)	0.167(0.010)	18.83(0.02)	0.123(0.009)	256.2(3.7)	6
J1449+1717	14:49:57.15	+17:17:29.3	9700(150)	6.08(0.05)	0.168(0.010)	17.62(0.02)	0.29075(0.00001)	228.5(3.2)	6
J1017+1217	10:17:07.11	+12:17:57.4	8330(130)	5.53(0.06)	0.142(0.012)	17.48(0.02)	...	< 30.2	7
J1355+1956	13:55:12.34	+19:56:45.4	8050(120)	6.10(0.06)	0.156(0.010)	16.10(0.02)	...	< 40.9	7
J1518+1354	15:18:02.57	+13:54:32.0	8080(120)	5.44(0.07)	0.147(0.018)	18.99(0.02)	0.577(0.007)	112.7(4.6)	7
J1735+2134	17:35:21.69	+21:34:40.6	7940(130)	5.76(0.08)	0.142(0.010)	15.90(0.01)	...	< 31.6	7
J2139+2227	21:39:07.42	+22:27:08.9	7990(130)	5.93(0.12)	0.149(0.011)	15.60(0.01)	...	< 22.0	7

explored the properties of pre-ELM WD pulsations in the evolutionary models of Althaus et al. (2013).

In this work, we assess the photometric variability of nine candidate ELM WD pulsators from The ELM Survey papers VI (ELM6; Gianninas et al. 2015) and VII (ELM7; Brown et al. 2016). We describe our candidate selection and observations in Section 5.2. We present an object-by-object analysis in Section 5.3. We discuss our new variable and non-variable objects in the context of the rapidly developing picture of ELM WD parameter space in Section 5.4 and conclude with a summary in Section 5.5.

5.2 Observations

Our observing campaign targeted all nine stars published in the ELM6 and ELM7 samples with $\log g < 7.0$ and $T_{\rm eff}$ within 500 K of the current empirical ELMV instability strip, which has been updated to reflect the spectroscopic corrections derived from 3D convection models in the ELM regime (Tremblay et al. 2015; Gianninas et al. 2015). Select physical parameters published for these stars by the ELM Survey are listed in Table 5.1.

We observed each of these targets with the ProEM camera on the McDonald Observatory 2.1-m Otto Struve Telescope. The ProEM camera is a frame-transfer CCD that obtains time series photometry with effectively zero readout time. The CCD has 1024×1024 pixels and a field of view of $1.6' \times 1.6'$. We bin 4×4 for an effective plate scale of $0.36''\,\mathrm{pix}^{-1}$. All observations were made through a 3 mm BG40 filter, which blocks light redward of ≈ 6500 Å to

reduce the sky background. A complete journal from 31 nights of observing these stars is provided in Table 5.2.

We obtained at least 31 dark frames of equal exposure time as our science frames, as well as dome flat field frames, at the start of each night.

Table 5.2: Journal of Observations

SDSS	Date (UTC)	Exposure Time (s)	Run Duration (h)
J0308+5140	11 Oct 2015	3	4.9
	12 Oct 2015	3	1.7
	13 Oct 2015	3	2.7
	06 Feb 2016	3	4.1
J1054−2121	15 Mar 2015	20	1.7
	20 Apr 2015	30	3.0
	21 Apr 2015	20	4.2
J1108+1512	19 Mar 2015	30	0.9
	12 Mar 2016	30	1.6
	12 Mar 2016	60	4.0
	16 Mar 2016	30	4.3
	01 May 2016	15	2.5
J1449+1717	23 Jul 2014	15	2.3
	24 Jul 2014	25	2.6
	14 Apr 2016	5	0.6
	14 Apr 2016	15	2.9
J1017+1217	08 Jan 2016	5	2.2
	09 Jan 2016	30	3.5
	11 Mar 2016	5	3.9
	17 Mar 2016	10	3.4
	30 Apr 2016	5	2.1
	03 May 2016	10	3.9
J1355+1956	14 Apr 2016	3	2.6
	04 May 2016	3	1.5
	05 May 2016	3	2.0
	06 May 2016	5	6.4
J1518+1354	15 Apr 2016	30	4.3

Table 5.2 (cont'd): Journal of Observations

SDSS	Date (UTC)	Exposure Time (s)	Run Duration (h)
J1735+2134	30 Apr 2016	3	4.5
	01 May 2016	3	0.9
	01 May 2016	3	3.0
	03 May 2016	3	4.1
	07 May 2016	5	2.5
J2139+2227	06 Jul 2016	5	4.3
	02 Aug 2016	10	5.3
	03 Aug 2016	10	4.5
	04 Aug 2016	10	7.2
	05 Aug 2016	15	6.9
	08 Aug 2016	5	2.8

5.3 Analysis

For each run, we measure circular aperture photometry in the dark-subtracted, flatfielded frames for the target and nearby comparison stars with the IRAF package CCD_HSP, which relies on tasks from PHOT (Kanaan et al. 2002). We use the WQED software (Thompson & Mullally 2013) to divide the target counts by the summed counts from available comparison stars to remove the effect of variable seeing and transparency conditions during each observing run. WQED also applies a barycentric correction to our timestamps to account for the light travel time to our targets changing as the Earth moves in its orbit.

We search for significant signals of astrophysical variability in the resultant light curves. We present individual analyses for each target below, sorted

into three groups by our ultimate classification of the objects: new pulsating stars, binary systems with photometric variability related to their orbits, and systems for which we can only put limits on a lack of photometric variability.

5.3.1 Pulsating Stars

Most pulsating stars, including most WD pulsators, oscillate at multiple simultaneous frequencies. We find multiple significant, independent frequencies of photometric variability in three of our targets: SDSS J1735+2134, SDSS J2139+2227 and SDSS J1355+1956.

5.3.1.1 SDSS J1735+2134

We observed SDSS J1735+2134 over 4 nights between 30 Apr and 07 May 2016. These light curves, displayed in Figure 5.1, evidence multi-periodic pulsations reaching up to 3% peak-to-peak amplitude.

We take an iterative approach to determining the pulsation properties of this target. To detect a new mode, we calculate the Fourier transform (FT) of the combined light curve and assess whether the highest peak exceeds an adopted $4\langle A\rangle$ significance threshold, where $\langle A\rangle$ is the mean amplitude in a local 1000 μHz region of the FT (this corresponds to $\approx$99.9% confidence; Breger et al. 1993; Kuschnig et al. 1997). If a significant signal is present, we find the non-linear least-squares fit of a sinusoid to the data, using the peak amplitude and frequency from the FT as initial guesses. We then "prewhiten" the light curve by subtracting out this best fit and compute the FT of the

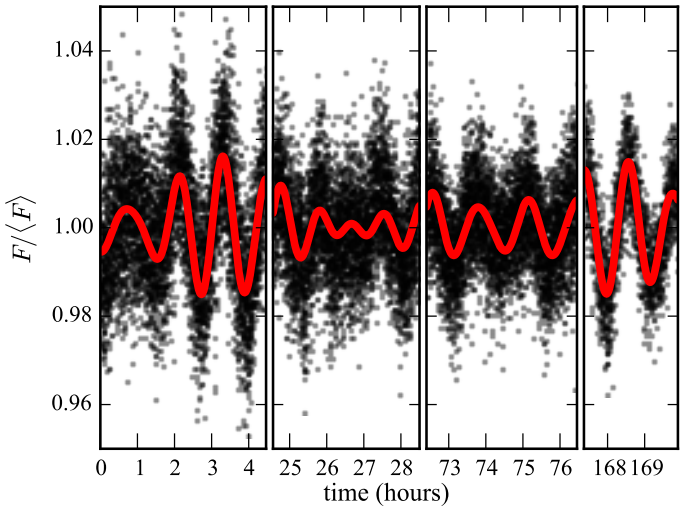

Figure 5.1: The light curves of SDSS J1735+2134 from 4 nights are displayed in black dots. The x-axis units are hours since the start of the 30 Apr 2016 run. The y-axis gives the ratio of the measured flux relative to the mean flux. Our 4-period model fit to the data is displayed as a solid line.

residuals. If another significant signal is detected above $4\langle A \rangle$ in the FT of the residuals, we redo the non-linear fit with a sum of sinusoids. We repeat this process until no new significant signals are found.

For SDSS J1735+2134, we find 4 significant signals corresponding to 4 eigenfrequencies of this pulsating star. Their properties are collected in Table 5.3, along with analytical uncertainties (Montgomery & Odonoghue 1999). We use millimodulation amplitude (mma) as our unit for pulsation amplitude, where 1 mma = 0.1% flux variation.

The sequence of FTs corresponding to all iterations of our mode detection algorithm is displayed in Figure 5.2. The original FT is in black, with

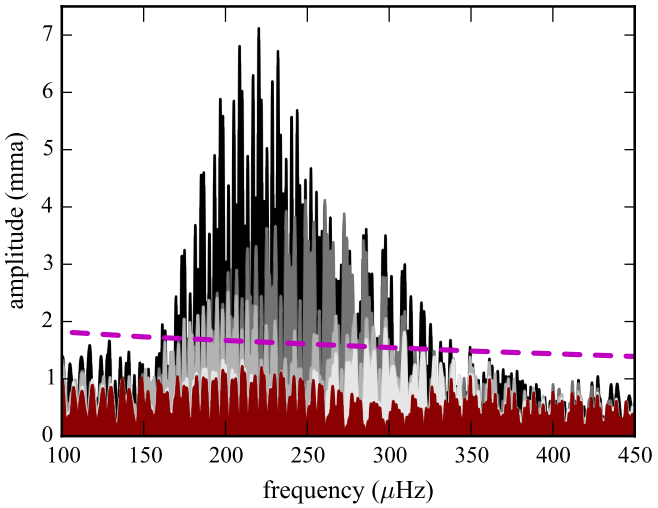

Figure 5.2: Fourier transforms of the original (black) light curves, increasingly prewhitened data (lighter shades of gray; see text), and final residuals (red) for SDSS J1735+2134 in the region of significant pulsational power. The dashed line is the final $4\langle A\rangle$ significance threshold for the data prewhitened by the four sinusoids characterized in Table 5.3.

increasingly lighter shades of gray representing the FTs of the prewhitened light curves after additional mode detections. The red FT is of the fully prewhitened data and the dashed line is the final $4\langle A\rangle$ significance threshold.

5.3.1.2 SDSS J2139+2227

We characterize the pulsations of SDSS J2139+2227 from 26 hours of photometry obtained over the span of 7 nights in early Aug 2016[1]. The same

[1]One nearby comparison star in the field of view, SDSS J213905.27+222709.1 (g = 16.77 mag), was incidentally observed to show deep eclipses while we were monitoring SDSS J2139+2227. The eclipses last ≈3 hours and decrease the flux in the $BG40$ filter by ≈16% at mid eclipse. We observed similar eclipses 1.848 days apart, but the binary

Table 5.3. Pulsation Properties of SDSS J1735+2134

Mode	Frequency (μHz)	Period (min)	Amplitude (mma)
f_1	220.172(0.013)	75.698(0.004)	7.60(0.11)
f_2	260.79(0.03)	63.909(0.007)	3.64(0.11)
f_3	201.56(0.03)	82.687(0.012)	3.38(0.11)
f_4	297.38(0.05)	56.046(0.009)	2.04(0.11)

Table 5.4. Pulsation Properties of SDSS J2139+2227

Mode	Frequency (μHz)	Period (min)	Amplitude (mma)
f_1	471.82(0.06)	35.324(0.004)	1.52(0.08)
f_2	402.85(0.09)	41.372(0.009)	1.02(0.08)
f_3	302.73(0.09)	55.055(0.016)	0.99(0.08)

iterative FT, least-squares fitting, and prewhitening process as used for the previous object reveals the three significant pulsation frequencies that are listed in Table 5.4. The FT before and after prewhitening is displayed in Figure 5.3. The pulsation amplitudes are too small relative to the photometric signal-to-noise ratio to be clearly apparent to the eye in the light curve.

period could be an integer fraction of that.

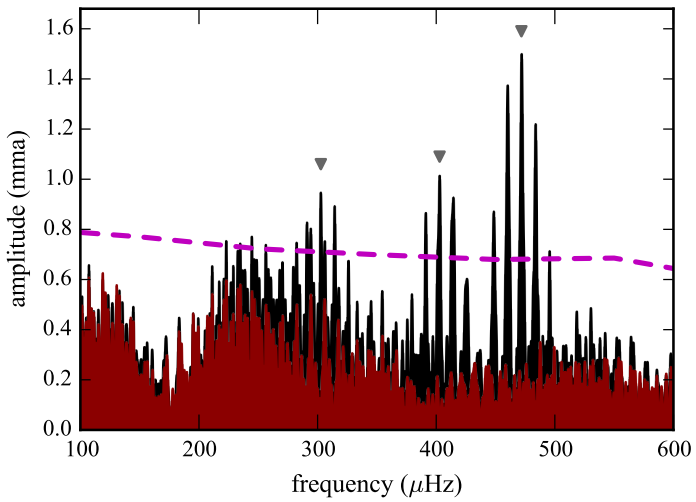

Figure 5.3: Fourier transform of the original (black) and fully prewhitened (red) light curves of SDSS J2139+2227 covering the full region of significant pulsational power. The dashed line is the final $4\langle A \rangle$ significance threshold for the data prewhitened by the three sinusoids characterized in Table 5.4 and indicated here with triangles.

5.3.1.3 SDSS J1355+1956

The target SDSS J1355+1956 shows a dominant signal with such a long period that only our 6.41 hr run from 06 May 2016 captured a full cycle. Figure 5.4 displays the light curves that we obtained on three consecutive nights, 04–06 May 2016. Since the durations of the earliest two runs are shorter than the dominant period, they suffer some non-ideal normalization in our standard reduction pipeline. To account for this, we fit multiplicative scaling factors to the different May 2016 runs simultaneously with the least-squares sinusoid-fitting step of our period search algorithm for renormalization.

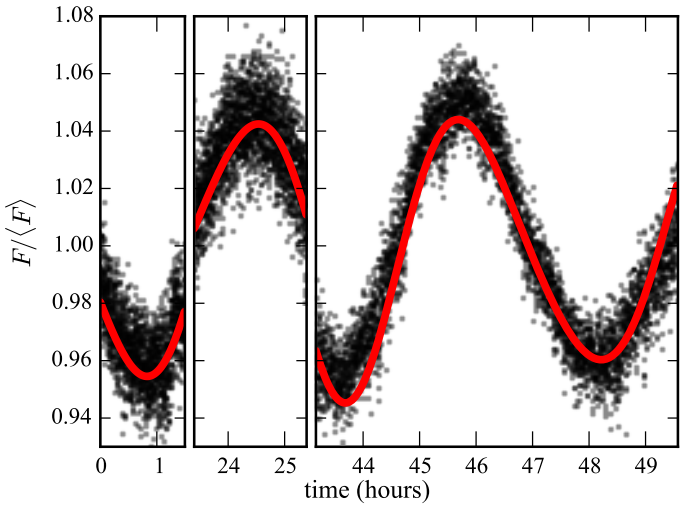

Figure 5.4: The light curves of SDSS J1355+1956 from three consecutive nights in May 2016. The best-fit two-sinusoid model is plotted over the data.

The FT of the 06 May 2016 run alone provided an initial guess of 4.74 hr for the dominant period; however, this value aligns poorly with the data from the two previous nights. The Catalina Sky Survey (CSS; Drake et al. 2009) Data Release 2[2] provides 321 epochs of well calibrated photometry from eight seasons of observations that we use to guide our mode selection from the complicated alias structure in the FT of our May 2016 data (Figure 5.5). Rather than the highest peak in the FT of our data (corresponding to 5.2604 ± 0.0011 hours), the CSS data prefer a period near 4.29 hours. We use this as an initial guess in calculating the least-squares single-sinusoid fit to the three-night light curve (with free renormalization parameters). The FT of the

[2] `http://nesssi.cacr.caltech.edu/DataRelease/`

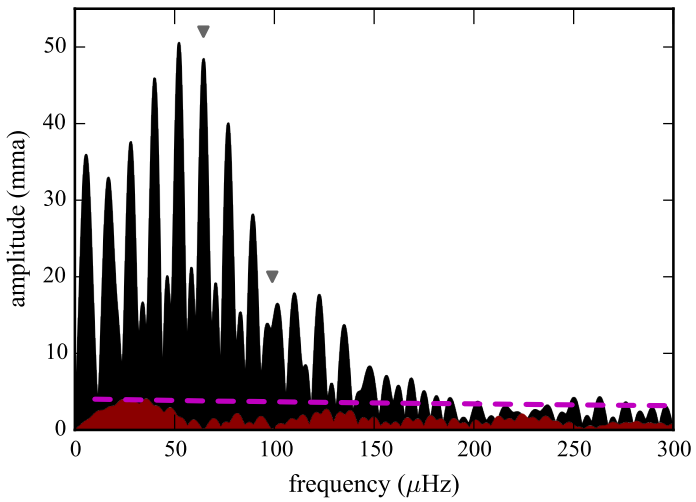

Figure 5.5: The Fourier transform of the scaled original (black) and fully prewhitened (red) light curves of SDSS J1355+1956 from May 2016. The dashed line shows the final $4\langle A \rangle$ significance threshold for the prewhitened light curve. The frequencies of the two significant modes in Table 5.5 are marked with triangles.

Table 5.5. Pulsation Properties of SDSS J1355+1956

Mode	Frequency (μHz)	Period (hr)	Amplitude (mma)
f_1	64.430(0.010)	4.3113(0.0007)	46.18(0.16)
f_2	98.94(0.05)	2.8075(0.0015)	8.94(0.16)

residuals supports the presence of a second significant frequency in this star. A simultaneous fit of two sinusoids to the data gives our final solution, with parameters listed in Table 5.5. This solution is plotted over the observed light curves in Figure 5.4.

Figure 5.5 includes the FTs of the rescaled light curve both before and after prewhitening our two-period solution. The dominant period exceeds the theoretical limit for pulsations in ELM WDs as discussed in Section 5.4. The residuals are just barely shy of our adopted significance criterion at a period of 7.295 hours. A pulsation mode of this duration could account for the apparent residual disagreement found in the last panel of Figure 5.4, though this could also be attributed to differential extinction between the target and comparison stars during this long run (see Section 5.3.3).

5.3.2 Photometric Binaries

Binary systems can be photometrically variable for many reasons: primary and secondary eclipses, ellipsoidal variations (tidal distortion), reflection, and relativistic Doppler beaming. We detect photometric variability related to the binary orbital periods determined from RV variations (see Table 5.1) in two of our targets.

5.3.2.1 WD J0308+5140

WD J0308+5140 is the only target that we observed that does not fall within the SDSS footprint; it was instead originally identified from a LAMOST (Large Sky Area Multi-Object Spectroscopy Telescope; Wang et al. 1996; Cui et al. 2012) spectrum. For convenience, we follow the convention of Gianninas et al. (2015) and include it in tables under the "SDSS" column header.

This target shows the longest-period RV variations in our sample at

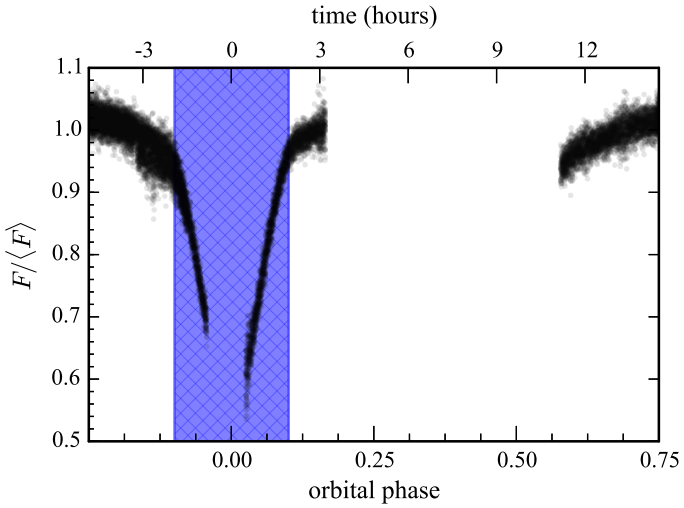

Figure 5.6: The phase-folded light curve of WD J0308+5140 shows evidence of eclipses that implies a primary star radius $\gtrsim 0.4\ R_\odot$. The blue hatched region marks the observed eclipse.

19.342±0.009 h. Our data reveal dramatic photometric variability related to the orbit in partial coverage of the binary period.

Figure 5.6 displays the light curve folded on the measured orbital period. We normalized the target counts summed in the aperture for WD J0308+5140 by those of a single, similarly bright ($B = 16.5$ mag) field comparison star—entry 1350-03091578 from USNO-A2.0 located at RA(2000) = $03^{\rm h}08^{\rm m}19\overset{\rm s}{.}87$, Dec.(2000) = $51°40'34.15''$ (Monet 1998)—so that the individual runs align smoothly.

While our phase coverage is not complete enough to precisely determine system parameters, we identify by eye the apparent start and end times of a deep primary eclipse. This range, centered on phase 0, is highlighted in

Figure 5.6.

We rely on five simplifying assumptions to calculate a lower limit on the radius of the primary star: (1) the stars are in circular orbits; (2) the relative velocity between the two stars equals the measured RV semi-amplitude of $K_1 = 78.9 \pm 2.7$ km s^{-1}; (3) the catalogued K_1 value represents only the speed of the primary star; (4) the system inclination is 90°; and (5) the two binary components have equal radii. Under this oversimplified model, the radius of the primary star is related to the measured eclipse duration, Δt, by the expression $R_1 = K_1 \Delta t/4$. With an eclipse duration of ≈4 hours, we have $R_1 \gtrsim 0.4\ R_\odot$. The first assumption is supported by the sinusoidal fit to the RV measurements in ELM6. If any of the latter four assumptions are false, we would find a larger radius for the primary star, so our result is a conservative lower limit.

5.3.2.2 SDSS J1054−2121

While we see no evidence of pulsational variability in the light curve of SDSS J1054−2121, it does show photometric variability related to the binary orbital period of 2.51 ± 0.16 h determined from RV measurements.

Because of the long gap between our short March 2015 run and our 7.28 h of data that April, we use only the April data in this analysis. Since both April runs exceed one full orbital cycle, we divide a straight line fit from each light curve to correct for differential extinction effects without concern for missing longer-timescale variations.

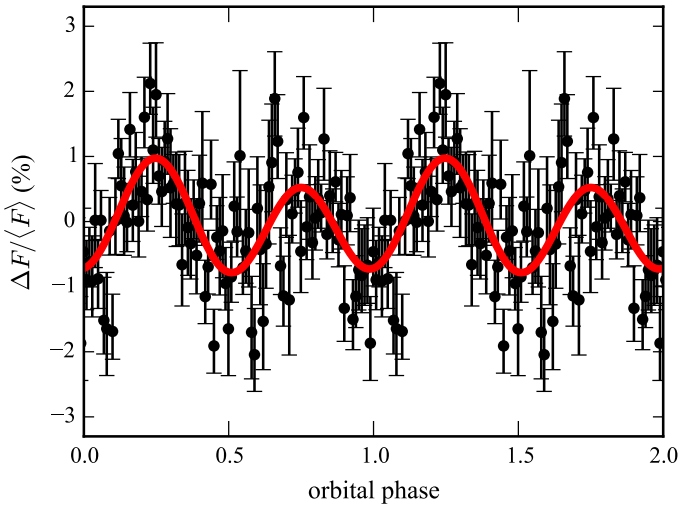

Figure 5.7: The phase-folded, binned light curve of SDSS J1054−2121 shows evidence of ellipsoidal variations and relativistic Doppler beaming. Our best fit model is plotted over the data in red.

The FT of these data reveals a dominant signal at 1.251 ± 0.004 h (with additional extrinsic uncertainty of ± 0.07 h from the aliasing structure of the spectral window) consistent with half the orbital period. We interpret this as the signature of tidally induced ellipsoidal variations of the star.

We phase-fold the April data on the refined binary period and then average the photometry within 100 phase bins, each having width 1.5 min and containing 7–16 measurements. We calculate the standard deviation of points within each phase bin and divide that by the square root of the number of points to get error bars for the binned, phase-folded light curve. This light curve is repeated through two full orbital cycles in Figure 5.7.

The dominant sinusoidal signal is from ellipsoidal variations, which has

Table 5.6. Least-squares Amplitudes

SDSS	$\cos 2\phi$ (%)	$\sin \phi$ (%)	$\cos \phi$ (%)
J1054−2121	0.75(0.08)	0.23(0.08)	0.03(0.08)

peaks twice per orbit when the elongated side of the tidally distorted ELM is presented to our line of sight. We refer to this as the $\cos 2\phi$ term with angular frequency 2 cycles orbit^{-1}—where phase zero ($\phi = 0$) is defined as when the ELM WD is furthest from us.

Doppler beaming is the modulation of the measured flux with the radial velocity of the target, caused by both the Dopper shift of flux in/out the observational bandpass and the relativistic beaming of light in the direction of motion (e.g., Rybicki & Lightman 1979; van Kerkwijk et al. 2010). With our phase convention, this has a $\sin \phi$ behavior with frequency 1 cycle orbit^{-1}. The amplitude of this effect is directly related to the RV semi-amplitude of the target through $A_{\rm DB} = -(3 - \alpha)K_1/c$, where $\alpha = d\log F_\nu / d\log \nu$ is the spectral index, which accounts for the Dopper shift of flux into the observational bandpass. We estimate the spectral index of SDSS J1054−2121 to be $\alpha = 0.956$ by averaging the mean α for our best-fit model spectrum in each of the two wavelength ranges 3200–3600 Å and 5500–6500 Å, which correspond approximately to the blue and red edges of the BG40 bandpass. With an RV semi-amplitude of $261.1 \pm 7.1\,{\rm km\,s^{-1}}$, we expect to measure a Doppler beaming signal of $\approx 0.18\%$ in this system.

A $\cos\phi$ component of the light curve could be present from reflection if the ELM WD's companion is sufficiently hot, but Hermes et al. (2014a) did not find this effect to a significant level in 20 double-degenerate binaries with low-mass primary stars.

We compute a least-squares fit for the $\cos 2\phi$, $\sin\phi$ and $\cos\phi$ amplitudes, along with the phase and an overall vertical offset, to the folded light curve. Our best-fit model is overplotted in red in Figure 5.7. The reduced χ^2 of this five-parameter fit is 0.85. The amplitudes of the three sinusoidal components are given in Table 5.6. We calculate the uncertainties from the diagonal elements of the covariance matrix after scaling the photometric uncertainties to give $\chi^2_{\rm red} = 1$.

The $\sin\phi$ amplitude is within 1σ of the expected 0.18% and the $\cos\phi$ term is consistent with zero. The $\cos 2\phi$ term is entirely consistent with ellipsoidal variations in an ELM WD. A more thorough analysis of this target, including a refinement of system parameters from the photometric data, will be presented in follow-up work.[3]

5.3.3 Null Results

For the remaining four targets of the present survey, we do not detect significant astrophysical signals in our data. However, the extent of our observational coverage is not sufficient to completely rule out photometric

[3]See Chapter 7.

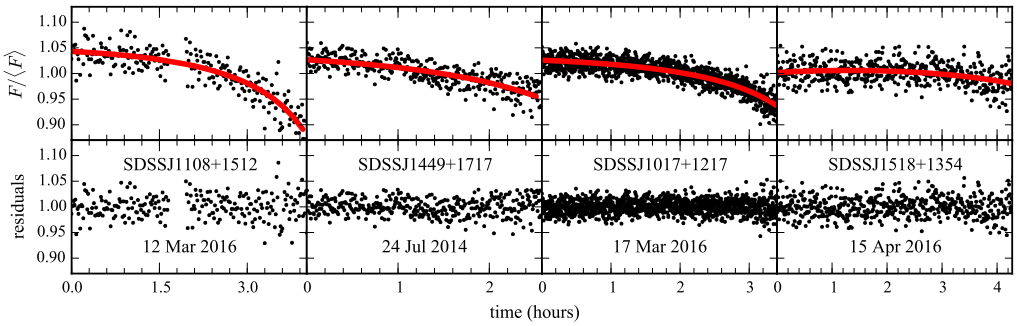

Figure 5.8: Each plot in the top panel displays the divided light curve with the largest overall trend for each of the four targets that do not show clear signs of intrinsic stellar variability. The solid red lines show the best-fit differential extinction model for each. Our analysis of the residuals displayed in the bottom panel reveals no significant astrophysical signal.

variability in these stars. Since stellar pulsations and orbital timescales can be on the order of hours for ELM WDs, we are careful not to classify a star as a nonvariable without multiple individual runs of at least this duration. We are cautious because multiple sources of variability (e.g., two pulsation modes) can happen to destructively combine during an individual night's observations, masking the signal. Sky and transparency conditions also commonly vary on timescales of hours and can leave signatures in the data.

For some observing runs on our remaining targets, we do see overall long-timescale trends throughout the divided light curves. This is likely due to differential extinction with changing airmass during a night's observations. Since the spectral energy of our targets is generally distributed differently (usually more toward shorter wavelengths) across the observational bandpass than nearby comparison stars, light from the target will experience a different

Table 5.7. Limits on Pulsations in NOVs

SDSS	Period or (h)	Amplitude (mma)
J1108+1512	> 4.0	< 13.4
J1449+1717	> 2.6	< 9.8
J1017+1217	> 3.9	< 5.3
J1518+1354	...	...

amount (usually more) of atmospheric scattering on the way to our detector.

For normal-mass WDs, where pulsation periods of ∼10 minutes are usually much shorter than the duration of observations, we typically mitigate this effect by fitting and dividing out a low-order polynomial (e.g., Nather et al. 1990). However, when searching for signals with timescales on the order of the run duration, this approach is inappropriate as it may mistakenly remove astrophysical signals of interest.

Instead, we divide from each light curve the least-squares fit of $a \exp bX$, where X is the airmass at each frame and a and b are free coefficients. This approach will not represent differential extinction well if there are major changes in atmospheric conditions during observations or if extinction has an azimuthal dependence at the observing site, but this first-order approach appears to fully explain the dominant trends found in the light curves of our remaining targets.

The top panels of Figure 5.8 display the light curves with the most pronounced airmass trend for each remaining target (from left to

right): SDSS J1108+1512, SDSS J1449+1717, SDSS J1017+1217 and SDSS J1518+1354. The solid lines are the least-squares fits of the differential extinction models, and the bottom panels show the final reduced light curves after dividing out these systematics. FTs of these fully reduced light curves, and those from all other runs on these targets, do not reveal significant signals to our $4\langle A\rangle$ significance threshold (see Section 5.3.1.1).

We place conservative limits on possible pulsation amplitudes and periods that may be present in these objects in Table 5.7. Since we impose a careful requirement of considering at least two multi-hour light curves before designating a star as not observed to vary (NOV), we do not provide limits for SDSS J1518+1354, the only target in our sample that was observed on only one night. For the others, we base our quoted limits on the two longest light curves for each object alone, claiming that no pulsations are present with periods shorter than the second-longest observing run and amplitudes greater than the largest $4\langle A\rangle$ threshold value in the FT of either run.

It is worth noting that a peak in the FT of the combined runs on SDSS J1017+1217 from 30 Apr and 03 May 2016 exceeds a lower $3\langle A\rangle$ level, and we consider this feature with period 48.569 ± 0.006 min and amplitude 2.7 ± 0.5 mma suggestive.

Additional observations of any of these targets could reveal lower amplitude or longer timescale variations.

5.4 Discussion

In our search for photometric variability from nine candidate pulsating ELM WDs, we identified significant signals in five targets. However, the observed properties of some of these targets are not in agreement with the ELM WD classification.

Since ELM WDs can only form through mass transfer in close binary systems, we expect to be able to measure orbital RV variations for these stars, except in very few nearly face-on ($i \lesssim 20°$) cases. Brown et al. (2016, Section 3.4) determine that the total 11 non-RV-variable objects (eight with $T_{\rm eff}$ $< 9{,}000$ K) out of 78 targets with $\log g < 7.15$ catalogued in the ELM Survey likely represents an overabundance to a 2.5σ significance compared with expectations from a random distribution of orbital orientations. This suggests that some of these non-RV-variable objects may not be bona fide ELM WDs.

For one of the non-RV-variable ELM WD candidates, SDSS J1355+1956, we measure an exceptionally long dominant pulsation period of 4.3113 ± 0.0007 hours. Following Hansen et al. (1985), we calculate the approximate theoretical maximum allowed nonradial gravity mode pulsation period of $P_{\rm max} \approx 45$ min for a WD with the published spectroscopic parameters of this target, assuming an Eddington gray atmosphere. The observed pulsations greatly exceed this theoretical limit for surface reflection in a WD, providing additional evidence that this star is individually a false positive in the ELM Survey. This strongly supports that SDSS J1355+1956 is not a WD, and its actual surface gravity is likely less than the spectroscopically determined

value $\log g = 6.10 \pm 0.06$. With the dominant mode amplitude reaching 41.51 mma, we are likely observing pressure-mode pulsations in a high-amplitude δ Scuti—a class of pulsating star typically found in the range $6000 \lesssim T_{\rm eff} \lesssim 9000$ K (e.g., Uytterhoeven et al. 2011). However, recent analysis of the hot, lead-rich subdwarf UVO 0825+15 by Jeffery et al. (2016) provides compelling evidence for pulsation periods that exceed the Hansen et al. (1985) limit, casting some doubt on the robustness of this theoretical result. Given the large amplitude and the upper limit on RV semi-amplitude from ELM7 of $K_1 < 40.9\,{\rm km\ s^{-1}}$, the observed variability cannot be attributed to ellipsoidal variations of an ELM WD (Morris & Naftilan 1993).

Of the remaining pulsating candidate ELM WD variables, only four out of eight show RV variations in time series spectroscopy: SDSS J184037.78+642312.3 (Hermes et al. 2012a), SDSS J111215.82+111745.0, SDSS J151826.68+065813.2 (Hermes et al. 2013a), and PSR J1738+0333 (Kilic et al. 2015a). The two other new pulsating stars described in this work are not RV variables, as is the case for the previously published pulsators SDSS J161431.28+191219.4 and SDSS J222859.93+362359.6 (Hermes et al. 2013c). It is unknown whether another claimed ELMV—SDSS J161831.69+385415.15 (Bell et al. 2015b) that was identified as an ELM candidate from SDSS spectroscopy (Kepler et al. 2015)—is RV variable. We submit that none of these non-RV-variable pulsating stars have been conclusively shown to be ELMVs. Some could be in nearly face-on binary systems, but when we simulate random binary orientations, we find the

probability of four out of eight systems with $i < 20°$ to be < 0.0008.

Kepler et al. (2016) found thousands of objects with SDSS DR12 spectra that are consistent with ELM WDs that they call "sdAs," with the ELM classification requiring confirmation of RV variations. The sdAs are strongly concentrated around $T_{\rm eff} \approx 8000$ K, which is where the DA WD instability strip extends through the ELM regime. There is no evolutionary scenario that predicts such an abundance of ELM WDs at this temperature, which may highlight an inaccuracy in current spectroscopic models or their application. We suspect that SDSS J1355+1956 and some of our other non-RV-variable pulsating stars are actually members of this sdA class. This does imply that the sdAs also pulsate in or near the same region of spectroscopic parameter space, revealing the potential for distinguishing between sdAs and ELM WDs asteroseismically.

We depict the present landscape of WD pulsations in $\log g$–$T_{\rm eff}$ space in Figure 5.9. We distinguish confirmed ELMVs (yellow diamonds) from pulsating candidate ELM WDs without measured RV variations (squares). The black square corresponds to SDSS J1355+1956, with a much longer pulsation period than expected from an ELM WD. The white square is SDSS J161831.69+385415.15 (Bell et al. 2015b), which does not have available time series spectroscopy. The symbols representing objects analyzed in this work are outlined with bold black borders. We include NOVs with limits on pulsational variability ($\times$), more massive ZZ Ceti variables (triangles), and pulsating pre-ELMs (orange narrow diamonds) for context. The empirical bounds of the DA

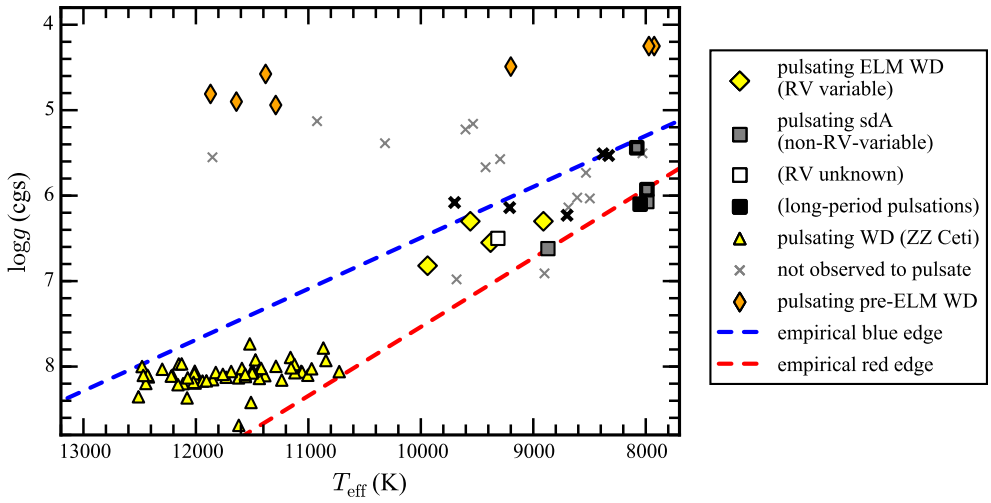

Figure 5.9: The locations of known pulsating stars with ELM-like spectra in $\log g$–$T_{\rm eff}$ space. Pulsating ELMVs confirmed with RV variations (Hermes et al. 2012a, 2013a; Kilic et al. 2015a) are indicated with yellow diamond markers. Pulsating ELM WD candidates without measured RV variations are marked with squares, including three objects from this work and the targets published in Hermes et al. (2013c) and Bell et al. (2015b). The filled black square represents SDSS J1355+1956, which cannot be a WD, and the white square is SDSS J1618+3854 (Bell et al. 2015b) that has not yet been observed with time series spectroscopy. Objects with constraints on a lack of pulsations from time series photometry are marked with $\times$ symbols (this work; Hermes et al. 2012a, 2013a,c). Pulsating pre-ELM WDs from Maxted et al. (2013, 2014); Corti et al. (2016) and Gianninas et al. (2016) are marked with orange narrow diamonds. Typical $\log g \sim 8$ ZZ Ceti pulsators from Gianninas et al. (2011), corrected for 3D convection effects (Tremblay et al. 2013), are marked with yellow triangles. The empirical DA instability strip published in Gianninas et al. (2015) is marked with dashed lines. The objects presented in this work are outlined with thicker black borders.

instability strip from Gianninas et al. (2015) are marked with dashed lines. If we redefine these boundaries based on only the confirmed ELMVs, we find a more narrow extension of the strip to low $\log g$.

We also observe variability from photometric binaries in our sample. Partial coverage of the 19.342-hour binary period of WD J0308+5140 reveals evidence of eclipses. The lower limit on the primary star radius of $R_1 \gtrsim 0.4$ $R_\odot$ is inconsistently large compared with the maximum expected radius for a cooling ELM WD. The evolutionary models of Althaus et al. (2013) give a maximum cooling-track radius of $\approx$0.13 $R_\odot$, while the Istrate et al. (2016a) models find a maximum of $\approx$0.17 $R_\odot$. However, the models with element diffusion enabled show that some ELM WDs can temporarily become much larger during CNO flashes as they settle onto their final cooling tracks (Althaus et al. 2013; Istrate et al. 2016a, and previous works referenced therein). *Kepler* photometry of the eclipsing system KIC 10657664 has demonstrated empirically that ELM WDs can be at least as large as 0.15 ± 0.01 $R_\odot$ (Carter et al. 2011). Additional photometry of WD J0308+5140 would provide some of the first precise constraints on the physical properties of sdA stars.

The presence of this false positive in the ELM Survey cautions that binary confirmation alone is not sufficient to positively identify an ELM WD. The properties of WD J0308+5140 are similar to another eclipsing system, SDSS J160036.83+272117.8, which was not included in the ELM6 sample due to eclipse durations that were inconsistent with the ELM WD classification (Wilson et al. 2015, 2017 in prep.). Only binary RV periods short enough to preclude non-degenerate stellar components ($P_{\rm orb} \lesssim 6\,{\rm hr}$), or those with supporting data as photometric binaries, should be interpreted as ELM WDs with confidence.

The other binary that we observe photometric variations of, SDSS J1054−2121, is just such a case. The ellipsoidal variation signature of $0.75 \pm 0.08\%$ amplitude is entirely consistent with that expected for a double-degenerate binary with an ELM WD primary. In future work, we will use the measured ellipsoidal variability amplitude to significantly improve our physical constraints on this system.

5.5 Summary and Conclusions

We identified nine candidate pulsating ELM WDs from the ELM Survey papers VI and VII. Each of these targets has spectroscopically determined $T_{\rm eff}$ and $\log g$ values that place them within 500 K of the empirical low-mass extension of the DA WD instability strip, which overlaps the population of sdA stars with $\langle T_{\rm eff} \rangle \approx 8000$ K. We obtained time series photometry of these systems from McDonald Observatory, most over many nights.

The following are our main results:

– Fourier analysis reveals that three targets—SDSS J1355+1956, SDSS J1735+2134, and SDSS J2139+2227—show significant pulsational variability. However, since these targets are among the few for which time series spectroscopy from ELM7 did not show the RV variations that are expected from an ELM WD, we do not consider them confirmed ELMVs.

– In particular, SDSS J1355+1956 pulsates with a dominant period of 4.3113± 0.0007 hours, far exceeding the theoretical limit for pulsations in a WD. This is likely a δ Scuti variable with an overestimated $\log g$ from spectroscopic

model fits.

– A total of 4 out of 8 other pulsating variable stars in the parameter space of ELM WDs do not show significant RV variations in time series spectroscopy. There is less than a 0.0008 probability that these are all nearly face-on ($i < 20°$) binaries. Some of these targets are likely sdA stars—a stellar population revealed in recent SDSS data releases (Kepler et al. 2016) of unclear nature.
– Our data on WD J0308+5140 reveal evidence for a deep ≈4 hr eclipse, implying that the primary star has radius $\gtrsim 0.4\ R_{\odot}$. This is not consistent with an ELM WD and demonstrates that a mere detection of RV variations is not sufficient to make this classification, though very short period binaries may exclude other classes.
– Ellipsoidal variation and Doppler beaming amplitudes measured in SDSS J1054−2121 are consistent with the ELM WD classification for this object.

We note that the remaining ambiguity of the nature of the non-RV-variable objects with ELM-like spectral lines will be largely resolved by Gaia astrometric solutions, including for all ELM Survey objects, within the next few years. This will allow us to determine not only the stellar types of individual objects, but also the relative sizes and spatial distributions of the different stellar populations that occupy this region of spectroscopic parameter space.

Chapter 6

Fishing in the sdAs: Pulsating Stars including an Extremely Low-Mass White Dwarf

The search for and characterization of pulsating extremely low-mass (ELM; $\lesssim 0.3\,M_{\odot}$) white dwarf stars was a very productive research area at the start of my work at McDonald Observatory. The senior graduate student of our research group, J. J. Hermes, had published the first five pulsating ELM white dwarf variables (ELMVs), all identified as candidates from the ELM Survey (Hermes et al. 2012a, 2013a,c). I led the continuation of this effort following his doctoral defense, and I described my results in Chapter 5 (published as Bell et al. 2017a). The main result of this work was the discovery of pulsation and eclipse timescales that imply radii that exceed the physical limits for cooling-track ELM white dwarfs near $T_{\rm eff} = 8{,}000$ K in more recent ELM Survey publications. There is also an overabundance of pulsating stars in this region of parameter space that do not show radial velocity (RV) variations expected of ELM white dwarfs given their theoretical formation in close binary systems. This implies that the ELM Survey is significantly contaminated at $T_{\rm eff} \lesssim 9{,}000$ K by stars that are larger than white dwarfs, and that spectroscopically determined $\log g$ values near this temperature may be systematically overestimated. With other stellar types being spectroscopically misclassified

as ELM white dwarfs, we adopt the more strict requirement for the positive identification of an ELM white dwarf that it is a confirmed member of a close binary from RV variations. This is a personal definition to this work and does not account for possible scenarios like mergers or ejection from a binary. This brings the number of confirmed ELMVs down to four: three from Hermes et al. (2012a, 2013a), and one more recently from Kilic et al. (2015a).

There have also been a few recent discoveries of pulsating pre-ELM stars that are still increasing in temperature as they contract toward their final cooling tracks. Maxted et al. (2013, 2014), Corti et al. (2016), Zhang et al. (2016), and Gianninas et al. (2016) all classified new pulsating variable stars as pre-ELMs. Some of these objects pulsate at higher temperatures than a simple extrapolation of the DA (hydrogen atmosphere) white dwarf instability strip to low $\log g$, which may be due to the contribution of atmospheric helium to the driving (Gianninas et al. 2016; Fontaine et al. 2017). Corti et al. (2016) suggest that their objects exist in a part of spectroscopic parameter space where they may be either pre-ELMs or high amplitude δ Scuti pulsators. While Zhang et al. (2016) claim to have observed gravity-modes in a pre-white-dwarf, the relationship they find between the rotational splitting of pulsation modes and the stellar rotation rate of the star is characteristic of pressure modes (p-modes), so they likely misidentified which binary component exhibits pulsations in this system (though p-modes are also theoretically expected in ELMs; e.g., Córsico & Althaus 2016a; Istrate et al. 2016b).

Concurrent with all of this, some exciting and unexpected results were

coming from new data releases of the Sloan Digital Sky Survey (SDSS). Fits of white dwarf atmosphere models to SDSS spectroscopy placed 376 stars in DR10 (out of 9088 with spectra consistent with new white dwarf models; Kepler et al. 2015) and 2675 in DR12 (out of 6576; Kepler et al. 2016) in the physical parameter space of ELM white dwarfs: $5.5 < \log g < 6.5$ and $T_{\rm eff} < 20{,}000\,{\rm K}$. This is a large population, in contrast to the 78 objects cataloged by the ELM Survey (67 in confirmed binary systems from RV measurements; Brown et al. 2016) that were identified as ELM candidates primarily from hot color cuts in SDSS photometry. Kepler et al. (2016) labeled these stars "sdA," which highlights their location below the main sequence without committing to a stellar evolutionary context.

A few different papers have weighed in on the potential nature of this sdA population. Pelisoli et al. (2017) propose three possible physical explanations of the sdAs (each with its own weakness): subdwarf plus main sequence binaries (yet most sdAs do not show the UV excess of a hot subdwarf); main sequence A stars with overestimated $\log g$ values (yet this would place many at high velocity in the Galactic halo, where young stars are not expected); and ELM or pre-ELM white dwarfs (but the SDSS subspectra do not show the expected RV variations of close binaries). Hermes et al. (2017a) compare colors, proper motions, and RV variations of SDSS subspectra between sdAs and confirmed ELM white dwarfs to argue that the vast majority of sdAs are *not* ELMs, based on the definition that ELM white dwarfs are all in short period binaries. Brown et al. (2017) published a thorough investigation of 22

sdA stars, demonstrating that many sdAs found to eclipse by Ingrid Pelisoli (private communication) in Catalina Sky Survey data (Drake et al. 2009) are consistent with metal-poor main sequence A stars. They did not consider pre-ELM stars that are converging to their white dwarf cooling tracks. Comparing pure-hydrogen white dwarf model atmospheres to metal-poor main sequence models, they demonstrate a systematic offset of $\sim +0.6$ dex in $\log g$ near the empirical $7000\,\mathrm{K} < T_{\mathrm{eff}} < 9000\,\mathrm{K}$ range of sdAs. They argue that only $\sim 1\%$ of the sdAs are ELMs, but this fraction is still contentious in the white dwarf community, especially since the authors of the original SDSS classification found that the majority of these spectra are specifically not consistent with main-sequence models.

The results from Bell et al. (2017a, and Chapter 5) demonstrate that objects other than cooling-track ELM white dwarfs in this region of spectroscopic parameter space also pulsate. I decided to obtain similar observations of some sdA stars with spectroscopic parameters that place them in or near the empirical low-mass extension of the DAV (hydrogen atmosphere pulsating white dwarf) instability strip. I intend to submit a revised version of this chapter for refereed publication following the defense of this thesis in July 2017, but for now I present only a preliminary analysis. I describe the observations and targets in Section 6.1. In Section 6.2, I characterize and interpret the observational properties of six new variable sdAs. I highlight a couple of noteworthy targets that we do not unambiguously detect pulsations from in Section 6.3 and look forward to future developments in our understanding of

sdA stars in Section 6.4.

6.1 Time Series Photometric Observations

Unlike the systematic evaluation of photometric variability of ELM Survey objects described in Bell et al. (2017a, and Chapter 5), it was not practical to carry out such an exhaustive study of the thousands of sdA stars revealed from recent SDSS data releases. Instead, observations were made in a mode that we call "fishing," and selection of sdA targets was influenced by many complicated, non-uniform factors. Following the SDSS DR12 release, which provided many bright ($g < 17$) sdAs near the empirical DAV instability strip, this project became largely our go-to backup for nights with poor seeing or transparency conditions that prevented us from observing fainter or shorter-timescale variables. B. G. Castanheira, Z. Vanderbosh, D. E. Winget, and K. I. Winget all contributed observations to this effort on targets that they individually selected while covering some of my allotted observing time on the 2.1-meter Otto Struve Telescope at McDonald Observatory. The target selection carries the complex biases of these observers and myself as we respond to changing observing conditions on the mountain. Furthermore, with the P.I. of the SDSS spectroscopic classification effort, S. O. Kepler, as a close collaborator and thesis committee member, I received preliminary parameters from pure-hydrogen atmosphere fits to the SDSS DR12 spectra before they were published, while our target selection following May 2016 was informed by still-unpublished parameters from solar-metallicity model fits (described

by Pelisoli et al. 2017). The shift in parameters between pure-hydrogen and solar-z fits moves some targets significantly in $\log g$–$T_{\rm eff}$ space. For all of these reasons, the final set of sdA stars that we observed is quite varied in atmospheric properties.

In total, we observed 24 sdA targets from McDonald Observatory. Their atmospheric parameters from pure-H and solar-z fits are given in Table 6.1. The quoted uncertainties are the formal, intrinsic uncertainties from the model fits. There are also extrinsic uncertainties in these parameters that should be added in quadrature, which Liebert et al. (2005) find to be of-order 1.2% in $T_{\rm eff}$ and 0.038 dex in $\log g$. We plot the best-fit parameters determined using both sets of models in $\log g$–$T_{\rm eff}$ space in Figure 6.1. The figure caption describes the various other objects that we included for context.

We note than the average shift from pure-H to solar-z parameters is not systematic in $\log g$as Brown et al. (2017) predicted, which does not directly support their explanation of sdAs as main sequence A stars.

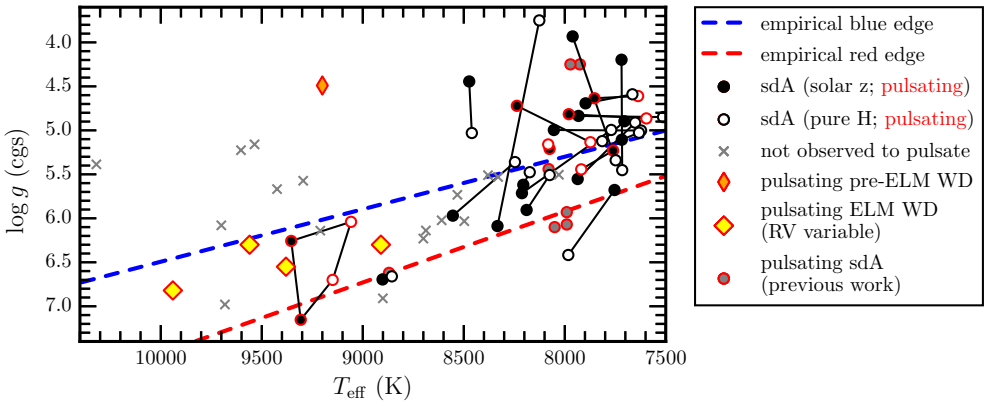

Figure 6.1: Positions of observed candidate pulsating sdAs in spectroscopic $\log g$–$T_{\rm eff}$ space. Black filled circles mark the parameters determined from solar-z models, while white filled circles are from pure-H models. Parameters determined for the same object are connected by lines. Circles outlined in red are new pulsating stars from this work. The diamonds mark ELMVs confirmed from RV variation measurements (Hermes et al. 2012a, 2013a; Kilic et al. 2015a). Gray circles mark previously published pulsating stars either without time series spectroscopic observations (Corti et al. 2016) or with no detected RV variation signals (Hermes et al. 2013c; Bell et al. 2017a).

Table 6.1. sdA Spectroscopic Parameters

SDSS	Plate-MJD-Fiber	$T_{\rm eff}$ (K; solar z)	$\log g$ (cgs; solar z)	$T_{\rm eff}$ (K; pure H)	$\log g$ (cgs; pure H)
J123831.40-014654.26	0335-52000-0497	7932(17)	4.836(0.081)	7864	5.03
J131011.61-014232.96	0340-51990-0426	8237(10)	4.721(0.060)	8224	5.33
J221524.54-005018.19	0374-51791-0131	7719(0)	4.197(0.000)	7838	5.72
J090804.54-000208.76	0470-51929-0076	8168(10)	5.039(0.036)	8130	5.33
J091416.42+004146.8	0472-51955-0499	8417(20)	5.883(0.081)	8440	5.71
J093003.42+054815.5	0992-52644-0435	8760(37)	6.240(0.105)	8656	5.52
J074939.74+194203.5	1582-52939-0406	7846(32)	5.958(0.094)	8042	6.71
J162953.16+220634.5	1658-53240-0584	8087(35)	5.833(0.122)	8057	5.08
J160410.81+062705.51	1729-53858-0213	7969(9)	5.473(0.039)	8097	5.71
J082900.96+084645.4	1758-53084-0449	8394(25)	5.995(0.100)	8195	5.16
J140119.77+351323.15	1838-53467-0506	8054(19)	4.996(0.094)	7908	5.21
J192253.84+783959.09	1857-53182-0494	7980(10)	5.328(0.032)	7904	5.24
J233258.96+490400.32	1888-53239-0477	8323(12)	6.210(0.036)	8283	5.77
J223831.92+125318.32	1892-53238-0249	7980(11)	4.816(0.056)	7999	5.03
J114224.61+374703.65	1997-53442-0225	8075(9)	5.211(0.037)	8082	5.16
J093356.45+191601.5	2361-53762-0308	8333(39)	6.088(0.127)	8126	3.75
J083054.47-035118.94	2807-54433-0499	8473(8)	4.444(0.042)	8460	5.03
J113143.46-074220.49	2861-54583-0078	7853(12)	4.635(0.064)	7637	4.61
J045309.80-041800.66	3123-54741-0483	7897(7)	4.693(0.042)	7665	4.59
J074013.22+481036.70	3668-55478-0370	7961(5)	3.932(0.021)	7748	5.34
J075644.33+502741.16	3679-55209-0229	7108(7)	4.045(0.027)	6875	5.34
J223716.61+052228.33	4291-55525-0872	8902(40)	6.695(0.017)	8856	6.66
J161831.69+385415.15	5189-56074-0177	9307(70)	7.153(0.096)	9149	6.70
J161831.69+385415.15[a]	5199-56067-0744	9354(54)	6.257(0.075)	9058	6.04

[a]This is a second, lower-S/N SDSS spectrum of the same object as above.

A full journal of the sdA targets that we observed from McDonald Observatory is provided in Table 6.2. Six new pulsating stars of particular interest appear above the horizontal line, and our null results are listed lower in the table. We observed each of these stars with the ProEM frame-transfer CCD camera at Cassegrain focus on the McDonald Observatory 2.1-meter Otto Struve Telescope through a red-cutoff BG40 filter to reduce sky noise. We obtained dark and dome flatfield calibration frames at the start of each night, which we use to reduce the science images with standard IRAF tasks. We then perform circular aperture photometry for the target and available comparison stars in the field with CCD_HSP (Kanaan et al. 2002) for a range of apertures of size 2–10 pixels (0.76–3.8″ at 4×4 binning). We divide the measured target by comparison star flux with WQED, which also applies a barycentric correction to the timestamps so that we can combine runs that span multiple nights. We perform our final analyses on the light curves from apertures that yield the highest signal-to-noise ratio in the Fourier transform.

6.2 Pulsating sdA Stars

The first six objects listed in Table 6.2 all exhibit clear pulsation signatures in our photometry. In this section, we use Fourier analysis to measure the pulsation frequencies of these stars and discuss their likely classifications. All Fourier transforms (FTs) were computed with the PERIOD04 software (Lenz & Breger 2004).

Table 6.2: Journal of Observations

SDSS	Date (UTC)	Exposure Time (s)	Run Duration (h)
J1618+3854	23 Apr 2014	20	6.5
	24 Apr 2014	25	6.4
	22 May 2014	30	1.0
	22 May 2014	20	3.9
	24 May 2014	30	2.6
	25 May 2014	30	5.9
	27 May 2014	30	7.8
	21 Apr 2015	20	4.6
	26 Apr 2015	30	5.7
	20 May 2015	20	3.2
	26 May 2015	30	7.7
J1131-0742	19 Jan 2015	10	3.7
	20 Jan 2015	5	5.0
J0756+5027	11 Feb 2015	1	7.1
J1142+3747	25 Apr 2015	3	2.0
	22 May 2017	15	3.2
	24 May 2017	30	3.2
J2238+1253	11 Aug 2015	5	4.5
	12 Aug 2015	5	1.6
	13 Aug 2015	5	0.8
	14 Aug 2015	3	5.1
	16 Aug 2015	3	1.0
J1604+0627	14 Sep 2015	3	1.7
	16 Sep 2015	5	2.3
	06 Jul 2016	1	3.1
J2237+0522	25 Jun 2014	30	3.2
	26 Jun 2014	30	3.0
	12 Sep 2015	60	5.0
	13 Sep 2015	20	6.1
J0453-0418	24 Jan 2015	10	2.7
J0830-0351	24 Jan 2015	10	2.5
J0740+4810	26 Jan 2015	15	3.6

Table 6.2 (cont'd): Journal of Observations

SDSS	Date (UTC)	Exposure Time (s)	Run Duration (h)
J1310-0142	14 Mar 2015	10	3.4
J1238-0146	15 Mar 2015	30	3.3
J1512-0303	25 Apr 2015	3	2.8
J0908-0002	26 Apr 2015	3	2.8
J2215-0050	14 Sep 2015	20	5.2
	15 Sep 2015	5	6.3
J2332+4904	16 Sep 2015	5	5.6
J1922+7839	17 Sep 2015	3	3.9
J1401+3513	07 Jan 2016	5	2.5
J1629+2206	06 Aug 2016	5	4.0
	07 Aug 2016	5	4.7
J0749+1942	28 Nov 2016	10	1.5
	28 Nov 2016	30	2.5
	29 Nov 2016	20	3.1
J0829+0846	01 Jan 2017	10	2.0
	02 Jan 2017	10	4.8
J0914+0041	20 Jan 2017	5	1.3
	20 Jan 2017	5	1.1
J0933+1916	26 Jan 2017	20	3.7
J0930+0548	03 Mar 2017	14	3.0

6.2.1 SDSS J1618+3854

SDSS J161831.69+385415.1 (hereafter SDSS J1618+3854) was the first candidate ELMV that I identified from the SDSS DR10 spectroscopic sample. This data release contained two spectra for this object, and the weighted mean parameters are $T_{\rm eff} = 9144 \pm 56\,{\rm K}$ and $\log g = 6.83 \pm 0.13$. If we apply the corrections from the 3D convection models of Tremblay et al. (2015), these become $T_{\rm eff} = 8939\,{\rm K}$ and $\log g = 6.54$.

We confirmed SDSS J1618+3854 as a pulsating variable star on 23 Apr 2014 and have observed it on a total of 10 nights. I presented this work as a poster at the 19th European White Dwarf Workshop in Montréal in August 2014 and published it as the sixth discovery of an ELMV in the conference proceedings (Bell et al. 2015b). We kept after the target hoping to obtain robust constraints on convection from nonlinear light-curve fitting, as was previewed in those proceedings, but the conditions were never good enough for a long observing stretch for me to complete this project. The discovery data are still the most useful, since the cycle count ambiguities associated with long gaps between later runs cause messy spectral windows. Figure 6.2 displays the light curves from Apr 2014.

The Fourier transform of the August 2014 light curve of SDSS J1618+3854 is displayed in Figure 6.3. We mark five significant signals, the properties of which are listed in Table 6.3. Two frequencies correspond to independent pulsation modes, while the other three are

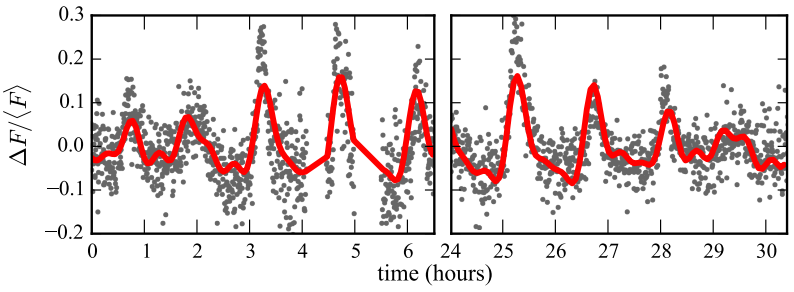

Figure 6.2: April 2014 observations of SDSS J1618+3854 with the best fit solution overlaid.

Table 6.3. Pulsation Properties of SDSS J1618+3854

Mode ID	Frequency (μHz)	Period (s)	Amplitude (%)
f_1	202.61(15)	4936(4)	6.19(19)
f_2	162.8(3)	6143(11)	3.35(19)
$f_1 + f_2$	365.4(3)	2740(20)	2.68(19)
$2f_1$	405.2(3)	2468(18)	2.66(19)
$2f_1 + f_2$	568.0(4)	1761(12)	1.88(19)

harmonics or combination frequencies.

This object is most likely a bona fide ELMV. One of the SDSS spectra

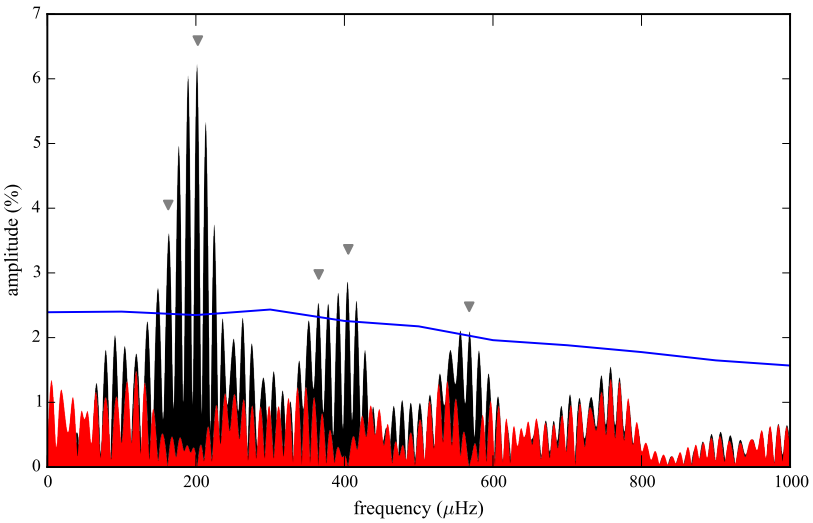

Figure 6.3: Fourier transform (FT) of the April 2014 light curve of SDSS J1618+3854 displayed in Figure 6.2. The significant peaks are marked with triangles, and the FT of the residuals (red) and final significance threshold (blue) are also displayed.

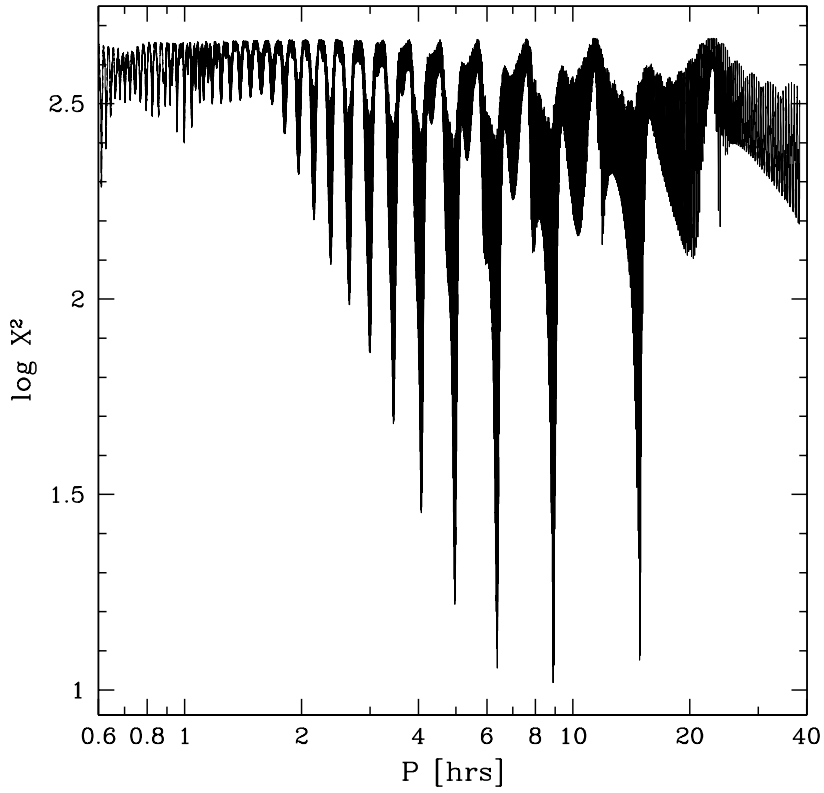

Figure 6.4: χ^2 versus orbital period for MMT RV measurements of SDSS J1618+3854. There are four significant period aliases that are described in Table 6.4. The phase folded RV curve of the strongest alias is plotted in Figure 6.5.

yields a RV measurement for SDSS J1618+3854 of $15 \pm 16\,\mathrm{km\,s^{-1}}$, while the other is at $-136\,\mathrm{km\,s^{-1}}$, indicating that it is clearly RV variable (S. O. Kepler, I. Pelisoli, private communication). My collaborator Warren Brown acquired another spectrum in March 2017 that showed a RV of $-224 \pm 15\,\mathrm{km\,s^{-1}}$ from MMT. He followed this up in June 2017, obtaining ten more spectra over three nights. The data reveal clear RV variations, but with four significant aliases.

Table 6.4. Significant Period Aliases of SDSS J1618+3854 MMT RV Data

Period (days)	K ($\mathrm{km\,s^{-1}}$)
0.20785	219 ± 12
0.26628	244 ± 14
0.37196	292 ± 20
0.6225	419 ± 36

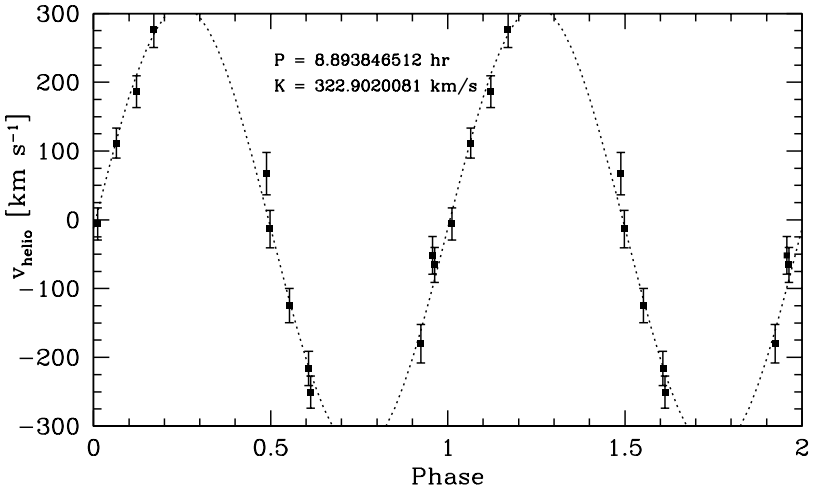

Figure 6.5: MMT RV measurements of SDSS J1618+3854 folded on the strongest period alias.

Warren's plot of χ^2 versus orbital period is displayed in Figure 6.4, and the best-fit properties of the competing solutions are listed in Table 6.4. A phase-folded RV curve of the strongest signal is plotted in Figure 6.5. Because of the strong aliasing, each of these solutions will have to be considered in our final analysis, and we may be able to dismiss some on physical grounds.

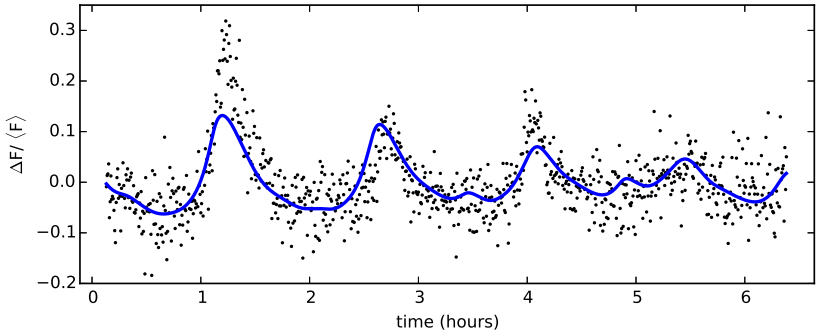

Figure 6.6: Best fit model of the pulsational nonlinearities of SDSS J1618+3854 to the 24 April 2014 light curve using the tools of Montgomery (2005). Figure from Bell et al. (2015b).

My advisor Mike Montgomery developed tools for fitting models of the parameterized response of white dwarf convection zones to the temperature variations of stellar pulsations (2005). I recognized an exciting opportunity to constrain the behavior of convection in a new physical regime from the nonlinear pulsation behavior of this ELMV. We explored this some in the conference proceedings that announced the discovery of this new ELMV (Bell et al. 2015b). The parameterized response of the convective timescale to temperature variations is expressed as $\tau_C = \tau_0 T_{\rm eff}^{-N}$. The results of a preliminary fit to the April and May 2014 light curves gave $N = 92$ and $\tau_0 = 810\,{\rm s}$ for a star with a pulsational axis inclined to $i = 87°$. This model is plotted over the April 2014 light curve in Figure 6.6 (borrowed from Bell et al. 2015b). These values seem reasonable, with N falling in the typical range of 90–95 found for other DAVs, with a longer value of τ_0, as expected for cooler white dwarfs. Despite this, we were concerned about how robust these results were with the data

in hand, and we were never quite able to obtain better observations on this target than the original discovery data. This is still a most promising object for exploring the temperature-response of convection in ELM white dwarfs.

6.2.2 SDSS J1131-0742

I selected SDSS J113143.46-074220.49 (hereafter SDSS J1131-0742) as a target based on excess scatter in the Catalina Sky Survey (CSS; Drake et al. 2009) data on this object. Observations over two nights in January 2015 confirmed this as a pulsating variable star. Figure 6.7 displays the light curves from these two nights. Figure 6.8 shows the corresponding FT, and the properties of the marked significant signals are listed in Table 6.5. The overall peak-to-peak variations are as large as 60%! If this is an ELMV, it would be by far the most dramatic example of its class. The measured $\log g$ of 4.6 is, however, at the low end for the sdAs, so this is more likely either a pulsating pre-ELM or a main sequence star with a slightly overestimated $\log g$—this exact ambiguity of classification was the main conclusion for the objects described in Corti et al. (2016).

From discussions with Michel Breger, UT's local expert on δ Scuti stars, this light curve is reminiscent of a high amplitude δ Scuti (HADS). These stars include the SX Phoenicis variables that Corti et al. (2016) propose as an alternate classification for their pre-ELM pulsator candidates. In fact, SDSS J1131-0742 was classified as a δ Scuti by Palaversa et al. (2013) based on data from the LINEAR survey. This is a readily tested hypothesis for this

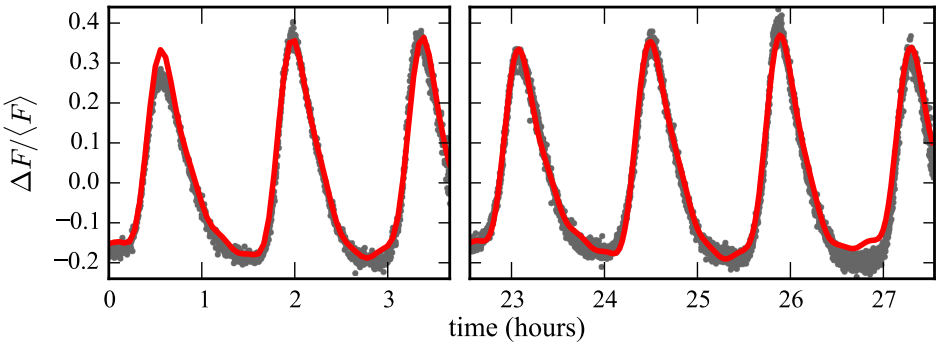

Figure 6.7: Light curve of SDSS J1131-0742 from two nights in January 2015.

star, since HADS variables have well defined period ratios between their two dominant modes. The ratio of the radial fundamental mode period to its first overtone will be in the range 0.76–0.80 for a HADS star, with some dependence on fundamental period and metallicity (Poretti et al. 2005; Pigulski et al. 2006).

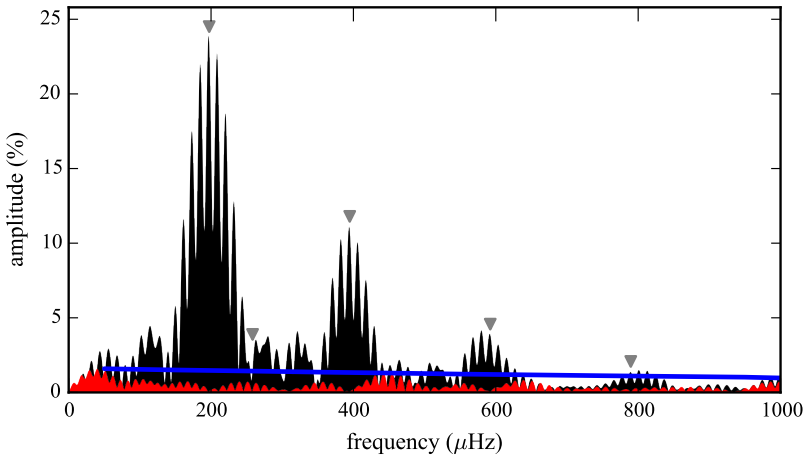

Figure 6.8: FT of SDSS J1131-0742 light curves from January 2015.

Table 6.5. Pulsation Properties of SDSS J1131-0742

Mode ID	Frequency (μHz)	Period (s)	Amplitude (%)
f_1	197.402(11)	5065.8(3)	23.21(5)
f_2	162.8(3)	6143(11)	1.89(5)
$2f_1$	394.80(2)	2532.90(15)	8.79(5)
$3f_1$	592.21(3)	1688.60(10)	3.58(5)
$4f_1$	789.61(5)	1266.45(7)	1.57(5)

The ratio of the two independent mode periods listed in Table 6.5 is above this range at 0.8246 ± 0.0016. However, due to gaps in the ground based data, it is possible that we have selected an incorrect alias for one or both of these modes by the daily aliasing gap of $\sim 11.6\,\mu$Hz (Chapter 8 demonstrates how common this is). Selecting different plausible aliases in this case does not support a likely ratio in the HADS range.

Being consistent with pulsations in HADS stars does not rule out all other classifications. Models of pre-ELMs evolve through this region of spectroscopic parameter space before settling onto their final cooling tracks. Evolutionary models suggest that some loop through this space repeatedly during a sequence of CNO flashes that burn residual hydrogen—those with masses $0.18\,M_\odot \lesssim M_{\rm WD} \lesssim 0.4\,M_\odot$ in the models of Althaus et al. (2013). Córsico & Althaus (2014a) carried out a pulsational analysis of those models, including for one star that is undergoing a CNO flash. These CNO flashes are short lived and therefore objects in this evolutionary stage should be found only

rarely, yet they have interesting structures and pulsation properties. During the flash, a second convective region is established between the helium core and the hydrogen envelope as the star swells in size, and nonadiabatic analysis of Córsico & Althaus (2014a) finds that only well separated modes that are trapped in the outer hydrogen envelope are strongly driven to observable amplitude at long periods. These modes could have characteristic period ratios analogous to the HADS stars that are sensitive to the evolutionary stage of pre-ELMs and their remaining hydrogen content. For the one model that they analyze in detail, Córsico & Althaus (2014a) measure a period ratio of ≈ 0.68, but a more complete analysis of how this ratio varies across their model grid would be quite valuable to assess the diagnostic potential.

The most recent graduate student to join the white dwarf group at UT-Austin, Zach Vanderbosch, recently added an automated filter wheel to the ProEM camera setup so that we can now take multi-color time series data. SDSS J1131-0742 was one of the targets of his second year defense and masters thesis observations. He compared the amplitudes of pulsations as measured through different filters to test whether the variations are consistent with gravity-modes in a cooling-track ELM white dwarf. He concluded that the measured r-band to g-band amplitude ratio for the primary mode of 0.690 ± 0.003 was not consistent with expectations from theoretical models and did not support this hypothesis.

I asked my collaborator Warren Brown if he could obtain some time series spectroscopy on SDSS J1131-0742 to search for a binary companion.

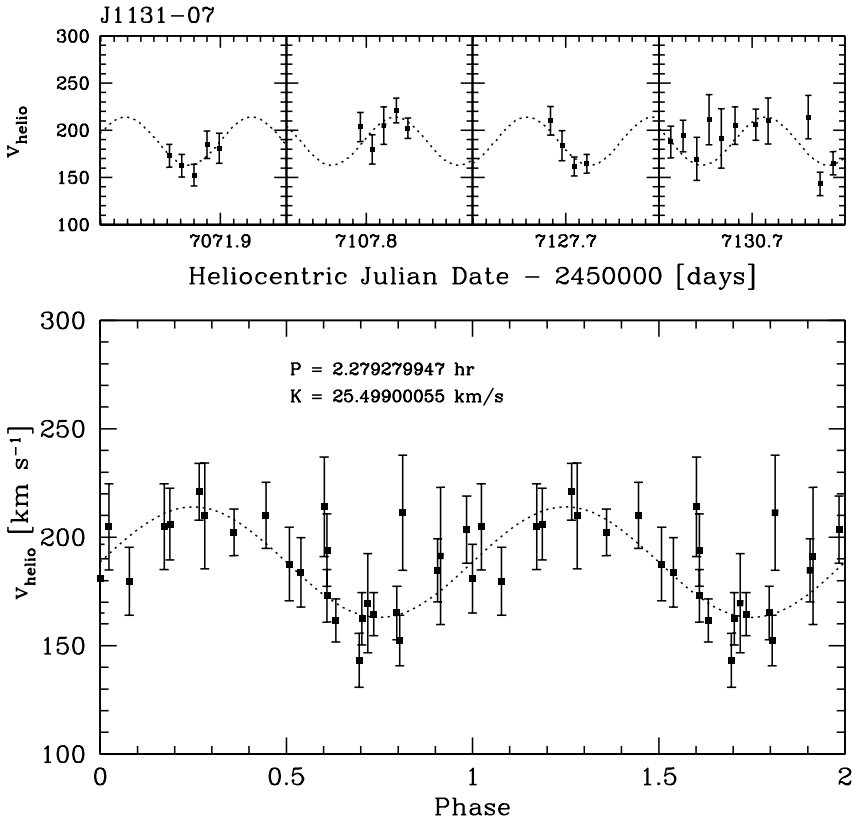

Figure 6.9: RV measures of SDSS J1131-0742 from Warren Brown.

The RV measurements across four nights are displayed in the top panels of Figure 6.9. The data were obtained with the FAST instrument on the 1.5 m at Mt. Hopkins. The bottom panel shows the data folded on the most compelling period of 2.28 hr, but this signal is not significant and the data are consistent with a constant value. Ingrid Pelisoli (private communication) has also obtained a few hours of time series spectroscopy on this target from SOAR that suggest an approximate orbital period of 4.67 hr (4.58 hr if she includes Warren's measurements in the period search).

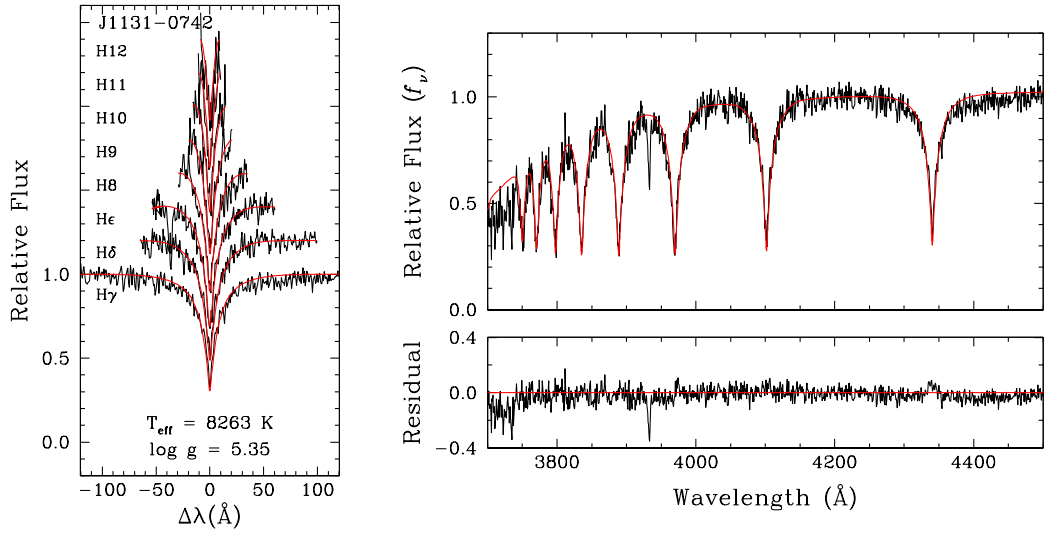

Figure 6.10: Alex Gianninas' best fit model to the FAST spectrum of SDSS J1131-0742.

I asked Alex Gianninas to fit his models to the Mt. Hopkins spectrum of SDSS J1131-0742 to get independent atmospheric parameters. Figure 6.10 displays the best fit model over the observed spectrum that yields parameters $T_{\rm eff} = 8260 \pm 130\,{\rm K}$ and $\log g = 5.35 \pm 0.13$. This $\log g$ value is higher than that determined from the SDSS spectrum, lending more weight to the pulsating pre-ELM hypothesis. The spectrum does not appear to be strongly contaminated by metal lines.

Finally, these objects must be placed in a Galactic context, which I will do for the final, published analysis. S. O. Kepler used SDSS J1131-0742 to emphasize this point to me. A $\delta Scuti$ (A star) is roughly $100\times$ more luminous than an ELM white dwarf, and therefore $10\times$ further away for a given apparent magnitude. With a galactic latitude of $b = 50^\circ$ and a measured g magnitude

of 15.95, SDSS J1131-0742 would be approximately 4600 pc above the disk if it were an A star. Based on its measured radial velocity and proper motion from the APOP catalog (Qi et al. 2015), it would take ∼10 Gyr to reach this distance from the plane—far exceeding the the main sequence lifetime of an A star!

6.2.3 SDSS J0756+5027

Like SDSS J1131-0742, SDSS J075644.33+502741.16 (SDSS J0756+5027) was selected as an observing target based on significant excess scatter in the Catalina Sky Survey data (Drake et al. 2009). Our single light curve from the night of 11 Feb 2015 in Figure 6.11 shows changes of more than a factor of two in brightness. Even with more than seven hours of coverage, we do not observe a complete period of the dominant pulsation mode.

Using the online periodogram feature of the Catalina Sky Survey DR2

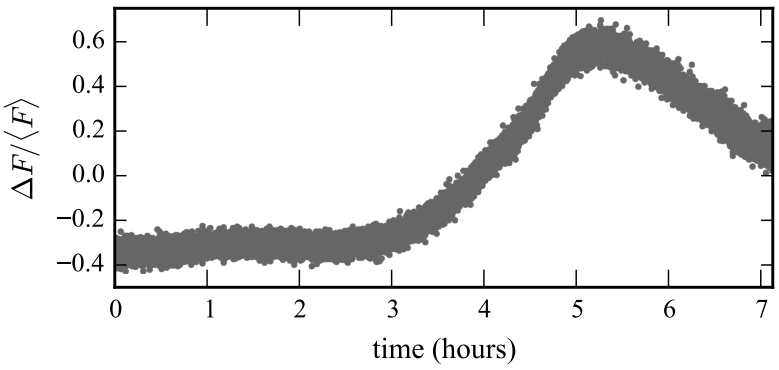

Figure 6.11: Light curve of SDSS J0756+5027 from McDonald Observatory on 11 Feb 2015.

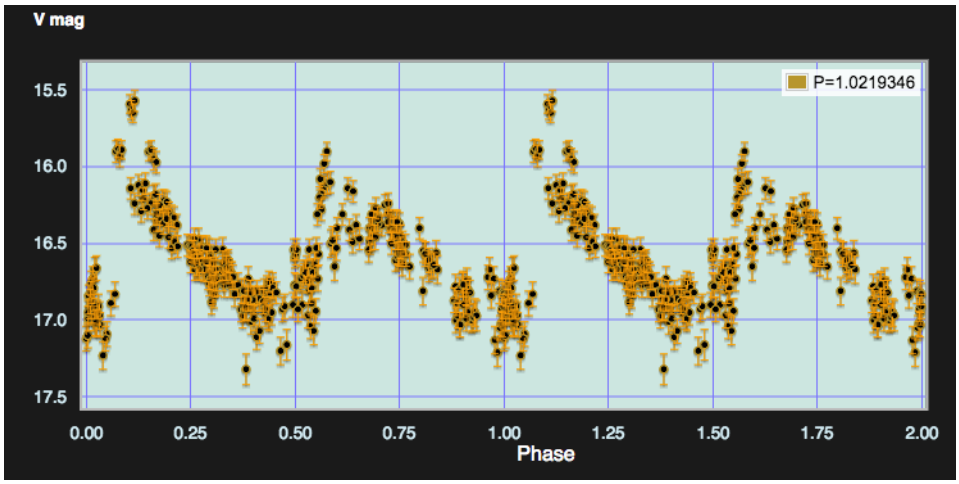

Figure 6.12: Phase folded CSS data on SDSS J0756+5027.

website[1] reveals a strong periodicity of roughly 29.3 hours. The CSS data, folded on this period, are displayed in Figure 6.12.

These pulsations are reminiscent in morphology to the photometric variations of RR-Lyrae stars. S. O. Kepler suggested that this object could be physically similar to the 0.26 $M_{\odot}$ star that exhibits RR-Lyrae-like pulsation described by Pietrzyński et al. (2012)—the recent product of mass transfer in a system that will eventually evolve to become a double-degenerate binary. Karczmarek et al. (2017) explore the theoretical properties and context of such binary mass-transfer products.

6.2.4 SDSS J1142+3747

Our 2-hour run from April 2015 showed some marginal evidence of photometric variability in SDSS J114224.61+374703.65 (SDSS J1142+3747). Based on this light curve, we decided to revisit this object during two nights in May 2017. These two nights of data are displayed in Figure 6.13. The Fourier

[1] `http://nesssi.cacr.caltech.edu/DataRelease/`

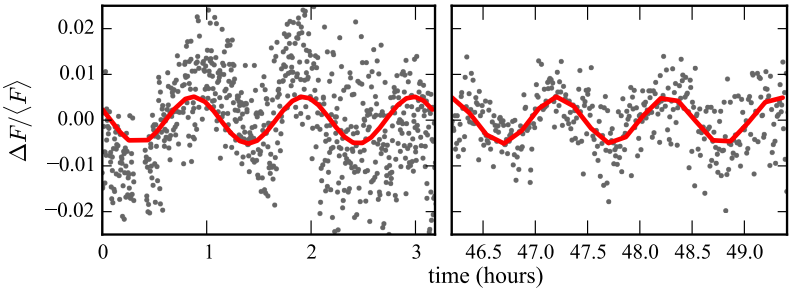

Figure 6.13: Light curve of SDSS J1142+3747 from two nights in May 2017.

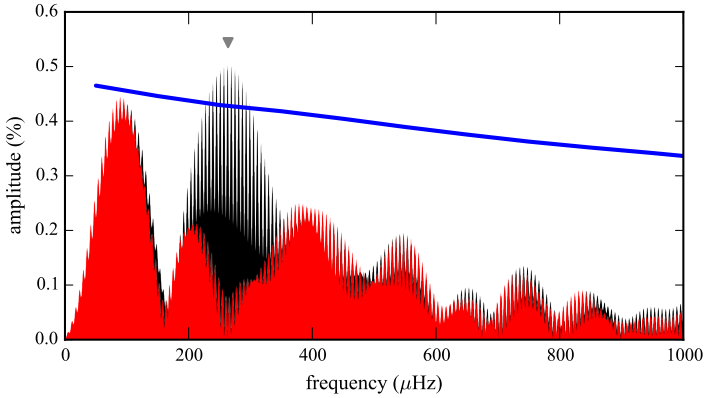

Figure 6.14: FT from two nights of data on SDSS J1142+3747 in May 2017.

transform is displayed in Figure 6.14. We detect only a single significant periodicity in these data, the strongest alias of which is at $263.8 \pm 0.2\,\mu$Hz (3791 ± 3 s period) with an amplitude of $0.51 \pm 0.04\%$. With only a single period detected, this data set is not of great asteroseismic value, but more data could reveal additional periodicities. The period detected is consistent with pulsations calculated for ELM white dwarf models (e.g., Córsico & Althaus 2014a). Alternatively, this could be the signature of ellipsoidal variations (photometric variations as the projected area of a tidally stretched star changes along its binary orbit), which are commonly observed from ELM white dwarfs in tight binary systems (Chapter 7; Hermes et al. 2014b; Bell et al. 2017a). Warren Brown obtained time series spectroscopy on this target from the 1.5-m FLWO telescope in June 2017 covering 2.1 hours (twice the photometric period) to test this hypothesis, and did not detect significant variations to the $\sim$10 km s^{-1} level, which rules against ellipsoidal variations. However, the high-S/N summed FLWO spectrum SDSS J1142+3747 does reveal a bounty of metal lines. This is perhaps a Am (metallic) or Ap (peculiar) star and a full abundance analysis may be more appropriate than the hydrogen-line fits that have been used to classify this target so far.

6.2.5 SDSS J2238+1253

SDSS J223831.92+125318.32 (SDSS J2238+1253) is similar to the previous object in that it exhibits a single significant periodicity with a similar period. Figure 6.15 displays the light curves obtained over five nights in Au-

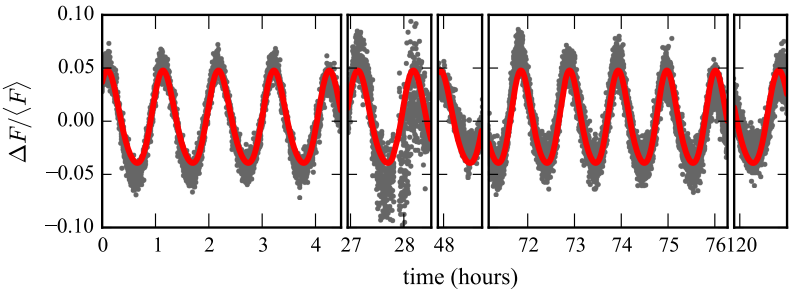

Figure 6.15: SDSSJ2238+1253 light curve.

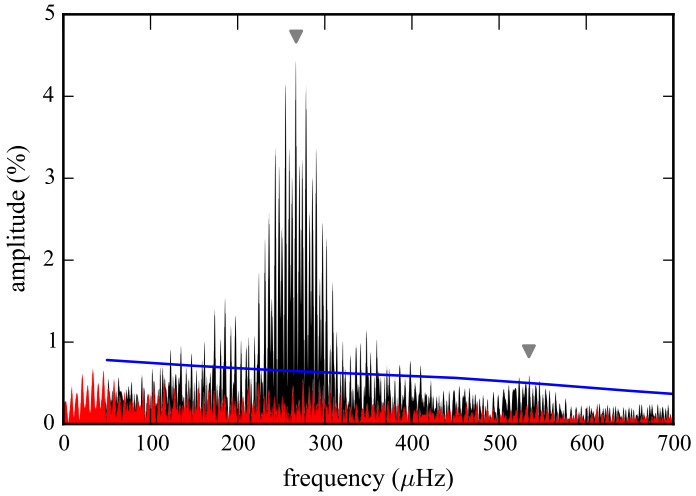

Figure 6.16: SDSSJ2238+1253 FT.

gust 2015. Figure 6.16 shows the FT of these data. The two marked signals are the main periodicity and its second harmonic: $f_1 = 267.114 \pm 0.005\,\mu$Hz ($3743.72 \pm 0.07$ s periodicity) with an amplitude of $4.329 \pm 0.018\%$ (harmonic amplitude at $0.488 \pm 0.018\%$). This solution is plotted over the data in Figure 6.15.

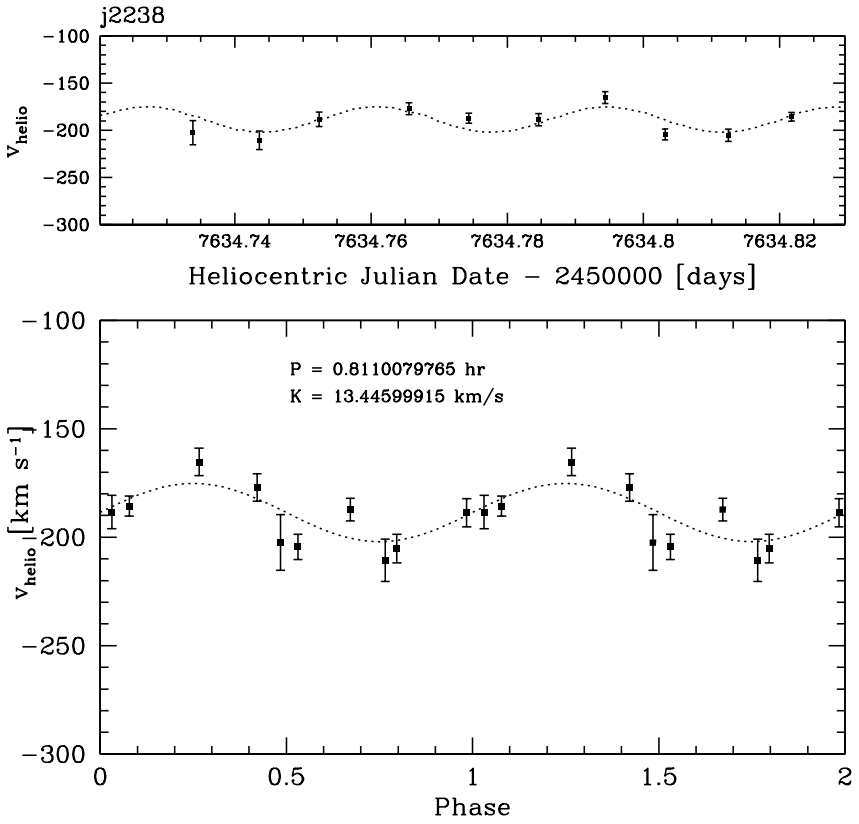

Figure 6.17: RV measurements of SDSS J2238+1253 from Warren Brown.

As with SDSS J1142+3747, a single independent frequency of photometric variability could be caused by ellipsoidal variations (although this would be a large amplitude for tidal distortion of an ELM white dwarf, a pre-ELM could plausibly show such a large signal). I asked Warren Brown to obtain time series spectroscopy covering the candidate 2.08 hr orbital period. The RV measurements are displayed in Figure 6.17. We do not detect a significant RV signal in these data, supporting the idea that the photometric variations of SDSS J2238+1253 are caused by stellar pulsations.

6.2.6 SDSS J1604+0627

The photometric variability that we observed in SDSS J160410.81+062705.51 (SDSS J1604+0627) is quite different in character from the other new variable sdAs. The single frequency of significant photometric variability that we detect in this star is quite high at $3651.35 \pm 0.19\,\mu$Hz (273.871 ± 0.014 s) with amplitude $0.37 \pm 0.02\%$. To help make the pulsations visible to the eye, we plot a running average over 10 adjacent measurements in the light curves displayed in Figure 6.18. The single significant periodicity that we detect is apparent in the Fourier transform plotted in Figure 6.19, and we overlay this solution on the data in Figure 6.18.

There are only a couple of known types of pulsating star that show this short of period. The spectral lines are too narrow for this to be a low-order g-mode in a pulsating white dwarf of typical mass. Rapidly Oscillating Ap stars (roAp) exhibit short, high-overtone p-mode periods, but a periodicity as short as 274 s has never been observed (Kurtz et al. 2006). Pressure modes in hot subdwarfs could show such short periodicities. In fact, Pelisoli et al. (2017)

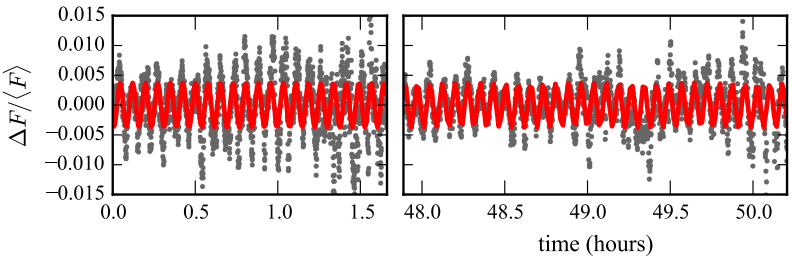

Figure 6.18: SDSSJ1604+0627 light curve.

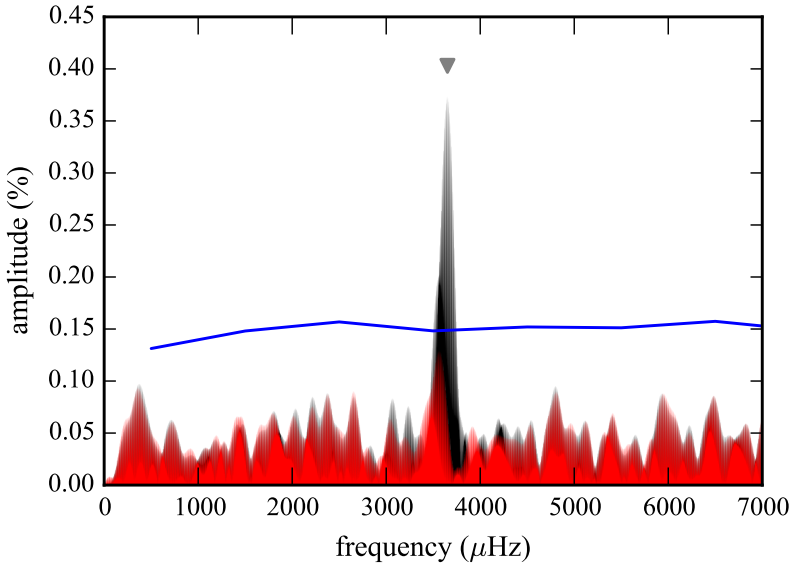

Figure 6.19: SDSSJ1604+0627 FT.

suggested that some sdAs may be binaries that contain a sdB star. These stars must be hotter than the zero-age horizontal branch, typically $\gtrsim$ 20,000 K, and therefore they will have a flux excess in the UV. Model fits to Balmer lines usually admit two solutions: a hot and cool solution. Multi-passband photometry is usually used to select between these. For SDSS J1604+0627, the hot solution gives $T_{\rm eff} = 19950 \pm 90$ K, which could plausibly correspond to a sdB star, but the GALEX nuv - g color (nuv$-g$) ≈ 2.79 is too large to be consistent with the subdwarf hypothesis.

The nonadiabatic pulsation analysis of ELM white dwarf models by Córsico & Althaus (2016a) suggests that this short period could correspond to low-k g-modes in ELMVs that likely require contributions to the driving

from the ϵ-mechanism to become unstable (Córsico & Althaus 2014b). Alternatively, this period is consistent with p-modes in pulsation calculations for pre-ELM models (Istrate et al. 2016b). The lack of longer period g-modes suggest that this star may fall in a narrow temperature range to the hot edge of the instability strip where only p-modes are unstable (e.g., Córsico & Althaus 2014a).

Finally, I note that the ELMV SDSS J1112+1117 exhibits pulsations with periods 108 s and 134 s that have been suggested to be p-mode pulsations (Hermes et al. 2013a). As we consider objects of lower $\log g$, these modes generally move to longer period, which could be what we are observing in SDSS J1604+0627.

6.3 Null Detections of Note

Having observed the majority of the non-variable targets only once, I do not feel comfortable assigning limits on the variability of most of these objects. These stars could easily have pulsation amplitudes that exceed the noise in their FTs if closely spaced modes with beat cycles exceeding the observing run durations happen to be destructively interfering during our observations. This cannot explain all of the null detections, so I infer that the majority of these objects are not high amplitude pulsators. I explore only a couple remaining objects in more detail in this manuscript because they do show some evidence of photometric variability.

6.3.1 SDSS J1310-0142

I obtained a single photometric run on SDSS J1310-0142 on 14 March 2015. The light curve and FT displayed in Figure 6.20 show compelling signs of multi-periodic variability. With such a short light curve, we likely have not resolved the individual pulsation frequencies in this target. We hope to obtain more coverage of this star during our next observing run (Zach Vanderbosch, private communication) to confirm and constrain its pulsation periods. Since parameters from the solar-metallicity fit to the SDSS spectrum of SDSS J1310-0142 yield a lower-log g value of 4.72 ± 0.06, it is plausible that this particular target may be a δ Scuti type variable.

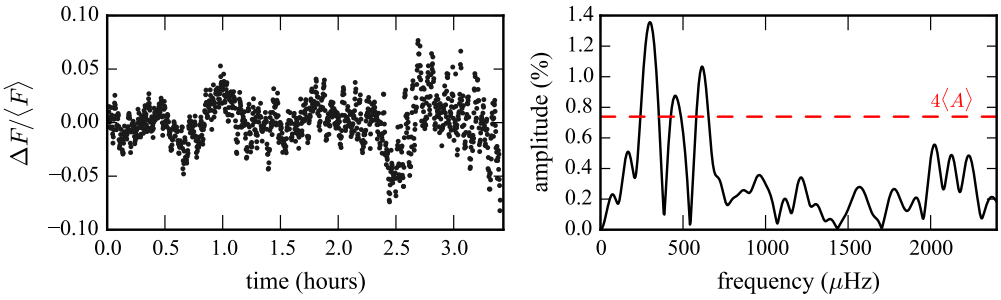

Figure 6.20: Left: light curve of SDSS J1310-0142 from 14 March 2015, boxcar smoothed over each 5 adjacent points. Right: FT of the raw light curve. The $4\langle A \rangle$ threshold is a rule-of-thumb significance criterion that supports that this star exhibits multi-modal pulsations.

6.3.2 SDSS J0908-0002

Catalina Sky Survey photometry indicated that SDSS J0908-0002 is an eclipsing binary system with a 9.15-hour orbital period, as shown in Figure 6.21. Our single run confirms this with incomplete coverage of an eclipse,

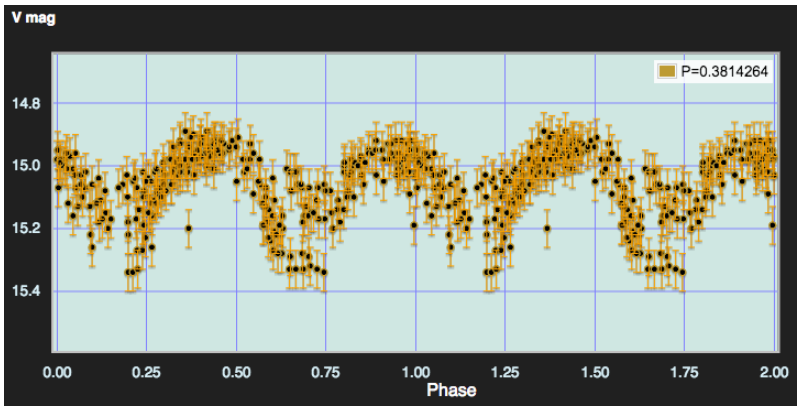

Figure 6.21: Catalina Sky Survey photometry of SDSS J0908-0002, folded on a period of 9.15 hours.

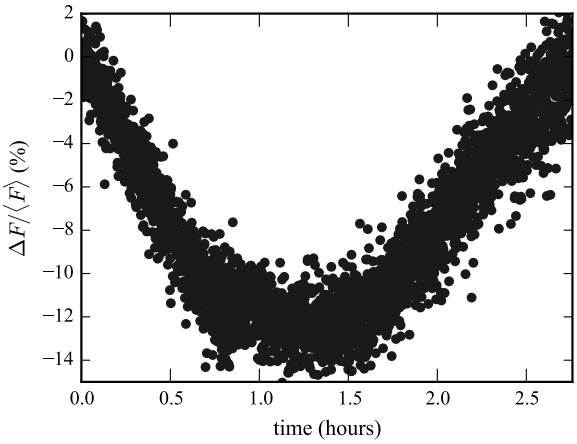

Figure 6.22: Short McDonald Observatory light curve of SDSS J0908-0002 from 26 April 2015 confirms the eclipsing system.

displayed in Figure 6.22. We see no obvious signatures of pulsations in addition to the eclipse signal from this single 2.8-hour run. The asymmetry in the eclipse profile may be caused by the changing airmass to this target through the observing run.

6.4 Conclusions and Future Work

Based on the characteristic of its pulsations and its high amplitude RV variations, SDSS J1618+3854 fits our adopted definition of an ELMV, though a more complete analysis of the implications of the competing orbital period aliases is still pending. Pulsations in the other sdAs that we observed are at least consistent with pulsating pre-ELMs. This is the most likely explanation for those with spectroscopic $\log g > 5.0$ from both pure-hydrogen and solar-metallicity spectroscopic fits.

The objects that occupy this spectroscopic parameter space are certainly interesting, but further classification from pulsations alone has proven quite challenging. With typically long periods, it takes a lot of observing time to resolve and precisely measure pulsation frequencies. For most of these new variables, we detect only a small number (often one) of independent modes, which severely limits their current asteroseismic utility.

Forthcoming astrometric measurements from *Gaia* will largely reveal the natures of the individual sdA stars. Distance constraints from parallax measures will allow us to infer absolute magnitudes. Combining absolute magnitudes with $T_{\rm eff}$ measurements enables us to constrain the radii of these stars,

allowing us to convert $\log g$ measurements to stellar masses. However, due to their high proper motions, astrometric solutions for most of these targets will not be included in the upcoming *Gaia* Data Release 2, scheduled for April 2018. Once the nature of sdA stars is fully elucidated, we can begin asteroseismically constraining the interior structures of these stars from the pulsation characteristics measured in this work, even for objects that exhibit few pulsation modes.

The main component of this work that remains to be completed before publication involves placing these objects into a Galactic context based on available radial velocity and proper motion data. Under the A star hypothesis, bright sdAs at high galactic latitude would be too far above the plane of the Milky Way given their velocities and main sequence lifetimes. If such objects turn out to be A stars, they must still be products of binary mass transfer to explain their ages; i.e., blue straggler stars.

Chapter 7

White Dwarf Radius Constraints from Ellipsoidal Variations in Tight Binaries

In a close binary system, tidal effects from one star can stretch the other, making it noticeably non-spherical. As the distorted star moves in its orbit, its projected area changes, causing a modulation of the measured flux. Since we see the broadest side of the star twice per orbit, the frequency of this ellipsoidal variation effect is twice the orbital frequency. Comparison of measured frequencies of photometric variability to orbital constraints from radial velocity measurements can help identify signals from ellipsoidal variations.

In Bell et al. (2017a, and Chapter 5), I detected this effect in a tight binary containing an extremely low-mass (ELM) white dwarf binary, SDSS J1054−2121. This could also be the source of mono-periodic photometric variations measured in SDSS J1142+3747 in Chapter 6, but time series spectroscopy is required to establish the connection between the photometric and orbital periods.

Hermes et al. (2014b) measured significant ellipsoidal variation signatures in the light curves of eight out of twenty observed low-mass white dwarf binary systems. They used the measured amplitude of this effect to constrain

the radii of the distorted stars. I wanted to apply those same tools to the observations of SDSS J1054−2121, but as I did my analysis, I decided to modify the approach. A version of the following originally was included in Section 3.2.2. of an early draft of Bell et al. (2017a), but fully describing my method for this single object caused that section to dominate the paper and to distract from the main narrative. Ultimately I decided to save this discussion for this thesis, and possibly another more focused publication.

7.1 Ellipsoidal Variations of SDSS J1054−2121

In Section 5.3.2.2, I measured a sinusoidal component of photometric variability from the ELM white dwarf SDSS J1054−2121 at twice its orbital frequency ($\cos 2\phi$ component) with an amplitude of $0.75 \pm 0.08\%$ through a $BG40$ filter. This observed amplitude of ellipsoidal variations allows us to better constrain the binary system parameters, particularly the mass of the secondary and the orbital inclination. We take a straightforward Monte Carlo approach to determining these new constraints, as well as improving our knowledge of the binary period and the ELM white dwarf $\log g$, mass, radius, and radial velocity semi-amplitude.

Our Monte Carlo analysis is inspired by the approach of Hermes et al. (2014b) to very similar data sets; it relies on solving their Equations 1–3 (reproduced below) for ellipsoidal variation amplitude, mass function, and surface gravity for random deviates drawn from probability density functions for $\log g$, $T_{\rm eff}$, $P_{\rm orb}$, and K_1 (RV semi-amplitude). The approach rests on a

few assumptions: (1) that the rotation period of the tidally deformed star $\approx$ the binary period; (2) that the light curve is a record of significant flux from only the primary star of this single-lined spectroscopic binary; (3) that the mass of the secondary is $< 3\ M_{\odot}$, corresponding to another white dwarf or neutron star; and (4) that there do not exist strong covariances between the four spectroscopically determined input quantities.

We have no a priori knowledge of the inclination angle, i, so we set a uniform prior on $\cos i$ between 0–1, corresponding to random orientations.

We adopt Gaussian prior probability distributions for $\log g$, $T_{\rm eff}$, $P_{\rm orb}$, and K_1 with mean and standard deviation values equal to those published in Gianninas et al. (2015). We use the original values from the direct model fits of $T_{\rm eff} = 9540 \pm 140$ K and $\log g = 6.27 \pm 0.13$, and apply the corrections for 3D convection from Tremblay et al. (2015) as part of our analysis. We generate 10 million sets of Monte Carlo deviates from these Gaussians, as well as from the distribution of orbital inclinations. We calculate for each set, as follows, the corresponding values for the limb-darkening coefficient (u_1), gravity-darkening coefficient (τ_1), primary ELM mass (M_1), ELM radius (R_1), and secondary mass (M_2), as well as the expected signature from ellipsoidal variations, the star-star separation (a), and the gravitational radiation merger timescale ($\tau_{\rm merge}$).

- We interpolate the linear limb darkening coefficient, u_1, for each $\log g$ and $T_{\rm eff}$ from Gianninas et al. (2013). We use the values calculated for the LSST

g band as a proxy for BG40, which has a similar central wavelength. We use the uncorrected $\log g$ and $T_{\rm eff}$ values to get these coefficients since they are computed directly from the model spectra.

- We apply the correction formulas from 3D convection simulations to $\log g$ and $T_{\rm eff}$ (Tremblay et al. 2015), which we use in all of the below calculations.
- We calculate temperature-dependent gravity-darkening coefficients, τ_1, following Morris (1985), using $\beta = 0.25$ (the law of von Zeipel 1924) and 5000 Å as a representative central wavelength of the $BG40$ bandpass.
- Direct bilinear interpolation of Table 3 from Althaus et al. (2013) gives a mean and standard deviation spread of their evolutionary ELM model masses that could correspond to each $\log g$ and $T_{\rm eff}$ deviate pair. We select a random deviate for M_1 from the corresponding Gaussian distribution.
- The ELM white dwarf radius, R_1, follows directly from the definition $\log g = GM_1/R_1^2$.
- We calculate the secondary mass, M_2, from the measured mass function:

$$P_{\rm orb}K_1^3/2\pi G = M_2^3 \sin^2 i/(M_1 + M_2)^2.$$

- We calculate the flux variation amplitude expected for the given input from (in cgs units)

$$A_{\rm EV} = \frac{3\pi^2(15 + u_1)(1 + \tau_1)M_2R_1^3 \sin^2 i}{5P_{\rm orb}^2(3 - u_1)GM_1(M_1 + M_2)}.$$

- The orbital separation, a, comes from solving Kepler's third law: $a^3 = GP^2(M_1 + M_2)/4\pi$.

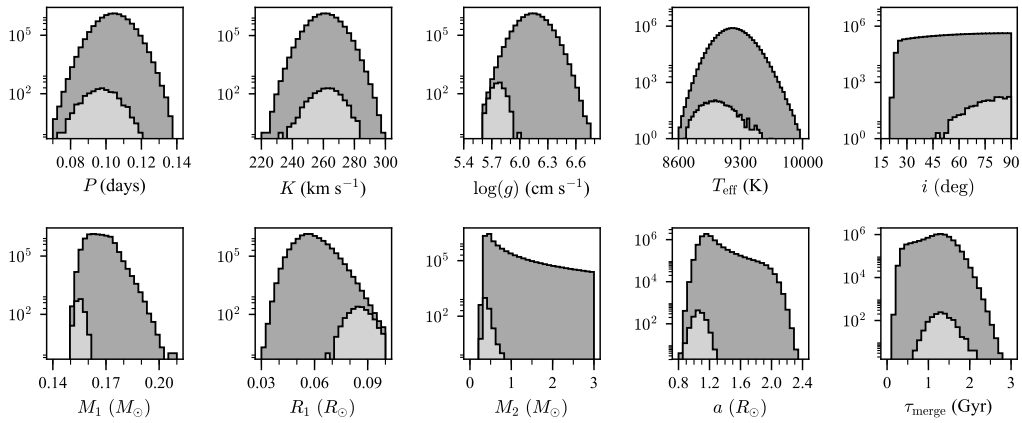

Figure 7.1: The results of Monte Carlo simulations of our constraints on the parameters of the binary system SDSS J1054−2121. The dark gray logarithmic histograms include all models with $M_2 < 3\ M_\odot$. The light gray histograms include only those models that were selected in proportion to the adopted Gaussian likelihood distribution for the system's ellipsoidal variation amplitude (Figure 7.2). Our improved constraints are summarized in Table 7.1.

- Finally, we calculate the timescale to a binary merger caused by the release of orbital energy from gravitational radiation using the relation (for mass in $M_\odot$, period in hours; Landau & Lifshitz 1958)

$$\tau_{\rm merge} = \frac{(M_1 + M_2)^{1/3}}{M_1 M_2} P^{8/3} \times 10^{-2}\ {\rm Gyr}.$$

Histograms of the marginal distributions of most of these parameters are displayed in dark gray in Figure 7.1. These represent the state of our understanding of this binary system from the spectroscopic results of Gianninas et al. (2015) alone (with the only added constraint that $M_2 < 3\ M_\odot$, eliminating 9% of possible solutions).

We do not apply a cut to systems that should eclipse due to meeting

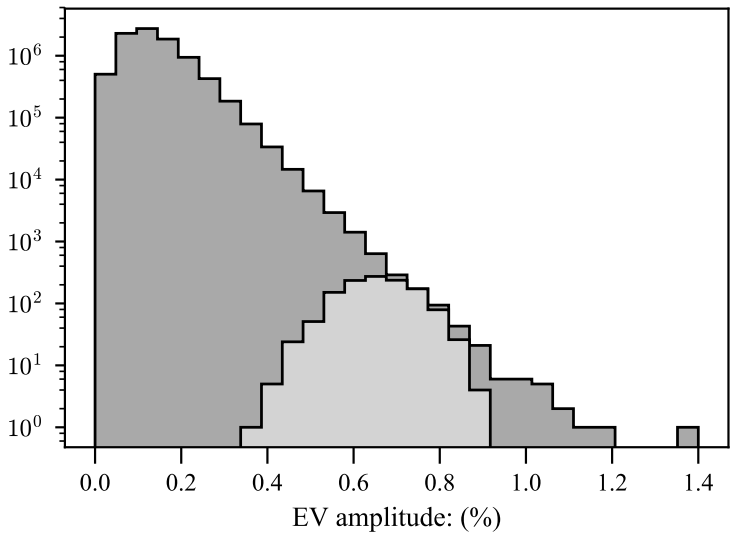

Figure 7.2: The distribution of expected EV amplitudes given prior spectroscopic constraints on the binary system SDSS J1054−2121 is displayed in dark gray. The light gray distribution shows the solutions that we accepted from our Monte Carlo simulations in proportion to a Gaussian distribution consistent with the photometric EV amplitude measurement.

the condition $a \cos i < R_1$ because some eclipses (e.g., those involving neutron star secondaries) would not be detectable in our light curve. These account for less that 0.006% of our models, and affect our final results negligibly.

The vast majority of these parameter combinations predict ellipsoidal variations—plotted in dark gray in Figure 7.2—that are incompatibly small compared to the measured amplitude. To improve our constraints on the system by imposing that it agrees with this new measurement, we accept Monte Carlo realizations in proportion to a Gaussian that is centered on the measured value with standard deviations that equals our 1σ errors. We plot in

Table 7.1. Revised System Parameters for SDSS J1054−2121

Parameter Name	Symbol	New Constraint	Units
Orbital Period	P	$0.097^{+0.007}_{-0.006}$	days
RV Semi-amplitude	K_1	262 ± 7	km s^{-1}
Surface Gravity	$\log(g)$	$5.77^{+0.04}_{-0.05}$	cm s^{-1}
Effective Temperature	$T_{\rm eff}$	9020^{+150}_{-130}	K
Orbital Inclination	i	77^{+6}_{-9}	deg
Primary ELM Mass	M_1	$0.1548^{+0.0016}_{-0.0014}$	$M_\odot$
Primary ELM Radius	R_1	$0.085^{+0.005}_{-0.004}$	$R_\odot$
Secondary Mass	M_2	$0.39^{+0.04}_{-0.03}$	$M_\odot$
Star Separation	a	$1.06^{+0.07}_{-0.06}$	$R_\odot$
Merger Timescale	$\tau_{\rm merge}$	1.3 ± 0.2	Gyr

light gray the distributions of the 0.014% of accepted EV amplitudes in Figure 7.2, and the marginal distributions of other important system parameters in Figure 7.1. The median values of these final distributions are listed in Table 7.1, with the quoted errors corresponding to the values ±34% to either side. This new measurement of the photometric ellipsoidal variation amplitude of SDSS J1054−2121 greatly improves our constraints on this system, implying that the secondary is a low-mass white dwarf. This would not be considered an ELM white dwarf under the definition that $M_{\rm ELM} < 0.3\,M_\odot$, though white dwarfs above this mass can still form with helium cores through mass transfer in a binary system.

Chapter 8

Destroying Aliases from the Ground and Space: Super-Nyquist ZZ Cetis in *K2* Long Cadence Data

Short-cadence *Kepler*/*K2* data are practically the ideal observations for measuring the signals of pulsations in white dwarfs. The extent of the data ensures that they are resolved, have high signal-to-noise, and can be measured precisely. The 1-minute exposure times sample white dwarf pulsations periods well, and the absence of large gaps in the data simplifies the spectral window in frequency space. Much of the work presented in Chapters 2, 3, and 4 utilized this type of data.

Signatures of white dwarf pulsations can be detected in long-cadence (30 min) *K2* data, but they suffer dramatic aliasing and amplitude reduction since they exceed the Nyquist frequency. J. J. Hermes alerted me of two DA white dwarfs that appeared to show multiple frequencies of variability in long-cadence *K2* data, and I decided to follow these up from McDonald Observatory. The ground-based data also suffer severe aliasing from daily gaps, but the types of problems in each of these non-ideal data sets help to mitigate the problems in the other. For a few of the significant signals in the *K2* observations, I was able to recover accurate measurements of pulsation frequencies

with the full precision of roughly 80 days of observations. EPIC 220274129, in particular, exhibits multiple rotational multiplets that support that this star shows photometric modulation on its rotation period and *twice* the rotation period. The physical cause of this subharmonic is unclear but a very interesting. In addition to the *K2* signals, I detect many additional pulsation modes in the ground-based data on these new ZZ Ceti variables, most of which the *K2* observations would not have been sensitive to.

I felt it necessary to include in this work a treatise on the myriad ways that observational details can affect the signatures of stellar pulsations in time series photometry, as well as limit our ability to accurately identify the pulsation frequencies. The instances where I am able to match signals between space- and ground-based data sets also serve as demonstrations of possible pitfalls in the analysis of either data set on its own.

Zach Vanderbosch obtained the light curves of EPIC 220274129 in October and November 2016. J. J. Hermes obtained spectra of both new ZZ Cetis from SOAR, which Pier-Emmanuel Tremblay fit models to determine their atmospheric parameters. Mike Montgomery calculated the expected amplitude ratio of $\ell = 1$ or 2 pulsations between the McDonald ProEM + $BG40$ filter and the *Kepler* photometric systems, and Don Winget provided important insights on how the temporal sampling affects the spectral window.

This is the most recent draft of a paper that I aim to submit to the AAS Journals shortly. The published version will be slightly improved based on feedback from my coauthors and referee.

8.1 Introduction

Stellar pulsations are extremely sensitive to the detailed interior structures of stars, and Fourier analysis of photometric light curves can reveal the eigenfrequencies of these physical systems. This is the only method by which we directly constrain stellar interiors. However, the measurement of accurate pulsation frequencies for precision asteroseismology requires extended photometric monitoring with few gaps and short exposure times. For data that do not meet these criteria, frequency determination is hindered by the aliasing of pulsation signals.

The atmospheres of the majority of white dwarf stars are dominated by hydrogen (DA white dwarfs). As these stars cool, partial ionization of hydrogen eventually causes an outer convection zone to develop. The modulation of the flux by convection can drive global nonradial oscillations (Brickhill 1991) that manifest as photometric variability of the star. Near the mean mass of 0.66 $M_{\odot}$ (Kepler et al. 2015), DA white dwarfs pulsate as ZZ Ceti variables (a.k.a., DAVs) in the range 12,500 $\gtrsim T_{\rm eff} \gtrsim$ 10,800 K (Tremblay et al. 2013), and exhibit pulsations with periods of 3–20 minutes.

White dwarf asteroseismology has flourished in the era of precision time series photometry from the *Kepler* spacecraft. *Kepler* saves data for pre-selected targets of interest in one of two observing modes: long cadence, with continuous exposures of roughly 30 minutes; and short cadence, with one-minute exposures for a limited number of targets (Howell et al. 2014). Short-cadence observations are required to sufficiently oversample typical white dwarf

pulsation periods for straightforward frequency measurements. Both in its original mission and while observing new fields along the ecliptic as *K2*, *Kepler* has targeted known and candidate pulsating white dwarf stars at short cadence, collecting the most extensive coverage of ZZ Ceti (hydrogen-atmosphere pulsating white dwarf) variability to date. This has enabled the precise determination of pulsation frequencies for asteroseismic analysis (Greiss et al. 2014; Hermes et al. 2014b, 2015a, 2017c,d; Bell et al. 2015c), as well as the discovery of a new pulsation-related outburst phenomenon that operates near the cool edge of the ZZ Ceti instability strip (Bell et al. 2015c, 2016, 2017b; Hermes et al. 2015b).

Long-cadence *K2* observations can potentially reveal white dwarf pulsations, but the signals suffer dramatic aliasing against the Nyquist frequency, as well as amplitude reduction, since the 30-minute cadence severely undersamples the pulsations. While the sub-Nyquist pulsation frequency aliases measured from these data are extremely inaccurate, they are of exceptionally high precision owing to the long observational baseline of *K2*.

High-speed photometry from individual ground-based observatories causes a different kind of aliasing: gaps in the data from daylight and weather introduce cycle-count ambiguities into the pulsation record. Selecting the correct alias among the comb of peaks that make up the observational spectral window is nontrivial.

By combining long-cadence *K2* data with single-site high-speed follow-up from McDonald Observatory, we can use the strengths of each data source

to resolve the aliasing of the other. We apply this method to two new ZZ Ceti variables in long-cadence *K2* data: EPIC 210377280 from Campaign 4 and EPIC 220274129 from Campaign 8. We describe the *K2* observations, as well as follow-up spectroscopy and high speed photometry, in Section 8.2. We discuss the instrumental and astrophysical effects that cause differences in the pulsation signatures between our ground- and space-based light curves in Section 8.3. We then carefully analyze these data sets together for both EPIC 210377280 and EPIC 220274129 in Section 8.4, identifying multiple significant pulsation frequencies in each star. We recover *K2*-level precision for those modes that we are able to match between data sets. We discuss the *K2* signals that are not matched in the ground-based light curves in the concluding Section 8.5.

8.2 Observations

8.2.1 Long-cadence *K2* photometry

EPIC 210377280 and EPIC 220274129 were both identified as white dwarf stars in *K2* fields 4 and 8, and were observed at long cadence for 70.82 and 78.66 days respectively. Both exhibit multiple significant periodicities of photometric variability.

For each target, we utilize the light curves extracted and processed by the EVEREST 2.0 pipeline (Luger et al. 2016, 2017), discarding all points with "quality" flags set. We further smooth the light curves by fitting a cubic

spline[1], tuning the fitting weights manually to remove residual noise at the lowest frequencies without affecting the measured amplitudes of the signals of astrophysical interest in the Fourier transform. We note that version 2.0 of the EVEREST pipeline accounts for contamination from nearby stars in the photometric aperture, which otherwise would dilute the amplitudes of variability measured in *Kepler*'s 4″ pixels.

The details of the *K2* observations of both stars are summarized in Table 8.1, including the total number of long-cadence observations in the final light curves.

[1]Using tools from SciPy: `http://www.scipy.org/`

Table 8.1. *K2* Target Observing Summary

K2 ID (EPIC)	Campaign	R.A. (h:m:s)	Dec. (d:m:s)	Begin Date (UTC)	End Date (UTC)	Good Obs. (#)	K_p (mag)
210377280	4	04:04:24.924	+12:55:43.38	08 Feb 2015	20 Apr 2015	3249	18.52
220274129	8	01:05:28.745	+02:05:01.14	04 Jan 2016	23 Mar 2016	3475	16.79

Table 8.2. Journal of McDonald Observations

EPIC	Date (UTC)	Exposure Time (s)	Run Duration (h)
210377280	04 Feb 2016	15	4.6
	05 Feb 2016	10	4.5
	07 Feb 2016	20	1.9
	07 Feb 2016	10	2.3
	08 Feb 2016	15	4.7
220274129	28 Oct 2016	3	5.5
	29 Oct 2016	20	2.0
	29 Oct 2016	30	3.0
	01 Nov 2016	10	6.0

8.2.2 Time series photometry from the ground

We confirmed the pulsational nature of the photometric variations of both targets from the ground with the ProEM camera on the 2.1-m Otto Struve Telescope at McDonald Observatory. At Cassegrain focus, the ProEM camera has a $1.6' \times 1.6'$ field of view, and with 4×4 binning, our effective plate scale is $0.38''$ pixel^{-1}. Each object was observed on four different nights, as detailed in Table 8.2. The data were acquired through a broad-band BG40 filter that transmits greater than 50% of flux between 3300–6000 Å to reduce sky noise.

We use standard IRAF tasks to dark-subtract and flatfield the images with calibration frames that we acquired each night. We extract circular aperture photometry for the target and comparison stars in the field using

CCD_HSP, an IRAF script that uses tasks from PHOT (Kanaan et al. 2002). We divide the measured target counts by a weighted sum of comparison star counts, then by a low-order best-fit polynomial to correct for airmass and transparency variations using the WQED tools (Thompson & Mullally 2013). WQED also applies a barycentric correction and accounts for the latest leap seconds to enable the reliable combination of multiple nights of data.

8.2.3 Spectroscopy

We acquired spectroscopic observations for both stars with the Goodman spectrograph (Clemens et al. 2004) on the 4.1-m SOAR telescope on Cerro

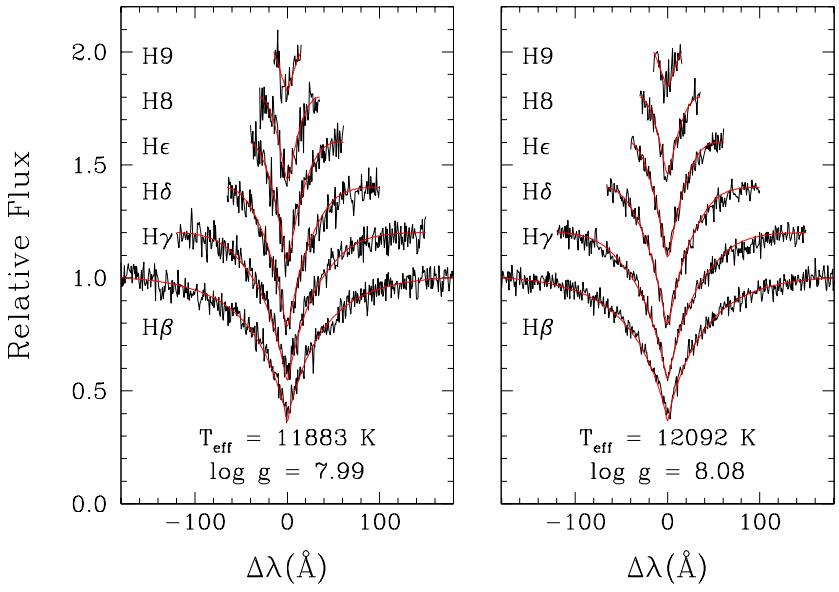

Figure 8.1: Balmer line profiles from the SOAR spectra of EPIC 210377280 (left) and EPIC 220274129 (right). The best fit 1D models are overplotted in red, and their parameters are indicated at the bottom of each panel.

Table 8.3. Spectroscopic Parameters

EPIC	$T_{\rm eff}$ (K; 1D)	$\log g$ (cgs, 1D)	$T_{\rm eff}$ (K; 3D)	$\log g$ (cgs, 3D)	Mass ($M_{\odot}$)
210377280	11890(200)	8.001(0.060)	11590	7.943	0.57(0.02)
220274129	12090(210)	8.077(0.054)	11810	8.029	0.62(0.02)

Pachón, Chile, using the setup described in Hermes et al. (2017d).

We fit the data to 1D atmosphere models following the methodology of Tremblay et al. (2011a), with the ML2/α = 0.8 mixing length theory parameterization. The uncertainties include the systematic effects estimated by Gianninas et al. (2011). We also apply the 3D convection corrections of Tremblay et al. (2013). Both sets of atmospheric parameters are provided in Table 8.3. A comparison of the best-fit models to the observed Balmer line profiles is displayed in Figure 8.1.

8.3 Comparability of Data Sets

There are a number of effects, both observational and astrophysical, that cause the signatures of pulsations in these stars to differ between the *K2* photometry and the follow-up ground-based light curves. We must factor in these considerations as we approach the task of matching signals between these data sets. In this section, we discuss the most significant of these effects and how we incorporate them into the analysis that follows.

8.3.1 Nyquist aliasing

The Nyquist critical frequency for evenly sampled data is $f_{\rm Ny} = 1/2\Delta t$, where Δt is the constant spacing in time between observations. Fourier transforms (FTs) of photometric light curves exhibit peaks at the accurate frequencies of intrinsic stellar brightness variations for signals that are bandwidth limited to below $f_{\rm Ny}$. However, frequencies of stellar photometric variability greater than $f_{\rm Ny}$ will be aliased into the range $0 < f < f_{\rm Ny}$. Figure 8.2 demonstrates the relationship between the underlying signal frequency and the location of its $0 < f < f_{\rm Ny}$ alias.

The long-cadence *K2* light curves are acquired onboard the spacecraft with a regular spacing of 29.43 minutes. These timestamps are then corrected for the changing distance between the spacecraft and the solar system barycenter, breaking the strict regularity of the time sampling. The Nyquist frequency is not so simply defined under these conditions. Eyer & Bartholdi (1999) show that the effective Nyquist frequency over which signals are exactly aliased is $f_{\rm Ny} = 1/2p$, where p is the greatest common factor of all time separations between pairs of observations. p is the longest period that the time series could be folded on to cause all samples to be coincident in phase. Koen (2006) points out that there is a practical lower limit on p (upper limit on $f_{\rm Ny}$) set by the recorded timestamp precision.

FTs of the *K2* data are significantly affected by Nyquist-like aliasing across lower frequencies due to the near-even spacing of *K2* observations. This pseudo-Nyquist behavior occurs at $f^*_{\rm Ny} = 1/2p^*$, where the time samples folded

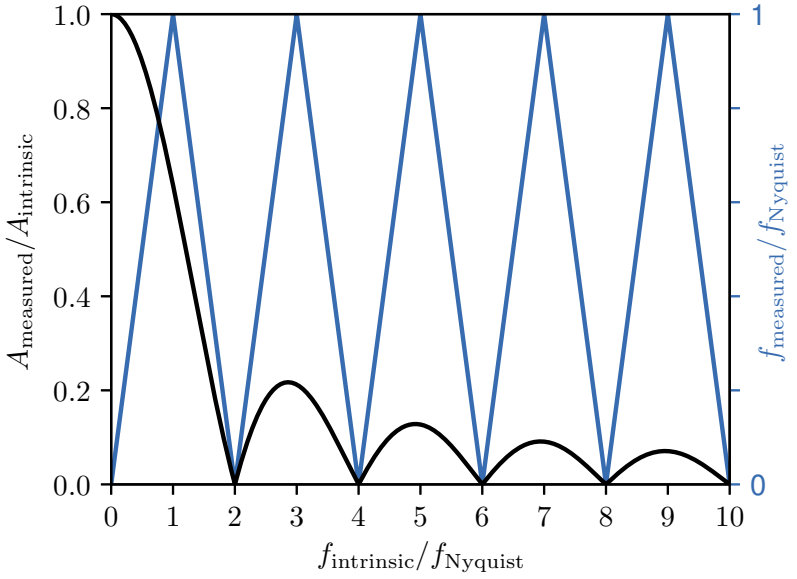

Figure 8.2: The effect of continuous time series sampling on the measured amplitude and frequency of a signal. Signals with intrinsic frequencies beyond the Nyquist frequency will be aliased into the sub-Nyquist regime (right axis) with significantly decreased amplitudes (left axis).

on p^* are highly concentrated in phase. Murphy et al. (2013) exploited the difference in aliasing behavior between this and the true Nyquist frequency to identify the intrinsic stellar pulsation frequencies for super-Nyquist pulsators in the original *Kepler* Mission.

Following the framework of Eyer & Bartholdi (1999), we identify the pseudo-Nyquist frequency by direct calculation of the spectral window (the signature in the FT of a pure sinusoid sampled as the data). The frequency of the first peak beyond zero in the spectral window with amplitude near unity is twice $f^*_{\rm Ny}$. The pseudo-Nyquist frequencies of EPIC 210377280 and

EPIC 220274129 are 283.2377 and 283.2388 μHz, respectively. The distinction is subtle, so we refer to $f^*_{\rm Ny}$ as simply the Nyquist frequency for the remainder of this paper.

8.3.2 Phase smearing

Finite exposure lengths of photometric observations have the effect of boxcar smoothing the underlying signal. The amplitudes measured from the data are therefore smaller than the intrinsic signal amplitudes, and a correction factor must be applied if accurate amplitudes are of interest. When exposures of duration $t_{\rm exp}$ are used to record a sinusoid of period P, its amplitude will appear smaller by a factor of η:

$$\eta = A_{\rm measured}/A_{\rm intrinsic} = \mathrm{sinc}\,(\pi t_{\rm exp}/P). \tag{8.1}$$

Figure 8.2 demonstrates this in terms of the ratio of the signal frequency to the Nyquist frequency, assuming continuous exposures with no overhead. This expression for phase smearing can be found in various works, including Hekker & Christensen-Dalsgaard (2017), where it is referred to as "apodization." A derivation is available in Murphy (2014, Section 1.2.2).

This effect has a major impact on the pulsation amplitudes measured from the *K2* data, where $t_{\rm exp} > P$. The equation also expresses *K2*'s lack of sensitivity to signals with periods that are near integer fractions of the exposure time.

8.3.3 Passband differences

Variations of the emergent flux from a star due to pulsations are wavelength dependent. This causes the same pulsations to have different measured amplitudes in different photometric systems. *Kepler* has a broad response function spanning roughly 4300–8900 Å[2], while the McDonald observations were made through Earth's atmosphere and a BG40 filter that spans 3300–6000 Å.

To account for this effect, we calculated the expected pulsation amplitude ratio as measured through these two passbands for a representative $T_{\rm eff} = 12{,}000$ K, $\log g = 8.0$ white dwarf model. We utilized the grid of spectroscopic models described in Koester (2010) for the emergent flux. We consider pulsations of spherical degree $\ell = 1$ and $\ell = 2$, since practically all available constraints on white dwarf pulsations are consistent with these two mode identifications (e.g., Winget & Kepler 2008). We expect the intrinsic amplitudes of both $\ell = 1$ and $\ell = 2$ pulsation modes to be larger in the McDonald data than the *K2* observations by a factor of roughly 1.128. While this is near unity, we include this scaling factor when comparing measurements between data sets throughout this work.

[2] `https://keplerscience.arc.nasa.gov/CalibrationResponse.shtml`

8.3.4 Spectral window

Gaps in data can cause confusion in the determination of pulsation frequencies by introducing an uncertainty in the number of cycles missed when observations were not being made. Our ground-based data suffer significant aliasing since they are distributed across multiple nights. As opposed to the intrinsic limitations on frequency precision set by the spectral resolution ($\propto 1/T$, where T is the total baseline of observations; Montgomery & Odonoghue 1999), aliasing introduces an additional *extrinsic* error in the accuracy of our frequency determinations, since we might select an incorrect alias peak.

The uncertainty introduced by these aliases is best understood by studying the spectral window: the signature of a pure sinusoid in the FT that arises solely from the time sampling. We plot the spectral windows for both stars as part of our analyses that follow. We characterize the magnitude of the potential frequency confusion by measuring the location of the highest non-central alias in the spectral window.

Any pulsation modes included in our frequency solutions based on the ground-based data alone are flagged as potentially suffering from spectral window alias ambiguities. We emphasize that this extrinsic error is non-Gaussian, and that any attempt at asteroseismic inference should carefully consider alternate frequency solutions for these stars that employ other viable aliases.

8.3.5 Intrinsic mode variation

Despite our best efforts to account for instrumental differences between the pulsation signatures in these data sets, we face an astrophysical limitation that is more difficult to surmount: the amplitudes and frequencies of stellar pulsations may have changed significantly between epochs of observation. The challenges of comparing multi-season pulsation measurements for ZZ Ceti variables that have cooled significantly beyond the hot edge of the instability strip is well established in the literature, particularly from Whole Earth Telescope (WET; Nather et al. 1990) campaigns. GD 154 (Pfeiffer et al. 1996), G29–38 (Kleinman et al. 1998), and HL Tau 76 (Dolez et al. 2006), for example, show such dramatic amplitude changes that significant modes from one year can be completely absent the next. With 9 and 7 month gaps between space- and ground-based campaigns on EPIC 210377280 and EPIC 220274129, we have no expectation that the same eigenmodes will be excited to similar amplitudes in both data sets.

Extended, continuous records from *Kepler* and *K2* have provided new insights into mode variations (e.g., Hermes et al. 2014b; Bell et al. 2015c, 2016). By inspecting the FTs of 27 ZZ Cetis observed by *Kepler* and *K2*, Hermes et al. (2017d) discovered a dichotomy of mode behavior: while some modes are notably coherent, others undergo significant modulation and appear as multiple closely spaced peaks in the FT. These bands of power are well fit by Lorentzians with half-widths-at-half-maximum of order 1 μHz. The amplitudes of the many individual peaks that make up these power bands

are typically smaller than the instantaneous, intrinsic amplitudes of the corresponding pulsation modes. Unlike the phase smearing and passband effects, we are unable to apply a corrective factor to pulsation amplitudes measured in *K2* data that accounts for this mode incoherence.

8.4 Comparing Data Sets

The ZZ Ceti pulsation signals in long-cadence *K2* data may have suffered any integer number of Nyquist reflections. We assess these candidate intrinsic frequencies through comparison with ground-based observations from McDonald Observatory. Pulsation frequencies that we are able to positively match between these data sets do not suffer measurement ambiguities from either the Nyquist aliasing of the *K2* data or the window function aliasing of the multi-night ground-based photometry. We conservatively accept only unique, unambiguous matches between data sets.

To determine the signals of statistical significance in the *K2* data, we use a bootstrapping approach to calculate a threshold in the FT that corresponds to a 0.1% false alarm probability (FAP). This is similar to the calculations made in, e.g., Greiss et al. (2014), Bell et al. (2015c, 2016)[3]. Signals are significant to better than 99.9% confidence[4] if they exceed the 99.9 per-

[3]We note that the application in these previous works was not strictly bootstrapping, as the resampled flux values were drawn without replacement (i.e., shuffled). The 0.1% FAP thresholds calculated through resampling with replacement agree to within 1% the values from resampling without replacement.

[4]This is a slightly conservative criterion, since this approach treats astrophysical signals as additional sources of noise.

centile of maximum peak amplitudes detected in the full FTs of 10,000 random bootstrap samplings of the *K2* light curves of each star.

The rule-of-thumb significance criterion for ground-based light curves is to accept peaks that reach amplitudes in excess of four times the mean noise, $4\langle A\rangle$, in a local region of the FT (Breger et al. 1993; corresponding to $\approx 0.1\%$ FAP; Kuschnig et al. 1997). For these data sets, a high density of pulsation signatures convolved with a broad spectral window makes this local measurement a challenge, and we instead interpolate between $4\langle A\rangle$ values calculated in regions on each side of the frequency range of pulsational power: 0–800 μHz and 6000–8000 μHz.

All FTs examined in this work were computed with the Period04 software package (Lenz & Breger 2004). We oversample the spectral resolution by a factor of 20 to obtain representative peak amplitudes. We average the ground-based light curves into 60 s bins (matching the least common multiple of exposure times used on different nights) to avoid giving runs with shorter exposure times undue weight in the FT.

While our primary analysis utilizes the *K2* light curves extracted by the EVEREST pipeline, we test the robustness of our signal detections by confirming their presence in the light curves produced by the *K2* Guest Observer pipeline (Twicken et al. 2010) and the extractions described by Vanderburg & Johnson (2014).

8.4.1 EPIC 210377280

The FT of the long-cadence *K2* light curve of EPIC 210377280 is displayed in the top panel of Figure 8.3. Our bootstrap calculation yields a 0.1% FAP significance threshold at 0.148% amplitude, which is indicated by the dashed red line. The peak marked with a $\times$ symbol is within $0.3\,\mu$Hz of a typical instrumental artifact at $\approx 50\,\mu$Hz caused by *K2*'s thruster firings (Van Cleve et al. 2016), so we exclude it from our analysis. We mark four significant signals of astrophysical interest with colored triangles. Their properties, computed from least-squares sinusoidal fits to the entire *K2* light curve, are listed in Table 8.4.

The spectral window from four nights of ground-based observations of EPIC 210377280 from McDonald Observatory is displayed in the bottom panel of Figure 8.3. Any signals in the ground-based data are convolved with this complex aliasing structure in the FT, making it difficult to select the correct pulsation frequencies. The x-axes of both panels of Figure 8.3 have the same scale, emphasizing the relative imprecision of ground-based signal detections. We aim to use the precise *K2* data to guide our selection of the correct alias peaks; in doing so, we determine the number of Nyquist bounces of the *K2* signals and recover accurate pulsation frequencies at *K2* precision. When the *K2* data do not assist our peak selection, we risk choosing the wrong aliases and adopting frequencies that are off by of-order $11.6\,\mu$Hz, as discussed in Section 8.3.4.

The FT of the ground-based observations of EPIC 210377280 in the full

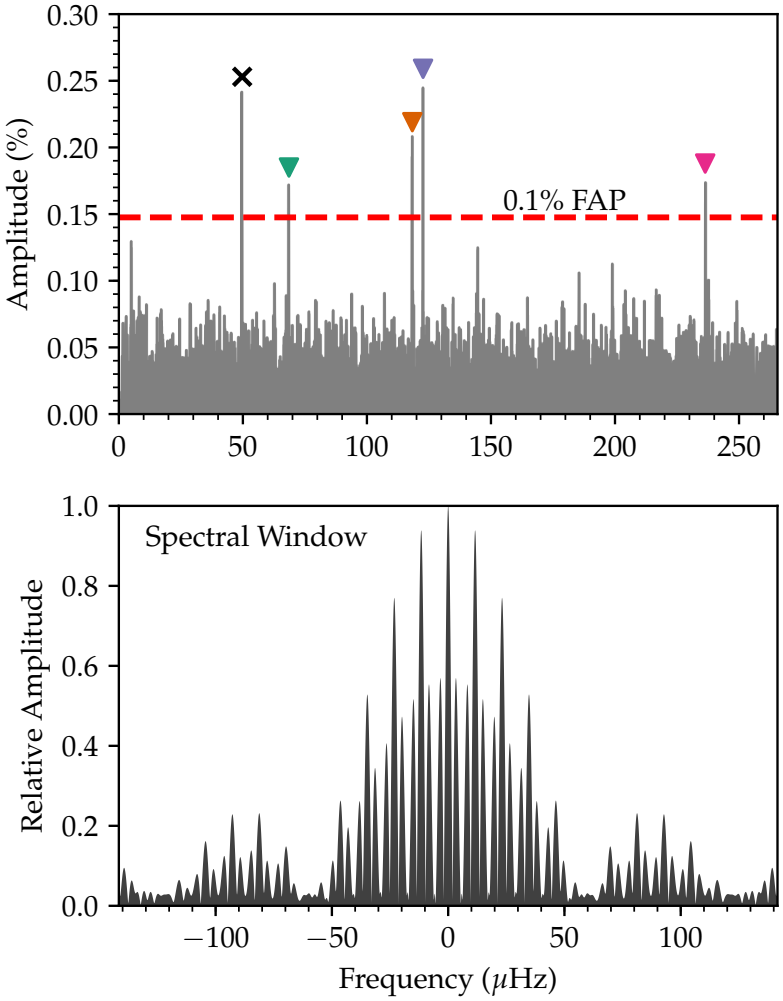

Figure 8.3: TOP: Fourier transform of the *K2* observations of EPIC 210377280 out to the Nyquist frequency with a 0.1% false alarm probability (FAP) significance threshold (see text). Significant signals are marked with colored triangles. BOTTOM: The spectral window from four nights of McDonald Observatory observations of EPIC 210377280 over a five night span in Feb 2016. The highest alias is located 11.6 μHz away from the central peak. The x-axes of both panels have the same scale.

Table 8.4. Significant *K2* Aliases for EPIC 210377280

	Frequency (μHz)	Period (s)	Amplitude (%)
◆ F_1	68.569(13)	14584(3)	0.17(3)
◆ F_2	118.297(11)	8453.3(8)	0.20(3)
◆ F_3	122.630(9)	8154.6(6)	0.24(3)
◆ F_4	236.362(13)	4230.8(2)	0.17(3)

range of pulsational power is presented in the top panel of Figure 8.4. The pink shaded region corresponds to the 0.1% FAP level for the *K2* data (dashed line in Figure 8.3), corrected for the effects of phase smearing (Section 8.3.2) and passband differences (Section 8.3.3). This essentially represents the sensitivity of the long-cadence *K2* observations to the pulsation signatures measured from the ground; if these light curves were obtained simultaneously, we would expect the signals above the pink shaded region in Figure 8.4 to rise above the 0.1% FAP threshold in Figure 8.3. Integer multiples of the Nyquist frequency are marked in the figure with vertical red lines, and the $4\langle A \rangle$ significance threshold for the ground-based data is displayed as the dashed red line. Notably, the *K2* observations would not be sensitive to the majority of significant pulsations that we detect from the ground.

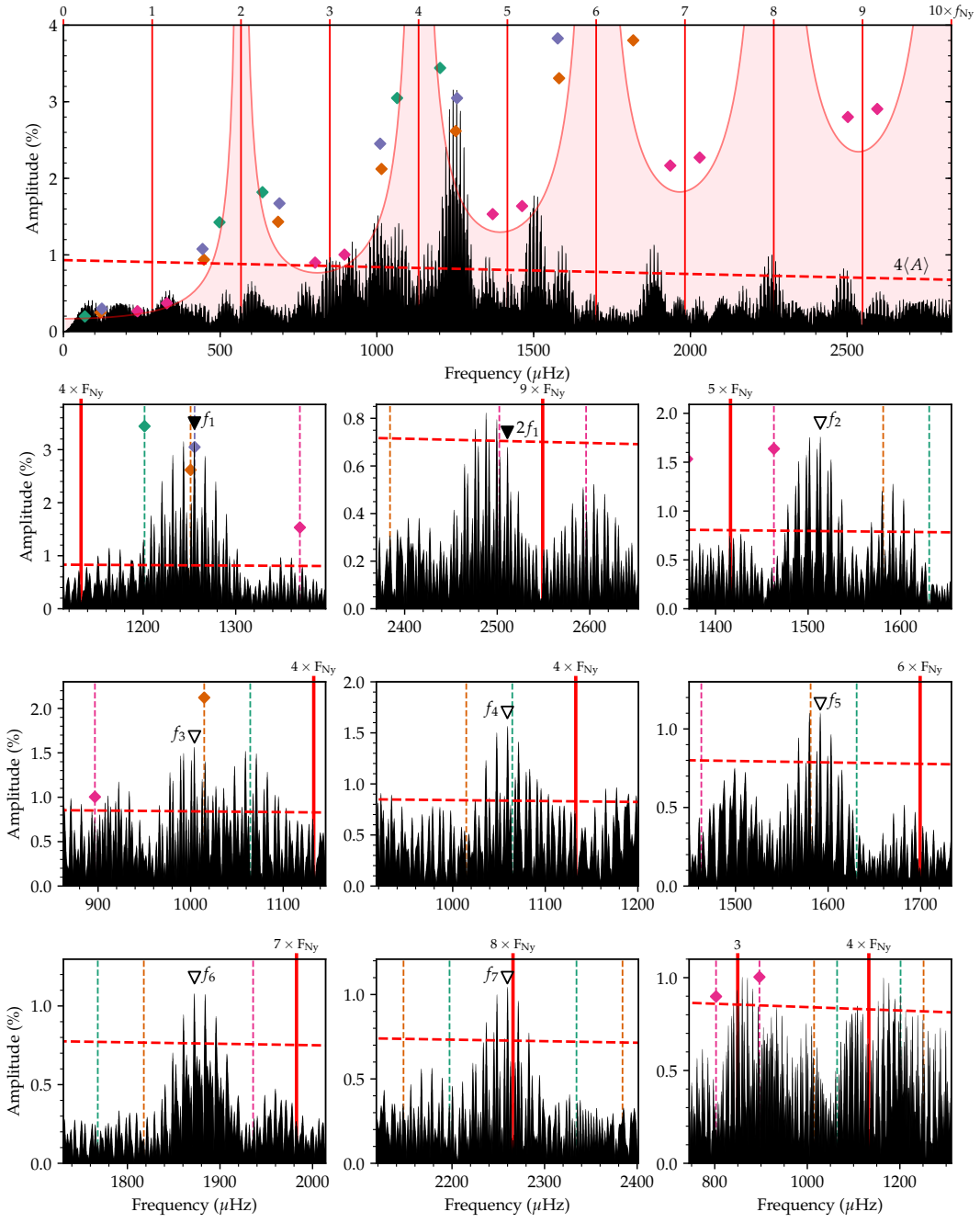

Figure 8.4: (Continued on the following page.)

Figure 8.4: TOP: Fourier transform of the McDonald observations of EPIC 210377280 with the *K2* sensitivity function overlaid (*K2* observations are not sensitive to the shaded region to a FAP of 0.1%). Vertical lines mark integer multiples of the *K2* Nyquist frequency. The possible intrinsic frequencies and expected amplitudes (corrected for phase smearing and bandpass differences) corresponding to the measured aliases in the *K2* FT are indicated with diamond markers (color coded to match the top panel of Figure 8.3). BOTTOM: Prewhitening sequence for EPIC 210377280 (progresses left to right, then down). Black arrows indicate alias frequency selections supported by *K2* observations; white arrows point to peaks selected from ground-based data alone. The red dashed line in all panels shows the $4\langle A \rangle$ significance threshold for the ground-based data. The last panel highlights the residual power in our fully prewhitened light curve.

Figure 8.4 also indicates the possible intrinsic frequencies and expected amplitudes corresponding to the significant signals measured in the *K2* data with diamonds that are color-coded to match Figure 8.3 and Table 8.4.

After adopting each new frequency from the ground-based data, we use a least-squares optimization in PERIOD04 to refine the overall solution. We then subtract (prewhiten) the best fit and search for additional significant signals in the FT of the residuals. The sequence of FTs in the smaller panels of Figure 8.4 demonstrates our process of frequency selection. Those signals marked with solid black triangles were informed by the precision *K2* data, while signals marked with white triangles were selected as the highest-amplitude peaks in the ground-based data and may be the incorrect aliases.

The modes are characterized in Table 8.5 in order of adoption, and this best-fit model is plotted over the McDonald light curve in Figure 8.5. We refer to frequencies detected in the *K2* data with a capital F_n (as in Table 8.4), and our final frequencies as f_n (Table 8.5). For frequencies matched to a *K2* signal, we refine the frequency value and uncertainty by doing a final least-squares fit of the correct alias to the *K2* data; otherwise, the values come from least-squares fits to the McDonald light curve. Uncertainties are determined following Montgomery & Odonoghue (1999).

The first small panel of Figure 8.4 depicts the first significant frequency that we adopt. This is a clear demonstration of the combined strength of these two data sets: one of the highest aliases (but not *the* highest; see discussion in Section 8.5) of the largest signal from the ground-based photometry precisely

Table 8.5. Frequency Solution for EPIC 210377280

Mode	Frequency (μHz)	Period (s)	Amplitude[a] (%)
f_1[b]	1255.581(9)	796.444(6)	3.33(14)
$2f_1$[b,c]	2511.162(19)	398.222(3)	0.64(14)
f_2[d]	1513.14(3)	660.88(6)	1.66(14)
f_3[d]	1004.17(13)	995.85(13)	1.62(14)
f_4[d]	1059.07(13)	944.22(12)	1.57(14)
f_5[d]	1591.54(19)	628.32(7)	1.11(14)
f_6[d]	1872.49(19)	534.05(5)	1.09(14)
f_7[d]	2259.8(2)	442.51(4)	1.05(14)

[a]Amplitude based on fit to ground-based data only.

[b]Alias matched to *K2* signal.

[c]Harmonic of previously found signal.

[d]Detected in ground-based data alone and may be incorrect alias of spectral window.

matches the four-Nyquist-bounce candidate intrinsic signal underlying F_3 in both amplitude and frequency. We fit and prewhiten this signal from the light curve to search for additional signals in the residuals. We also identify the second harmonic of this mode, which is displayed in the second small panel of Figure 8.4; the exact 2:1 ratio of harmonics informs this alias selection. Since F_3 has been positively matched to a ground-based signal, we exclude other possible underlying solutions for this mode in later panels. The final frequency values listed for f_1 and $2f_1$ in Table 8.5 are based on a least-squares

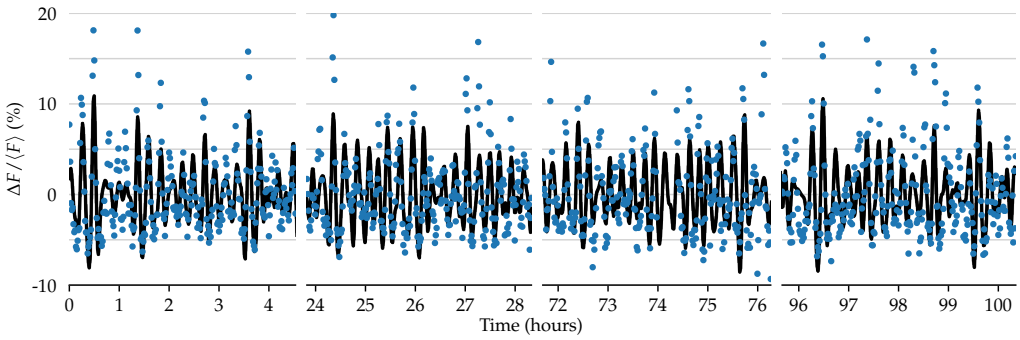

Figure 8.5: The frequency solution overlaid on the ground-based observations of EPIC 210377280 from McDonald Observatory.

fit of f_1 to the *K2* light curve.

The other frequencies that we adopt do not unambiguously resolve *K2* aliases. For instance, F_2 has candidate frequencies close to aliases of both f_3 and f_5. We simply adopt the highest alias peaks associated with each signal in Table 8.5. At the amplitudes observed in the McDonald data, many of these would not be detectable at long cadence by *K2* due to amplitude suppression from phase smearing (Section 8.3.2). An exception to this is f_2, which was most likely not excited to such high amplitude throughout the *K2* observations, as discussed in Sections 8.3.5 and 8.5.

The bottom-right panel of Figure 8.4 displays part of the FT of the final residuals relative to our significance threshold. While some remaining peaks exceed our adopted significance criterion, alias selection is non-trivial and not attempted.

8.4.2 EPIC 220274129

The FT of the *K2* photometry on EPIC 220274129 displayed in the top panel of Figure 8.6 reveals a greater number of signals that exceed our 0.1% FAP threshold (0.059% amplitude) than for the previous object. These are characterized in Table 8.6. While matching these signals between data sets may initially seem daunting, we are able to exploit the physics of stellar oscillations to largely sort them out.

Rotation can break the azimuthal degeneracy of spherical harmonic pulsation patterns, splitting a mode of spherical degree ℓ into $2\ell+1$ multiplet components of integer azimuthal order number $-\ell \leq m \leq \ell$. For the nonradial gravity mode pulsations of white dwarfs, modes of adjacent m have frequency spacings $\delta\nu_{k\ell m} = (m/P_{\rm rot}) \times (1 - C_{k\ell})$, where $P_{\rm rot}$ is the rotation rate (assumed solid body) and $C_{k\ell}$ is the Ledoux constant that describes the effect of the Coriolis force on a particular mode (Ledoux 1951). In the asymptotic limit of high radial order, k, $C_{k\ell} = 1/\ell(\ell+1)$, but generally $C_{k\ell} \leq 1/\ell(\ell+1)$.

We identify among the *K2* signals three sets of triplets that share a similar frequency spacing near 11.6 μHz. These are marked with connected arrows in Figure 8.6. If these are rotationally split $\ell = 1$ triplets, they correspond to a rotation period consistent with the signal at $2F_1$ for reasonable values of $C_{k\ell} \approx 0.487$. Only the spacing measured between the two highest frequencies gives a problematic $C_{k\ell} > 0.5$, but this is easily explained if the signal very near the Nyquist frequency (dashed arrow in Figure 8.6) was aliased one more (or fewer) time than the other multiplet components. Based on this

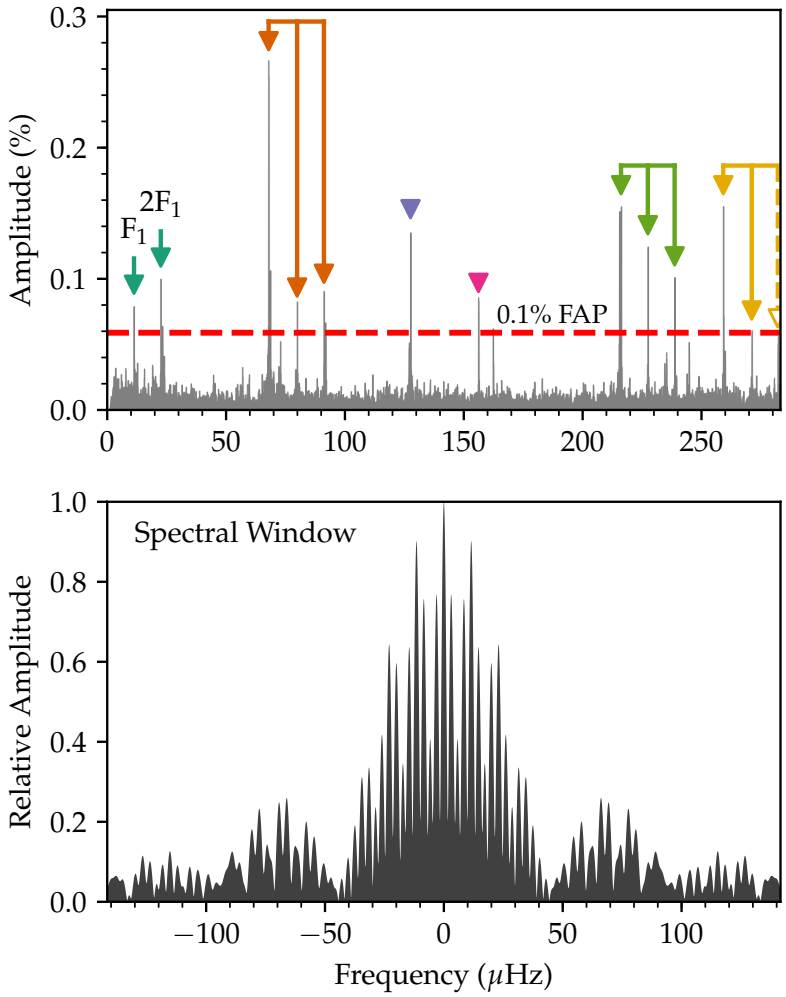

Figure 8.6: TOP: Fourier transform of the *K2* observations of EPIC 220274129 out to the Nyquist frequency with a 0.1% false alarm probability (FAP) significance threshold (see text). We identify rotationally split mode triplets with connected arrows (see text). BOTTOM: The spectral window from four nights of McDonald Observatory observations of EPIC 220274129 over a five night span in Oct/Nov 2016. The highest alias is located 11.5 μHz away from the central peak. The x-axes of both panels have the same scale.

Table 8.6. Significant *K2* Aliases for EPIC 220274129

	Frequency (μHz)	Period (s)	Amplitude (%)
◆ F_1[a]	11.266(7)	88770(60)	0.081(7)
◆ $2F_1$[a]	22.540(6)	44360(12)	0.101(7)
◆ F_2 (m=$\mp$1)[b]	67.901(2)	14727.4(5)	0.266(7)
◆ F_2 (m=0)[b]	79.890(8)	12517.2(1.2)	0.078(7)
◆ F_2 (m=$\pm$1)[b]	91.159(7)	10969.8(8)	0.089(7)
◆ F_3	127.589(4)	7837.8(3)	0.138(7)
◆ F_4	156.169(7)	6403.3(3)	0.082(7)
◆ F_5 (m=$\mp$1)[b]	216.156(4)	4626.29(8)	0.156(7)
◆ F_5 (m=0)[b]	227.427(5)	4397.02(9)	0.126(7)
◆ F_5 (m=$\pm$1)[b]	238.701(6)	4189.34(10)	0.102(7)
◆ F_6 (m=$\mp$1)[b]	259.161(4)	3858.60(6)	0.156(7)
◆ F_6 (m=0)[b]	271.145(10)	3688.07(13)	0.061(7)
◆ F_6 (m=$\pm$1)[b,c]	282.130(11)	3544.47(14)	0.055(7)

[a]F_1 is a subharmonic of the rotation rate, $2F_1$.

[b]Component of a rotationally split ℓ=1 triplet.

[c]This signal was reflected one more or fewer time than the other components of this triplet (see text).

evidence, we identify the sub-Nyquist $2F_1$ signal as starspot modulation on EPIC 220274129's rotation period of 44360 ± 12 s (12.324 ± 0.003 hr) with a photometric subharmonic present at F_1. This period is typical of white dwarfs with measured rotation rates (Kawaler 2015; Hermes et al. 2017d). We do not attempt to match the rotation signals against the ground-based data.

The spectral window of our McDonald observations is displayed in the

bottom panel of Figure 8.6. The near coincidence between the location of the highest alias at 11.5 μHz and the splitting of $\ell = 1$ multiplets underscores the insensitivity of single-site ground-based observations for asteroseismic measurements of typical white dwarf rotation rates.

Because we have measured the splittings of the $\ell = 1$ triplets, we can determine the intrinsic frequencies of each set to *K2* precision by resolving the super-Nyquist ambiguity of any one component. For triplets that we match to the ground-based data, we are also able to identify which signals correspond to the $m = +1$ versus $m = -1$ components.

We exclude a few peaks that reach significant amplitudes from Table 8.6 that are within 1 μHz of other, higher-amplitude signals. These are likely caused by amplitude modulation during the *K2* observations distributing the power into a set of closely spaced peaks (Section 8.3.5). Though it is just shy of our conservative significant threshold, we include the highest frequency component of F_6 because it is also supported by matching the rotational frequency splitting seen in other modes.

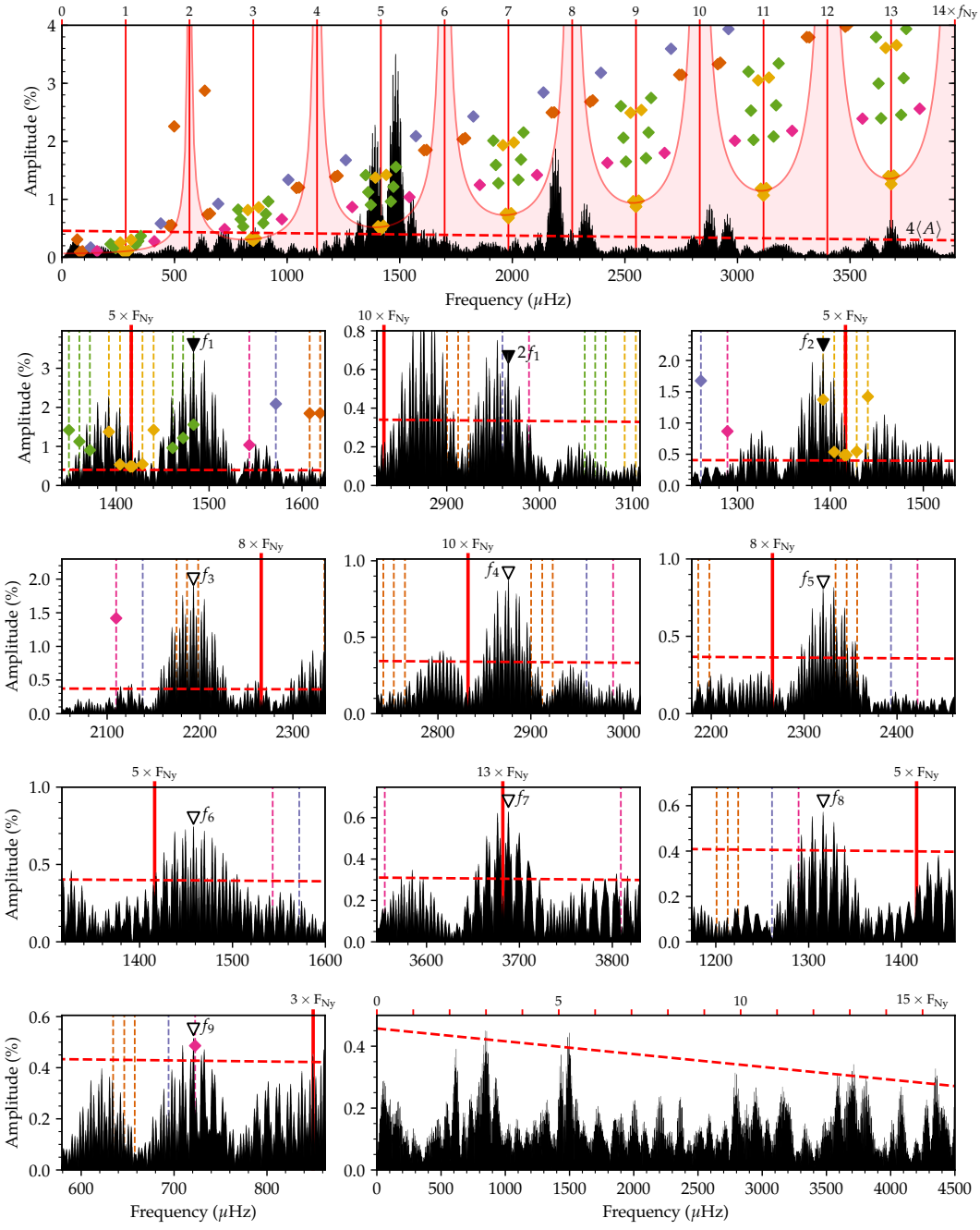

Figure 8.7: (Continued on the following page.)

Figure 8.7: Same as Figure 8.4, except for EPIC 220274129. Mode-by-mode frequency adoption and prewhitening progresses in the sequence of smaller panels from left to right, then top to bottom. The vertical dashed lines and diamonds indicate candidate frequencies and amplitudes underlying the *K2* signals, color-coded to match the triangles in Figure 8.6. The last panel highlights residual power in the fully prewhitened light curve.

The top panel of Figure 8.7 depicts our comparison of possible frequencies underlying the *K2* pulsation signals to the FT of the McDonald data in the full range of significant pulsational power. Like Figure 8.4 for the previous object, the pink shaded region highlights the sensitivity of the *K2* data, and the diamonds are color-coded to match Figure 8.6 and Table 8.6.

We adopt and prewhiten pulsation signals from the ground-based data in each of the smaller panels. First, we recognize that the largest signal from the ground matches a candidate frequency for the highest-amplitude component of the F_5 triplet. Resolving that these signals were aliased off the Nyquist five times in the *K2* data, we can refine the frequencies of all three components by fitting the correct signals to the full *K2* light curve. These precise frequencies are provided in Table 8.7. Because there is a ground-based aliasing degeneracy that matches the $\ell = 1$ rotational splitting, we can only prewhiten the single dominant component from the ground based data. We report a ground-based amplitude for this signal in Table 8.7, but this may not be physical due to the proximity of the other modes. As with EPIC 210377280, we also identify the second harmonic of the dominant signal, as displayed in the second small panel of Figure 8.7.

The third small panel of Figure 8.7 indicates agreement between the next strongest ground-based signal and the triplets of the F_6 detection. We use the *K2* data to refine these fits in Table 8.7.

The *K2* data do not clearly prefer a strong alias of the FT structures around the other signals that we detect from the ground. We prewhiten the

Table 8.7. Frequency Solution for EPIC 220274129

Mode	Frequency (μHz)	Period (s)	Amplitude[a] (%)
f_1 (m=−1)[b]	1460.731(6)	684.589(3)	n/a
f_1 (m=0)[b]	1472.007(5)	679.345(2)	n/a
f_1 (m=+1)[b]	1483.276(4)	674.1832(17)	3.62(7)
$2f_1$ (m=+1)[b,c]	2966.553(8)	337.092(3)	0.64(7)
f_2 (m=−1)[b]	1392.117(4)	718.331(2)	1.92(7)
f_2 (m=0)[b]	1404.099(10)	712.200(5)	n/a
f_2 (m=+1)[b]	1417.303(11)	705.565(5)	n/a
f_3[d]	2192.95(5)	456.006(11)	1.85(7)
f_4[d]	2875.83(11)	347.725(13)	0.90(7)
f_5[d]	2320.67(12)	430.91(2)	0.81(7)
f_6[d,e]	1457.98(10)	685.88(5)	0.97(7)
f_7[d]	3688.13(16)	271.140(11)	0.63(7)
f_8[d]	1315.75(16)	760.02(9)	0.61(7)
f_9[d]	720.89(19)	1387.2(4)	0.51(7)

[a]Amplitude based on fit to ground-based data only, where applicable.

[b]Alias refined by *K2* signal.

[c]Harmonic of previously found signal.

[d]Detected in ground-based data alone and may be incorrect alias of spectral window.

[e]This peak is suspected to be redundant with the f_1 triplet that could not be completely fit out of the ground-based data.

highest aliases one-at-a-time through f_9. Though f_9 does appear to closely match a candidate solution for F_4, the match was not compelling before

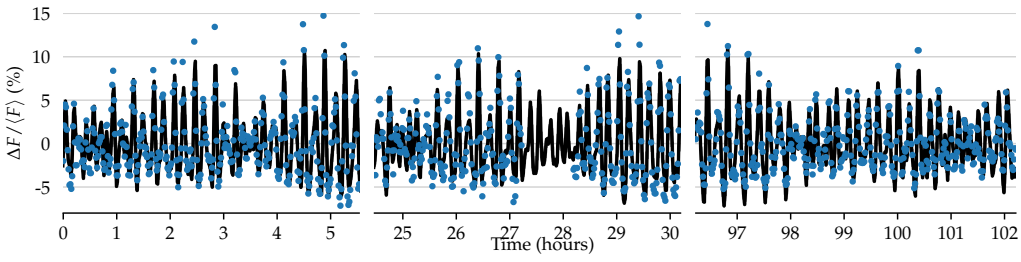

Figure 8.8: The frequency solution overlaid on the ground-based observations of EPIC 220274129 from McDonald Observatory.

prewhitening many ground-based signals that likely include multiple incorrect alias selections, so we err on the side of caution by not claiming *K2* precision for this mode. We also note that f_6 falls within the triplet structure of f_1, which we were unable to completely fit out of our McDonald light curve because of the degeneracy between rotational splitting and the daily ground-based aliasing; we therefore suspect that this signal is redundant with the f_1 triplet properties already refined from *K2* data.

As with Figure 8.4, the last panel displays residual power that is formally significant but difficult to select aliases from; we assert that additional pulsations are likely excited near these frequencies, but we decline to characterize them from these data.

Our final frequency solution for EPIC 220274129 is listed in Table 8.7, and the best fit to the McDonald observations is plotted over the light curve in Figure 8.8.

8.5 Discussion and Conclusions

Using a few nights of ground-based photometry, we have successfully resolved the frequency ambiguities underlying a few of the super-Nyquist signals in the long-cadence *K2* observations of two new ZZ Ceti pulsating white dwarfs, EPIC 210377280 and EPIC 220274129. While each of these data sets is non-ideal for asteroseismic measurements, they complement each other such that we can measure pulsation frequencies to a precision of $\sim 0.01\,\mu$Hz. We used a similar approach in Hermes et al. (2017c) to confirm the super-Nyquist nature of a rotationally split $\ell = 1$ triplet centered on 109.15103 s in the short-cadence *K2* light curve of the ZZ Ceti star EPIC 211914185, but this is the first example of recovering frequencies beyond 4–5 times the Nyquist.

By using the *K2* data to resolve the ground-based aliasing, we have demonstrated the difficulty in selecting the correct peaks. The *K2* data selected the second most probable alias of f_1 from the FT of McDonald data on EPIC 210377280, rather than the marginally higher-amplitude peak. For the *K2*-informed second harmonics of f_1 in both stars, the correct peaks do not have the highest amplitudes locally. Frequency selection from ground-based data alone can be off by many times the daily aliasing of $\approx$11.6 μHz, as many of the frequencies in our solutions certainly are. This error can be much larger than the offset from assuming the wrong azimuthal order, m, which Metcalfe (2003) found to affect but not negate the usefulness of asteroseismic investigations. Prewhitening by incorrect aliases can also adversely impact the properties of pulsation modes later inferred from the residuals. Any comparison of

asteroseismic models to data with gaps should ideally consider thoroughly the many viable combinations of aliases that can describe the light curves.

Our identification of rotationally split $\ell = 1$ triplets in EPIC 220274129 and their correspondence to a photometric rotation period of 44360 ± 12 s (12.32 hr) increases the scientific value of this data set. Similar to the work of Hermes et al. (2017b) for the pulsating helium-atmosphere (DB) white dwarf PG 0112+104 with rotational splittings and a photometric rotation period, detailed asteroseismic analysis of the splittings measured in EPIC 220274129 can test models of differential rotation and empirically constrain values of $C_{k\ell}$.

An unexplained aspect of EPIC 220274129's rotation signature is the presence of a precise subharmonic. The FT of the *K2* data on PG 0112+104 exhibited significant peaks at the rotation rate and its second harmonic, corresponding to the non-sinusoidal morphology of the spot modulation in the light curve (Hermes et al. 2017b), but a subharmonic implies that the spot signature is different every other rotation. Kurtz et al. (2011) suggest that the subharmonic of the rotation frequency of a pulsating roAp star observed by *Kepler*, KIC 10195926, represents a torsional (r-mode) oscillation; however, Balona (2013) highlights our lack of understanding why only one r-mode with $\ell = m = 3$ would be excited to detectable amplitude. To our knowledge, this is the first detection of a rotational subharmonic in a ZZ Ceti star, and while it could correspond to an r-mode oscillation, we refrain from overinterpreting this signal without better models.

Besides those pulsation signals that we were able to refine to *K2* pre-

cision by positively matching between data sets, we identify ≥ 6 additional pulsation signatures from the ground-based light curves of each star. These are measured to lower precision and may be incorrect aliases from the spectral window, but they will still be useful for asteroseismically constraining the interior structures of these rich ZZ Cetis. The *K2* data would not have been sensitive to most of these at their observed amplitudes.

There are also significant signals in the *K2* data that we were unable to confidently match to the McDonald observations. As discussed in Section 8.3.5, pulsation amplitudes of ZZ Ceti stars have been observed to change drastically on month timescales, potentially explaining the apparent absence of many of these during ground-based observations. For instance, the highest multiplet component of F_2 in EPIC 220274129 was almost certainly the dominant mode during *K2* observations, since super-Nyquist signals that are aliased closer to zero frequency generally suffer greater phase smearing. We also neglected some compelling candidate matches to be cautious against overinterpretation.

It is possible that the difference between the pseudo-Nyquist frequency and true Nyquist behavior (described in Section 8.3.1) could also be exploited to place additional constraints on the intrinsic frequencies of the *K2* signals as in Murphy et al. (2013, applied to *Kepler* data). This would provide an important confirmation to our frequency solutions and enable the precise identification of the *K2* aliases that we did not match in our ground based data. The addition of these precise frequencies to the solutions for these stars would increase our leverage on asteroseismically constraining their interiors. The

sensitivity of this method to *K2* data, where light curve durations are much shorter than a spacecraft orbit, has not yet been demonstrated (S. Murphy, private communication).

The spectra and light curves of EPIC 210377280 and EPIC 220274129 are available online at `http://www.k2wd.org`, alongside the published data for short-cadence ZZ Cetis observed with *Kepler* and *K2* (Hermes et al. 2017d).

Chapter 9

Pulsating White Dwarfs in Sparse Time Domain Surveys

Most of my thesis work on pulsating and other variable stars has focused on the analysis of time series photometry. In these observations, we take pains to develop strategies for data acquisition that will ease their later frequency analysis. For *Kepler*/K2, this means submitting likely pulsating white dwarfs for short-cadence observations (an effort that collaborator J. J. Hermes has led). From McDonald, this means using short enough exposure times to keep the Nyquist frequency above the frequency range of astrophysical interest, to obtain enough data to detect low-amplitude signals in Fourier transforms, to have long enough observational baselines to resolve closely spaced signals, and to minimize gaps as much as possible to limit the complexity of the spectral window. Section 8.3 describes in detail the main ways that the characteristics of this type of data can complicate the reliable measurement of stellar variability timescales.

While this has been the arena of my primary thesis efforts, I concurrently developed an interest in another type of astronomical data: time domain survey photometry. Being in the periphery of my focus over the past few years,

my study of stellar pulsation in synoptic astronomical surveys has been mostly anticipatory. Given the speed and sensitivity of upcoming surveys such as the Zwicky Transient Facility (ZTF) and Large Synoptic Survey Telescope (LSST), I have identified this as a most productive area for white dwarf and other stellar variability research over the coming decades. Just considering the increase in survey footprints from *Kepler/K2*, which has been responsible for arguably the most important recent advances is stellar astrophysics from pre-selected targets in a handful of fields, to these deep all-sky time-domain surveys highlights their promise for revealing important new stellar variables. I hope to steer my career toward deeper involvement in these efforts as a postdoctoral researcher or in a longer term position.

Since the goal of synoptic survey design is to capture data that are useful to many areas of astronomy, these tend to not be ideal for the particular subfield of asteroseismology. Still, these efforts will amass a large amount of quality observations over time on a large number of stars. These data will capture the signatures of stellar variability to various degrees of interpretability. I have done some light exploration of the sensitivity and limitations of these data for stellar seismology work, especially for LSST, since an extensive simulation framework exists for that project. The main goal of this work has been to advocate for pulsating star science to the ZTF and LSST communities while these projects are still in their design phases.

I sought involvement with LSST following a discussion with thesis committee member Chuck Claver on the utility of the survey for variable white

dwarf science. I joined the LSST Transients and Variable Stars (TVS) Science Collaboration in 2014 and gave a talk that summer on the prospects of LSST data for the study of pulsating white dwarfs at the 19th European White Dwarf Workshop at the Université de Montréal (Bell et al. 2015a). I was immersed in the details of the project at the 2015 LSST Project and Community Workshop in Bremerton, WA, and quickly became proficient in assessing the sensitivity of simulated surveys with the Metrics Analysis Framework (MAF; Jones et al. 2014). I presented my analyses at the TVS Roadmap Workshop at Argonne National Laboratory in March 2016 (where I also coauthored the "Pulsating Variables" roadmap[1]), the Hot-wiring the Transient Universe V meeting at Villanova University in October 2016, and the ZTF Galactic Plane Science Workshop at Caltech in March 2017.

In this chapter I summarize three separate approaches that I have developed to characterizing the detectability of stellar pulsations in synoptic photometric surveys. These successively relax assumptions about the "good" behavior of the stars, but each suffers certain oversimplifications. They are meant as demonstrations of the potential of these surveys for variable star science. In Section 9.1, I explore the extent to which aliasing caused by sparse—by which I mean infrequently and irregularly sampled—photometric data will muddy the determination of pulsation frequencies. In Section 9.2, I develop a new analytical technique that is applicable for constraining the energetics of pulsating stars that are incoherent in frequency but that have constant

[1] `https://tvs.science.lsst.org/node/23`

pulsation amplitudes. Finally, I test the basic detectability of photometric variations in ZZ Cetis from LSST, assuming no phase, frequency, or amplitude consistency in Section 9.3.

9.1 Frequency Detection in Sparse Time Domain Survey Photometry[2]

Stellar pulsations arise from the excitation of eigenmodes in stars. These vibrations are global; they pass through and are affected by stellar interiors. Thus, measured frequencies of photometric variability can be studied to constrain sub-photospheric structure. Precision asteroseismology requires accurate determination of pulsational eigenfrequencies, typically through Fourier analysis of time series photometry. For evenly sampled data, this relies on four primary observational requirements:

- The signal-to-noise ratio in the Fourier transform is sufficient to reveal pulsations ($S/N \propto \sqrt{\#\text{pts}}$).
- The time series is long enough to resolve closely spaced signals (frequency resolution = 1/duration; i.e., duration exceeds beat periods).
- The Nyquist frequency exceeds the highest pulsation frequency of interest ($f_{\text{Nyq}} = 1/2\tau_{\text{revisit}}$, where τ_{revisit} is the exposure time for continuous observations).

[2]This section is based closely on an indefinitely unpublished extended abstract that I submitted to the Hot-wiring the Transient Universe V meeting.

- Gaps are minimized to avoid aliasing from cycle count ambiguity.

These conditions are not met by most large upcoming surveys; e.g., the baseline cadence for LSST has a 0.02% duty cycle for the main survey. However, the situation for pulsating stars is not as dire as this implies. The left panel of Figure 9.1 shows an example light curve with a single 700 μHz signal at 2.9% amplitude plus 1.2% Gaussian noise sampled for a simulated wide-fast-deep pointing at the current baseline cadence (`minion_1016`) of LSST. The right panel displays the discrete Fourier transform of these data. While this simplistic treatment ignores variations in photometric signal-to-noise and filter changes, it does reveal how the observing strategy affects frequency recoverability. The power in the Fourier transform is centered on the input frequency of 700 μHz, demonstrating that it is safely below the Nyquist frequency, which can be far higher than the average sampling frequency in unevenly sampled data (Eyer & Bartholdi 1999). The spread in the spectral window is a direct reflection of the cadence, with the fine alias spacing caused by daily gaps and the wider envelope by the scheduled 3-hour revisit time. This broad profile may cause confusion in multi-periodic pulsators, but the fine spectral resolution from a 10-year baseline should limit alias overlap. Still, the spectral window could be simplified by optimization of the observing cadence, improving the potential for precision asteroseismology from LSST and other surveys.

This simple analysis supposes that the frequencies and amplitudes of pulsations remain constant for the duration of the survey. This is an unrealistic expectation for pulsating white dwarf stars, but this exercise demon-

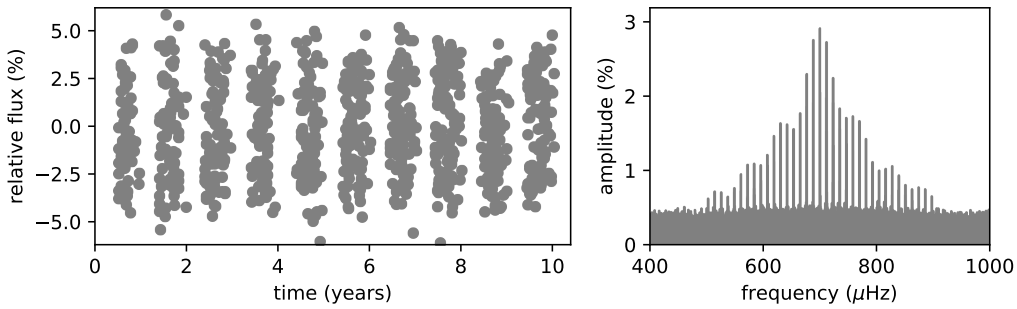

Figure 9.1: Simulated light curve (left) and Fourier transform (right) of a mono-periodic pulsating star in the LSST wide-fast-deep survey. See text for discussion.

strates that some of the classical observer's gut instincts about the limitations of sparsely sampled data may not apply in this situation. The effects of phase/frequency/amplitude variations on pulsation signatures in the frequency domain still need to be explored, and optimal analysis techniques for these situations need to be developed. I will note that I employed the Fourier transform for this analysis purely because of access and familiarity to Fourier software implementations. Because of the uneven phase coverage of synoptic survey data, the Lomb-Scargle periodogram is a more appropriate choice that makes for easier interpretation of the signal-to-noise of peaks, but the same lessons about aliasing still apply. GATSPY provides a fast Lomb-Scargle implementation in Python (VanderPlas 2016), and its author has written an excellent treatise on the algorithm (VanderPlas 2017).

9.2 A New Amplitude-Only Signal Processing Technique

As a thought experiment, I considered our ability to measure individual pulsation amplitudes in sparse time domain photometric surveys. This would be useful for stars with constant pulsation amplitudes, but for which we are unable to measure the individual frequencies. This could be the cases when aliasing is too complicated to disentangle, or for modes that are incoherent in frequency. The latter case may not be a very good approximation to actual pulsating stars (as this is likely accompanied by amplitude variations). The new analytical technique that I developed for this situation is likely applicable to other signal processing problems, astrophysical or otherwise.

This technique was developed over many conversations with my advisor Mike Montgomery. I worked this approach out conceptually, relying mostly on my intuition about Fourier transforms. In order to convince himself, Mike validated the method with a rigorous mathematical proof, which I do not include here. In this section, I present my plausibility argument for a method to disentangle the energetics of individual pulsation modes from the measured distribution of flux values.

The first ingredient of this technique is the probability density function (PDF) of instantaneous flux values with an underlying sinusoidal signal. For a sinusoid of unit semi-amplitude, this takes the form

$$1/\pi\sqrt{1-a^2}, \tag{9.1}$$

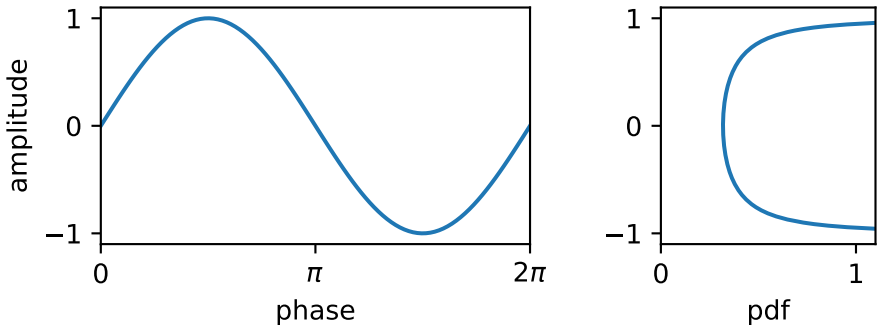

Figure 9.2: Left: a sinusoid plotted through one period. Right: the probability density function (PDF) of values randomly sampled from a sinusoid.

as depicted in Figure 9.2 (with normalization required for signals of different amplitude). A random sampling of a sinusoid is more likely to yield values near the extrema because of the slow rate of change there.

For multi-periodic variables, the PDF of flux values is the convolution of the individual signal PDFs. The convolution theorem states that the Fourier transform (FT) of a convolution of signals is the product of the FTs of the individual signals (see, e.g., Robinson 2016). We assume that the survey observations are essentially random in phase (revisit times far exceed pulsation periods), thus the distribution of measured flux values approximates the PDF. If the FT of Equation 9.1 lends itself to ready interpretation, we may be able to disentangle information about the individual sinusoid amplitudes present in a large set of flux measurements.

It turns out that the FT of Equation 9.1 has the form of a Bessel function of the first kind, which crosses the x-axis with a signature pattern.

FTs obey an uncertainty property, such that the more concentrated the input signal is, the more spread it will be in Fourier space. One important result of this is the Heisenberg uncertainty principle, which states that there are certain pairs of conjugate variables that cannot both be determined to infinite precision in a quantum mechanical system; a precise measurement of the the position of a particle, for example, comes at the cost of being fundamentally unable to precisely measure its momentum.

The zero-crossings of the FT of the measured distribution of flux values for a high-amplitude pulsator therefore are scaled closer together than the zero-crossings for a low-amplitude variable. Since the product of functions with zero-crossings exhibits *all* of these crossings, we expect to be able to detect the number and amplitudes of sinusoids underlying a randomly sampled signal by studying the FT of the histogram of measured values.

Mike Montgomery worked out a fitting routine that uses the Bayesian information criterion to select the most likely number of signals underlying a set of measurements. Testing this method for 2000 randomly timed observations of a signal made up of three sinusoids of amplitudes 5.0, 1.3, and 0.6, we can recover that there are most likely three signals present. The best fit of Bessel functions to the FT of the measured histogram of flux values, both shown in Figure 9.3, produces the amplitude measurements listed in Table 9.1.

So far our numerical tests have been exploratory and quite limited, but we have established a proof-of-concept that this approach can recover information in cases where usual signal-processing assumptions fail (no help

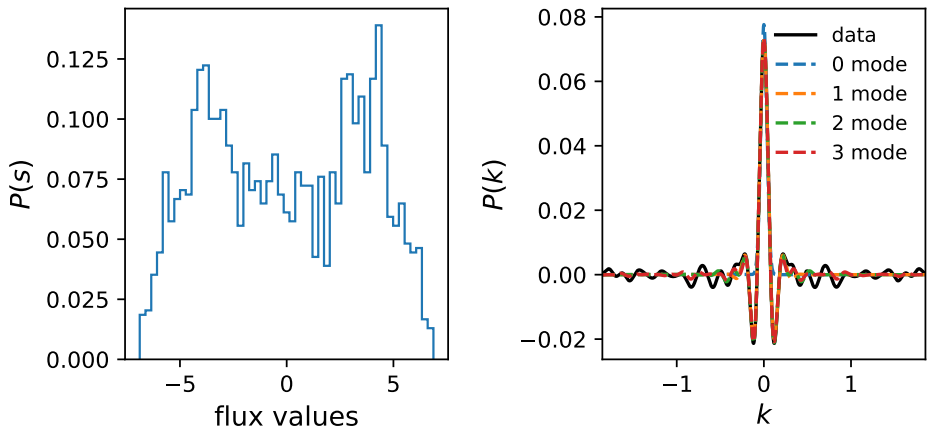

Figure 9.3: Left: measured histogram of flux values for randomly sampled 3-sinusoid signal. Right: Fourier transform of histogram and best-fit Bessel function decompositions.

Table 9.1: Best Fit Amplitudes for Example Simulation

Mode	Amp in	Amp out	Error (%)
1	5.0	4.92	1.6
2	1.3	1.34	-2.9
3	0.6	0.71	-18

from the frequencies). We still need to explore the sensitivity and limitations of this method with more systematic numerical experiments. We especially need to include the effects of noise and quantify uncertainties in the fit parameters. It would also be interesting to explore how the presence of harmonics to the pulsation signals affects the measured flux distribution; the odd (sine) terms of the FT may reveal information about nonlinear pulsation behavior.

9.3 Variability Depth and ZZ Cetis in LSST

LSST solicited community input on how their observing strategy design will impact the scientific yield of the project. For this purpose, they developed an extensive simulation framework for generating hypothetical data products for different assumed strategies (Connolly et al. 2014). Researchers from many astronomical subfields have developed metrics to quantify how well these different simulated surveys serve their scientific needs. These calculations make use of the Metrics Analysis Framework (MAF; Jones et al. 2014), which interprets the simulated pointing and photometric quality records of the LSST Operations Simulator (OpSim; Delgado et al. 2014). This work was produced for inclusion in the LSST Observing Strategy White Paper[3], and I include some excerpts here. The VarDepth MAF metric described here will be used to evaluate the comparative usefulness of different proposed LSST observing strategies to stellar variability studies.

While LSST data should be useful for studying many types of pulsating stars, it is only "synoptic" in this context if it is sensitive to all varieties. For this reason, I treat ZZ Ceti variables as an important benchmark; if LSST will provide sufficient data to significantly advance our understanding of this faintest, lowest-amplitude class of pulsators, then nearly all types of pulsating star science will benefit from the LSST data. We hope to be able to measure frequencies and amplitudes for individual pulsation modes from the

[3]In prep: `github.com/LSSTScienceCollaborations/ObservingStrategy`

LSST data alone, but the realities of frequency and amplitude variability on year timescales may make this more difficult than it seems from my idealistic analyses in the previous sections. For LSST to really revolutionize the field of ZZ Ceti pulsations, we would like to see an order of magnitude increase in the number of known ZZ Cetis, with robust measurements of overall pulsational power in multiple filters. This means a detection of 1000+ ZZ Cetis from excess scatter in the multi-epoch photometry alone, including in the u filter, where we stand to statistically learn the most about the ℓ-identifications of excited modes (Brassard et al. 1995).

With this goal defined, I developed a simple method of predicting the number of ZZ Cetis detected as significantly variable in each band at the end of LSST operations. OpSim provides the observing details for simulated 10-year surveys, including the fields observed, the filters used, and the photometric sensitivity (given as the 5σ depth, $m_{5\sigma}$, the magnitude of a star detected to signal-to-noise 5). I wrote a MAF metric that calculates from these records the limiting magnitude at which a star of a given intrinsic root-mean-squared variability (r.m.s.) would be correctly identified as variable within given tolerances of completeness and contamination in a given filter by the end of the survey, which I call the "variability depth." To do this, I generate 10,000 random realizations of the photometric scatter at each pointing for a set of test magnitudes both with and without underlying intrinsic signal. Figure 9.4 demonstrates this calculation for a single pointing and test magnitude. Because of the effectively random timing of the observations in phase (given

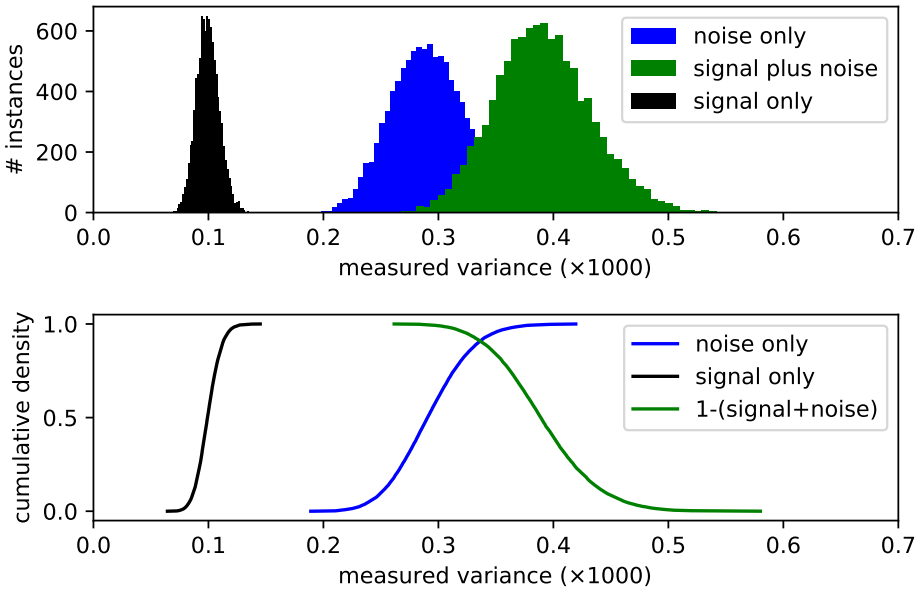

Figure 9.4: An example calculation of the probability density functions of a photometric variable measured for pure-signal, pure-noise, and signal+noise sources at a generic input test magnitude and signal for a single pointing. The top panel shows histograms, and the bottom shows cumulative distributions, which better indicate the percentage of overlap. See text for discussion.

the short periods of white dwarf pulsations compared to typical survey revisit times), there is a spread in the possible measured variances from the same pure underlying intrinsic signal, indicated in black. We model the variability with a Gaussian distribution, which is justified for a multi-modal pulsator by the central limit theorem. The realization of the random noise also populates a probability density function (PDF), which is very sensitive to the magnitude of the target and the total number of observations. The PDF of the measured variance when both measurement noise and intrinsic signal are present will be

greater than the noise-only or signal-only cases on average, but there can still be significant overlap. We can be confident that we will identify the majority of variable stars of an assumed intrinsic signal to a limiting magnitude where the signal+noise PDF is well resolved from the noise-only case. For the LSST Observing Strategy White Paper, I allowed for a 90% completeness goal and 10% contamination, meaning that the 90% point of the noise-only cumulative density distribution overlaps the 10% levels of the signal+noise distribution at the variability depth, which is roughly the condition depicted in the bottom panel of Figure 9.4.

For LSST, each patch of sky is observed a different number of times and through different filters and conditions. I can calculate the variability depth as a function of position and filter for any intrinsic signal of interest. Figure 9.5 shows a map of the variability depth in the r band after 10 simulated years of the baseline cadence (OpSim run name minion_1016) for 1% r.m.s. variables. We see that for most of the survey area, 1% variables with r-band magnitudes of 19 will be detected with 10% contamination and 10% incompleteness. Brighter targets will be more reliable recovered. Areas of the sky that receive fewer or greater numbers of r-band observations have shallower and deeper variability depths, respectively.

To estimate the number of ZZ Cetis from which LSST will detect significant excess photometric scatter, I created maps of the expected ZZ Ceti magnitude distribution across the sky in different filters. I built this by querying the CatSim database at the University of Washington, which contains a repre-

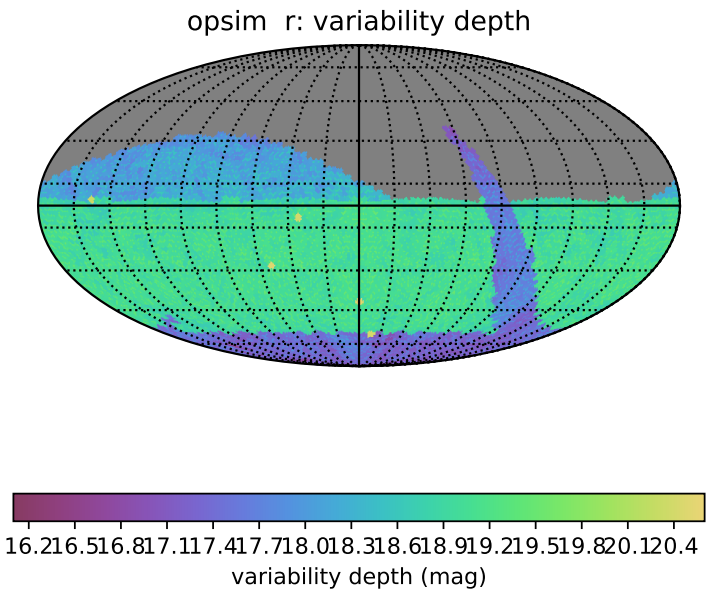

Figure 9.5: Example output of the VarDepth MAF metric run on the current baseline cadence, minion_1016, after 10 years of survey operations. Input parameters and SQL queries were set to calculate the magnitude limit for detecting 90% of pulsators with 1% r.m.s. variability from a cut on the measured variance in the r band (allowing contamination from 10% of nonvariable sources).

sentative model of the Galactic stellar content, including white dwarf spectral energy distributions based on the Pierre Bergeron et al. cooling tracks[4]. I accept any simulated DA white dwarf with $10{,}600 \leq T_{\rm eff} \leq 12{,}500\,{\rm K}$ as a ZZ Ceti, where neglecting the slight $\log g$-dependence of the instability strip should not prohibit representative statistics. The map of ZZ Ceti density between $16 < r < 27$ is displayed in Figure 9.6 (the northernmost declinations

[4] `http://www.astro.umontreal.ca/~bergeron/CoolingModels/`

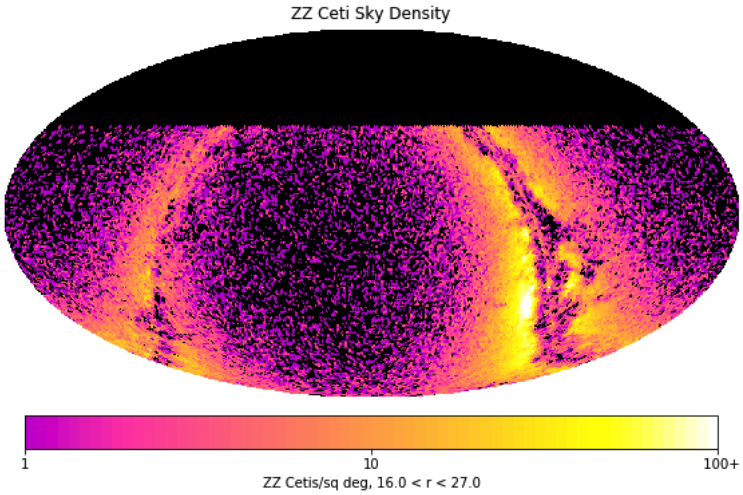

Figure 9.6: Simulated distribution of Galactic ZZ Cetis with r-band magnitudes between 16 and 27.

are irrelevant to LSST).

By combining these ZZ Ceti density maps with the results of the VarDepth metric, I can estimate the number of ZZ Cetis that LSST will detect in different passbands. To simplify the calculations, we model all ZZ Cetis as showing the same overall amount of photometric variability (so that VarDepth only has to be calculated once across the sky). Mukadam et al. (2006) measured the rms pulsational power of ZZ Cetis across the instability strip and found that the lowest-amplitude variables showed about a 1% standard deviation to their underlying flux variations. If we assume 1% variability for all ZZ Cetis and calculate the corresponding VarDepth (allowing 10% contamination and 10% incompleteness) and sum the number of ZZ Cetis to that survey limit, we expect to detect the number of ZZ Cetis listed in Table 9.2. I present counts from both the r and u bands for two

OpSim outputs: minion_1016, which is the current baseline LSST cadence, and kraken_1045, which obtains u band exposures with double the exposure time (60 s instead of 30 s).

Table 9.2: ZZ Ceti Recovery for 1% R.M.S. Variability

OpSim Run	Filter	# ZZ Cetis
minion_1016	u	9
	r	127
kraken_1045	u	17
	r	123

This calculation predicts over 100 ZZ Ceti detections in the r band and $\sim$10 in the u band, which is far below the goal of 1000+ in multiple bands. However, one must recall that most ZZ Cetis show greater variability than the 1% rms assumed for ZZ Cetis in this first calculation. The conclusion is that LSST will generally not be sensitive to the lowest-amplitude ZZ Cetis.

To get a more realistic count of the total number of ZZ Cetis expected from LSST, we can model all ZZ Cetis as having the average rms scatter of roughly 3% (Mukadam et al. 2006). Under this assumption, we calculate the expected counts listed in Table 9.3.

Table 9.3: ZZ Ceti Recovery for 3% R.M.S. Variability

OpSim Run	Filter	# ZZ Cetis
minion_1016	u	197
	r	1601
kraken_1045	u	325
	r	1534

These numbers support that LSST will make considerable new discoveries of ZZ Cetis, yielding over 1500 from the r band alone. The ZZ Cetis that will be detected purely from the u band are not so numerous, but it is important to remember that these observations will not be analyzed in isolation. A variable source will be best identified by considering the observations in all bands together, and then constraints on the variability in different bands can be made. Still, robust measurements of u band amplitudes are most important for doing ZZ Ceti astrophysics directly from the LSST observations, so I advocate for any observing strategy that increases the number of expected ZZ Ceti detections in the u band. We see from Tables 9.2 and 9.3 that doubling the exposure times in u increases the number of detections in u considerably more than it detracts from the expected detections in r, which are already plentiful.

Appendices

Appendix A

Contributed Observations

Over the course of 225 nights personally observed at McDonald Observatory as a graduate student, I have had the privilege to contribute observations to numerous exciting projects led by my collaborators. Most of these targeted known or candidate pulsating white dwarfs, the majority being DAVs. Some have focused on the opposite extremes of the DAV instability strip than have been the primary topic of this thesis: high-mass DAVs (e.g., Curd et al. 2017) and long-term modeling of stable modes in hot DAVs to constrain secular evolution and reflex motions from planetary companions (follow-up work to Mullally et al. 2008; Winget et al. 2015). I have also observed many white dwarfs in *Kepler*/*K2* fields, either to identify new pulsators or to complement the space-based data with a faster cadence or a different passband. In this appendix, I want to highlight the diversity of my observational work by briefly presenting some light curves that I obtained on white dwarfs that are *not* pulsating. For those works that are not yet published, the light curves are presented with the permission of the project PIs.

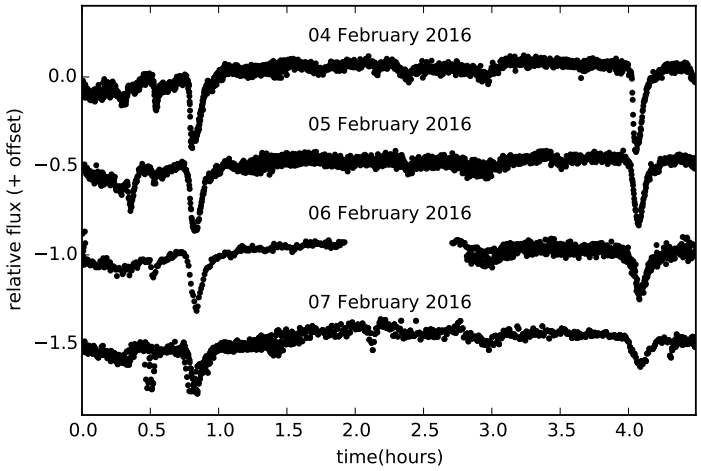

Figure A.1: Light curves of WD 1145+017 from four consecutive nights in February 2016 show transits of multiple planetesimals around the white dwarf, the morphologies of which evolve over these few nights. The light curves are folded on an average orbital period of 4.493 days, with each night offset by −0.5 in relative flux.

A.1 WD 1145+017 – disintegrating planetesimals transiting a white dwarf

The discovery of disintegrating planetesimals transiting WD 1145+017 in *K2* photometry by Vanderburg et al. (2015) was one of the most important recent results in the search for exoplanets around white dwarfs. This sparked extensive ground-based follow-up from small and large telescopes in multiple passbands. One such update came from Gänsicke et al. (2016), who used high speed photometry to track the orbital evolution of different planetesimal chunks. After realizing that our ProEM camera can be rotated on the sky to just fit a bright comparison star in the opposite corner from WD 1145+017, I

began to contribute additional observations to the continued monitoring effort led by Boris Gänsicke. This evolution is apparent in the light curves that I obtained from the 2.1-meter Otto Struve Telescope during four consecutive nights in February 2016 run at McDonald Observatory, displayed in Figure A.1. Over the past two years we have observed this target dozens of times as part of a larger campaign that includes observations from the Thai National Telescope and the Issac Newton Telescope.

A.2 SDSS J0651+2844 – eclipsing double white dwarf binary decaying from gravitational radiation

This is the object that I have observed the most at McDonald Observatory during my graduate work, with our group obtaining well over 100 hours of coverage over the last three years. This object was identified as a double-white-dwarf eclipsing binary system with a 12.75-minute orbit by Brown et al. (2011). Hermes et al. (2012b) were the first to make the exciting measurement of orbital decay of this system caused by gravitational radiation. After J. J. Hermes departed from UT-Austin, I took over as the primary observer for the continued monitoring of orbital decay in this system. A typical light curve of this system is displayed in the sample screen shot of my online reduction software in the next section, Figure B.1. Primary and secondary eclipses, as well as ellipsoidal variations (from tidal distortions) are all clearly visible in this light curve. By the end of the 2017 observing season, we were measuring mid-eclipse arrival times more than three minutes earlier than they would

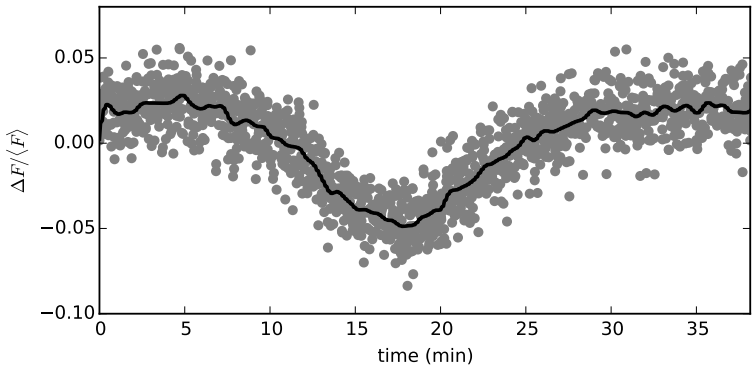

Figure A.2: Folded discovery light curve of spot modulation in the massive DA white dwarf SDSS J1529+2928 from McDonald Observatory on 09 June 2015 (gray) with a smoothed version plotted in black.

have been if gravitational radiation was not shrinking the orbits. A detailed publication of this work is forthcoming.

A.3 SDSS J1529+2928 – starspot modulation from a massive white dwarf

Originally observed as a candidate pulsating massive white dwarf for the survey published in Curd et al. (2017), my data from the McDonald Observatory 2.1-meter Otto Struve Telescope revealed striking variability with a period of 38 minutes. This discovery light curve is displayed in Figure A.2 (some observations of this system from the Apache Point Observatory 3.5-meter predate this light curve, but the data were not reduced until after the discovery from McDonald). Our model of starspot modulation is described by Kilic et al. (2015b). We followed this system up with multiple filters to constrain the temperature of the spot. The Hubble Space Telescope will obtain

a light curve of this system in the UV with the Cosmic Origins Spectrograph in the coming months to further test this model. These observations may confirm a suspected flux redistribution from metals concentrated by magnetic fields onto a spot, i.e., brightening in the UV while dimming occurs in the optical.

Appendix B

OLD MAID: OnLine Data Management And Interactive Display Software*

When obtaining time series photometry at the telescope, it is important for the observer to be able to visualize their data on-the-fly to inform their decisions about when to change targets. Real-time light curves and Fourier transforms can signal a number of important situations: a signal in Fourier space has reached the target signal-to-noise; signals have become sufficiently resolved; an upper limit on the presence of some signal has been set sufficiently low to accept the null result; the event of interest (e.g., and eclipse) is over; or there is not sufficient signal-to-noise in the light curve for it to be of practical value. Real time displays can also help the observe to monitor observing conditions and to easily tweak the telescope focus.

I wrote the OnLine Data Management And Interactive Display (OLD MAID) Software with PyQt 4[1] and PyQtGraph[2] to serve this need. This program was presented to the UT-Austin astronomy community at the

* Some of this chapter was published in Bell, K. J., 2015, *OnLine Data Management And Interactive Display Software for time series photometry with the ProEM Camera on the McDonald Observatory 82" Otto Struve Telescope*, Proceedings of the Frank N. Bash Symposium 2015, 23.

[1] `https://riverbankcomputing.com/software/pyqt`

[2] `http://www.pyqtgraph.org/`

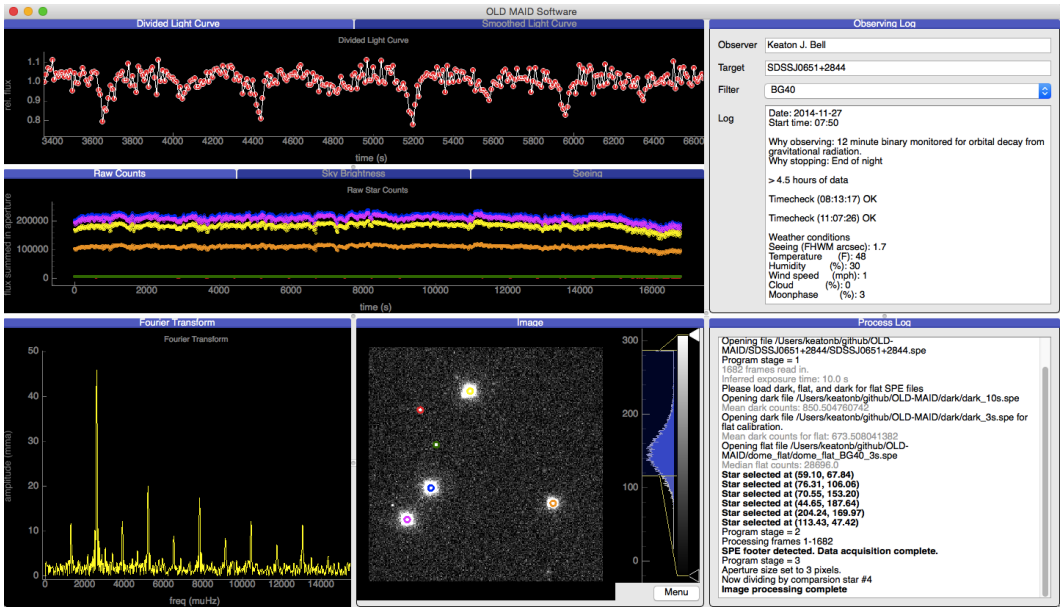

Figure B.1: Screen shot of the OLD MAID software working on time series photometry of the 12.75-minute eclipsing double-white-dwarf binary SDSS J0651+2844 (Hermes et al. 2012b, 2017 in prep; Section A.2).

2015 Frank N. Bash Symposium on the topic of New Horizons in Astronomy and summarized in a short proceedings paper (Bell 2015). A screen shot of the program in action is displayed in Figure B.1.

The key features are: automatic dark subtraction and flatfielding, display of most recent image with marked apertures, selection of target and comparison stars with the mouse, raw light curves, divided light curves (optionally smoothed), records of seeing and sky brightness over time, Fourier transform, ability for user to select aperture size and comparison star to divide by, and manual rejection of "bad" points. The observing log fields are not currently saved automatically, but a screenshot of the program and all visible fields is au-

tomatically saved when the end of data acquisition is automatically detected. A record of per-frame timestamps is also saved at this point.

OLD MAID could benefit from additional development, especially to handle multi-filter data, which we are beginning to obtain a lot of now that Zach Vanderbosch has installed an automatic filter wheel in the light path. I aim to generally clean the program up to make it easier for others in the group to update as needed in future years. The program is publicly available at `https://github.com/ccd-utexas/OLD-MAID`.

Bibliography

Aerts, C., Christensen-Dalsgaard, J., & Kurtz, D. W. 2010, Asteroseismology, Astronomy and Astrophysics Library, Springer-Verlag, Berlin

Althaus, L. G., Córsico, A. H., Isern, J., & García-Berro, E. 2010, A&A Rev., 18, 471

Althaus, L. G., Miller Bertolami, M. M., & Córsico, A. H. 2013, A&A, 557, A19

Armstrong, D. J., Kirk, J., Lam, K. W. F., et al. 2015, A&A, 579, A19

Balona, L. A. 2013, MNRAS, 436, 1415

Baran, A. S., Koen, C., & Pokrzywka, B. 2015, MNRAS, 448, L16

Barentsen, G. 2015, Astrophysics Source Code Library, ascl:1503.001

Bell, K. 2015, Proceedings of the Frank N. Bash Symposium 2015 (BASH2015). 18-20 October. The University of Texas at Austin, USA, 23

Bell, K. J., Claver, C. F., Krughoff, K. S., et al. 2015a, 19th European Workshop on White Dwarfs, 493, 425

Bell, K. J., Gianninas, A., Hermes, J. J., et al. 2017a, ApJ, 835, 180

Bell, K. J., Hermes, J. J., Bischoff-Kim, A., et al. 2015c, ApJ, 809, 14

Bell, K. J., Hermes, J. J., Montgomery, M. H., et al. 2016, ApJ, 829, 82

Bell, K. J., Hermes, J. J., Montgomery, M. H., et al. 2017b, 20th European White Dwarf Workshop, 509, 303

Bell, K. J., Hilton, E. J., Davenport, J. R. A., et al. 2012, PASP, 124, 14

Bell, K. J., Kepler, S. O., Montgomery, M. H., et al. 2015b, 19th European Workshop on WDs, 493, 217

Benz, A. O., & Güdel, M. 2010, ARA&A, 48, 241

Bergeron, P., Fontaine, G., Billères, M., Boudreault, S., & Green, E. M. 2004, ApJ, 600, 404

Bergeron, P., Wesemael, F., Lamontagne, R., et al. 1995, ApJ, 449, 258

Binzel, R. P., Hanner, M. S., & Steel, D. I. 2000, Allen's Astrophysical Quantities, 315

Bischoff-Kim, A., Montgomery, M. H., & Winget, D. E. 2008, ApJ, 675, 1505

Bischoff-Kim, A., & Østensen, R. H. 2011, ApJ, 742, L16

Bischoff-Kim, A., Østensen, R. H., Hermes, J. J., & Provencal, J. L. 2014, ApJ, 794, 39

Blanton, M. R., & Roweis, S. 2007, AJ, 133, 734

Borucki, W. J., Koch, D., Basri, G., et al. 2010, Science, 327, 977

Brassard, P., Fontaine, G., & Wesemael, F. 1995, ApJS, 96, 545

Breger, M., Stich, J., Garrido, R., et al. 1993, A&A, 271, 482

Brickhill, A. J. 1975, MNRAS, 170, 405

Brickhill, A. J. 1991, MNRAS, 251, 673

Brown, W. R., Gianninas, A., Kilic, M., Kenyon, S. J., & Allende Prieto, C. 2016, ApJ, 818, 155

Brown, W. R., Kilic, M., Allende Prieto, C., Gianninas, A., & Kenyon, S. J. 2013, ApJ, 769, 66

Brown, W. R., Kilic, M., Allende Prieto, C., & Kenyon, S. J. 2010, ApJ, 723, 1072

Brown, W. R., Kilic, M., Allende Prieto, C., & Kenyon, S. J. 2012, ApJ, 744, 142

Brown, W. R., Kilic, M., & Gianninas, A. 2017, ApJ, 839, 23

Brown, W. R., Kilic, M., Hermes, J. J., et al. 2011, ApJ, 737, L23

Bryson, S. T., Jenkins, J. M., Gilliland, R. L., et al. 2013, PASP, 125, 889

Calcaferro, L. M., Córsico, A. H., & Althaus, L. G. 2017, A&A, 600, A73

Carter, J. A., Rappaport, S., & Fabrycky, D. 2011, ApJ, 728, 139

Castanheira, B. G., Kepler, S. O., Costa, A. F. M., et al. 2007, A&A, 462, 989

Chandrasekhar, S. 1931, ApJ, 74, 81

Chatfield, C. 2007, The Analysis of Time Series: An Introduction, (6th ed.; Florida, US: CRC Press)

Christensen-Dalsgaard, J., & Thompson, M. J. 2011, IAU Symposium, 271, 32

Clarke, B., Kolodziejczak, J. J, & Caldwell, D. A. 2014, American Astronomical Society Meeting Abstracts #224, 224, 120.07

Clemens, J. C., Crain, J. A., & Anderson, R. 2004, Proc. SPIE, 5492, 331

Clemens, J. C. 1993, Baltic Astronomy, 2, 407

Connolly, A. J., Angeli, G. Z., Chandrasekharan, S., et al. 2014, Proc. SPIE, 9150, 915014

Córsico, A. H., & Althaus, L. G. 2014a, A&A, 569, A106

Córsico, A. H., & Althaus, L. G. 2014b, ApJ, 793, L17

Córsico, A. H., & Althaus, L. G. 2016a, A&A, 585, A1

Córsico, A. H., Althaus, L. G., Miller Bertolami, M. M., & Bischoff-Kim, A. 2012, A&A, 541, A42

Córsico, A. H., Althaus, L. G., Serenelli, A. M., et al. 2016c, A&A, 588, A74

Corti, M. A., Kanaan, A., Córsico, A. H., et al. 2016, A&A, 587, L5

Cui, X.-Q., Zhao, Y.-H., Chu, Y.-Q., et al. 2012, Research in Astronomy and Astrophysics, 12, 1197

Curd, B., Gianninas, A., Bell, K. J., et al. 2017, MNRAS, 468, 239

Davenport, J. R. A., Hawley, S. L., Hebb, L., et al. 2014, ApJ, 797, 122

Delgado, F., Saha, A., Chandrasekharan, S., et al. 2014, Proc. SPIE, 9150, 915015

De Marco, O., Long, J., Jacoby, G. H., et al. 2015, MNRAS, 448, 3587

Di Stefano, R. 2011, White Dwarf Atmospheres and Circumstellar Environments, 89

Dolez, N., Vauclair, G., Kleinman, S. J., et al. 2006, A&A, 446, 237

Drake, A. J., Djorgovski, S. G., Mahabal, A., et al. 2009, ApJ, 696, 870

Dziembowski, W. 1977, Acta Astron., 27, 1

Epanechnikov, V. A. 1969, Theory Probab. Appl., 14, 153

Eyer, L., & Bartholdi, P. 1999, A&AS, 135, 1

Falcon, R. E., Winget, D. E., Montgomery, M. H., & Williams, K. A. 2010, ApJ, 712, 585

Fontaine, G., Brassard, P., & Bergeron, P. 2001, PASP, 113, 409

Fontaine, G., & Brassard, P. 2008, PASP, 120, 1043

Fontaine, G., Istrate, A., Gianninas, A., Brassard, P., & Van Grootel, V. 2017, 20th European White Dwarf Workshop, 509, 347

Fuchs, J. T., Dunlap, B. H., Clemens, J. C., et al. 2017, 20th European White Dwarf Workshop, 509, 263

Gänsicke, B. T., Aungwerojwit, A., Marsh, T. R., et al. 2016, ApJ, 818, L7

García-Berro, E., & Oswalt, T. D. 2016, NewAR, 72, 1

Gershberg, R. E. 1972, Ap&SS, 19, 75

Gianninas, A., Bergeron, P., & Fontaine, G. 2005, ApJ, 631, 1100

Gianninas, A., Bergeron, P., & Ruiz, M. T. 2011, ApJ, 743, 138

Gianninas, A., Curd, B., Fontaine, G., Brown, W. R., & Kilic, M. 2016, ApJ, 822, L27

Gianninas, A., Kilic, M., Brown, W. R., Canton, P., & Kenyon, S. J. 2015, ApJ, 812, 167

Gianninas, A., Strickland, B. D., Kilic, M., & Bergeron, P. 2013, ApJ, 766, 3

Gilliland, R. L., Brown, T. M., Christensen-Dalsgaard, J., et al. 2010a, PASP, 122, 131

Gilliland, R. L., Jenkins, J. M., Borucki, W. J., et al. 2010b, ApJ, 713, L160

Goldreich, P., & Wu, Y. 1999a, ApJ, 511, 904

Goldreich, P., & Wu, Y. 1999b, ApJ, 523, 805

Greiss, S., Gänsicke, B. T., Hermes, J. J., et al. 2014, MNRAS, 438, 3086

Greiss, S., Hermes, J. J., Gänsicke, B. T., et al. 2016, MNRAS, 457, 2855

Hansen, C. J., Winget, D. E., & Kawaler, S. D. 1985, ApJ, 297, 544

Hawley, S. L., Davenport, J. R. A., Kowalski, A. F., et al. 2014, ApJ, 797, 121

Heber, U. 2016, PASP, 128, 082001

Hekker, S., & Christensen-Dalsgaard, J. 2017, A&A Rev., 25, #1

Hermes, J. J., Brown, W. R., Kilic, M., et al. 2014a, ApJ, 792, 39

Hermes, J. J., Charpinet, S., Barclay, T., et al. 2014b, ApJ, 789, 85

Hermes, J. J., Kilic, M., Brown, W. R., et al. 2012b, ApJ, 757, L21

Hermes, J. J., Gänsicke, B. T., Bischoff-Kim, A., et al. 2015a, MNRAS, 451, 1701

Hermes, J. J., Gänsicke, B. T., & Breedt, E. 2017a, 20th European White Dwarf Workshop, 509, 453

Hermes, J. J., Gänsicke, B. T., Kawaler, S. D., et al. 2017d, in prep.

Hermes, J. J., Kawaler, S. D., Bischoff-Kim, A., et al. 2017b, ApJ, 835, 277

Hermes, J. J., Kawaler, S. D., Romero, A. D., et al. 2017c, ApJ, 841, L2

Hermes, J. J., Kepler, S. O., Castanheira, B. G., et al. 2013b, ApJ, 771, L2

Hermes, J. J., Montgomery, M. H., Bell, K. J., et al. 2015b, ApJ, 810, L5

Hermes, J. J., Montgomery, M. H., Gianninas, A., et al. 2013c, MNRAS, 436, 3573

Hermes, J. J., Montgomery, M. H., Winget, D. E., et al. 2012a, ApJ, 750, L28

Hermes, J. J., Montgomery, M. H., Winget, D. E., et al. 2013a, ApJ, 765, 102

Hermes, J. J., Mullally, F., Østensen, R. H., et al. 2011, ApJ, 741, L16

Hewett, P. C., Warren, S. J., Leggett, S. K., & Hodgkin, S. T. 2006, MNRAS, 367, 454

Hilton, E. J. 2011, Ph.D. Thesis, University of Washington

Hilton, J. L. 2002, Asteroids III, 103

Holberg, J. B., & Bergeron, P. 2006, AJ, 132, 1221

Horne, K. 1986, PASP, 98, 609

Howell, S. B., Sobeck, C., Haas, M., et al. 2014, PASP, 126, 398

Istrate, A. G., Fontaine, G., Gianninas, A., et al. 2016b, A&A, 595, L12

Istrate, A. G., Marchant, P., Tauris, T. M., et al. 2016a, A&A, 595, A35

Jeffery, C. S., Baran, A. S., Behara, N. T., et al. 2017, MNRAS, 465, 3101

Jones, R. L., Yoachim, P., Chandrasekharan, S., et al. 2014, Proc. SPIE, 9149, 91490B

Jura, M. 2008, AJ, 135, 1785

Kanaan, A., Kepler, S. O., & Winget, D. E. 2002, A&A, 389, 896

Karczmarek, P., Wiktorowicz, G., Iłkiewicz, K., et al. 2017, MNRAS, 466, 2842

Karoff, C. 2014, ApJ, 781, L22

Kawaler, S. D. 2004, Stellar Rotation, 215, 561

Kawaler, S. D. 2015, 19th European Workshop on White Dwarfs, 493, 65

Kawka, A., & Vennes, S. 2006, ApJ, 643, 402

Kepler, S. O., Costa, J. E. S., Castanheira, B. G., et al. 2005, ApJ, 634, 1311

Kepler, S. O., Koester, D., Romero, A. D., Ourique, G., & Pelisoli, I. 2017, 20th European White Dwarf Workshop, 509, 421

Kepler, S. O., Nather, R. E., Winget, D. E., et al. 2003, A&A, 401, 639

Kepler, S. O., Pelisoli, I., Koester, D., et al. 2015, MNRAS, 446, 4078

Kepler, S. O., Pelisoli, I., Koester, D., et al. 2016, MNRAS, 455, 3413

Kilic, M., Brown, W. R., Allende Prieto, C., et al. 2011a, ApJ, 727, 3

Kilic, M., Brown, W. R., Kenyon, S. J., et al. 2011b, MNRAS, 413, L101

Kilic, M., Brown, W. R., Allende Prieto, C., et al. 2012, ApJ, 751, 141

Kilic, M., Gianninas, A., Bell, K. J., et al. 2015b, ApJ, 814, L31

Kilic, M., Hermes, J. J., Gianninas, A., & Brown, W. R. 2015a, MNRAS, 446, L26

Kilic, M., Stanek, K. Z., & Pinsonneault, M. H. 2007, ApJ, 671, 761

Kinemuchi, K., Barclay, T., Fanelli, M., et al. 2012, PASP, 124, 963

Kleinman, S. J., Kepler, S. O., Koester, D., et al. 2013, ApJS, 204, 5

Kleinman, S. J., Nather, R. E., Winget, D. E., et al. 1998, ApJ, 495, 424

Kochanek, C. S., Shappee, B. J., Stanek, K. Z., et al. 2017, PASP, submitted

Koen, C. 2006, MNRAS, 371, 1390

Koester, D. 2010, Mem. Soc. Astron. Italiana, 81, 921

Koester, D. 2013, Planets, Stars and Stellar Systems. Volume 4: Stellar Structure and Evolution, 4, 559

Koester, D., Kepler, S. O., Kleinman, S. J., & Nitta, A. 2009a, Journal of Physics Conference Series, 172, 012006

Koester, D., Voss, B., Napiwotzki, R., et al. 2009b, A&A, 505, 441

Koester, D., & Wilken, D. 2006, A&A, 453, 1051

Kowalski, P. M., & Saumon, D. 2006, ApJ, 651, L137

Kurtz, D. W., Cunha, M. S., Saio, H., et al. 2011, MNRAS, 414, 2550

Kurtz, D. W., Elkin, V. G., Cunha, M. S., et al. 2006, MNRAS, 372, 286

Kuschnig, R., Weiss, W. W., Gruber, R., Bely, P. Y., & Jenkner, H. 1997, A&A, 328, 544

Lamb, D. Q., & van Horn, H. M. 1975, ApJ, 200, 306

Landau, L. D., & Lifshitz, E. M. 1958, The Classical Theory of Fields, (Oxford: Oxford Pergamon Press)

Landolt, A. U. 1968, ApJ, 153, 151

Latter, W. B., Schmidt, G. D., & Green, R. F. 1987, ApJ, 320, 308

Lawlor, T. M., & MacDonald, J. 2006, MNRAS, 371, 263

Ledoux, P. 1951, ApJ, 114, 373

Lenz, P., & Breger, M. 2004, The A-Star Puzzle, 224, 786

Liebert, J., Bergeron, P., & Holberg, J. B. 2005, ApJS, 156, 47

Luger, R., Agol, E., Kruse, E., et al. 2016, AJ, 152, 100

Luger, R., Kruse, E., Foreman-Mackey, D., Agol, E., & Saunders, N. 2017, arXiv:1702.05488

Marsh, T. R. 1989, PASP, 101, 1032

Marsh, T. R., Dhillon, V. S., & Duck, S. R. 1995, MNRAS, 275, 828

Maxted, P. F. L., Serenelli, A. M., Marsh, T. R., et al. 2014, MNRAS, 444, 208

Maxted, P. F. L., Serenelli, A. M., Miglio, A., et al. 2013, Nature, 498, 463

Metcalfe, T. S. 2003, Baltic Astronomy, 12, 247

Mestel, L. 1952, MNRAS, 112, 583

Moffett, T. J. 1974, ApJS, 29, 1

Monet, D. G. 1998, Bulletin of the American Astronomical Society, 30, 120.03

Montgomery, M. H. 1998, Ph.D. Thesis

Montgomery, M. H. 2005, ApJ, 633, 1142

Montgomery, M. H., & Odonoghue, D. 1999, Delta Scuti Star Newsletter, 13, 28

Morris, S. L. 1985, ApJ, 295, 143

Morris, S. L., & Naftilan, S. A. 1993, ApJ, 419, 344

Montgomery, M. H., Provencal, J. L., Kanaan, A., et al. 2010, ApJ, 716, 84

Mukadam, A. S., Montgomery, M. H., Winget, D. E., Kepler, S. O., & Clemens, J. C. 2006, ApJ, 640, 956

Mukadam, A. S., Montgomery, M. H., Kim, A., et al. 2007, 15th European Workshop on White

Mukadam, A. S., Mullally, F., Nather, R. E., et al. 2004, ApJ, 607, 982 Dwarfs, 372, 587

Mukadam, A. S., & Nather, R. E. 2005, Journal of Astrophysics and Astronomy, 26, 321

Mullally, F., Winget, D. E., De Gennaro, S., et al. 2008, ApJ, 676, 573

Murphy, S. J. 2014, Ph.D. Thesis

Murphy, S. J., Shibahashi, H., & Kurtz, D. W. 2013, MNRAS, 430, 2986

Nather, R. E., Winget, D. E., Clemens, J. C., Hansen, C. J., & Hine, B. P. 1990, ApJ, 361, 309

Nelemans, G., Yungelson, L. R., Portegies Zwart, S. F., & Verbunt, F. 2001, A&A, 365, 491

Nitta, A., Winget, D. E., Kepler, S. O., et al. 1999, 11th European Workshop on White Dwarfs, 169, 104

Østensen, R. H., Bloemen, S., Vučković, M., et al. 2011, ApJ, 736, L39

Palaversa, L., Ivezić, Ž., Eyer, L., et al. 2013, AJ, 146, 101

Pamyatnykh, A. A. 1999, Acta Astronomica, 49, 119

Pelisoli, I., Kepler, S. O., Koester, D., & Romero, A. D. 2017, 20th European White Dwarf Workshop, 509, 447

Perlmutter, S., Aldering, G., Goldhaber, G., et al. 1999, ApJ, 517, 565

Pfeiffer, B., Vauclair, G., Dolez, N., et al. 1996, A&A, 314, 182

Pietrzyński, G., Thompson, I. B., Gieren, W., et al. 2012, Nature, 484, 75

Pigulski, A., Kołaczkowski, Z., Ramza, T., & Narwid, A. 2006, Mem. Soc. Astron. Italiana, 77, 223

Planck Collaboration 2016, A&A, 594, A1

Poretti, E., Suárez, J. C., Niarchos, P. G., et al. 2005, A&A, 440, 1097

Press, W. H., & Rybicki, G. B. 1989, ApJ, 338, 277

Qi, Z., Yu, Y., Bucciarelli, B., et al. 2015, AJ, 150, 137

Renedo, I., Althaus, L. G., Miller Bertolami, M. M., et al. 2010, ApJ, 717, 183

Riess, A. G., Filippenko, A. V., Challis, P., et al. 1998, AJ, 116, 1009

Robinson, E. L., Kepler, S. O., & Nather, R. E. 1982, ApJ, 259, 219

Robinson, E. L. 2016, Data Analysis for Scientists and Engineers, (Princeton University Press)

Rybicki, G. B., & Lightman, A. P. 1979, Radiative Processes in Astrophysics (New York: Wiley)

Saio, H. 2013, European Physical Journal Web of Conferences, 43, 05005

Salaris, M., Domínguez, I., García-Berro, E., et al. 1997, ApJ, 486, 413

Schatzman, E. 1945, Annales d'Astrophysique, 8, 143

Shanks, T., Metcalfe, N., Chehade, B., et al. 2015, MNRAS, 451, 4238

Shappee, B. J., Prieto, J. L., Grupe, D., et al. 2014, ApJ, 788, 48

Shporer, A., Kaplan, D. L., Steinfadt, J. D. R., et al. 2010, ApJ, 725, L200

Still, M., & Barclay, T. 2012, Astrophysics Source Code Library, 1208.004

Thompson, S., & Mullally, F. 2013, Astrophysics Source Code Library, ascl:1304.004

Tremblay, P.-E., & Bergeron, P. 2008, ApJ, 672, 1144

Tremblay, P.-E., & Bergeron, P. 2009, ApJ, 696, 1755

Tremblay, P.-E., Bergeron, P., & Gianninas, A. 2011a, ApJ, 730, 128

Tremblay, P.-E., Gianninas, A., Kilic, M., et al. 2015, ApJ, 809, 148

Tremblay, P.-E., Ludwig, H.-G., Steffen, M., Bergeron, P., & Freytag, B. 2011b, A&A, 531, L19

Tremblay, P.-E., Ludwig, H.-G., Steffen, M., & Freytag, B. 2013, A&A, 559, A104

Twicken, J. D., Chandrasekaran, H., Jenkins, J. M., et al. 2010, Proc. SPIE, 7740, 77401U

Unno, W., Osaki, Y., Ando, H., Saio, H., & Shibahashi, H. 1989, Nonradial oscillations of stars, Tokyo: University of Tokyo Press, 2nd ed.

Uytterhoeven, K., Moya, A., Grigahcène, A., et al. 2011, A&A, 534, A125

Van Cleve, J. E., Howell, S. B., Smith, J. C., et al. 2016, PASP, 128, 075002

Van Grootel, V., Dupret, M.-A., Fontaine, G., et al. 2012, A&A, 539, A87

Van Grootel, V., Fontaine, G., Brassard, P., & Dupret, M.-A. 2013, ApJ, 762, 57

van Horn, H. M. 1971, White Dwarfs, 42, 97

Van Horn, H. M. 2015, Unlocking the Secrets of White Dwarf Stars, Astronomers' Universe, ISBN 978-3-319-09369-7. Springer International Publishing Switzerland

van Kerkwijk, M. H., Rappaport, S. A., Breton, R. P., et al. 2010, ApJ, 715, 51

Vanderburg, A., & Johnson, J. A. 2014, PASP, 126, 948

Vanderburg, A., Johnson, J. A., Rappaport, S., et al. 2015, Nature, 526, 546

VanderPlas, J. 2016, Astrophysics Source Code Library, ascl:1610.007

VanderPlas, J. T. 2017, arXiv:1703.09824

von Zeipel, H. 1924, MNRAS, 84, 665

Wang, F. Y., & Dai, Z. G. 2013, Nature Physics, 9, 465

Wang, S.-G., Su, D.-Q., Chu, Y.-Q., Cui, X., & Wang, Y.-N. 1996, Appl. Opt., 35, 5155

Walkowicz, L. M., Basri, G., Batalha, N., et al. 2011, AJ, 141, 50

Wickramasinghe, D. T., & Ferrario, L. 2000, PASP, 112, 873

Williams, K. A., Bolte, M., & Koester, D. 2009, ApJ, 693, 355

Wilson, R. F., Bell, K. J., Harrold, S. T., et al. 2015, Proceedings of the Frank N. Bash Symposium 2015 (BASH2015), 18

Winget, D. E. 1982, Ph.D. Thesis,

Winget, D. E., Hansen, C. J., Liebert, J., et al. 1987, ApJ, 315, L77

Winget, D. E., Hermes, J. J., Mullally, F., et al. 2015, 19th European Workshop on White Dwarfs, 493, 285

Winget, D. E., & Kepler, S. O. 2008, ARA&A, 46, 157

Winget, D. E., Nather, R. E., Clemens, J. C., et al. 1991, ApJ, 378, 326

Wood, M. A. 1990, Ph.D. Thesis, The University of Texas at Austin

Wu, Y., & Goldreich, P. 2001, ApJ, 546, 469

Zhang, X. B., Fu, J. N., Li, Y., Ren, A. B., & Luo, C. Q. 2016, ApJ, 821, L32